

LEUCOCRATIC & GABBROIC
XENOLITHS FROM HUALĀLAI VOLCANO, HAWAI'I

A THESIS SUBMITTED TO THE GRADUATE DIVISION OF THE
UNIVERSITY OF HAWAI'I IN PARTIAL FULFILLMENT
OF THE REQUIREMENTS FOR THE DEGREE OF

MASTER OF SCIENCE

IN

GEOLOGY & GEOPHYSICS

DECEMBER 2004

By
Patrick J. Shamberger

Thesis Committee:

Julia E. Hammer, Chairperson
Michael O. Garcia
John Sinton

We certify that we have read this thesis and that, in our opinion, it is satisfactory in scope and quality as a thesis for the degree of Master of Science in Geology & Geophysics.

THESIS COMMITTEE

Chairperson

ACKNOWLEDGEMENTS

I am grateful to D. Clague for the loan of his Hualālai xenolith collection and for discussions on the PWW trachyte episode. Thanks to J. Sinton for the use of his unpublished W Maui data. Special thanks to K. Ross and C. Fraley for EMP and XRF support, S. Krot for access to SEM facilities, and J. Sinton for access to XRF facilities. This thesis has greatly benefited from discussions with my committee members, M. Garcia and J. Sinton, and the countless hours invested by my advisor, J. Hammer. Research was supported by the following: NWS fellowship (SOEST), H.T. Stearns grant (Dept. of Geol. & Geophys., UH-Manoa), graduate student research grant (Geological Society of America), thesis completion grant (UH-Manoa).

ABSTRACT

The magma storage conditions of the distinctive Pu‘u Wa‘awa‘a (PWW) trachyte eruption on Hualālai Volcano remain poorly understood. New mineral and whole-rock compositional data of plutonic nodules with similar evolved alkaline geochemical affinities may constrain these conditions. These advances offer insight into changes in magma storage depth during the shield to post-shield transition at Hualālai Volcano. Summit xenoliths compose three suites: (1) chilled alkalic liquids and alkali-feldspar bearing gabbro cumulates, (2) sub-alkaline gabbro-norite cumulates, and (3) diverse xenoliths not apparently related to groups (1) or (2). Series (1) xenoliths may be related to the PWW trachyte. Thermodynamic models of clinopyroxene and feldspar compositions, fractionating assemblages inferred from bulk major and trace element compositions, and normative compositions of intermediate melts all indicate that the trachyte formed at pressures ~3-7 kbar. This pressure range suggests reservoir depths significantly deeper than previous models of the PWW trachyte magma chamber and may indicate a shift to deeper magma storage at the onset of the post-shield stage. Fine-grained dioritic xenoliths of series (1), which may approximate original liquid compositions, are all mildly silica-saturated, suggesting that the PWW trachyte fractionated from a hypersthene-normative alkalic or transitional parent, consistent with Pb isotopic evidence. Bulk compositions of these xenoliths partially fill the gap between erupted alkalic basalts (MgO >4 wt%, SiO₂ <49 wt%) and trachytes (MgO <0.5 wt%, SiO₂ >60 wt%). Such a large compositional gap is not a common feature of Hawaiian alkalic suites, despite their similar liquid lines of descent. This suggests that bimodal

volcanism on Hualālai is not caused solely by compositionally dependent mechanisms, such as viscous trapping, as proposed at other ocean island volcanoes (e.g., Rarotonga).

TABLE OF CONTENTS

ACKNOWLEDGEMENTS.....	iii
ABSTRACT.....	iv
LIST OF TABLES	ix
LIST OF FIGURES.....	x
CHAPTER 1. INTRODUCTION.....	1
GEOLOGIC BACKGROUND	6
CHAPTER 2. METHODS.....	9
X-RAY FLUORESCENCE SPECTROMETRY TECHNIQUES	9
ELECTRON MICROPROBE TECHNIQUES	13
MODE CALCULATIONS.....	14
NOMENCLATURE.....	15
CHAPTER 3. PETROGRAPHY	19
SYENO-XENOLITH SERIES	19
GABBRONORITE SERIES	27
COINCIDENT SERIES.....	33
Poikilitic Gabbros	34
Anorthosites	34
CONTACT RELATIONS	38

CHAPTER 4. RESULTS.....	42
WHOLE ROCK COMPOSITIONS	42
MINERAL COMPOSITIONS.....	42
Monzodiorites	46
Diorites.....	50
Syenogabbro	51
Gabbronorites.....	51
Coincident Xenoliths	52
THERMOBAROMETRIC CALCULATIONS	53
Fe-Ti Oxides	54
QUIIF	56
Ternary Feldspar Models	60
Pyroxene Geobarometers	66
CHAPTER 5. DISCUSSION.....	73
PETROGENESIS OF PLUTONIC FRAGMENTS.....	73
Cumulates vs. Solidified Magmas	74
Syeno-xenolith Series	82
Gabbronorite Series	97
Coincident Xenoliths	100
ALKALIC LIQUID LINE OF DESCENT.....	101
Liquidus Phases	102
Mass Balance Modeling.....	106

Comparison with MELTS and Experimental Data.....	110
Comparison with Evolved Post-Shield Hawaiian Alkalic Series	115
Three-phase Saturated Pseudo-cotectic	121
COMPOSITIONAL GAP	126
Causes for Compositional Gap	127
Role of Extrinsic Factors	130
Trachyte Minimum	132
CHAPTER 6. SHIELD TO POST-SHIELD TRANSITION ON HUALĀLAI	
VOLCANO	135
CHAPTER 7. CONCLUSIONS	140
APPENDIX A. GEOCHEMICAL DATA.....	143
APPENDIX B. MASS BALANCE CALCULATIONS.....	155
APPENDIX C. GEOCHEMICAL DATA SOURCESREFERENCES	159
REFERENCES.....	168

LIST OF TABLES

<u>Table</u>	<u>Page</u>
2.1 Mineralogical Modes	16
3.1 Xenolith Grain Sizes and Textures	20
4.1 Summary of Thermodynamic Calculations	57
4.2 Experimental Melt Compositions used in Ti/Al Cpx geobarometer	68
5.1 Whole Rock, Mineral, and Equilibrium Melt Mg Numbers	80

LIST OF FIGURES

<u>Figure</u>	<u>Page</u>
1.1 Map of Hualālai Volcano	7
2.1 Summit Map of Hualālai Volcano	11
2.2 Summit Xenolith Componentry	12
2.3 Xenolith Classifications (QAPF diagram)	17
3.1 Photomicrographs of Syeno-xenolith Series	24
3.2 BSE Images of Syeno-xenolith Series	26
3.3 Photomicrographs of Gabbonorite Series	30
3.4 BSE Images of Gabbonorite Series	31
3.5 Photomicrographs of Coincident Series	36
3.6 BSE Images of Coincident Series	37
3.7 Photomicrographs of Lithological Contacts	40
3.8 BSE Images of Lithological Contacts	41
4.1 Xenolith Whole Rock Compositions (MgO variation diagrams)	44
4.2 Xenolith Whole Rock Compositions (TAS diagram)	45
4.3 Feldspar Compositions	47
4.4 Pyroxene and Olivine Compositions	48
4.5 Fe-Ti Oxide Compositions	49
4.6 Results of Fe-Ti Oxide Pair Thermobarometry	55
4.7 Results of Ternary Feldspar Modeling	64

4.8	Calculated Feldspar Solvi	65
4.9	Clinopyroxene Ti/Al Ratios	69
4.10	Results of Nimis & Ulmer Pyroxene Geobarometer	71
5.1	Mineral Mg Number Equilibria	79
5.2	Nb vs. Zr	85
5.3	Nb vs. MgO	86
5.4	Nb vs. Nb/Zr	87
5.5	Mineral Compositions (plagioclase An # and mafic mineral Mg #)	89
5.6	Silica-saturation of Hualālai Lavas and Plutonics	93
5.7	Silica-saturation of Laupāhoehoe and Hāwī Series	95
5.8	Trace element inferred LLDs	103
5.9	Mass balance end-members (TAS diagram)	107
5.10	Results of fractional crystallization MELTS modeling	111
5.11	Results of equilibrium crystallization MELTS modeling	112
5.12	Hawaiian Alkalic LLDs (MgO variation diagrams)	118
5.13	Hawaiian Alkalic LLDs (TAS diagram)	119
5.14	Hawaiian Alkalic Fe-enrichment (AFM plot)	120
5.15	1 bar Pseudo-cotectic in the Basalt Tetrahedron	122
5.16	Ol-Cpx-Ne Pseudo-ternary Diagram	123
5.17	Ol-Cpx-Ne-Qz Tetrahedral Diagram	124
5.18	Silica Concentrations with Crystallinity ($d[\text{SiO}_2]/d\phi$)	128
5.19	Petrogeny's Residua	133

6.1 Magma Storage Model 136

CHAPTER 1. INTRODUCTION

The trachytic Pu‘u Wa‘awa‘a (PWW) pumice cone and the coeval Pu‘u Anahulu (PA) lava flow dominate the northern flank of Hualālai in the North Kona region of the island of Hawai‘i. These prominent features record a unique, and poorly understood, episode in the evolution of a Hawaiian volcano. Highly evolved alkalic magma on the Hawaiian islands tends to erupt in small volumes (Macdonald, 1963), accompany intermediate composition lavas (Spengler & Garcia, 1988; Frey *et al.*, 1990), and occur late in the post-shield alkalic period. However, none of these generalizations are true of the Hualālai trachyte. The large combined volume of PWW cone and PA flow, estimated at $\sim 5.5 \text{ km}^3$, make this the largest known single eruption on the island of Hawai‘i (Moore *et al.*, 1987); this volume is similar in size to major silicic eruptions such as 1991 Pinatubo ($3.7\text{-}5.3 \text{ km}^3$ of erupted magma (3.7-5.3 km³ of erupted magma, Scott *et al.*, 1996). Equally intriguing is the observed gap in silica contents of Hualālai alkalic lavas between the PWW and PA trachytes ($\text{SiO}_2 \sim 61\text{-}64 \text{ wt}\%$), and the most evolved hawaiites found on the subaerial surface ($\text{SiO}_2 < 49 \text{ wt}\%$). Finally, the trachyte eruption followed soon after the end of tholeiitic volcanism (within 20 kyr), prior to the onset of the post-shield alkalic period (Cousens *et al.*, 2003). These characteristics suggest that the PWW / PA eruption represents a departure from standard patterns of Hawaiian alkalic volcanism, and therefore may provide insight into the effects of subtle variations in both extrinsic (e.g., confining pressure) and intrinsic (e.g., magma supply) controls on the development of Hawaiian magma chamber systems.

The circumstances leading to the genesis of the trachyte magma remain unclear. Cousens *et al.* (2003) suggest that it derived from an alkalic parent through extensive crystal fractionation, citing isotopic evidence linking the trachyte to other erupted alkali basalts. These authors support a shallow level magma chamber hypothesis (~3-7 km deep) based on: (1) the lack of peridotite xenoliths found in the trachyte and (2) the presence of felsic xenoliths (presumably the remnants of the trachyte magma chamber) over a very limited region near the summit. Additionally, the timing of the trachyte genesis corresponds to the transition between the tholeiitic shield stage and the alkalic post-shield stage, and presumably to a decrease in magma supply (Cousens *et al.*, 2003). Clague (1987b) argued that the corresponding decrease in heat flux through the system led to the rapid crystallization of a shallow Kilauea-like chamber that was no longer sustainable under low magma supply conditions. Residual magma from this chamber then erupted as the highly evolved trachyte.

Shallow genesis of the trachyte magma contrasts with the notion of a deep-rooted magma chamber (~8 kbar) proposed by Frey *et al.* (1990) to explain the moderately evolved late stage, post-shield alkalic volcanics found on Mauna Kea. In this case, high pressure conditions shift the olivine-plagioclase-clinopyroxene saturated pseudo-cotectic towards olivine, and affect the liquid line of descent of erupted lavas. Recent experimental studies on hydrous fractionation trends (Nekvasil *et al.*, 2004) suggest that, in addition to increased pressure, increased $p\text{H}_2\text{O}$ might also favor the formation of trachyte in hypersthene-normative alkalic suites. As with pressure, greater $p\text{H}_2\text{O}$ delays the onset of plagioclase crystallization, increasing the magmatic alkali concentration.

Low pressure and high pressure fractionation histories require very different mechanisms and have distinct implications for the development of the magmatic system at Hualālai. Specifically, the fractionation pressure of the PWW trachyte magma may indicate the general response of magma storage depth to the transition from shield to post-shield stages. Despite the importance of resolving the conditions during crystal fractionation, the lack of both intermediate lavas and phenocrysts (with the exception of nepheline) in the trachyte makes this nearly impossible.

Crystal fractionation is thought to be the dominant process responsible for producing differentiated magmas in ocean island settings (e.g., Ascension Island (Kar *et al.*, 1998), Canary Islands (Freundt & Schmincke, 1995)). However, a paucity of intermediate composition lavas, expected to be generated during crystal fractionation, is observed at many of these island chains (e.g., Ascension Island (Daly, 1925), Canary Islands (Chayes, 1977; Freundt & Schmincke, 1995), Rarotonga (Thompson *et al.*, 2001)). Explanations for this paradox, referred to as the ‘Daly Gap’, include: (1) buoyant and viscous controls impeding the eruption of intermediate compositions (Marsh, 1981; Bedard *et al.*, 1984; McBirney *et al.*, 1985), (2) a rapid rate of compositional change with degree of crystallinity ($d[\text{SiO}_2]/d\phi$) over ~50-60 wt% SiO₂ leading to a decreased abundance of intermediate magmas relative to both end-members (Clague, 1978), and (3) the possibility of competing thermochemical steady states in the magma chamber (i.e., basaltic and trachytic) linked by a rapid, catastrophic transition (Bonnefoi *et al.*, 1995). The diversity of conceptual models for this phenomenon attests to its unresolved status. The relative prevalence of bimodal alkalic volcanism on ocean island chains other than

the Hawaiian islands may imply a contrast in processes occurring in these settings. As the Hawaiian islands have been vigorously studied and serve as the standard model for basaltic ocean islands, addressing this contrast is an important step in understanding ocean island volcanism in general. The PWW and PA eruption of trachyte at Hualālai Volcano is the most prominent example of bimodal volcanism in Hawai‘i, and therefore represents an opportunity to test suggested models.

Evolved crystalline xenoliths erupted from Hualālai may allow us to further study the magmatic differentiation process that ultimately led to the eruption of trachyte. Moore *et al.* (1987) suggest that felsic nodules found in the summit region, referred to by these and subsequent authors as ‘syenites’, are cumulates related to the trachyte magma chamber. Principle evidence supporting this supposition includes the dominance of plagioclase and alkali feldspar, and the presence of late stage and hydrous minerals including apatite, zircon, and biotite. Plutonic rocks with this assemblage are exceedingly rare in Hawai‘i, and have only been reported in one other case (Fodor, 2001). In his study of Mauna Kea xenoliths, Fodor describes leucocratic diorites with mineral assemblages nearly identical to the ‘syenites’ of Hualālai. These xenoliths are also thought to be associated with crystallization of post-shield alkalic magmas (transitional between the Hamākua and the Laupāhoehoe series). The large volume trachyte eruption at Hualālai necessitates an even larger volume, by up to a factor of 20x (Cousens *et al.*, 2003), of subsurface cumulate minerals produced during crystal fractionation, so it is not at all surprising that crystalline rocks should exist within the volcanic edifice.

Crystalline nodules, studied both in Hawai‘i and elsewhere, have led to insights into conditions in fractionating magma chambers. A wealth of information is recorded in mineral assemblages and compositions, which both depend on the intrinsic parameters of the crystallizing environment (Fodor & Vandermeijden, 1988; Tait *et al.*, 1989; Fodor & Galar, 1997; Thompson *et al.*, 2001). Plutonics have also successfully served as proxy for intermediate composition magmas when erupted lavas exhibited a compositional gap. Such nodules were interpreted as the product of melt segregation during crystal fractionation (Freundt-Malecha *et al.*, 2001).

This study seeks to understand three principle questions that can only be approached through a thorough analysis of the evolved crystalline xenoliths. Questions addressed include: (1) Are the PWW trachytes the product of crystal fractionation of an alkalic parent, as proposed by Cousens *et al.* (2003)? (2) What are the intensive properties of the magmatic system during crystal fractionation (P, fO_2 , pH_2O , etc.)? (3) What are possible causes of the large compositional gap on Hualālai? To achieve this goal, bulk and mineral compositions were determined for Hualālai xenoliths. Bulk compositions of select xenoliths are used to reconstruct the trachyte liquid line of descent (LLD) and to infer parental composition. Mineral data are interpreted in light of different thermodynamic models, constraining magma conditions. Finally, the inferred LLD at Hualālai is compared to other Hawaiian alkalic LLDs in order to test hypotheses explaining the existence of a large compositional gap.

Geologic Background

Hualālai Volcano is located on the western coast of the island of Hawai‘i, due west of Mauna Kea and northwest of the summit caldera of Mauna Loa (see fig. 1.1). The third youngest volcano on the island, Hualālai has erupted as recently as 1801. A month-long seismic swarm in 1929 may have indicated further magmatic activity within the volcanic edifice (Macdonald *et al.*, 1983). A thin layer of alkalic and transitional basalts mantle the subaerial volcanic edifice. Tholeiite lavas predating alkalic volcanism have only been recovered from the submarine flanks of the volcano and from water wells drilled into its surface (Clague, 1982; Garcia *et al.*, 1989; Hammer & Shamberger, 2003). The youngest known tholeiite eruption occurred ~133 ka, as determined from the age of a submerged reef mantled by tholeiite lavas (Moore & Clague, 1992).

The oldest subaerial surficial lavas on Hualālai, dated at 113.5 ± 3.2 ka, are the ~1.5 km diameter trachyte Pu‘u Wa‘awa‘a pumice cone and >275 m thick Pu‘u Anahulu lava flow (Cousens *et al.*, 2003). These units compose the Waawaa Trachyte Member of the Hualālai Volcanics. Nepheline-bearing trachytes of similar ages (92.0 ± 6.0 ka – 107 ± 9.8 ka) have also been found in water well drill holes at the NW tip of the main rift zone, and as blocks in a maar deposit (Cousens *et al.*, 2003). The presence of a low-amplitude gravity high displaced south of the summit and rift zone (Kauahikaua *et al.*, 2000), as well as a pronounced aeromagnetic low over the summit and rift zone regions, has been interpreted to result from large volumes of subsurface trachyte (Moore *et al.*, 1987). These observations suggest that the total volume of trachytes could be

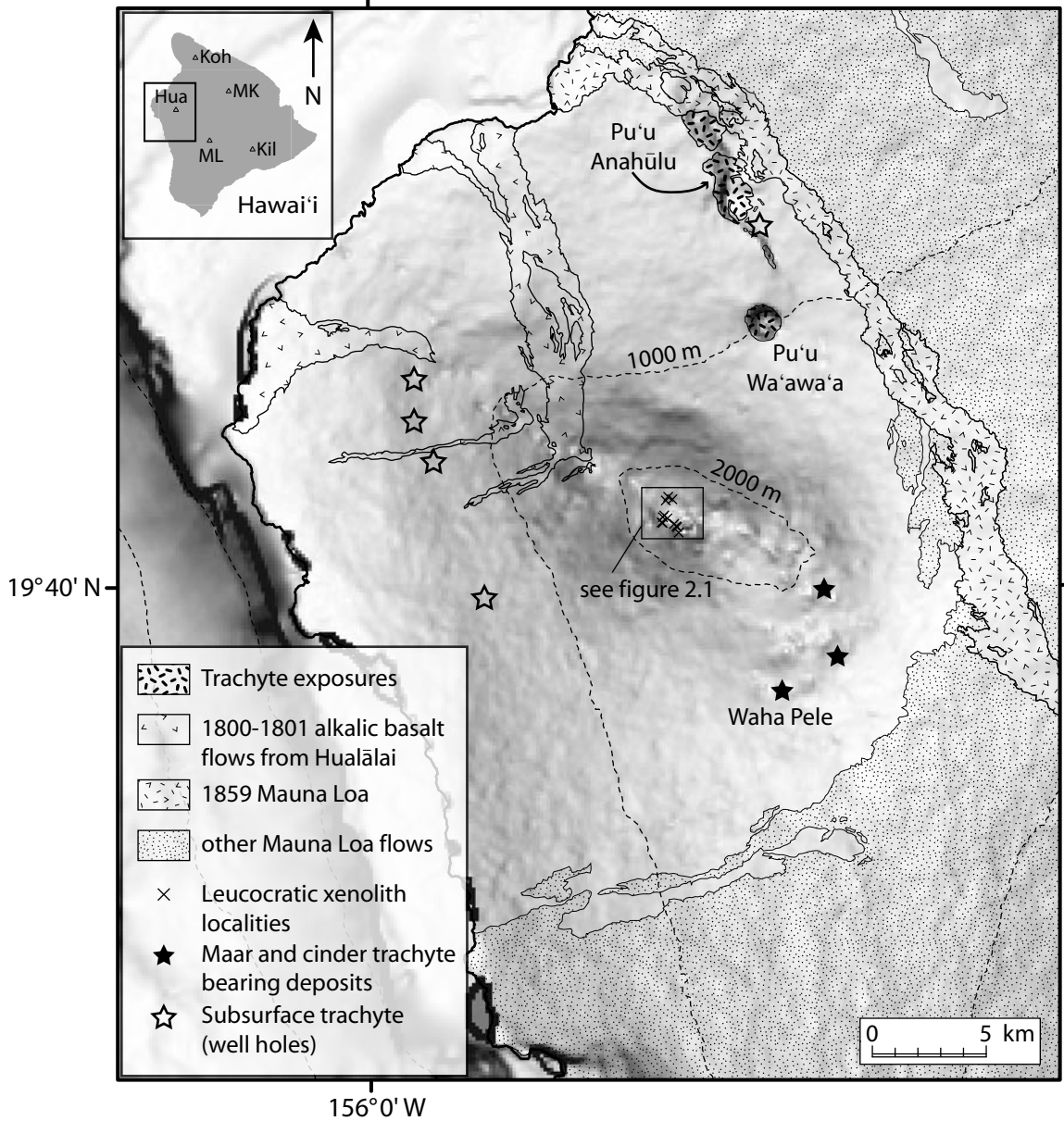


Figure 1.1: Map of Hualālai indicating trachyte and leucocratic xenolith localities. All xenoliths described in this study were collected at summit sites (×). Trachyte exposures include the Pu'u Wa'awa'a obsidian and pumice cone and the Pu'u Anahū trachyte flow. Inset locates Hualālai (Hua) with respect to Kilauea (Kil), Mauna Loa (ML), Mauna Kea (MK), and Kohala (Koh). Geologic units from the Geologic Map of Hualālai Volcano, Hawai'i (Moore & Clague, 1991), trachyte occurrences described in Cousens *et al.* (2003).

significantly greater than estimates based on surface exposures, which comprise a prodigious 5 km³ (Moore *et al.*, 1987).

Other alkalic members of the Hualālai Volcanics mantle the remaining ~98% of Hualālai's surface. These vents, cones, and flows extend compositionally from transitional alkalic basalts to hawaiites (up to ~49 wt% SiO₂). Eruptions are focused primarily along Hualālai's NW and SSE rift zones, although a third poorly-defined rift zone, containing less than 5% of the exposed vents, extends to the north (Moore *et al.*, 1987). Most vents are marked by cinder and spatter cones smaller than those produced by the late eruptions of Mauna Kea and Kohala (Macdonald *et al.*, 1983). The oldest of the alkalic basalts is ~13 ka (Moore *et al.*, 1987). The Ka'ūpūlehu eruption (ca. 1800), is notable for its prominent ultramafic xenolith deposits, which have sparked debate about the fluidity of the lava and possible rapid rates of emplacement (Chen-Hong *et al.*, 1992; Baloga *et al.*, 1995; Guest *et al.*, 1995; Kauahikaua *et al.*, 2002). While mafic crustal xenoliths occur in many lava flows on the flanks of Hualālai, leucocratic xenolith localities identified thus far are limited to the summit region (fig. 1.1). Leucocratic gabbro and diorite nodules are concentrated in tephra and spatter deposits of small-volume ~3-5 ka eruptions (Moore & Clague, 1991). The known distribution of the leucocratic xenoliths is an area about 2 km in diameter centered on 19°41'38"N, 155°52'28"W, and includes at least five separate vents of similar age (Moore & Clague, 1991).

CHAPTER 2. METHODS

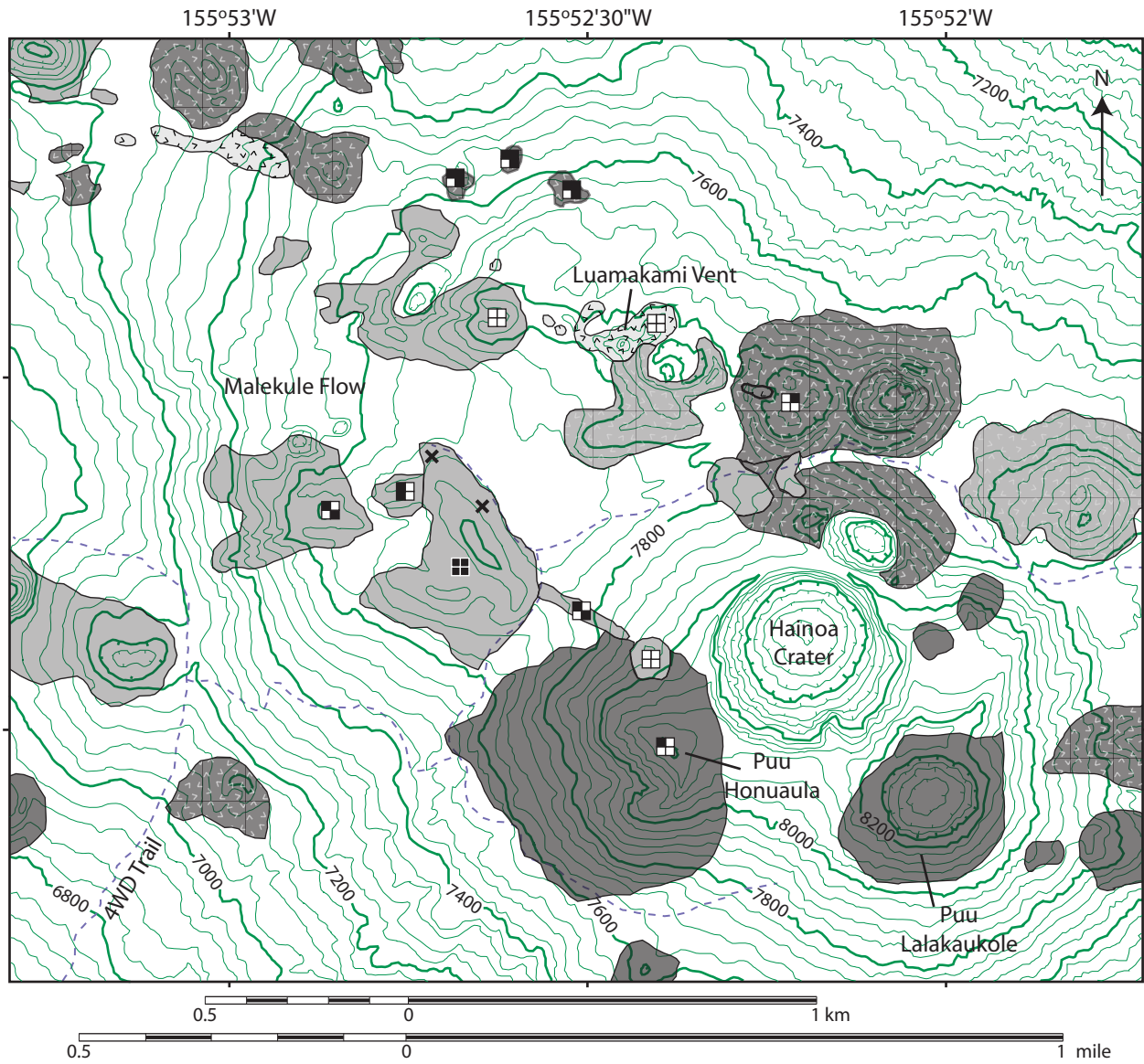
Over 250 crystalline nodules were collected from the study area at the summit of Hualālai Volcano (fig. 2.1). Individual xenoliths ranged from less than 10 g to nearly 4 kg. These samples were classified as gabbronorites, olivine gabbronorites, syenogabbros, diorites, poikilitic gabbros and anorthosites, based on mineralogy, estimated modes, and grain size. Gabbronorites are the most common xenolith lithologies present in this area (fig. 2.2). Thin sections were prepared from 36 xenoliths representative of each of the initial classifications. Thin sections from 48 additional nodules collected at the summit site were provided by D. Clague (MBARI). Detailed petrography (see petrography section) shows that the preliminary classification of samples closely matches the formal assessment of sample lithologies. From the combined set of 84 thin sections, we selected 13 samples representing the principle lithologies and spanning the variation within those lithologies for detailed chemical and petrographic analysis. Whole rock compositional analysis of 16 xenoliths and two trachyte lava samples were obtained by x-ray fluorescence (XRF) spectrometry. Sample suites overlapped whenever possible, however small volumes of a few samples from the original set of thirteen precluded the possibility of obtaining whole rock compositions of those samples.

X-ray Fluorescence Spectrometry Techniques

X-ray fluorescence spectrometry was performed on the University of Hawai‘i Siemens 303AS fully automated, wavelength-dispersive, XRF spectrometer. Samples were crushed in a tungsten carbide (WC) hydraulic splitter. Less visibly altered and

Figure 2.1: Map of the Hualālai summit study region. Each vent is labeled according to xenolith lithologies present in associated tephra and spatter deposits (GN = gabbronorites, OGN = olivine gabbronorites, D = diorites and monzodiorites, SG = syenogabbros). Diorites and syenogabbros principally correspond with 3-5 ka vents. Vents which erupted only spatter and fluid lava flows (e.g., Luamakami) may have exhumed xenoliths now covered by lava. Two bulk samples (×) were gathered from a single vent to determine xenolith componentry. Topography and geologic units from the Geologic Map of Hualalai Volcano, Hawai'i (Moore & Clague, 1991). Contour elevations are indicated in feet.






11



Lithologies Present:

GN	OGN
D	SG

Age of Vents:

-  0.75-1.5 ka
-  1.5-3 ka
-  3-5 ka
-  5-10 ka
-  10-25 ka

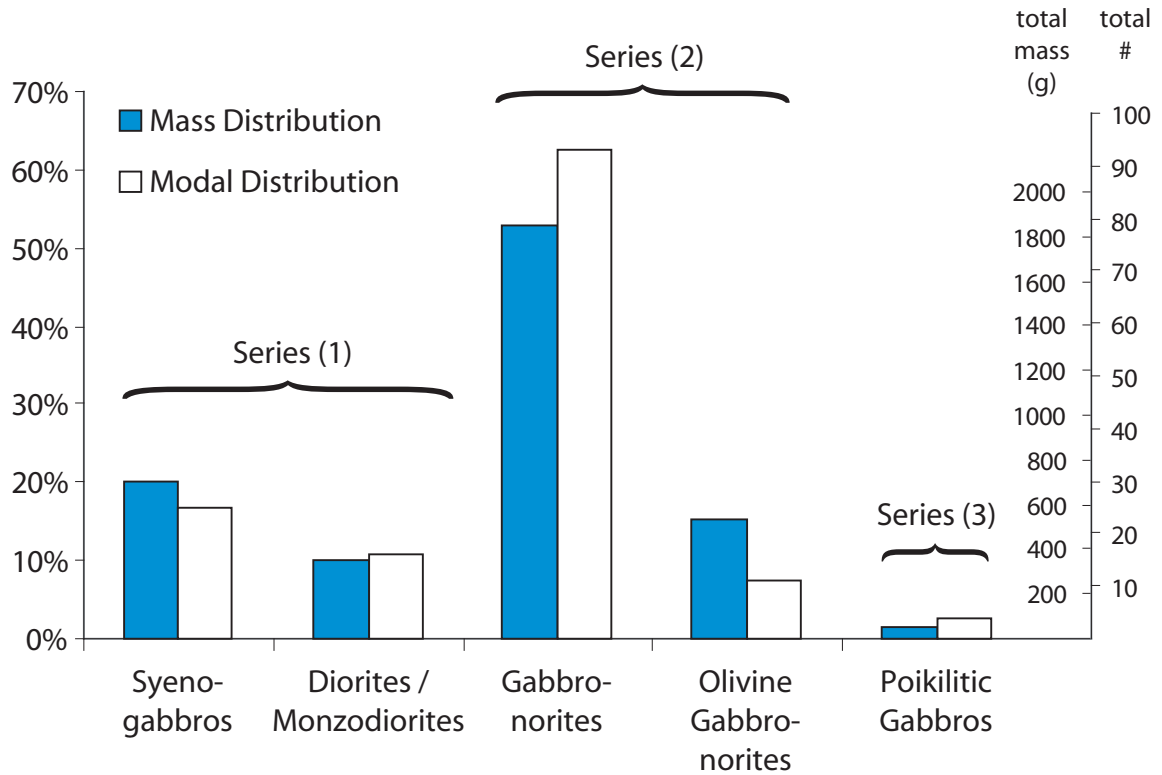


Figure 2.2: Representative componentry of summit xenolith deposits. Lithological proportions are determined from componentry analysis of two bulk samples (diameters -6.0 to -3.5 ϕ) from a single vent (fig. 2.1). n = 149 xenoliths, and total mass = 3.49 kg.

oxidized chips were picked, rinsed in water and ground in either a WC ball mill or small WC swing mill into a fine powder. Duplicate fused buttons and a pressed powder pellet were prepared for samples following methods similar to Noorish & Hutton (1969) and Chappell (1991). Samples were analyzed for major and trace elements (Sc, V, Cr, Co, Ni, Zn, Rb, Sr, Y, Zr, Nb, Ba, Pb, and Th).

Analytical uncertainty of major and minor elements is estimated from repeat analysis of standards. Absolute accuracies of all elements are less than 0.25 oxide wt%. Minor element oxides TiO₂, MnO, K₂O, and P₂O₅ are accurate within 0.03 oxide wt%. Absolute accuracy for each oxide is reported alongside bulk compositions (appx. A). Analytical precision is typically smaller than the reported accuracy due to high count rates.

Electron Microprobe Techniques

Electron microprobe (EMP) analysis was performed at the University of Hawai'i CAMECA SX-50 five-spectrometer electron microprobe. Accelerating voltage was maintained at 15 kV and beam current between 10-30 nA in a beam-regulated mode. Minerals susceptible to volatile loss (feldspars, clinopyroxene, and biotite) were probed at lower beam currents (10-20 nA) with a defocused spot (5-10 μm diameter). Olivine, Fe-Ti oxides, and amphiboles generally occur as small grains and required a focused spot (1-3 μm diameter). Whenever analyzed, Na was counted first. Counting time for all analyses was at least 30 s on peaks, but lasted up to 60 s for certain minor elements in order to improve counting statistics. Backgrounds were determined linearly from two

points on either side of the peak; these points were each counted for half of the peak count time. Calibrations were performed on natural and synthetic mineral standards provided primarily by the Smithsonian Institute. Reported concentrations were calculated using a PAP correction procedure (Pouchou & Pichoir, 1988).

Analytical accuracy was determined by comparing repeat analyses of mineral standards (collected both before and after analysis of xenolith samples) against their published compositions. Major elements deviate by $\leq \sim 1\%$ relative, while minor and trace elements deviate by $\leq \sim 10\%$. Absolute accuracy, determined from repeated analysis of mineral standards, are reported in appendix A.

Mode Calculations

Modes were determined using two independent techniques: point counting of thin sections (350 - 500 points per section, dependent on grain size) using a standard petrographic microscope, and image analysis of 5 to 8 low-magnification (75x) backscatter electron (BSE) images captured on a JEOL scanning electron microscope. In the latter method, phases were identified in spot mode using an energy-dispersive spectrometer, facilitating registration of gray scale values for each phase. An additional 2 to 7 images were necessary to distinguish ratios of different Fe-Ti oxides (e.g., magnetite, ilmenite, hematite) and apatite, as these phases appear saturated in images collected at conventional SEM brightness settings. Area percentages of phases were determined using the Scion Image freeware package (based on the public domain NIH Image program, developed at the U.S. National Institutes of Health and available on the Internet

at <http://rsb.info.nih.gov/nih-image/>). Stereology indicates that area-based modes are equivalent to volume-based modes if random two dimensional sections are sampled from isotropic materials (Russ, 1986). The lack of fabric in Hualālai xenoliths allows area-based results from a single thin section to be interpreted as volumetric.

For most samples, these two techniques converged to within 5 vol.% for all phases. Modes reported in table 2.1 are those calculated using the image analysis technique, except for two very coarse grained samples (HM45 and HM47) for which the point-counting results are given. Oxide (ilm:mag), feldspar (plag:K-fs), and mafic mineral (cpx:opx:ol) ratios have been adjusted for these samples to reflect the relative abundances observed in BSE images. This technique combines advantages of both point counting (larger sample coverage) and image analysis (accurate phase discrimination – e.g., alkali feldspar vs. plagioclase). Multiple samples (e.g., HM02) include two distinct contacting lithologies. Each lithology was treated separately and modes were calculated for both halves. These pairs will be referred to as parts ‘a’ and ‘b’ (e.g. HM02a), where both parts are distinct lithologic members of a single xenolith.

Nomenclature

Formal classification of xenoliths according to mineralogy, modes, and feldspar composition corresponds well with our provisional categorizations based solely on observation of hand samples. Following Le Maitre *et al.* (2002), feldspars, quartz and feldspathoids are normalized to 100 vol.% for plotting on a quartz-alkali feldspar-plagioclase-feldspathoid (QAPF) diagram (fig. 2.3). Diorites and gabbros contain 90-

Table 2.1: Modes of xenoliths determined by image analysis and point counting^a.

Sample ID: Lithologies ^d :	Syeno-Xenoliths							Gabbronorite Xenoliths				Coincident Xenoliths			
	HM06	HM01a ^b	HM43	HM02a ^b	HM12	HM19	HM45 ^c	HM44	HM47 ^c	HM50a ^b	HM53	HM02b ^b	HM23	HM35	HM50b ^b
	MD	MD	D	D	D	D	SG	GN	GN	HGN	OGN	A	A	PG	HGN
Plagioclase	64	73	61	67	59	76	72	68	62	24	35	92	92	54	37
K-Feldspar	13	9	7	6	1	1	1	-	-	-	-	8	2	-	-
Clinopyroxene	2	8	17	20	20	11	17	18	22	52	14	< 1	6	46	4
Orthopyroxene	7	< 1	-	< 1	< 1	3	-	10	10	< 1	28	-	-	-	13
Olivine	-	-	-	-	1	-	< 1	< 1	1	-	21	-	-	-	-
Biotite	4	< 1	4	< 1	4	< 1	5	< 1	< 1	1	-	-	< 1	-	4
Amphibole	-	-	< 1	-	-	-	< 1	1	< 1	20	-	-	-	-	40
Apatite	2	1	< 1	< 1	2	3	1	< 1	< 1	-	< 1	< 1	< 1	-	< 1
Zircon	< 1	-	< 1	< 1	< 1	-	-	-	-	-	-	-	< 1	-	-
Fe-Ti Oxides															
Magnetite	3	6	7	< 1	8	3	3	2	4	3	-	-	< 1	-	1
Ilmenite	2	2	4	6	5	4	1	1	2	< 1	< 1	< 1	< 1	-	-
Hematite	< 1	-	-	< 1	-	-	-	-	-	-	< 1	-	< 1	-	-
Fe-Sulfide	-	-	< 1	-	-	-	-	-	-	-	1	-	-	-	-
Quartz	3	-	-	-	-	-	-	-	-	-	-	-	-	-	-
Re-normalized ternary modes															
Plag	80	89	90	92	99	99	98					92	98		
K	16	11	10	8	1	1	2					8	2		
Qz	4	-	-	-	-	-	-					-	-		

^a Modes gathered from a series of back-scatter scanning electron microscope (SEM) images and confirmed with point counts of 500 points per thin section. ^b Xenoliths with two lithologies (compositionally and petrographically distinct from each other) are labeled as a pair (e.g., HM02a / HM02b) and are treated separately throughout this paper. ^c Very coarse grain size samples whose modes in SEM images deviate from point count tabulated modes. Reported modes for these samples are based on point counts, but with Fe-Ti oxide, felsic, and mafic ratios corrected to reflect the ratios of these elements observed in the SEM images (see methods section for a complete discussion of techniques). ^d Lithologies: MD = monzodiorite, D = diorite, SG = syeno-gabbro, GN = gabbronorite, HGN = hornblende gabbronorite, OGN = olivine gabbronorite, A = anorthosite, PG = poikilitic gabbro.

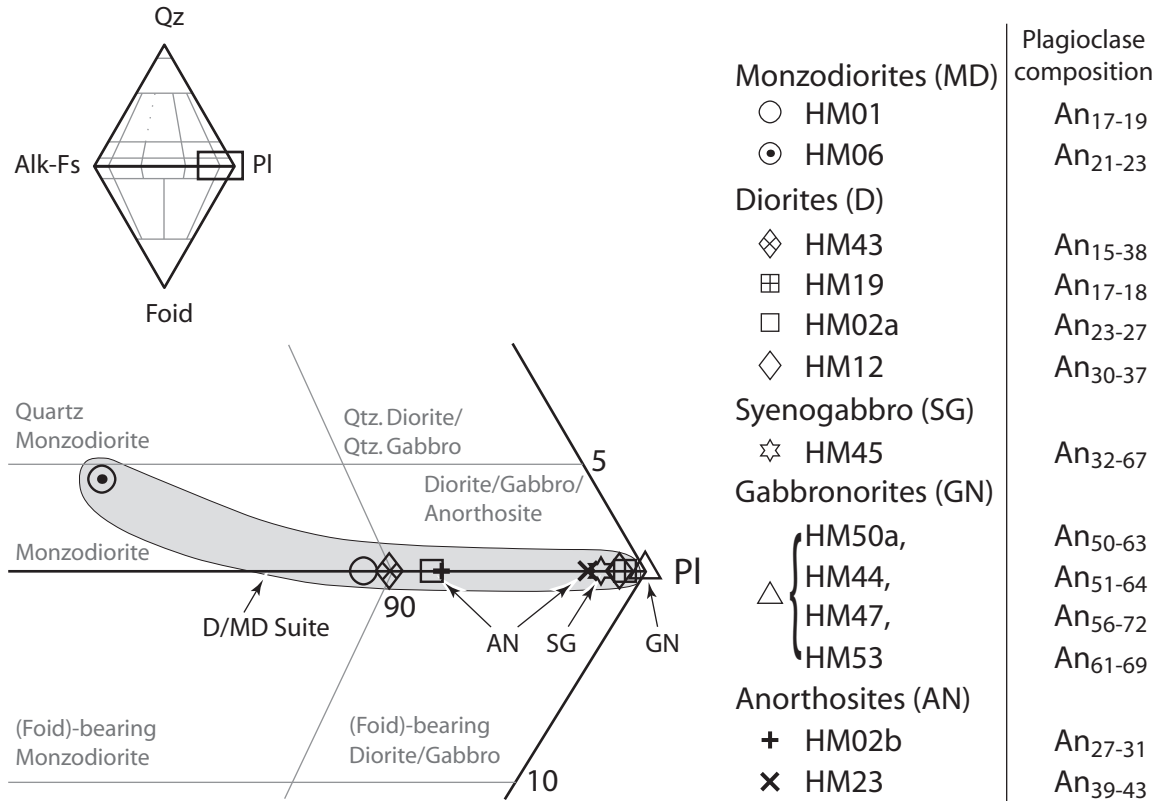


Figure 2.3: Quartz - Alkali feldspar - Plagioclase - Feldspathoid (QAPF) classification scheme for xenoliths. No xenoliths contain feldspathoids, and only one (HM06) is quartz-bearing. All gabbronorites are devoid of alkali feldspar and sit at the plagioclase apex. Diorites are differentiated from gabbros on the basis of plagioclase composition (gabbro contains $>An_{50}$). The most leucocratic xenoliths collected were selected for point counting to find those with the highest quartz and alkali feldspar fractions. The extent of the known diorite and monzodiorite suite is indicated.

100% normalized plagioclase, and are distinguished from each other by greater An content in gabbro plagioclase ($>An_{50}$). The significant presence of anorthitic phenocrysts rimmed by albitic plagioclase complicates the classification scheme and in such cases the estimated average composition of plagioclase is used. Gabbros have been further classified, based on modes of clinopyroxene, orthopyroxene, olivine, and plagioclase, as well as accessory minerals, and have been given appropriate modifiers (table 2.1). Those xenoliths reported as 'poiklitic gabbros' are not orthopyroxene-bearing and are *sensu stricto* gabbros. Notably, none of the xenoliths contain feldspathoids or significant (>5 vol.%) quartz. None of our samples are *sensu stricto* syenites, although this term has been used previously to describe the leucocratic xenoliths found in this area (Moore *et al.*, 1987).

CHAPTER 3. PETROGRAPHY

Xenoliths were grouped into three series based on textural, modal and compositional affinities: (1) *Syeno-xenoliths*, including monzodiorite, diorite, and syenogabbro lithologies (i.e., all alkali feldspar bearing species), (2) *Gabbronorite xenoliths*, consisting of gabbronorites, olivine gabbronorites, and hornblende gabbronorites, and (3) *Coincident xenoliths*, containing both uncommon anorthosites and rare poikilitic gabbros. All xenoliths described below are holocrystalline, with the exception of the poikilitic gabbros of the coincident series which contain both vesicular glass pockets as well as glass inclusions in plagioclase. Xenolith hand specimens are commonly rounded or sub-angular, and many are coated by a weathered, vesicular rind of host lava. Minerals in contact with such coatings have neither melted nor visibly reacted with host lava (fig. 3.7h). Oxidized iron stains many of the xenoliths along internal fracture planes.

Syeno-xenolith Series

Xenoliths of this series are dominated by plagioclase and clinopyroxene, with K-feldspar, biotite, magnetite, ilmenite, apatite, \pm orthopyroxene, \pm olivine, \pm amphibole (tr.), \pm zircon (tr.) also locally present, although modes vary in detail (table 2.1). A single monzodiorite is also quartz-bearing (3 vol.%). Grain size variations between samples of a single lithology (e.g., diorites) exceed differences between monzodiorites and diorites. Both lithologies contain fine-grained (\sim 0.1-0.2 mm; HM06, HM19) and medium-grained

Table 3.1: Xenolith grain sizes and textures

Syeno-Xenoliths								
Sample ID:	HM06	HM01a	HM43	HM02a	HM12	HM19	HM45	
Lithologies ^a :	MD	MD	D	D	D	D	SG	
Sample Texture:	allotriomorphic						orthocumulate	
Plagioclase								
habit:	amorphous grains, consertal interfingered boundaries, equant to stubby						subhedral, tabular	
$1/w^b$	[1]	1.4	1.3	1.9	1.5	1.4	1.6	3.1
$\sqrt{l \times w}$	[mm]	0.2	0.4	1.6	0.4	1.3	0.2	2.2
2σ		(0.2)	(0.7)	(1.5)	(0.5)	(1.6)	(0.2)	(3.2)
Clinopyroxene								
habit:	anhedral, rounded, stubby						oikocrystal, anhedral	
$1/w$	[1]	1.6	1.7	1.8	1.6	1.5	1.8	^c
$\sqrt{l \times w}$	[mm]	0.1	0.2	1.9	0.3	0.4	0.1	^c
2σ		(0.1)	(0.2)	(1.8)	(0.2)	(0.4)	(0.1)	^c
Other minerals								
habit:								
$1/w$	[1]							
$\sqrt{l \times w}$	[mm]							
2σ								
Reactions and exsolution textures ^d :	Some lamellar oxide exsolution in cpx, Bt-rimmed Fe-Ti oxides					Some lamellar oxide exsolution in cpx, Bt-rimmed Fe-Ti oxides		

^a Lithologies as in table 2.1. ^b Aspect ratio (length/width) and geometric mean of the two principal axes ($\sqrt{\text{length} \times \text{width}}$) are gathered from at least 30 mineral grains per sample. ^c Clinopyroxenes present as large oikocrystal grains for which size and shape could not be accurately determined. ^d Minerals: amph = amphibole, bt = biotite, cpx = clinopyroxene, opx = orthopyroxene.

Table 3.1 (continued): Xenolith grain sizes and textures

Gabbronorite Xenoliths				Coincident Xenoliths			
HM44	HM47	HM50a	HM53	HM02b	HM23	HM35	HM50b
GN	GN	HGN	OGN	A	A	PG	HGN
mesocumulate		polygonal mosaic texture		heterogranular, allotriomorphic		poikilitic	heterogranular
sub to euhedral tabular to stubby		subhedral stubby	polygonal equant to stubby	amorphous, interfingered, equant to stubby		euhedral prismatic	subhedral prismatic
2.1	2.2	1.5	1.5	2.0	1.5	1.6	3.4
0.7	0.6	0.4	0.2	0.6	0.6	0.7	0.1
(0.9)	(0.8)	(0.6)	(0.1)	(0.7)	(1.5)	(1.0)	(0.1)
subhedral, stubby		subhedral, stubby	polygonal equant to stubby		anhedral, rounded	oikocrystal, anhedral	
1.5	1.5	1.4	1.4	-	1.9	c	-
1.0	1.5	0.8	0.2	-	0.1	c	-
(1.1)	(1.1)	(0.8)	(0.1)	-	(0.1)	c	-
Olivine				Amphibole			
polygonal equant to stubby				polygonal blocky			
1.4				2.0			
0.1				0.1			
(0.1)				(0.1)			
Lamellar oxide exsolution in cpx, opx exsolution in cpx, bt-rimmed Fe-Ti oxides, opx rimmed ol, hydrolysis of cpx (to bt and amph)	Bt-rimmed Fe-Ti oxides, extensive hydrolysis of cpx (to bt and amph), ubiquitous amph halos	Uncommon lamellar oxide exsolution in cpx	Bt-rimmed Fe-Ti oxides	None	Some lamellar oxide exsolution in cpx		

(~0.5 mm; HM01a, HM02a) members, and some diorites are coarse grained (>1 mm; HM43; table 3.1).

Mineral shapes and textures are comparable in both diorites and monzodiorites (fig. 3.1, 3.2). Plagioclase feldspar and clinopyroxene are both nearly equant and anhedral. Grain boundaries between anhedral plagioclase grains commonly interfinger, forming a consertal texture (fig. 3.1g). Alkali feldspar occurs as irregular patches pervasively distributed throughout sodic plagioclase in a spongy texture (fig. 3.2d). Biotite and oxide blebs are rounded and amoeboid in shape. These phases are commonly interstitial or even enclosing, surrounding small plagioclase or clinopyroxene grains (fig. 3.2a, b). Coarser xenoliths are texturally homogeneous, with localized concentrations of Fe-Ti oxides creating symplectite or bleb-like textures (fig. 3.2g, h). In general, dioritic xenoliths (both diorites and monzodiorites) have an allotriomorphic texture, formed of a dense network of anhedral grains. There is no textural indication that these rocks are cumulates.

Rare prismatic plagioclase phenocrysts (~1-2 mm) are conspicuous in fine-grained diorites and monzodiorites (fig. 3.1d). Phenocrysts are generally calcic plagioclases, however they are rimmed with sodic plagioclase in optical continuity with neighboring grains of matrix plagioclase. Larger plagioclase phenocrysts are present in the coarse diorite HM43 (fig. 3.2e), identifiable compositionally by their higher anorthite content. Small (<0.1 mm) prismatic, euhedral apatite crystals, as well as Fe-Ti oxide blebs, are common inclusions in both sodic feldspars and clinopyroxene. In coarser xenoliths (e.g., HM43) apatite prisms grow up to 3.5 mm in length.

Figure 3.1: Optical photomicrographs of syeno-xenoliths captured under cross-polars (except (h) which was taken using plane-polarized light). Representative textures of medium- and fine-grained monzodiorite fragments (a, b) are very similar to diorite fragments with equivalent grain sizes (c, d). Both species exhibit allotriomorphic textures, containing only anhedral grains. Apatite rods (~1mm long) are common as inclusions within feldspar and biotite grains in coarse diorites and monzodiorites (e). Plagioclase phenocrysts in syenogabbros form loose orthocumulate networks, surrounded by oikilitic clinopyroxene and interstitial Fe-Ti oxides and biotite (f). Plagioclase grains in the syeno-xenolith series (with the exception of phenocrysts) share interpenetrative boundaries, forming consertal textures (g). Coarser xenoliths tend to have heterogeneous textures, including localized concentrations of Fe-Ti oxides (h). Minerals: Ap = apatite, Bt = biotite, Cpx = clinopyroxene, Ox = Fe-Ti oxide, Pl = plagioclase, pheno = phenocryst. Lithologies: MD = monzodiorite, D = diorite, SG = syenogabbro.

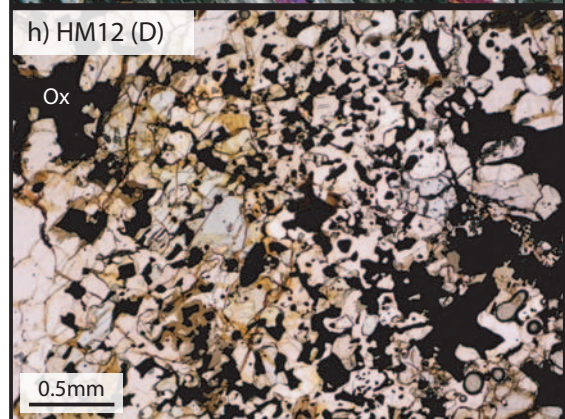
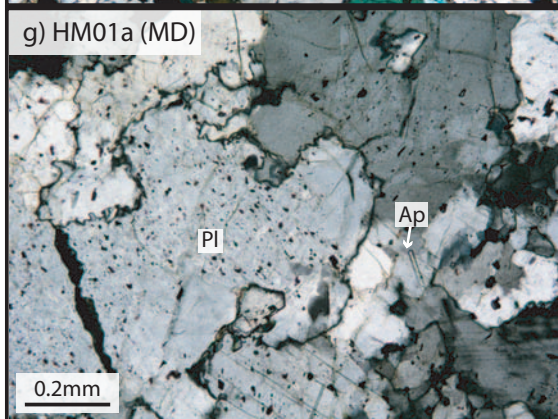
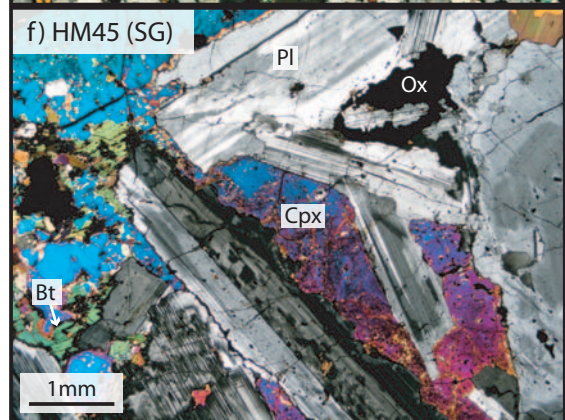
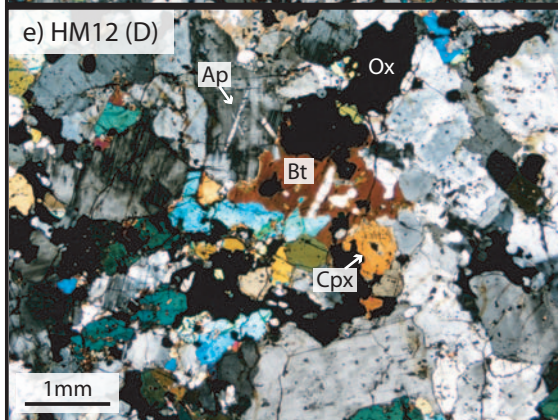
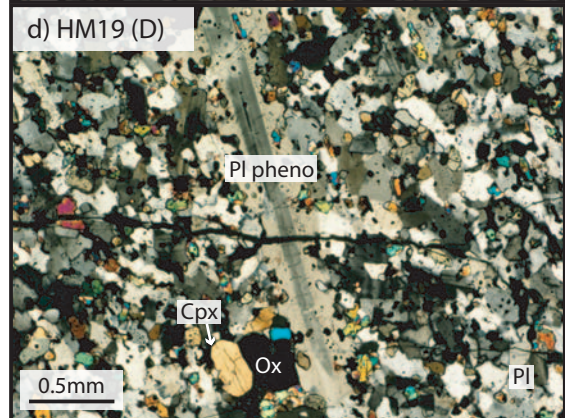
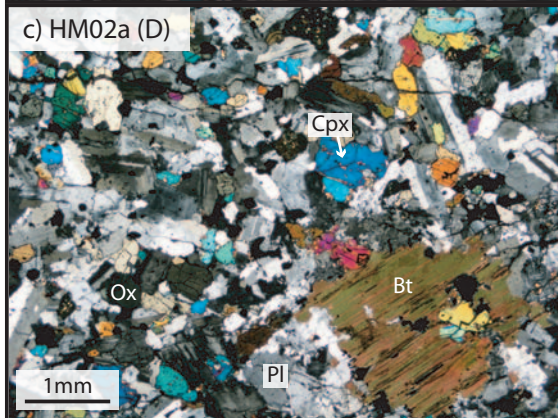
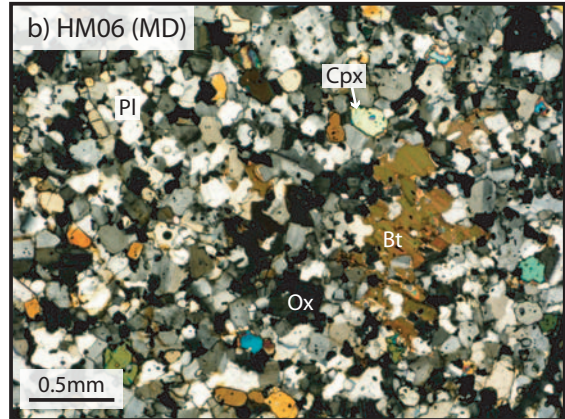
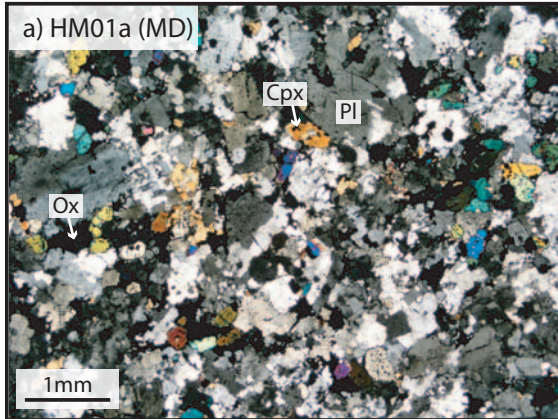
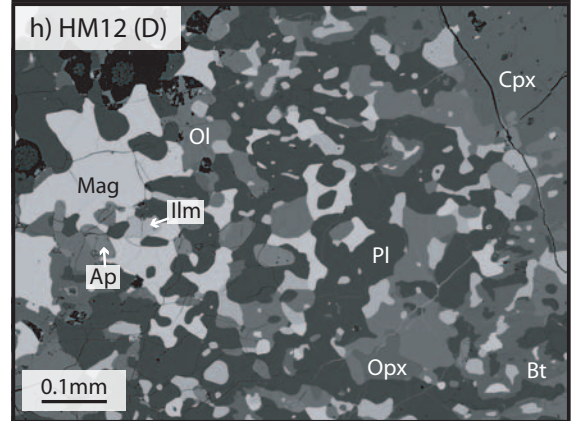
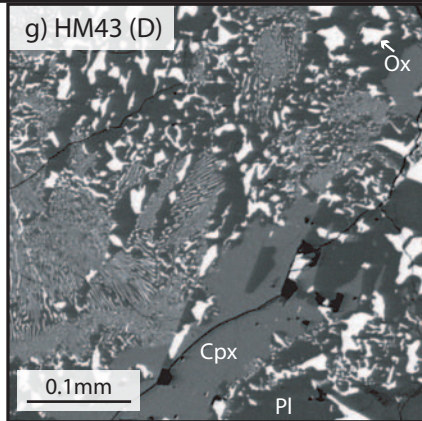
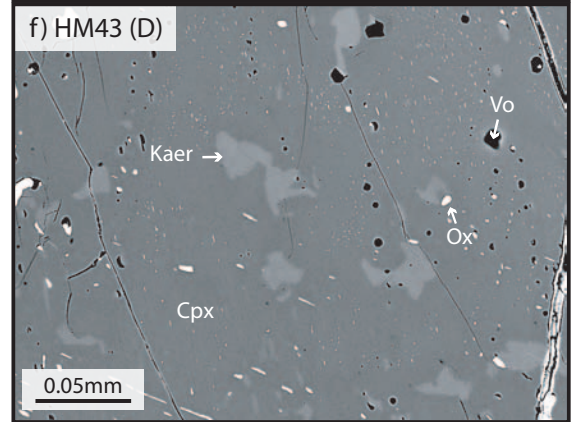
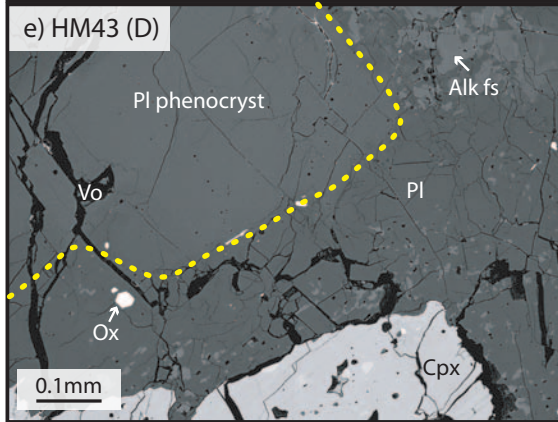
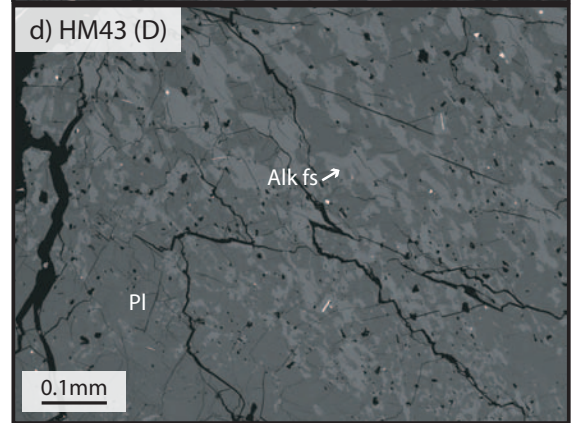
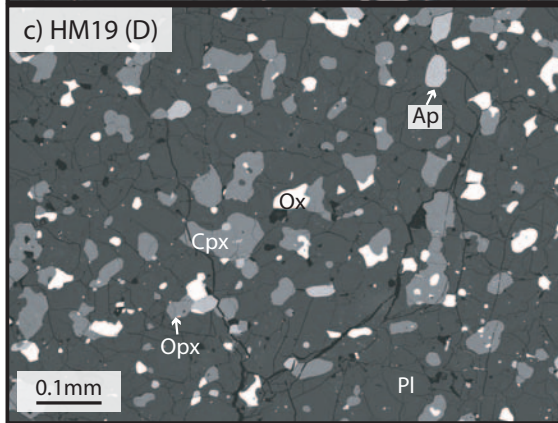
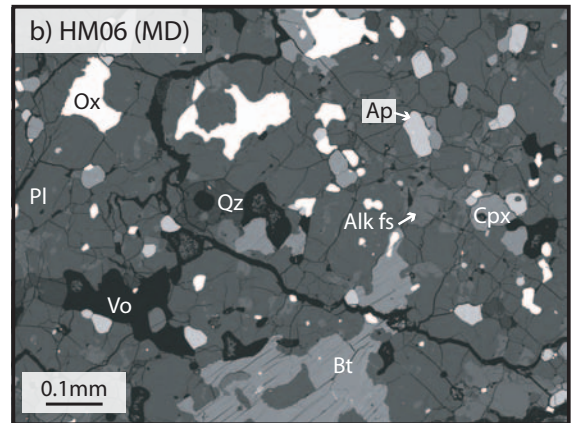
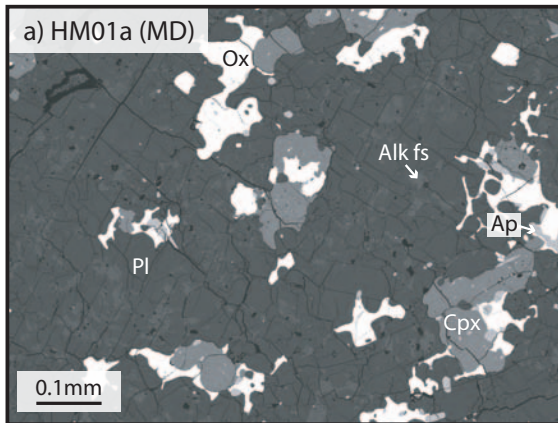


Figure 3.2: Back-scatter electron (BSE) images of syeno-xenoliths collected by scanning electron microscope and electron microprobe. Fe-Ti oxides and biotite are amorphous interstitial to enclosing phases (a, b). Less enclosing mineralization is visible in fine-grained xenoliths (c). Exsolved patches of alkali feldspar surrounded by albitic plagioclase give the feldspar matrix of this series a mottled or spongy texture (a, b, d, e). Anorthitic plagioclase phenocrysts in HM43 are surrounded by rims of albitic plagioclase with exsolved alkali-feldspar (e), and contain small Fe-Ti oxide blebs (visible only at high magnification). Amoeboid blebs of kaersutite are present within clinopyroxene grains in the coarsest diorites and in the gabbronorite series, and are often present in conjunction with oxide blebs (f). Fe-Ti oxides in coarse diorites are found in localized concentrations with both symplectite (g) and bleb-like (h) textures. Minerals and lithologies as in previous figure. Also, Alk fs = alkali feldspar, Ilm = ilmenite, Kaer = kaersutite, Mag = magnetite, Opx = orthopyroxene, Ol = olivine, Qz = quartz, Vo = void space.



Syenogabbros differ from other syeno-xenoliths in their high concentration of large (~3-9 mm) tabular plagioclase laths forming a loosely packed crystalline framework (fig. 3.1f). Void space in this mesh of phenocrysts is occupied by clinopyroxene oikocrysts (up to ~1 cm diam.) as well as interstitial Fe-Ti oxides, and a second more sodic plagioclase. The sodic plagioclase contains exsolved alkali feldspar in spongy patches similar to that found in diorites and monzodiorites. Except for the euhedral to subhedral plagioclase phenocrysts, all other grains are anhedral. These anhedral phases (~30-45 vol.% of the xenolith) conform to the plagioclase crystalline network giving the syenogabbros an orthocumulate texture. Grain sizes are coarser than in other syeno-xenoliths (table 3.1).

Gabbronorite Series

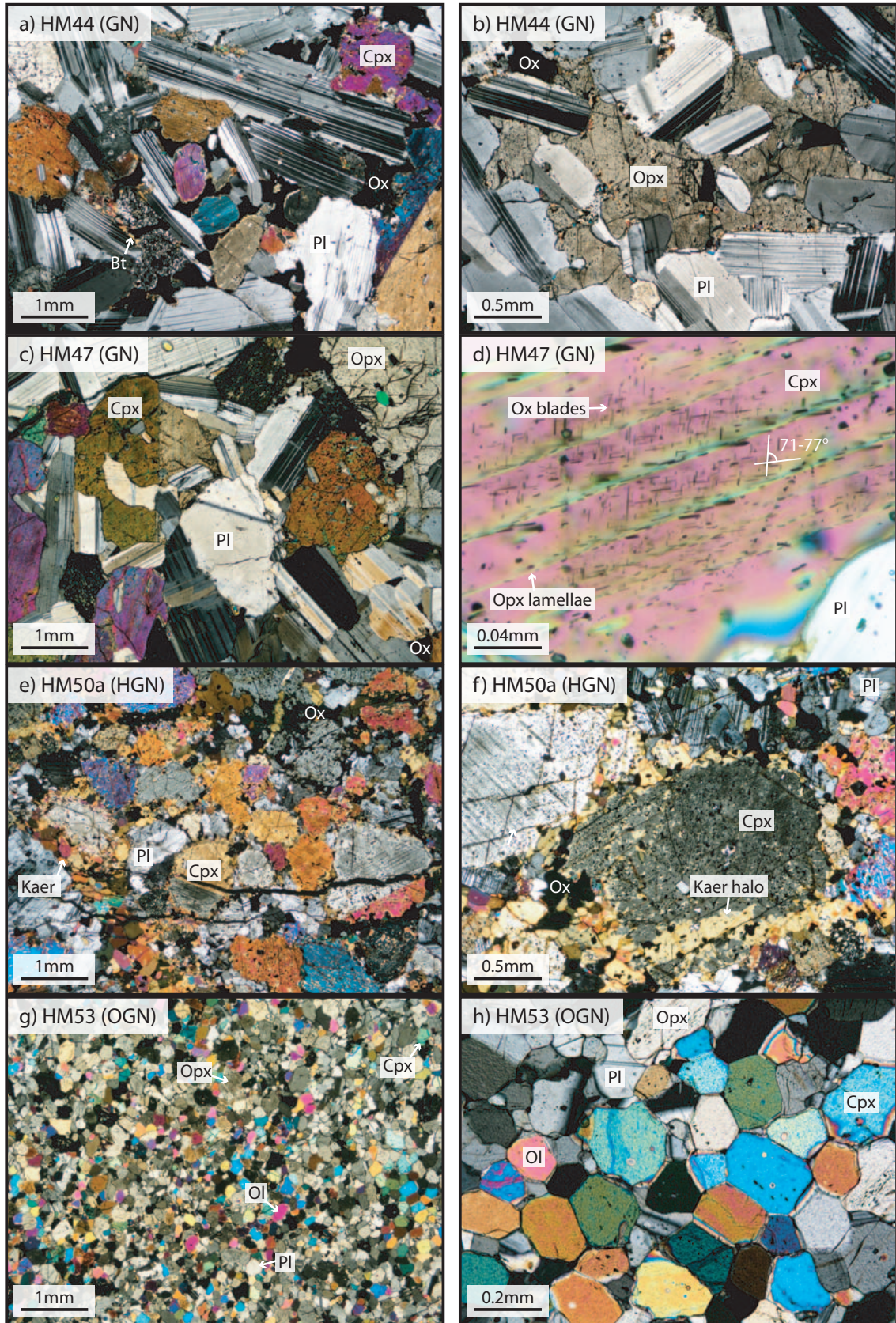
There are greater variations in lithology and texture among this series than among the syeno-xenolith series. All members of this group contain plagioclase, clinopyroxene, orthopyroxene, and Fe-Ti oxides. Olivine gabbronorites contain substantial (~20 vol.%) olivine. Ordinary gabbronorites contain minor amounts of olivine (<1 vol.%), in addition to minor amounts of the hydrous phases amphibole and biotite (~0-2 vol.% combined). The single hornblende gabbronorite sample (HM50a/b) contains significantly more hornblende (~20 vol.%) than other samples, and lacks olivine. The hornblende gabbronorite also contains a lesser amount of orthopyroxene relative to total pyroxene abundance. However, the reported mode probably underestimates actual orthopyroxene content due to the difficulty of identifying heavily reacted pyroxenes when gathering

point counts. This sample is intersected by a hornblende-dominated fine grained vein (see HM50b in table 2.1).

Minerals in olivine gabbonorite samples are relatively fine-grained and equigranular (table 3.1). These samples exhibit an annealed polygonal texture, with ubiquitous grain intersections forming $\sim 120^\circ$ angles (fig. 3.3g, h). In contrast, ordinary and hornblende gabbonorites are both moderately coarse-grained (table 3.1). Plagioclase and clinopyroxene crystals are mostly equant to slightly elongate, and form a closely packed mesocumulate texture (fig. 3.3a). Interstitial and enclosing orthopyroxene, commonly surrounding small plagioclase crystals, and amorphous interstitial biotite-rimmed Fe-Ti oxides fill the gaps between clinopyroxene and plagioclase grains. Amphibole is generally found only as small blebs ($\sim 10 \mu\text{m}$) within clinopyroxene grains (fig. 3.2f) except in hornblende gabbonorite, where amphibole grains form halos around all clinopyroxenes (fig. 3.3f). These phases only account for a combined 15-25 vol.%, the remainder consisting of cumulus plagioclase and clinopyroxene grains. This cumulate texture dramatically contrasts the intergrown allotriomorphic texture exhibited by the diorites (fig. 3.1a-d).

Pyroxene grains in gabbonorites display a number of disequilibrium late-stage magmatic and subsolidus reactions. The majority of clinopyroxene grains contain parallel orthopyroxene exsolution lamellae. Fe-Ti oxides have also exsolved from clinopyroxene grains, forming elongate blades aligned in two distinct orientations (with an acute angle between 71° and 77° ; fig. 3.3d). The orientations of Fe-Ti oxide blades are reflected across the contact plane of simple twins in clinopyroxene grains. Additionally,

Figure 3.3: Optical photomicrographs of the gabbronorite family of xenoliths captured under cross-polars. In gabbronorites and hornblende gabbronorites, the cumulus phases plagioclase and clinopyroxene form a densely packed structure (a, c, e). The remaining volume (~15 vol%) consists of interstitial Fe-Ti oxides and biotite (a), as well as oikilitic orthopyroxene (b). Nearly all clinopyroxene grains contain orthopyroxene exsolution lamellae and bladed Fe-Ti oxide exsolutions (d). Hornblende gabbronorite textures are very similar to those observed in gabbronorites, with the noticeable distinction of ubiquitous kaersutite lining grain boundaries (e, f). Kaersutite blebs within clinopyroxene grains (fig. 3.2e) are also prevalent. Olivine gabbronorites are distinct from other gabbronorite xenoliths, as mineral grains have recrystallized to form a nearly equigranular mosaic texture (g). Junctions of multiple grains often form $\sim 120^\circ$ angles (h). Minerals as in previous figures. Lithologies: GN = gabbronorite, HGN = hornblende gabbronorite, OGN = olivine gabbronorite.



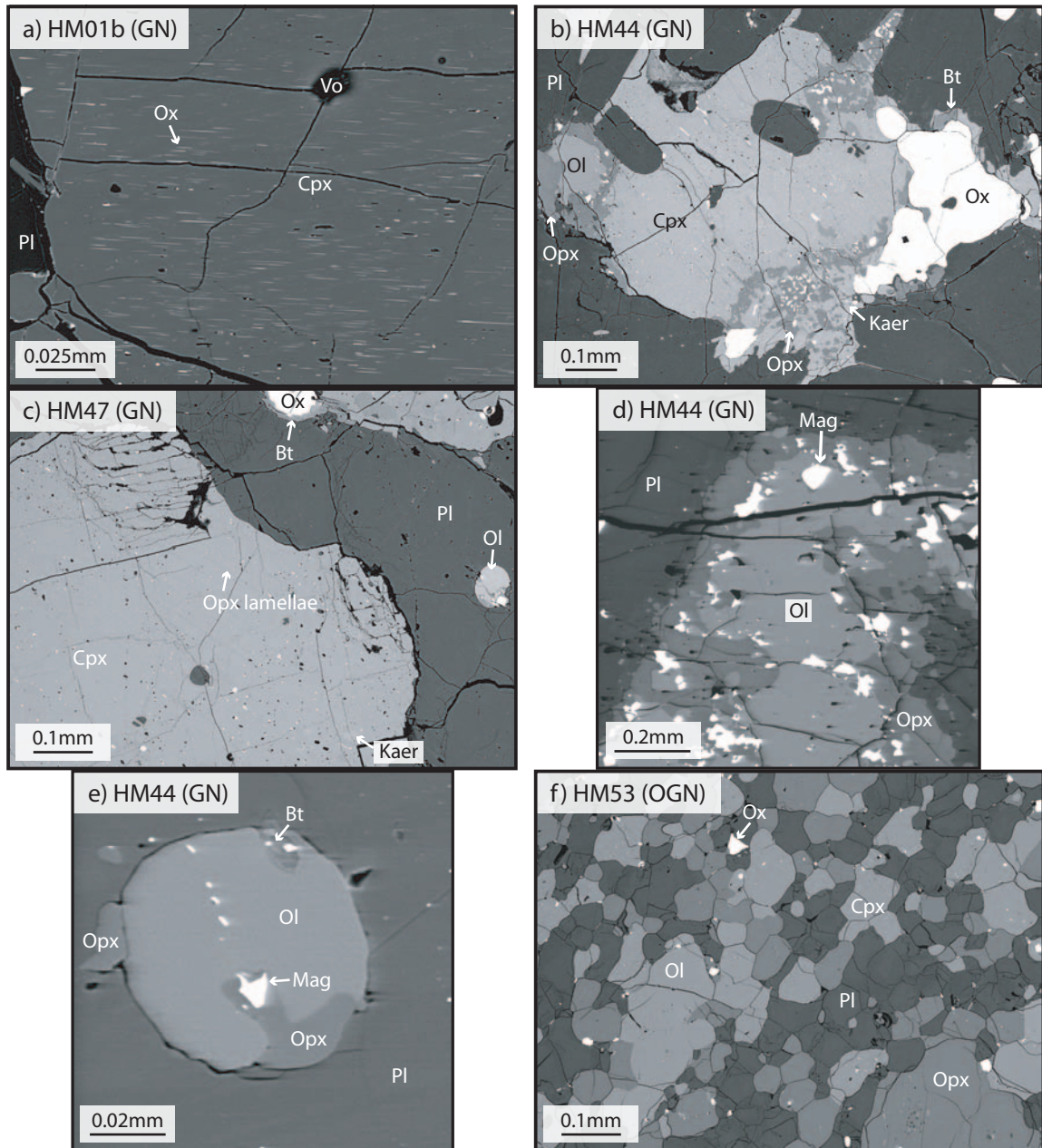
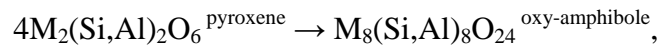


Figure 3.4: BSE images of gabbronorite xenoliths collected by scanning electron microscope and electron microprobe. Parallel Fe-Ti oxide exsolution blades (a), orthopyroxene exsolution lamellae (b, c), and kaersutite blebs (c) are ubiquitous in clinopyroxene grains in gabbronorites. Less commonly, kaersutite forms along grain boundaries (b). Olivine in gabbronorites is always enclosed in a sheath of orthopyroxene, with large blebs of magnetite present along the contact (d). Plagioclase in this series contains rare multi-phase spherical inclusions interpreted as crystalline remnants of glass inclusions (c, e). Clinopyroxene grains in olivine gabbronorites do not share the exsolution and reaction features of those in ordinary gabbronorites (f). Minerals and lithologies as in previous figures.

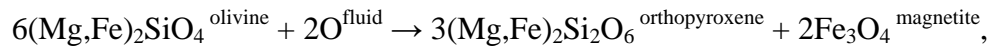
blades found within orthopyroxene exsolution lamellae are oriented at a slightly different angle than those occurring in the host clinopyroxene. These observations suggest crystallographically controlled oxide exsolution, similar to that described by Fleet *et al.* (1980). Fe-Ti oxide exsolution blades are most common in the gabbronorites, occurring in dense concentrations within most clinopyroxene grains, but also occur in the coarsest of the syeno-xenoliths. Clinopyroxene grains in gabbronorites, coarse diorites, and the hornblende gabbronorite also contain rare irregular amphibole blebs (fig. 3.2f). These blebs are distributed throughout the clinopyroxene, in contrast to the ubiquitous amphiboles formed along grain boundaries in the hornblende gabbronorite. It is not clear whether these amphiboles represent an isochemical exsolution reaction of the generalized form:



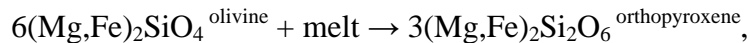
or a diffusion-controlled alteration reaction, as the two processes are petrographically indistinguishable. Accurate amphibole and host pyroxene compositions are required to distinguish the two possibilities (and will be discussed in the results section).

Olivine in the gabbronorites is nearly always rimmed by orthopyroxene of variable thickness (fig. 3.4d). The contact between olivine and orthopyroxene in these cases contains numerous rounded magnetite blebs. The fact that the reaction appears to proceed inward from the mineral edges and that the magnetite blebs are located at the contact suggests a diffusion-limited reaction converting olivine into orthopyroxene and magnetite. For magnetite to result from a reaction between olivine and pyroxene, iron

must change its oxidation state from Fe²⁺ to Fe³⁺, implying the need for an oxidizing agent. A reaction of the form:



where the oxygen is contributed by an oxidizing agent (e.g., aqueous fluid), could affect such a change. This might represent a late-stage subsolidus reaction driven by circulating oxidizing fluids. The similar peritectic reaction:



might also create orthopyroxene rims on olivine crystals, but would not be expected to crystallize magnetite at the olivine-orthopyroxene interface.

Mineral inclusions within plagioclase and clinopyroxene grains in the gabbronorites are generally restricted to Fe-Ti oxides. Rare spherical, multi-phase inclusions (olivine, orthopyroxene, ± biotite, ± magnetite) are also present in plagioclase (fig. 3.4c, e) and appear to be the crystalline remnants of former melt inclusions. Plagioclase may have also crystallized from the melt along the boundary with the host plagioclase grain.

Coincident Series

The syeno-xenolith and gabbronorite series (and their relationships to trachyte and tholeiite volcanism on Hualālai, respectively) are of primary interest to this study.

Summit xenoliths collected from Hualālai which do not belong in these two families (poikilitic gabbros, anorthosites, and the hornblende-rich vein) are grouped in a third series, the coincident series. For reasons described in a subsequent section, poikilitic

gabbros are thought to be genetically unrelated to the syeno-xenolith and gabbronorite series. A genetic link between anorthosites and a hornblende-rich vein (HM50b, found bounding the hornblende gabbronorite) and either of these two series is neither proven nor disproven. We describe them here, as they may be important to some aspects of Hualālai's magmatic system, but do not revisit them in later discussions.

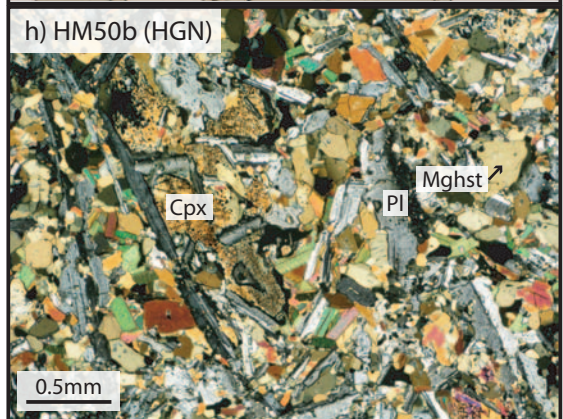
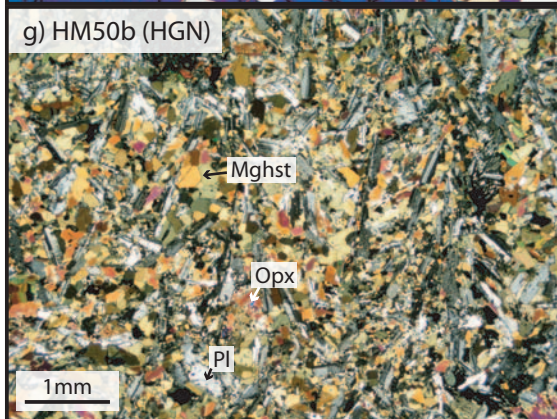
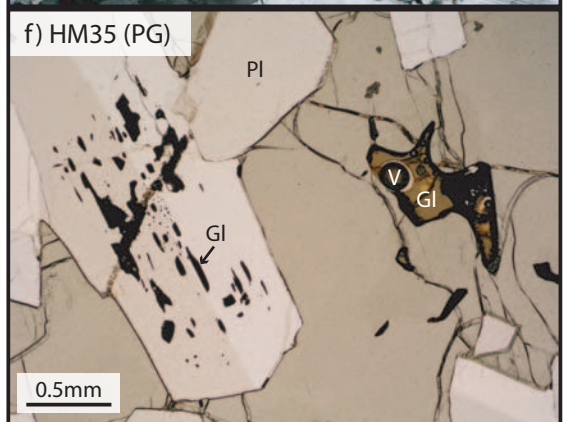
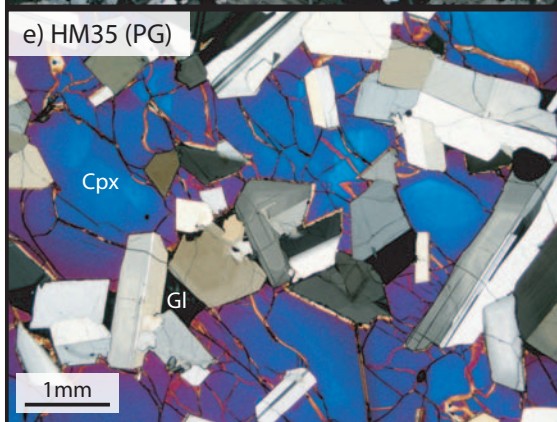
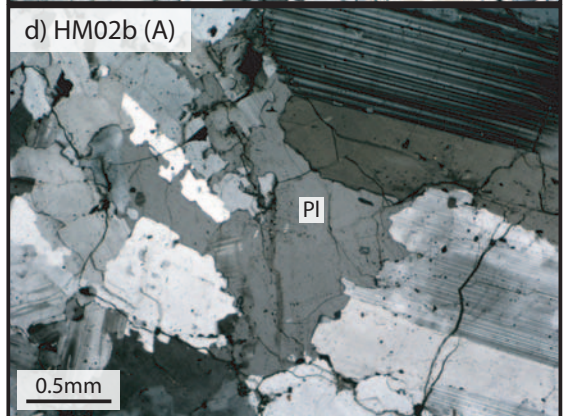
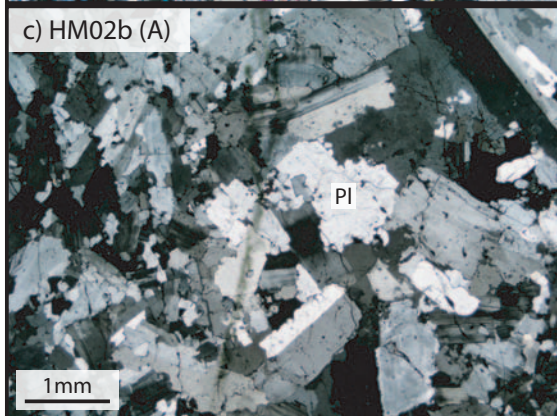
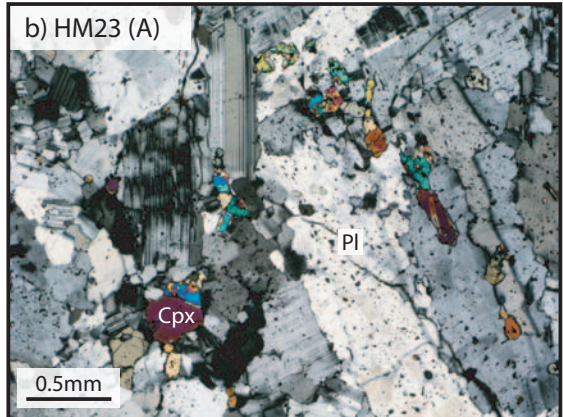
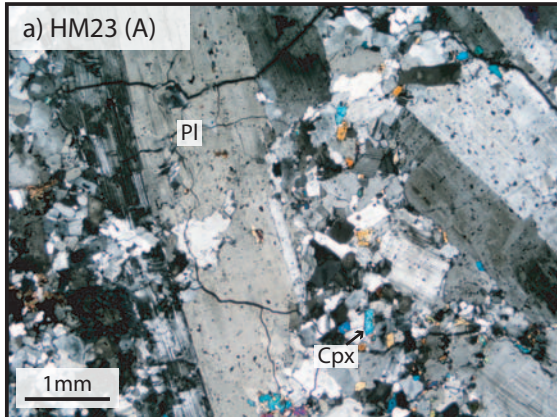
Poikilitic Gabbros

These xenoliths contain only plagioclase and clinopyroxene. Plagioclase grains are perfectly euhedral and are surrounded by large (>2 cm diameter) oikocrysts of clinopyroxene (fig. 3.5e, f). No other inclusions, exsolution features, or reaction textures are present in the clinopyroxene. Fractures in the clinopyroxene grain form conchoidally rather than along parallel cleavage planes. Zonation is optically visible in the plagioclase crystals and, to a lesser degree, in the clinopyroxene oikocrysts. Pockets of vesicular glass containing small Fe-Ti oxides occur along grain boundaries or in interstices (fig. 3.6a). These glass pockets are traceable to the host alkalic basalt lava rimming the xenolith, with which they share identical major element chemistry. The glass and associated oxides are therefore considered secondary features. Several hawaiite glass inclusions (more evolved than the host lava) also exist within plagioclase grains (fig. 3.6b).

Anorthosites

Anorthosites are present as both felsic veins of various thicknesses (mm- to cm-scale) bisecting several of the samples and as discrete cm-scale felsic plutonic fragments.

Figure 3.5: Optical photomicrographs of coincident xenoliths captured under cross-polars (except (f) which was taken using plane-polarized light). Anorthosites are dominated by the consertal texture of interdigital feldspar grains (a-d). Clinopyroxene in poikilitic gabbros does not contain any reaction or exsolution textures and is conchoidally fractured (e). Glass inclusions in plagioclase, as well as vesicular intergranular pockets of glass are both present in the poikilitic gabbros (f). The hornblende-rich vein (HM50b) contains prismatic plagioclase and stubby magnesiohastingsite grains (g, h). Minerals as in previous figures. Also, Gl = glass, Mghst = magnesiohastingsite, V = vesicle. Lithologies: A = anorthosites, PG = poikilitic gabbro, HGN = hornblende gabbro.



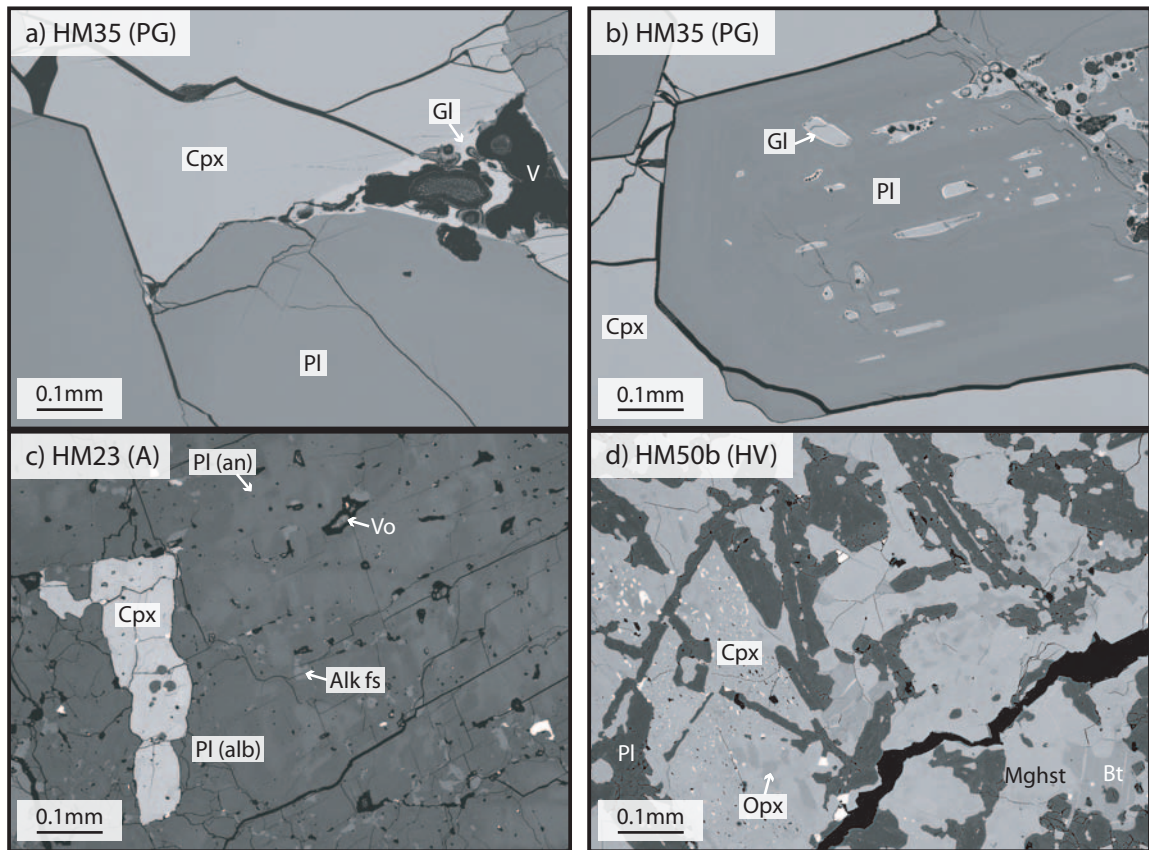


Figure 3.6: BSE images of coincident xenoliths collected with a scanning electron microscope. Poikilitic gabbros contain both vesicular glass pockets (a) and Fe-Ti oxide-lined glass inclusions in plagioclase grains (b). Compositions of vesicular glass pockets are identical to glass found in the lava rind, but more evolved than glass inclusions (fig. 4.1). Feldspar in anorthosites exhibits a mottled texture with patches of both anorthitic plagioclase and alkali feldspar surrounded by albitic plagioclase (c). Plagioclase grains in the hornblende-rich vein (HM50b) are euhedral to subhedral and are surrounded by anhedra magnesiohastingsite grains (d). Minerals and lithologies as in previous figures.

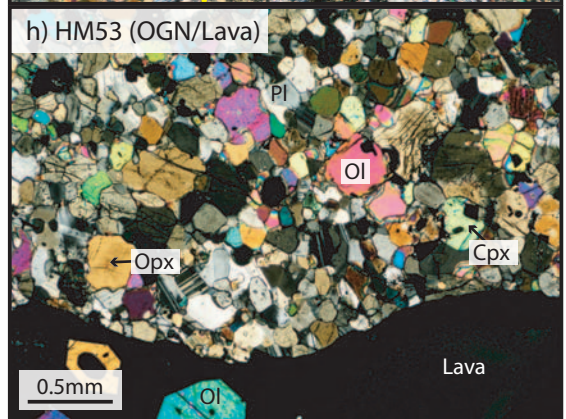
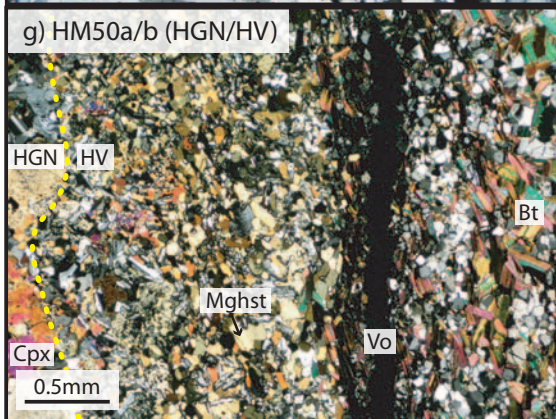
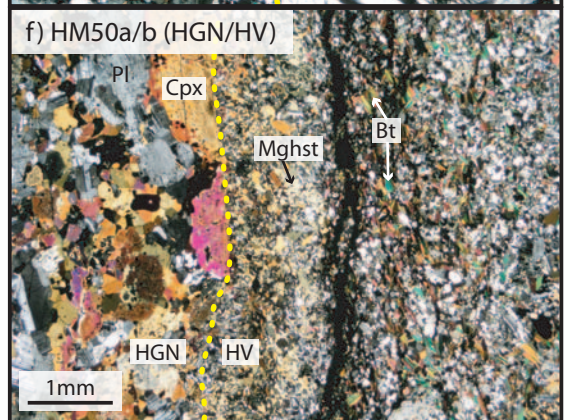
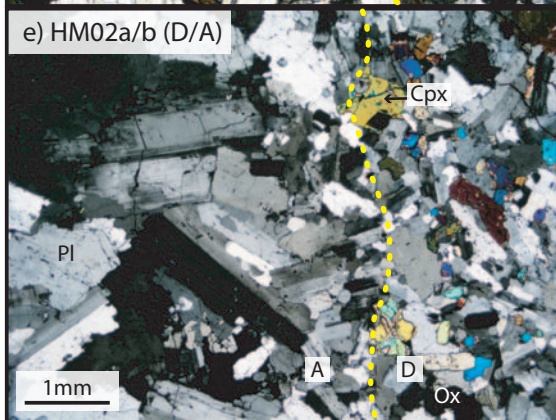
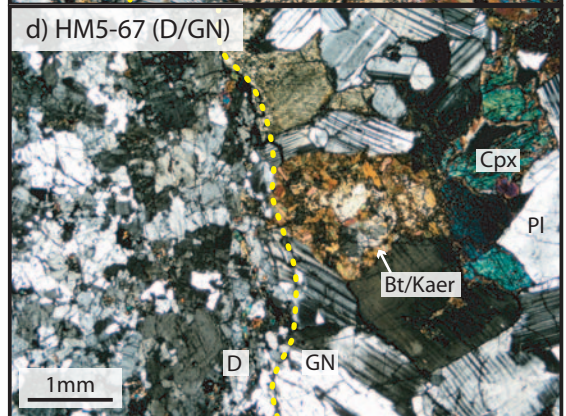
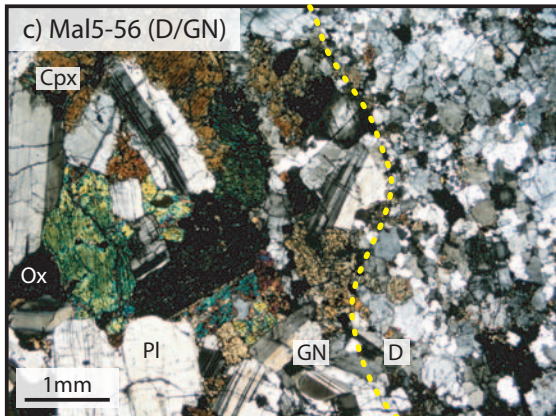
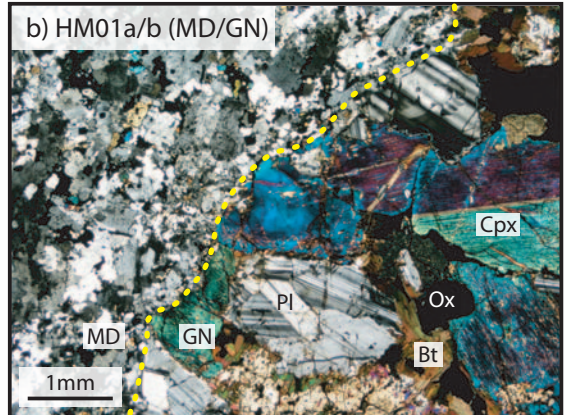
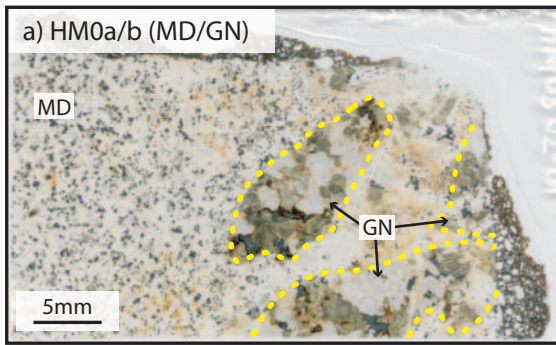
Anorthosites contain > 90 vol.% plagioclase, as well as small amounts of K-feldspar, clinopyroxene, and occasional Fe-Ti oxides. Anorthosites appear to have a wide range of grain sizes (table 3.1). Tabular, aligned subhedral plagioclase laths are surrounded by finer anhedral plagioclase grains. Clinopyroxene grains are smaller than the large plagioclase grains and are interstitial to the large tabular laths.

Contact Relations

Rare xenolith samples juxtapose lithologies from different series (e.g., a diorite and a gabbronorite). The most common example of this is the felsic veins described above. These crosscut both members of the syeno-xenolith and gabbronorite series. Grain size typically decreases in the felsic member within ~1 mm of the contact (fig. 3.7e).

Contacts between gabbronorite and diorite lithologies also exist (fig. 3.7a-d). These are present as both dm-scale contacts visible in hand samples, as well as cm-scale gabbronorite clots surrounded by a diorite matrix (HM01 - fig. 3.7a). Contacts generally truncate both clinopyroxene and plagioclase grains in the gabbronorite. Additionally, the hydrous phases biotite and amphibole, as described in the gabbronorite series section, are more prevalent in gabbronorites nearer to the diorite contact. Grain size of the diorite matrix decreases within ~1 mm of the contacts and the localized mode becomes increasingly felsic (fig. 3.7b).

Figure 3.7: Inter-lithologic contacts in thin section photographs (a) and optical photomicrographs captured under cross-polars (b-h). In sample HM01, clots of gabbronorite measuring ~1 cm diameter (HM01b) are engulfed in a monzodiorite matrix (HM01a) (a). Grain size of the monzodiorite matrix decreases with proximity to the contact with the clots, and pyroxene and feldspar grains on the gabbronorite side are truncated (b). This relationship is held out in all instances of contacts between gabbronorites and diorites or monzodiorites (c, d). Feldspar grains in anorthosites proximal to contacts also decrease in size (e). Clinopyroxene grains on the gabbronorite side of the contact between hornblende gabbronorites and the hornblende-rich vein (HV) are truncated (f). Grain size of the hornblende-rich vein increases away from the contact, and there is a 1-2 mm thick biotite-rich layer ~3 mm into the vein from the contact (g). Mineral grains in contact with lava rinds have neither melted nor reacted visibly (h). This is true for all lithologies. Minerals and lithologies as in previous figures. Also, HV = hornblende gabbronorite vein (HM50b).



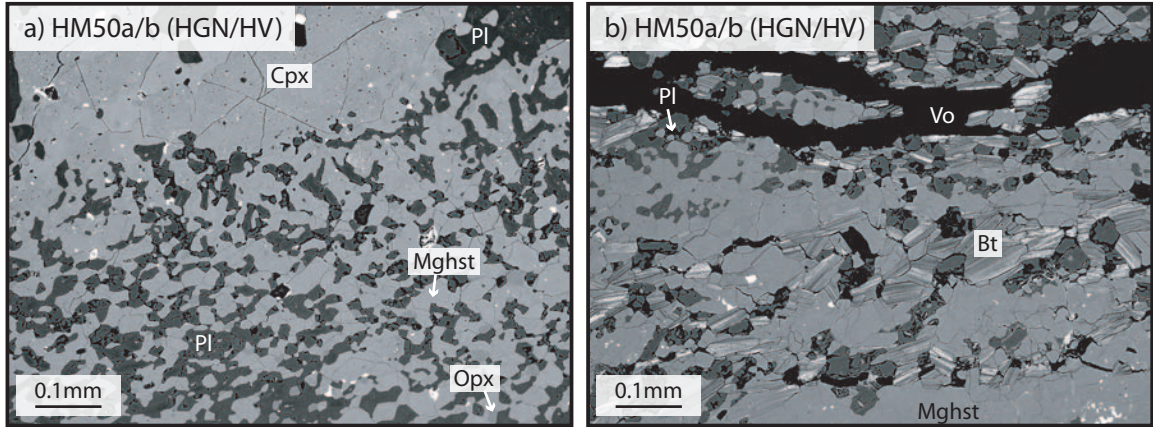


Figure 3.8: BSE images of the hornblende gabbro (HM50a)/hornblende-rich vein (HM50b) contact, collected by scanning electron microscope. Grain size of the hornblende-rich vein decreases significantly with proximity to the contact and plagioclase crystals appear to penetrate the large clinopyroxene grains on the other side of the contact (a). The biotite-rich layer close to the contact (fig. 3.7g) is composed of at least three separate contiguous biotite horizons, one of which separated during thin section preparation (b). Minerals and lithologies as in previous figures.

CHAPTER 4. RESULTS

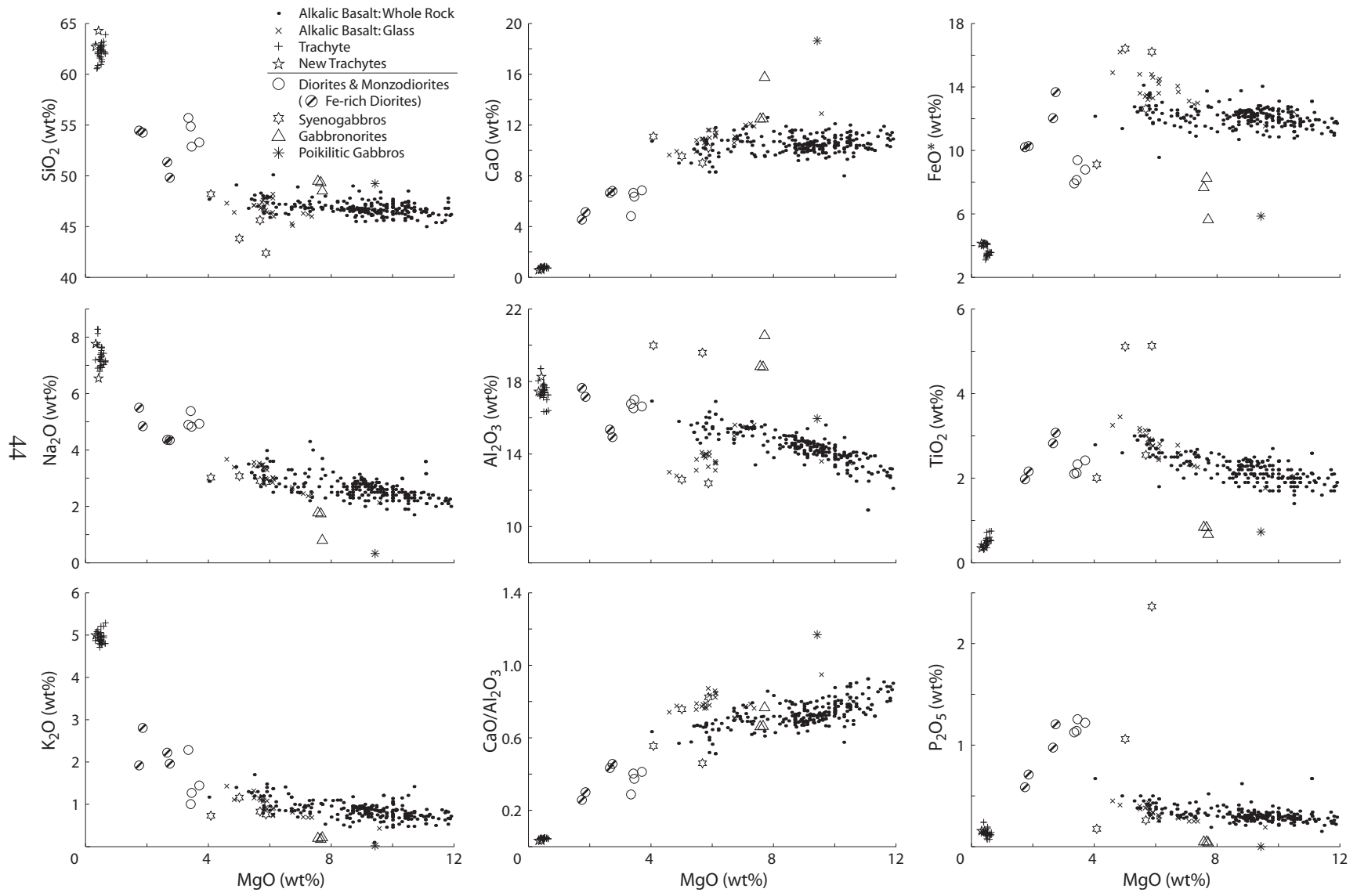
Whole Rock Compositions

XRF analyses of 16 xenoliths (reported together with 2 trachytes in appendix A) represent the first whole-rock analyses of the leucocratic xenoliths of Hualālai. Major elemental compositions of xenoliths and previously reported Hualālai lavas (see appx. C.1 for sources) are displayed in MgO and SiO₂ variation diagrams (fig. 4.1, 4.2). Different lithologies, defined on the basis of petrography and mineral chemistry, have distinctive bulk compositions. MgO concentrations effectively distinguish poikilitic gabbros (~9.5 wt%), gabbronorites (~7.5-8 wt%), syenogabbros (~4-6 wt%), and dioritic xenoliths (including both diorites and monzodiorites, ~1.5-4 wt%; fig. 4.1). Diorites have intermediate MgO contents relative to trachyte and alkalic basalt lavas. Alkalic basalts (~5-16 wt% MgO) span the entire range of MgO content of non-dioritic xenoliths, but are generally compositionally dissimilar to plutonic fragments (e.g., Al₂O₃, FeO*, fig. 4.1). All syeno-xenoliths (dioritic xenoliths and syenogabbros) fall in the alkalic region of Macdonald & Katsura (1962), while both gabbronorites and poikilitic gabbros are sub-alkalic (fig. 4.2). Again, dioritic xenoliths are intermediates between basaltic lavas and trachytes.

Mineral Compositions

Repeat analyses of pyroxene, olivine, phlogopite, and Fe-Ti oxide mineral grains (but not all feldspars) yielded 2 σ variations similar to repeat analyses of mineral

Figure 4.1: MgO variation diagrams illustrating whole rock composition of newly analyzed summit xenoliths and previously published alkalic lavas and glasses (see appx. C.1 for sources). Dioritic xenoliths include both diorites and monzodiorites. Analytical uncertainty is less than symbol size in all diagrams. Dioritic xenoliths partially fill the compositional gap between alkalic basalt and trachyte lavas.



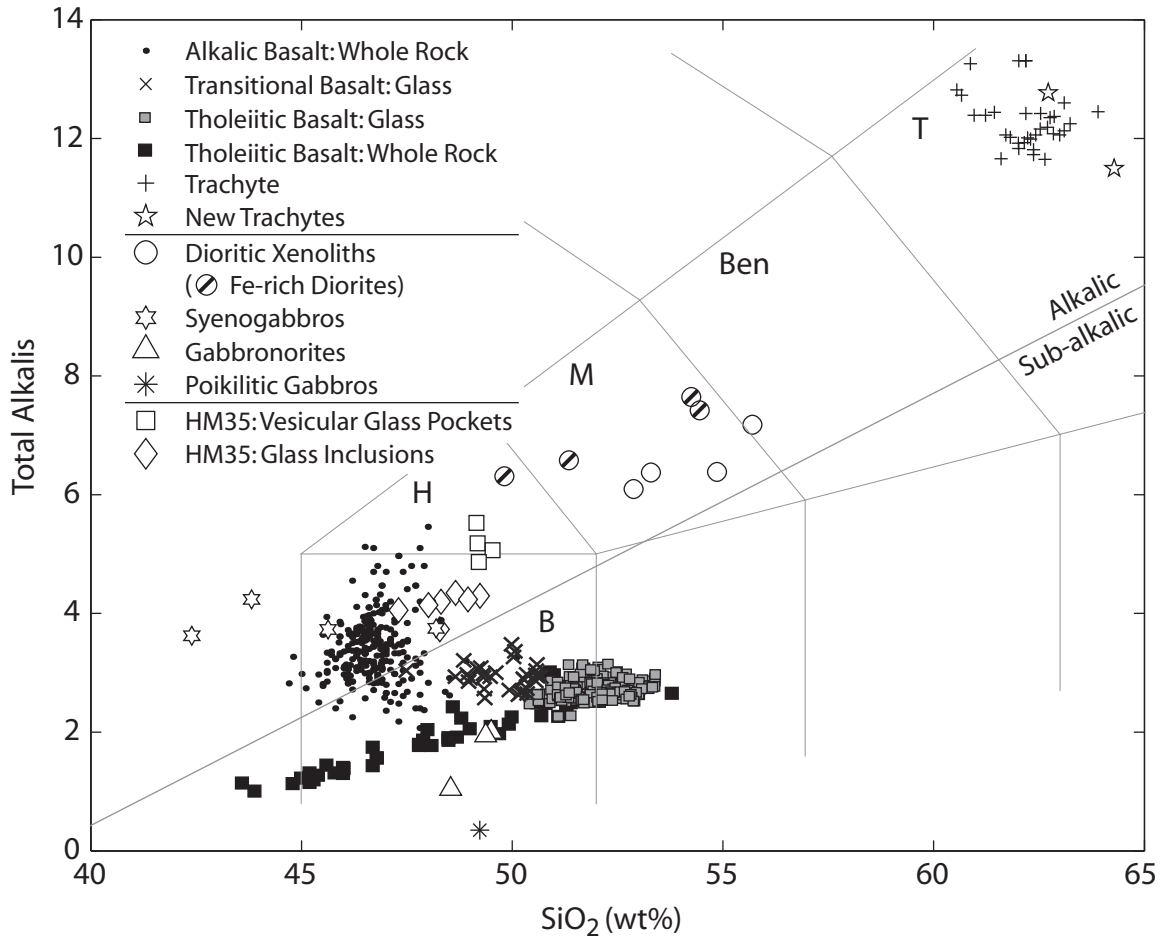


Figure 4.2: Total-alkalis silica (TAS) diagram illustrating whole rock composition of newly analyzed summit xenoliths and previously published alkalic lavas and glasses (see appx. C.1 for sources). Glass analyses from HM35 are also shown.

standards (<1% relative for most major elements), indicating remarkable homogeneity of the xenolith phases. Because of this homogeneity, reported mineral compositions are averages of multiple analyses (generally three) of individual mineral grains (appx. A). For grains larger than ~50 μm in diameter, these include locations in both grain centers and edges. Feldspar rim compositions are generally homogeneous, however some crystals contain more anorthitic cores. In these cases, either individual or average rim compositions and individual core compositions are reported separately. Contiguous grains of titanomagnetite and hemo-ilmenite were analyzed whenever possible.

Compositional data for feldspars, the mafic minerals clinopyroxene, orthopyroxene, and olivine, and for Fe-Ti oxides are shown in figures 4.3, 4.4, 4.5, respectively. All of the phases in each of the five principle lithologic groups are described separately in the following sections.

Monzodiorites

Plagioclase grains in monzodiorites are strongly albitic ($\text{An}_{17-23}\text{Or}_{5-10}$), while alkali feldspar grains have compositions of $\text{An}_{2-3}\text{Or}_{55-62}$. Clinopyroxene grains span a narrow compositional range ($\text{En}_{47-49}\text{Wo}_{41-43}\text{Fs}_{9-10}$) with Mg numbers between 73.6-76.4. Orthopyroxene is also Fe-rich ($\text{En}_{68-70}\text{Wo}_{1-2}\text{Fs}_{28-30}$) and has Mg numbers ($\text{Mg\#}_{\text{opx}} \approx \text{En}_{\text{opx}}$) only slightly lower than clinopyroxene. Titanomagnetite (Usp_{12-24}) has Mg numbers from 5-7, and Cr numbers from 0-4. Hemo-ilmenite (Ilm_{65-79}) has both larger Mg numbers (Mg# 9-14), and Cr numbers (Cr# 0-20). Phlogopite (Mg# 67.4-78.7) is Ti-rich (1.9-6.0 wt% TiO_2 ; appx. A). Fluorine contents (0.8-1.6 wt% F) are moderate, and chlorine contents (0.3-0.4 wt% Cl) are relatively low.

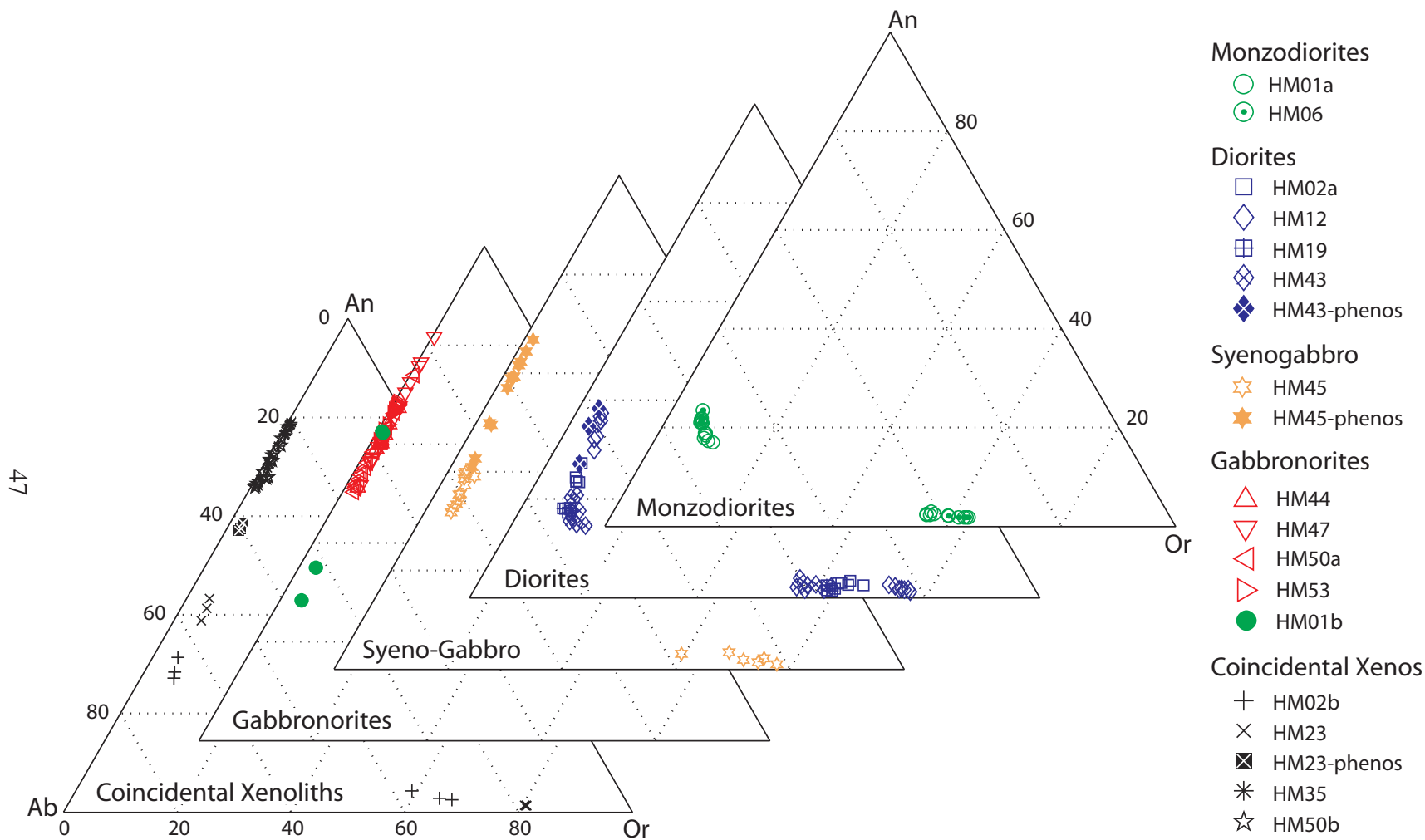


Figure 4.3: Xenolith feldspar compositions (albite - anorthite - orthoclase components), separated by lithology. Compositions are average or individual analyses of plagioclase rims, plagioclase cores, and alkali feldspar blebs. Neither gabbronorites nor poikilitic gabbros (HM35) contain alkali feldspar. Plagioclase phenocrysts are generally more anorthitic than matrix plagioclase.

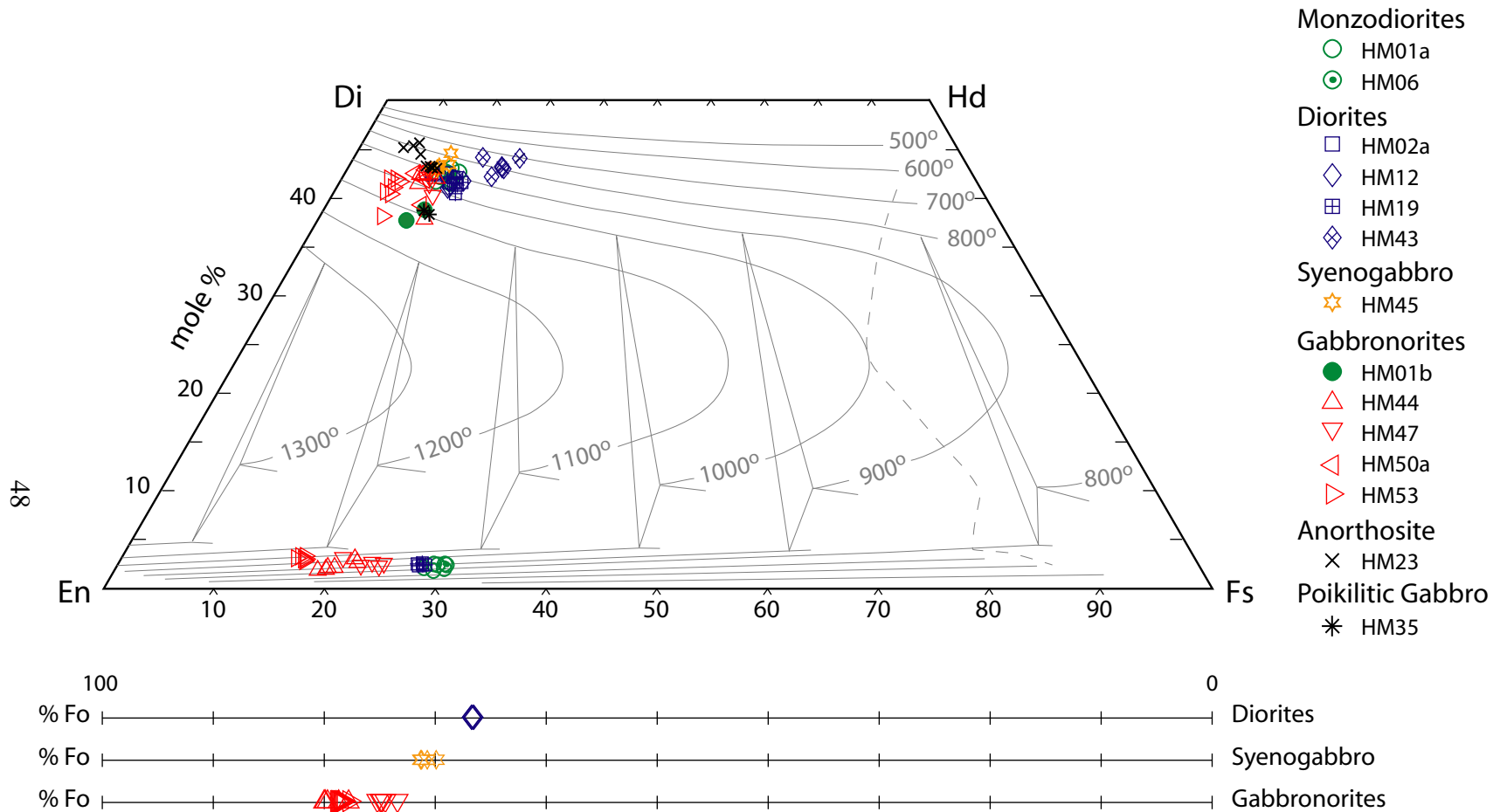


Figure 4.4: Xenolith mafic mineral (clinopyroxene, orthopyroxene, and olivine) compositions. Pyroxene compositions are displayed on the 5 kbar stability diagram of Lindsley (1983). Forsterite contents are indicated below for all analyzed olivines ($Fo = 100 \cdot Mg / (Mg + Mn + Fe^{total})$, atomic basis). All compositions are averages of multiple analyses of individual grains.

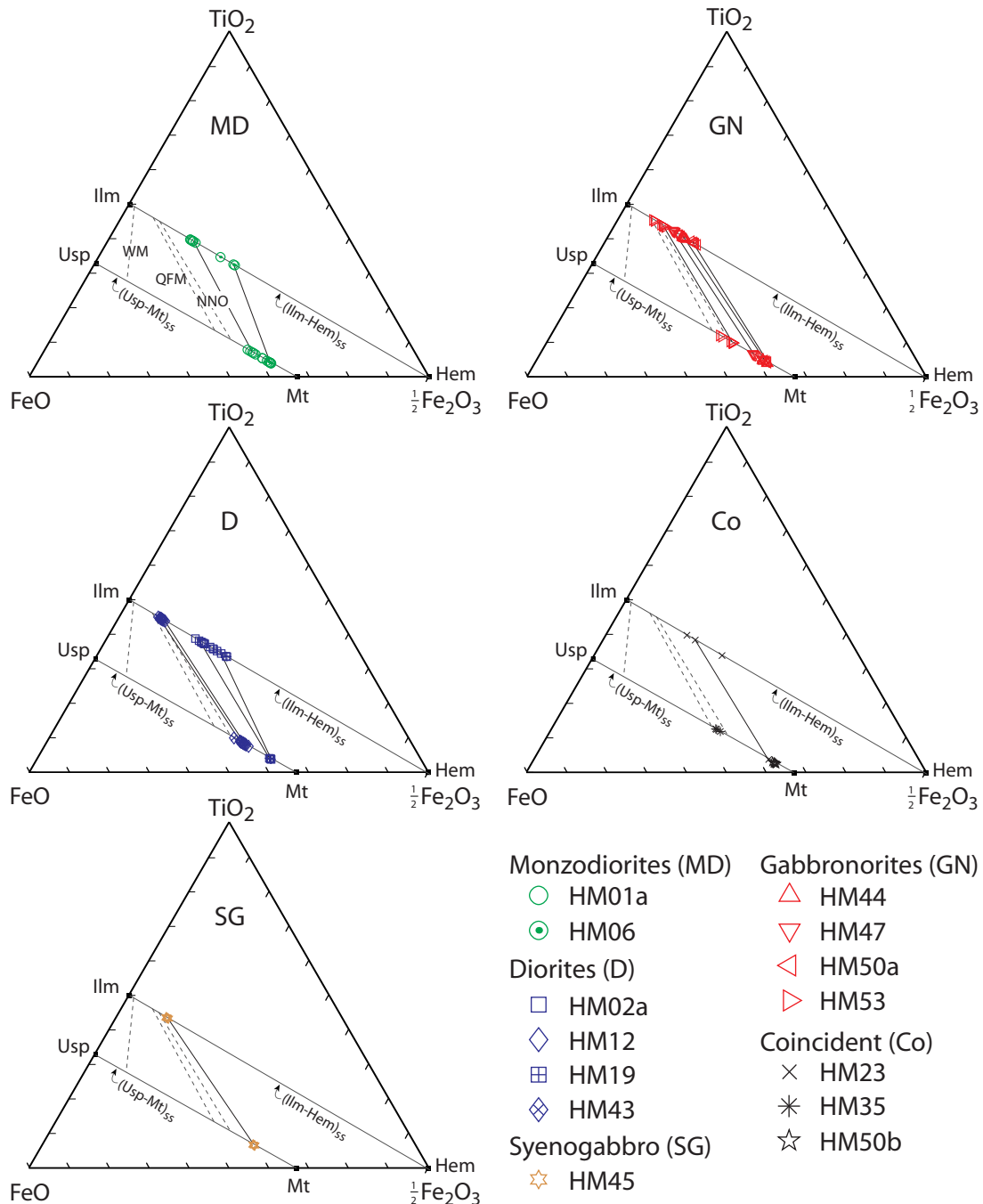


Figure 4.5: Xenolith titanomagnetite and hemo-ilmenite compositions, separated by lithology. FeO and Fe₂O₃ concentrations in titanomagnetite and hemo-ilmenite are calculated from raw electron microprobe data using the stoichiometric approach of Carmichael (1967) and projected to ideal atomic % ilmenite and ulvöspinel following Stormer (1983). Tie-lines connect representative oxide pairs. For comparison, Fe-Ti oxide compositions in equilibrium with the WM, QFM, and NNO buffers are shown for P = 1-2 kbar, T = 800° C (Lindsley, 1991). All hematites are interpreted as secondary alteration and their compositions are not shown in this figure.

A gabbroic clots of phenocrysts (HM01b; fig. 3.7b) in one monzodiorite contains An-rich plagioclase cores ($An_{62}Or_1$) and Mg-rich clinopyroxene ($En_{52-54}Wo_{38-39}Fs_{8-9}$). Clinopyroxenes also have higher concentrations of minor elements (approximately twice the Al and up to eight times the Cr) than clinopyroxenes in the monzodiorite matrix. Titanomagnetite grains in the clots are similar compositionally to those in the matrix, but have greater Cr numbers (Cr# 19.2-22.0). These mineral compositions largely correspond with those found in gabbroic rocks.

Diorites

Plagioclase grains in the diorites ($An_{15-37}Or_{4-13}$) are similar to those in the monzodiorites. Phenocrysts in HM43 (An_{27-38}) are more An-rich than matrix plagioclase in that xenolith, however they are comparable to plagioclase compositions in other diorites of this study (e.g., HM12). Alkali feldspar compositions ($An_{1-4}Or_{56-77}$) encompass the monzodiorite range, but extend towards higher Or content. Clinopyroxene ($En_{40-49}Wo_{40-44}Fs_{8-15}$, Mg# 67.5-78.4) and orthopyroxene ($En_{70-71}Wo_2Fs_{27-28}$) compositions are nearly equivalent to those of monzodiorites, with slightly greater orthopyroxene Mg numbers. Minor oxide concentrations in pyroxenes (e.g., Na_2O , Al_2O_3 , TiO_2 , Cr_2O_3) are also nearly identical to those found in monzodiorites. Olivines, not present in the monzodiorites, have $Fo_{66.4-66.6}$ (fig. 4.4). Magnetite (Usp_{12-30} , Mg# 4-8, Cr# 0-21) and ilmenite (Ilm_{67-90} , Mg# 9-16, Cr# 0-43) are similar compositionally to those in monzodiorites; chrome numbers vary greatly due to low abundances of Cr and Al. Phlogopite (Mg# 60.2-77.8) is even more titaniferous than in monzodiorites (4.3-8.0 wt % TiO_2). Again, fluorine concentrations (0.85-3.10 wt% F) are greater than chlorine

concentrations (0.22-0.33 wt% Cl). Calcic-amphibole blebs (Mg# 59.5-61.7) are not isochemical to their clinopyroxene hosts (appx. A). These amphiboles are nominally classified as kaersutites, but extend into the pargasite and magnesiohastingsite fields (Leake *et al.*, 1997).

Syenogabbro

A single syenogabbro sample was analyzed. Matrix plagioclase ($An_{32-40}Or_{3-5}$) is compositionally similar to that found in diorite and monzodiorite lithologies, but dominant normally-zoned phenocrysts ($An_{41-67}Or_{1-4}$) are far more An-rich. Alkali feldspar and clinopyroxene compositions also closely resemble those found in diorites (appx. A). Olivine grains ($Fo_{69.8-71.2}$) have higher forsterite contents than those in diorites, but concentrations of minor elements are all identical. Chrome numbers of titanomagnetites (Cr# 0-2) and hemo-ilmenites (Cr# 0-20) are both less than those observed in diorites (Cr# 0-21, 0-43, respectively), however, Mg numbers are similar to the diorites. Ideal fraction ulvospinel and ilmenite for these solid-solution series both fall within the compositional region defined by diorites HM12 and HM43 (fig. 4.5). Phlogopite is again highly titaniferous (6.3-7.7 wt% TiO_2), but fluorine (0.76-0.88 wt% F) is less abundant than in either the monzodiorites or the diorites. Kaersutite (Mg# 62.9-65.4) has slightly higher Mg number than that present in diorites.

Gabbronorites

Plagioclase in gabbronorites ($An_{50-81}Or_{1-2}$) is normally zoned. Clinopyroxene compositions ($En_{49-52}Wo_{38-42}Fs_{5-10}$, Mg# 77.1-80.7) are also more mafic than syeno-

xenoliths. Clinopyroxenes in olivine gabbro (Mg# 81.6-83.7) have even greater Mg numbers. Orthopyroxenes follow a similar trend; those found in gabbro (En₇₃₋₈₀Wo₂₋₃Fs₁₈₋₂₄) are slightly less Mg-rich than those from olivine gabbro (En₈₀₋₈₁Wo₃Fs₁₆₋₁₇). Olivines (Fo_{73.3-79.9}) are again more Mg-rich than those in syeno-xenoliths. Titano-magnetite (Usp₁₂₋₂₀, Mg# 7-13, Cr# 4-14) and hemo-ilmenite (Ilm₇₆₋₈₅, Mg# 14-24, Cr# 0-25), however, have very similar compositions to Fe-Ti oxides found in syeno-xenolith lithologies. Fe-Ti oxides in olivine gabbro are significantly different than those in other gabbros. Titano-magnetite is both Cr-rich (12.4-17.6 wt% Cr₂O₃, Cr# 60-63) and Mg-rich (Mg# 16-20). Hemo-ilmenite is also enriched in these elements (Mg# 23-26, Cr# 62-67) but not to the extent of titano-magnetite. Kaersutite (Mg# 66.5-73.6) is also more mafic than that present in syeno-xenoliths.

Coincident Xenoliths

Plagioclase in the poikilitic gabbro (An₆₇₋₇₉Or₀₋₁) is normally zoned. Plagioclase crystals are surrounded by only two large clinopyroxene oikocrysts (En₅₁₋₅₂Wo₃₈₋₃₉Fs₉₋₁₀; Mg# 75.3-78.0). Trapped host glass pockets are hawaiitic in glass composition and contain titano-magnetite crystals (Usp₃₆₋₃₈, Mg# 24-26, Cr# 1-18). Glass inclusions in plagioclase (Mg# 41.8-43.6) are also hawaiites.

Plagioclase grains in anorthosites (An₂₇₋₅₉Or₂₋₆) vary greatly, as do alkali feldspars (An₁₋₃Or₅₉₋₈₀). Clinopyroxenes (En₄₉₋₅₀Wo₄₃₋₄₆Fs₄₋₈, Mg# 77.2-82.4) are slightly more Mg-rich, but otherwise similar in composition to those found in diorites. Fe-Ti oxides are also similar in composition to those in the diorites.

The single hornblende-rich vein (HM50b) is notable for containing magnesiohastingsite, a low-Ti, low-Al(VI) amphibole not present in other xenoliths. Plagioclase crystals in this hornblende gabbro-norite are strongly anorthitic ($An_{66-76}Or_{0-2}$). Pyroxenes in this sample were not analyzed.

Thermobarometric Calculations

Hualālai xenolith assemblages contain a number of well-studied mineral systems, in which chemical equilibria are strongly dependent on P, T, or fO_2 . Quantitative expressions relating intensive parameters to the compositions of co-existing phases provide estimates of the intensive conditions at which minerals last equilibrated. These estimates present a means of exploring the relationships between xenolith lithologies and the depth of the magmatic system from which they formed. Results of thermobarometric calculations are grouped below by the model applied. Models include the magnetite-ilmenite geothermometer/ fugacity-barometer of Andersen & Lindsley (1985), the QUIIF model of Lindsley & Frost (1992), ternary feldspar geothermobarometers (Fuhrman & Lindsley, 1988; Lindsley & Nekvasil, 1989; Elkins & Grove, 1990), and the pyroxene geobarometers of Nekvasil (2004) and Nimis & Ulmer (1998). All other common igneous geobarometers, most notably the Al in hornblende geobarometer (e.g., Hammarstrom & Zen, 1986; Johnson & Rutherford, 1989b), are not applicable due to the absence of necessary phases (e.g., quartz). For each model, we only utilize those mineral compositions deemed most likely to be in chemical equilibrium with surrounding phases, as indicated by proximity of grains and independent indicators of chemical equilibrium

(e.g., Mn partitioning in Fe-Ti oxides (Bacon & Hirschmann, 1988)). Temperature estimates determined by mineral equilibria in plutonic rocks reflect the blocking temperature of different phases, and do not necessarily yield consistent magmatic values.

Fe-Ti Oxides

Fe²⁺ and Fe³⁺ assignments for Fe-Ti oxides are calculated from raw electron microprobe data using the stoichiometric approach of Carmichael (1967). These compositions are then projected into ideal ulvospinel and ilmenite end-members following Stormer (1983) for use in the geothermometer/fugacity-barometer of Andersen & Lindsley (1985). Temperature and oxygen fugacity are calculated from individual analyses of oxides, rather than mineral grain averages, in order to explore the maximum compositional variability. Analyses were taken near rims of oxides and, if present, near ilmenite-magnetite contacts. As grains were generally analyzed in triplicate, a single pair of oxide grains occasionally produced multiple estimates of temperature and fO₂. On average, the range of intra-grain temperature and fO₂ estimates is ~40% of the total range of a given sample, or ~2% relative (fig. 4.6a, b).

Only oxides which satisfied the Bacon & Hirschmann (1988) Mg/Mn partitioning criteria and which had oxide totals of between 98.5 and 101.0 wt% were used in calculations. Rhombohedral and spinel oxide pairs in physical contact were analyzed whenever present in order to ensure maximum likelihood of obtaining thermal and chemical equilibrium (not possible for HM02a, HM06, and HM23; oxide analyses in these samples were taken from proximal oxides). Inherent 2σ uncertainties in the

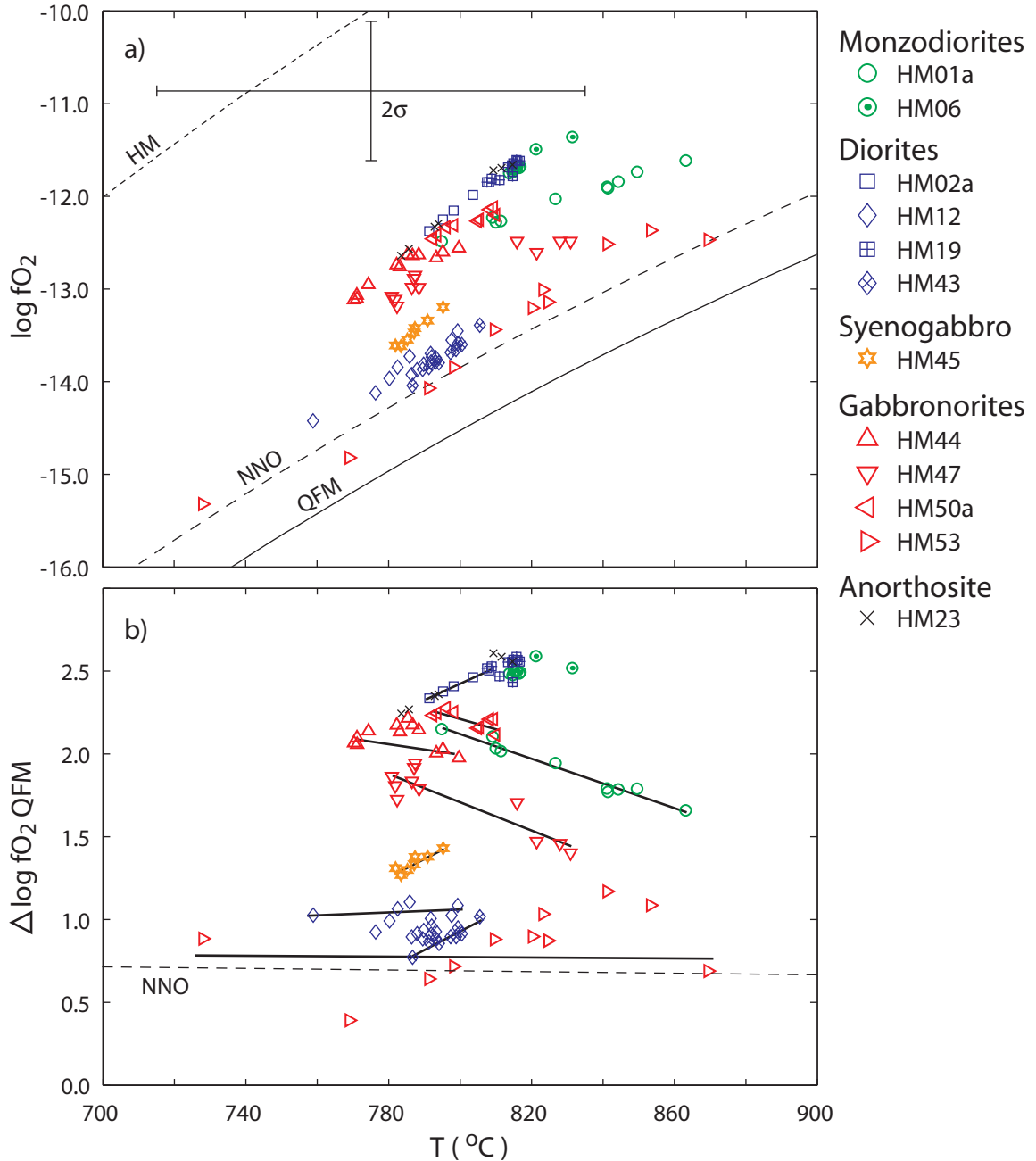


Figure 4.6: Equilibrium temperatures and oxygen fugacities indicated by Fe-Ti oxide pair thermobarometry (Andersen & Lindsley, 1985). a) Temperature vs. absolute oxygen fugacity (\log units f_{O_2}). Multiple oxide pairs in a single sample span a ~ 20 - $80^{\circ}C$ temperature range. b) Temperature vs. oxygen fugacity relative to the QFM buffer ($\Delta \log f_{O_2} \text{ QFM}$). These pairs often produce coherent T - f_{O_2} trends. Slopes vary from positive to negative (relative to the QFM buffer) with no correlation to lithology.

geothermometer/fugacity-meter of Andersen and Lindsley are ~40-80°C and ~0.5 to 1.0 log units f_{O_2} (Spencer & Lindsley, 1981).

Temperature ranges indicated by members of each lithology are essentially coincident with the overall range for the suite of 13 samples, spanning 770-840°C (table 4.1, fig. 4.6a). That is, there is no correspondence between temperature recorded in Fe-Ti oxides and bulk composition or lithology. Oxygen fugacities fall primarily between -11.5 and -14.0 log units f_{O_2} , corresponding to ~0.75 to 2.5 log units f_{O_2} above the QFM buffer (QFM + 0.75 to 2.5). Fugacities also show no consistent variation with lithology (monzodiorite samples record both the highest and lowest values of $\Delta \log f_{O_2}$ QFM). Individual xenoliths define a relatively restricted $\Delta \log f_{O_2}$ QFM (fig. 4.6a) and commonly produce coherent T- f_{O_2} trends. While all trends indicate a decrease in absolute oxygen fugacity during cooling, the slope of this trend varies slightly with respect to the QFM buffer (fig. 4.6b). Some xenoliths lie along oxidizing trends, others along reducing trends (both with respect to the QFM buffer). Again, there is no apparent correlation between lithology and the change in oxygen fugacity with temperature. We attribute these variations to heterogeneities between local crystallization environments (e.g., different H_2O concentrations).

QUIIF

The QUIIF system (Lindsley & Frost, 1992) involves 13 independent equilibria among augite, pigeonite, orthopyroxene, olivine, quartz, titano-magnetite, and hemo-ilmenite. The computer program QUIIF minimizes Gibbs' free energy for a set of user-specified phase compositions and finds the temperature, pressure, and oxygen fugacity at

Table 4.1: Summary of thermodynamic calculations

		Fe-Ti oxide equilibria				QUIIF ^a			Ternary feldspar modelling ^b		Ti/Al Cpx ratio	Nimis & Ulmer Cpx barometer ^c			
		Temp [°C]		fO ₂ [- log units]		Temp [°C]			P _{max} [kbar]	Temp [°C]	P [kbar]	P [kbar]			
Lithology:		avg.	2σ	avg.	2σ	Cpx	Opx	Combined Px				avg.	2σ	# anal.	
Syeno-Xenoliths															
	HM01a	MD	839	(38)	11.9	(0.4)	955	902	886	6	755 - 785	7	5.1	-	(1)
	HM06	MD	818	(12)	11.6	(0.3)	939	916	893	4	725 - 745	7.5	5.9	(0.7)	(4)
	HM02a	D	799	(13)	12.1	(0.4)	949	^d	^d	7.5	715 - 775	6	5.9	(0.4)	(4)
	HM12	D	787	(20)	13.8	(0.5)	971	^d	^d	10	670 - 765	5.5	6.1	(1.4)	(14)
	HM19	D	813	(6)	11.7	(0.2)	969	939	929	9	700 - 775	7	5.4	(1.5)	(3)
	HM43	D	796	(11)	13.7	(0.4)	830 ^e	-	-	10	730 - 795	2.5	4.0	(1.9)	(14)
	HM45	SG	787	(9)	13.5	(0.3)	898 ^e	-	-	5.5	705 - 780	6	5.0	(0.7)	(12)
Gabbro-norite Xenoliths															
57	HM01b	GN	814	(39)	12.2	(0.5)	-	-	-				4.7	(2.8)	(5)
	HM44	GN	783	(20)	12.8	(0.4)	1018	956	955				3.2	(1.5)	(14)
	HM47	GN	799	(40)	12.8	(0.5)	1007	992	970				2.7	(1.1)	(13)
	HM50a	HGN	802	(14)	12.3	(0.2)	1002 ^e	-	-				2.4	(1.6)	(4)
	HM53	OGN	812	(79)	13.5	(1.9)	1069	1070	1008				3.8	(1.9)	(12)
Coincident Xenoliths															
	HM02b	AN	-		-		-	-	-	1.5	750 - 760				
	HM23	AN	799	(26)	12.1	(0.9)	893 ^e	-	-	>10	620 - >740				
	HM35	PG	-		-		1103 ^e	-	-	-	-				
	HM50b	HGN	-		-		-	-	-	-	-				

^a QUIIF calculations all run at p = 2kbar, errors estimated at ~25°C. ^b Ternary feldspar compositions used with the model of Lindsley & Nekvasil (1989). $P_{max} \equiv P_{|sum(dT)|=80}$. ^c Nimis & Ulmer geobarometer run at T = 970°C for syeno-xenoliths, and T = 1020°C for gabbro-norites, based on QUIIF cpx temps. Syeno-xenoliths run with MA calibration, gabbro-norites with TH calibration. ^d Orthopyroxene is present, but composition undetermined. ^e No orthopyroxene is observed. Clinopyroxene temperature estimate is a minimum.

which the mineral assemblage is stable (Andersen *et al.*, 1993). The full set of thermodynamic equilibria is mathematically overdetermined, which allows QUIIF to be used even in the absence of some phases. Pressure determinations, however, rely on the equilibrium between quartz, olivine, and orthopyroxene, and therefore require that silica activity is known.

Equilibrium temperatures and oxygen fugacities determined using only Fe-Ti oxide compositions are very similar to those found using the geothermometer/fugacity-barometer of Andersen and Lindsley (within $\sim 50^\circ\text{C}$ and 1-2 log units $f\text{O}_2$; table 4.1). The QUIIF Fe-Ti oxide formulation differs from the Andersen and Lindsley model by including Fe/Mg and Fe/Mn partitioning between the two phases. These additional constraints cause QUIIF to fail to converge for most of the xenolith oxide pairs. This indicates that, despite meeting the Bacon-Hirschmann criteria, Mg and Mn are not partitioned in perfect equilibrium, according to the solution models. Apparent disequilibrium may be caused by both analytical uncertainty of these low-abundance elements and the tendency of oxides to expel Mg and Mn during cooling (Frost & Lindsley, 1992). Temperatures and oxygen fugacities determined with Fe-Ti oxides through QUIIF are not reported because of the apparent Mg and Mn disequilibria.

Ca, Mg, and Fe equilibria in orthopyroxene and clinopyroxene pairs are sensitive to crystallization temperature, but relatively insensitive to ambient pressure. If only one pyroxene is present, its composition indicates a minimum temperature (Lindsley, 1983); if both orthopyroxene and clinopyroxene are known to be present, either pyroxene compositions can function as an independent geothermometer. Average pyroxene

compositions were used for each sample, as there was little overall inter-grain chemical heterogeneity. Estimated combined uncertainty from the QUILF program and compositional variation is $\sim 25^{\circ}\text{C}$. Whenever possible, we calculated three temperatures for each sample: T_{cpx} , T_{opx} , and $T_{\text{combined px}}$. Invariably, the temperature obtained using orthopyroxene compositions (T_{opx}) is less than that indicated by clinopyroxene (T_{cpx}). This suggests that the blocking temperature, the temperature at which a mineral composition last equilibrates chemically, is higher for clinopyroxene than for orthopyroxene. Orthopyroxenes in equilibrium with the observed clinopyroxene compositions would have higher Mg numbers than those observed, according to QUILF calculations. The variation in Fe/Mg necessary to bring both pyroxenes into equilibrium is greater than that observed within any single sample. That is, no two pyroxenes constitute an equilibrium pair. Therefore, the use of two-pyroxene geothermometry for these pyroxene compositions is invalid.

Equilibrium temperatures determined from clinopyroxene compositions (T_{cpx}) ranged from $939\text{-}971^{\circ}\text{C}$ for the syeno-xenolith series (not including minimum temperature estimates). Gabbro-norite series xenoliths record higher T_{cpx} , ranging from $1007\text{-}1069^{\circ}\text{C}$ (the highest temperature corresponding with HM53, an olivine gabbro-norite). These temperatures are similar to those obtained graphically from pyroxene compositions (fig. 4.4) using the projection method of Lindsley (1983).

Both pyroxenes were also significantly out of equilibrium with Fe-Ti oxides. Predicted temperatures for pyroxene and Fe-Ti oxide equilibria deviate by $\sim 100\text{-}150^{\circ}\text{C}$, with oxides recording the lower temperature (table 4.1). The difference increases in the

gabbro series, where deviations between predicted Fe-Ti oxide and pyroxene temperatures extend to 250°C. The QUIF system does not converge for combined Fe-Ti oxide and pyroxene assemblages, nor does it converge for any assemblages containing additional phases (e.g., olivine, quartz). This is the result of inter-mineral variations in blocking temperature ($T_{cpx}^{blocking} > T_{opx}^{blocking} > T_{Fe-Tioxides}^{blocking}$). All xenoliths most likely experience significant sub-solidus re-equilibration. Therefore, calculated temperatures likely reflect blocking temperature rather than any magmatic temperature. Exsolution lamellae in clinopyroxenes were too fine to determine accurate compositions, making estimates of reconstructed pyroxene compositions impossible.

Ternary Feldspar Models

Ternary feldspar models utilize the extensive solid solution that exists in the albite-anorthite-orthoclase (Ab, An, Or, respectively) ternary system at high temperatures. Ternary models offer significant advantages over simple binary models as they do not require projections onto the binary Ab-Or and Ab-An axes. For two feldspars to exist in equilibrium, activities of each end-member component must be balanced in both plagioclase and alkali feldspar. Each component equation (e.g., $a_{Ab}^{afs} = a_{Ab}^{plag}$) provides an independent constraint on T and P for a given set of mixing parameters; therefore, compositions of coexisting feldspars yield a temperature estimate if pressure is treated as a known parameter. Simultaneous thermobarometry has been attempted using pressure dependent activity expressions (Green & Usdansky, 1986; Renzulli & Santi, 2000). Fuhrman & Lindsley (1988) strongly caution against this approach because predicted pressure is highly sensitive to small variations and uncertainties in composition

(i.e., composition is only weakly pressure dependent). The absence of high resolution pressure indicators (e.g., Al-in-hornblende geobarometer or kyanite-andalusite-sillimanite phase stability) motivates us to consider the pressure-dependence of feldspar pairs as relevant, even if the uncertainties are large. Recognizing the limitations of these estimates, we have developed a method to simultaneously provide a first-order estimate of the equilibrium pressure, as well as a range of possible equilibrium temperatures.

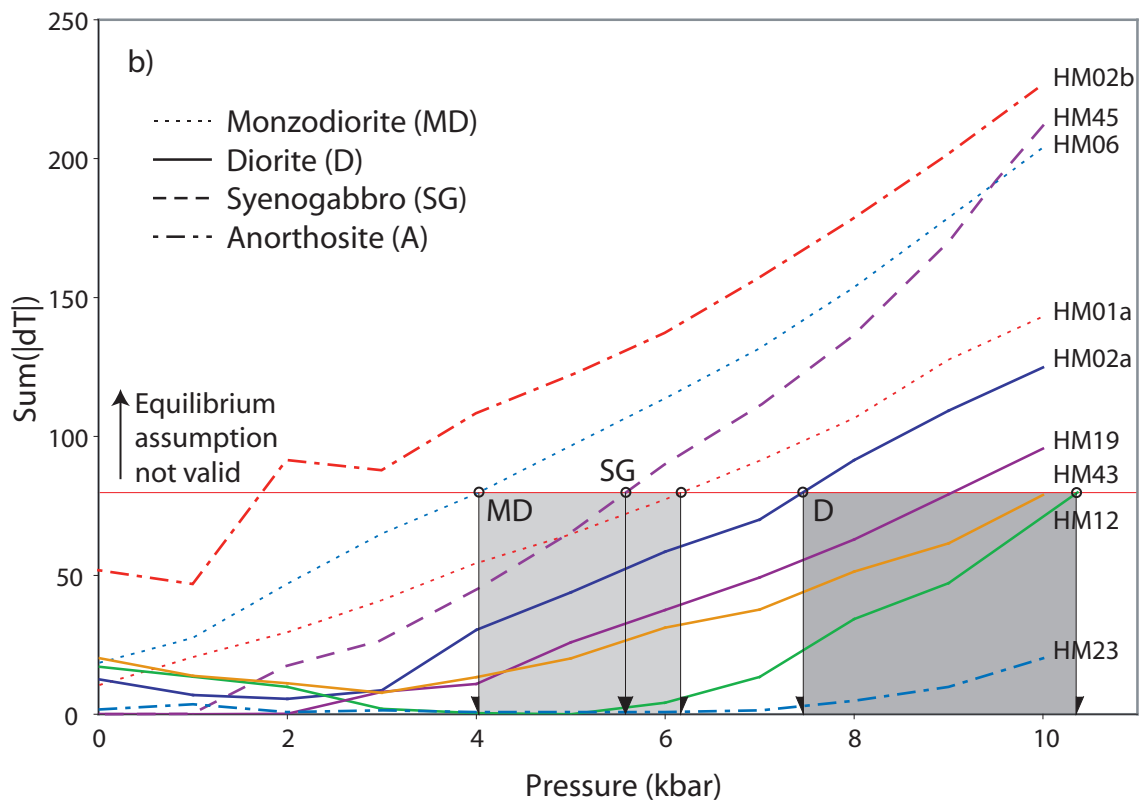
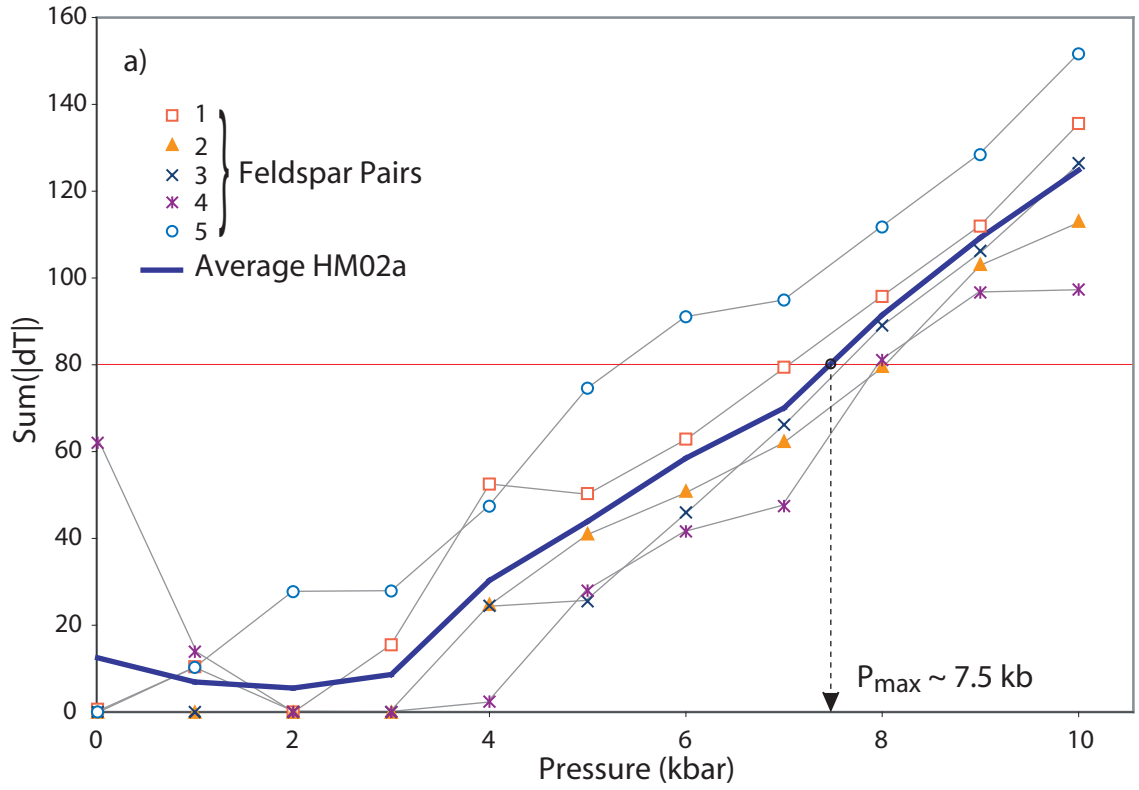
Our method employs the interactive computer program SOLVCALC (Shaoxiong & Nekvasil, 1994) to determine the pressures at which feldspar compositions best correspond with ternary feldspar models. SOLVCALC solves for the equilibrium temperature of a feldspar pair at a specified pressure. The program varies feldspar compositions within a user-defined interval to minimize a residual, $sum(|dT|)$ (defined as the sum of the differences in predicted temperatures for each end-member component, or $sum(|dT|) = |T_{Ab}-T_{An}| + |T_{Ab}-T_{Or}| + |T_{An}-T_{Or}|$). $Sum(|dT|)$ is zero if all three components predict a single temperature and the system is well-defined. Greater values imply either compositional error, a poorly calibrated mixing model, or disequilibrium between the feldspars. Assuming that the residual is primarily a function of the final case, the average $sum(|dT|)$ of a sample indicates whether feldspar pairs are in equilibrium at the pressure being considered. By testing pressures iteratively, an optimum (i.e., equilibrium) pressure range is defined for each xenolith.

All members of the syeno-xenolith series contain albitic plagioclase rims with alkali feldspar exsolution blebs; these are the only samples for which ternary feldspar modeling is possible. Only those average rim compositions of plagioclase and alkali

feldspar in which oxides total 98.5-101 wt%, tetrahedral cations total 4.00 ± 0.02 , and interstitial cations total 1.00 ± 0.02 were used. Between 4-7 feldspar pairs were analyzed from each sample. End-member compositions were allowed to vary ± 1 mole% from the average, since multiple analyses of individual grains tended to vary less than this amount (repeating our procedure with accuracy of ± 2 mole% gives very similar results). For each feldspar pair, equilibrium temperature and residual, $sum(|dT|)$, were determined as functions of pressure ($P = 0.01$ -10 kbar at 1kbar intervals).

This technique was employed using the ternary feldspar mixing model of Lindsley & Nekvasil (1989), and residuals were compared as a function of pressure for multiple pairs in a single sample (e.g., fig. 4.7a). While it is rare that all feldspar pairs conform exactly at any temperature (i.e., $sum(|dT|) = 0$), pairs do show increasingly poor fits at greater pressures. Average residuals were computed for all feldspar pairs in each alkali feldspar-bearing xenolith (fig. 4.7b). The trend illustrated by sample HM02a in figure 4.7a is common to most xenoliths. This includes a relatively stable residual at pressures < 4 kbar and a steady increase in residual with increasing pressure. Within this trend, different xenoliths averaged greater or lesser residuals depending on how well their compositions were described by the available mixing models. All xenoliths have minimum residuals at pressures ≤ 5 kbar. Increasing residuals lead to clearly visible deviations between the observed feldspar pair compositions and calculated feldspar solvi (fig. 4.8). Similar results were also obtained using the mixing models of Fuhrman & Lindsley (1988) and Elkins & Grove (1990).

Figure 4.7: Results of ternary feldspar modeling. a) Temperature residuals of individual feldspar pairs (numbered 1-5) as a function of pressure. Temperature residuals indicate how well observed feldspar compositions are described by ternary feldspar models at a specific T and P. Residuals are calculated from the SOLVCALC program of Shaoxiong & Nekvasil (1994) using the ternary feldspar model of Lindsley & Nekvasil (1989). $P_{\max} = P_{|\sum(dT)|} = 80$, above which the assumption of equilibrium is no longer valid. b) Average temperature residuals as a function of pressure for all two-feldspar bearing samples. Each line represents the average of 3-7 feldspar pairs. All xenoliths are most conformable at low pressures and lead to increasing temperature residuals at higher pressures. Shaded zones represent ranges of P_{\max} for the indicated lithologic group. MD = monzodiorites, D = diorites, SG = syenogabbro.



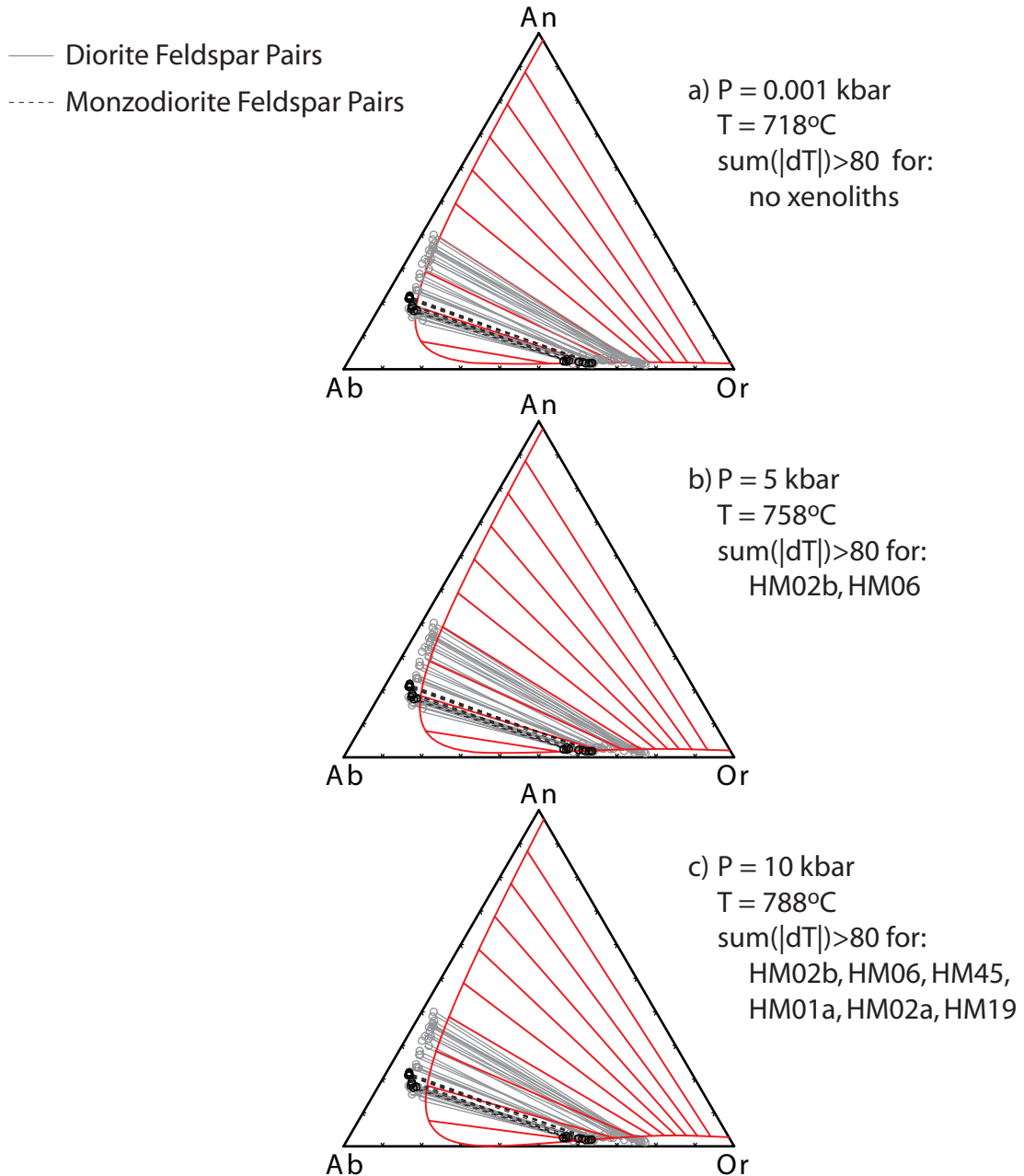


Figure 4.8: Calculated feldspar solvi (from SOLV CALC) and observed feldspar pairs. Solvi are generated at a) 0.001 kbar, b) 5 kbar, and c) 10 kbar at the average best-fit temperature of all xenoliths for each pressure. Solvi calculated using the ternary feldspar model of Lindsley & Nekvasil (1989). Both feldspar compositions and slopes of tie-lines connecting feldspar pairs greatly deviate from predicted values at pressures >5 kbar.

Maximum pressure (P_{\max}) is defined as the pressure above which the residual $\sum(|dT|)$ is greater than 80 (table 4.1), an arbitrary cutoff defined by Fuhrman and Lindsley (1988) above which the equilibrium assumption is not satisfied. Residuals of this magnitude result in significant deviation from the predicted solvus (as illustrated in fig. 4.8). Applying the even more stringent condition that all feldspar pairs must remain in equilibrium (rather than the average residual) decreases maximum pressure estimates by up to a few kilobars (figure 4.7a). Reported temperatures are the best-fit temperatures found over the pressure range $P = 0$ - P_{\max} and have inherent uncertainty of $\sim 40^\circ\text{C}$.

In summary, P_{\max} ranges from 4-6 kbar for monzodiorites, 7.5-10 kbar for diorites, and ~ 5.5 kbar for the syenogabbro. The anorthosite HM02b that shares a contact with a diorite has $P_{\max} \sim 1.5$ kbar. While the minimum residual is commonly found at lower pressures (< 4 kbar) the sensitivity of this method to mineral compositions suggests that these estimates are unreliable. Due to this inherent uncertainty, we chose instead to emphasize the maximum likely equilibrium pressures. Associated temperatures range from 620 - 795°C . Temperature estimates for individual samples span ~ 20 - 100°C ranges (table 4.1). Temperature estimates do not appear correlated with lithology, and are all significantly lower than the pyroxene and Fe-Ti oxide thermometry estimates.

Pyroxene Geobarometers

Two experimentally calibrated pyroxene geobarometers provide additional pressure estimates for the system. These compositional geobarometers include (1) an empirical study of pressure dependent Ti/Al ratio in pyroxenes (Thy, 1991; Nekvasil *et*

al., 2004), and (2) a structural geobarometer calibrated for multiple liquid compositions (Nimis & Ulmer, 1998; Nimis, 1999).

For rocks with similar bulk compositions, the Ti/Al ratio in pyroxenes decreases nearly linearly with increasing pressure. Experimental data for pyroxenes in equilibrium with mildly alkalic melts (from fig. 11 of Thy (1991) and fig. 13 of Nekvasil *et al.* (2004); see table 4.2) are used to create a new pressure calibration (fig. 4.9a). Overlap between the two experimental data sets is generally good, but pyroxene Ti/Al ratios from Nekvasil *et al.* are slightly higher. Only a single data point is given for intermediate pressures (4.3 kbar of Nekvasil) leaving the calibration of moderate Ti/Al ratios poorly constrained.

Median pyroxene compositions from syeno-xenoliths indicate equilibrium pressures for these rocks between 2.5-7.5 kbar (fig. 4.9b, table 4.1). Natural pyroxenes span a much smaller range in Al content (0.03-0.13 cations Al / 6 O), and contain less Al than experimental pyroxenes in the Thy (0.16-0.61 cations) and Nekvasil (0.17-0.43 cations) calibration sets. This approach is not appropriate for determining pressure estimates for gabbro-norites, as their assemblages suggest that they might not have crystallized from mildly alkalic liquids. Since the full extent of pyroxene Ti/Al dependence on bulk compositions is unknown, it is safest to only compare pyroxenes in equilibrium with similar melts.

The Nimis and Ulmer structural geobarometer calculates cell volume as a function of composition. Trivalent octahedral aluminum significantly decreases cell volume, leading to preferential uptake of Al in this cation site at higher pressures. Unlike

Table 4.2: Major element composition (in oxide wt%) of experimental melts used in calibrating the Ti/Al clinopyroxene geobarometer.

Sample ID:	Thy (1991): Surtsey alkalic basalt ^a				Nekvasil et al. (2004): Nandewar alkalic basalt ^b				
	Run 18	Run 27	Run 26	Run 19	A	A	A	A	B
notes:	(n = 16) ^c 1 σ	(n = 4) ^c 1 σ	(n = 1) ^c	(n = 7) ^c 1 σ	9.3 kbar 1080°C	0 kbar 1104°C	9.3 kbar 1040°C	0 kbar 1065°C	9.3 kbar 1040°C
SiO ₂	47.17 (0.80)	47.44 (0.14)	47.54	47.57 (0.50)	47.25	50.00	52.25	54.69	48.09
TiO ₂	3.42 (0.14)	4.02 (0.14)	4.57	4.37 (0.24)	3.14	4.36	1.24	2.63	2.18
Al ₂ O ₃	12.77 (0.17)	13.07 (0.13)	13.20	12.22 (0.17)	17.24	12.57	17.80	14.16	15.68
FeO ^{tot}	13.59 (0.20)	13.98 (0.36)	13.59	14.21 (0.20)	10.04	11.34	8.29	8.17	11.06
MnO	0.25 (0.04)	0.29 (0.14)	0.23	0.27 (0.05)	0.10	0.13	0.26	0.11	0.15
MgO	5.32 (0.12)	5.55 (0.04)	4.80	4.14 (0.09)	4.42	4.92	2.53	2.80	3.43
CaO	11.71 (0.23)	11.01 (0.29)	9.16	10.16 (0.14)	7.05	9.41	5.63	5.42	6.22
Na ₂ O	3.25 (0.11)	3.58 (0.18)	3.63	3.37 (0.13)	3.24	3.02	3.79	3.39	3.82
K ₂ O	0.71 (0.04)	0.72 (0.06)	1.16	1.08 (0.05)	1.90	2.19	2.42	4.18	2.42
P ₂ O ₅	0.43 (0.06)	0.50 (0.03)	0.61	0.63 (0.06)	0.67	0.79	1.10	1.55	1.78
SUM	98.62	100.16	98.49	98.02	95.05	98.72	95.33	97.12	94.83

^a All one atmosphere experiments. ^b All no volatiles added (N.V.A.) experiments. ^c Number of microprobe analyses averaged to determine glass composition.

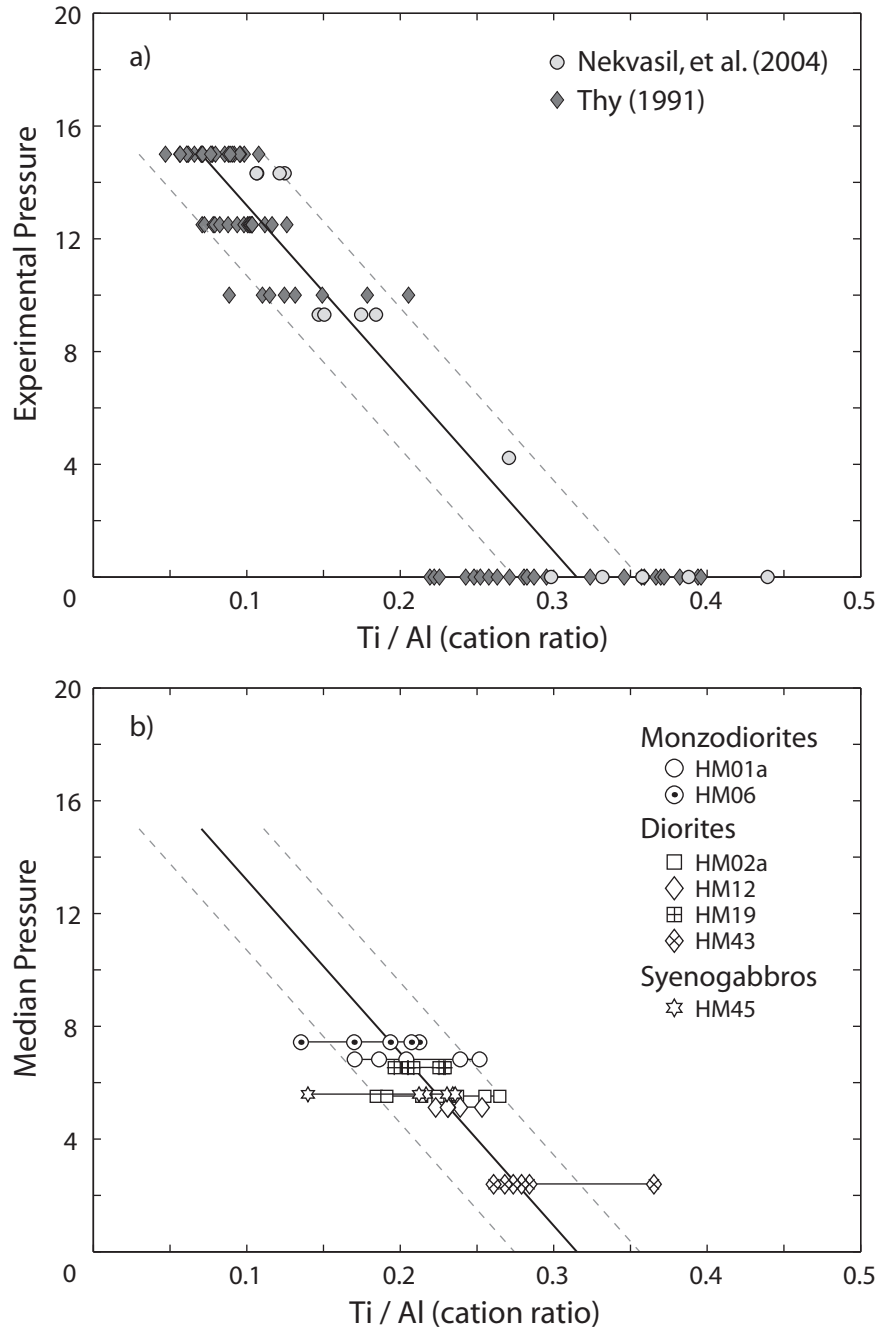


Figure 4.9: The Ti/Al ratio in clinopyroxenes in equilibrium with similar composition melts is a function of total pressure. a) Experimentally calibrated pyroxene compositions in equilibrium with mildly alkalic melts from Thy (1991) at $P = 0.001$ kbar, 4.3 kbar, 9.3 kbar, and 14.3 kbar and from Nekvasil et al. (2004) at $P = 0.001$ kbar, 10 kbar, 12.5 kbar, 15 kbar. Data has been fit with a least-squares regression (as a function of experimental pressure). 95% confidence intervals are indicated by dotted lines. b) Clinopyroxene compositions of Hualalai xenoliths, and pressures indicated by the median Ti/Al cation ratio.

earlier proposed pyroxene geobarometers (Grove *et al.*, 1989), the compositional effect on cell volume, and therefore the compositional dependence on pressure, is not limited to aluminum. Multiple calibrations of this geobarometer were introduced for different coexisting liquid compositions, including both anhydrous basaltic (BA) and hydrous basaltic (BH) liquids (Nimis & Ulmer, 1998), as well as basic to acidic compositions along both the tholeiitic (TH) and mildly alkaline (MA) trends (Nimis, 1999). All of these calibrations are temperature-dependent except for the BA model. While all calibrations were considered, the MA calibration was used with pyroxenes from syenogabbros and the TH calibration was used with those from gabbro-norites. These were selected as the calibrations which most closely resemble hypothetical parent liquids for the xenoliths (as discussed later). Both of these calibrations are highly temperature dependent ($dP/dT \sim -0.05 \text{ kbar}/^\circ\text{C}$). Temperatures used in calculations correspond to maximum estimates for a lithology calculated using the QUIIF model and clinopyroxene compositions (for monzodiorites and diorites, $T_{\text{cpx}} = 970^\circ\text{C}$, for gabbro-norites, $T_{\text{cpx}} = 1020^\circ\text{C}$). In using these temperatures, we implicitly assume that blocking temperatures are similar for all elements in clinopyroxene. Because we are using maximum temperatures and dP/dT is negative, pressure estimates are minima. If further sub-solidus equilibration occurs below temperatures indicated by the QUIIF model, the Nimis and Ulmer geobarometer will underestimate the real pressure.

Diorite pressures of crystallization range from ~4-6 kbar (fig. 4.10, table 4.1). Monzodiorites (~5-6 kbar), and syenogabbros (~5 kbar) are restricted to smaller pressure ranges, probably due to a smaller number of investigated samples. Gabbro-norites span a

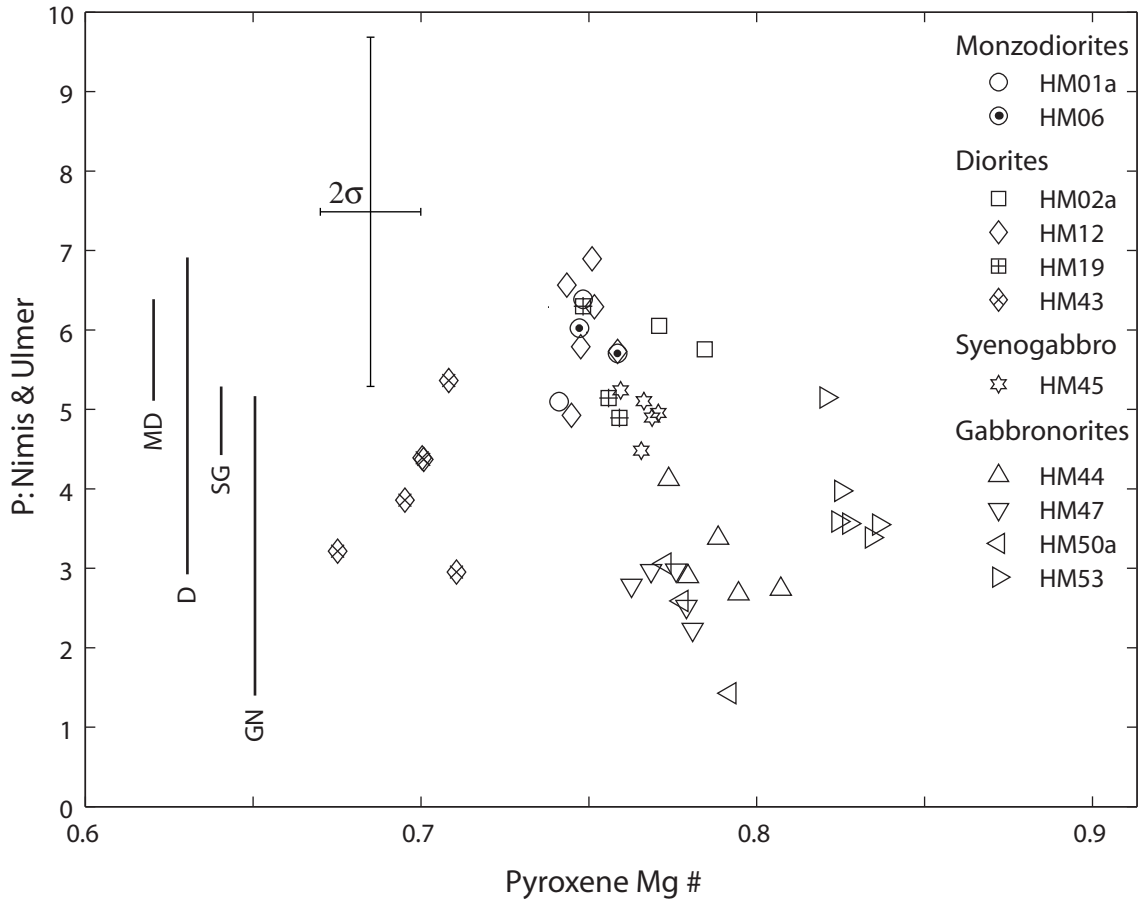


Figure 4.10: Equilibrium pressures of natural clinopyroxenes predicted by the structural geobarometer of Nimis & Ulmer (Nimis & Ulmer, 1998; Nimis, 1999). Data points indicate average clinopyroxene compositions. Only those analyses with oxide totals between 98.5-100.5 wt% and cation sums between $T = 1.998-2.002$ and $M = 1.995-2.005$ were considered. Pressure results for syeno-xenoliths (monzodiorites, diorites, and syenogabbros) were calculated for $T_{eq} = 970^{\circ}\text{C}$ and with the mildly alkaline (MA) experimental calibration. Results for gabbronorites were calculated for $T_{eq} = 1020^{\circ}\text{C}$ and with the tholeiitic (TH) calibration. 2σ uncertainties = ± 2.2 kbar; $dP/dT \sim -0.05$ kbar/ $^{\circ}\text{C}$. MA calibration included 69 clinopyroxenes; maximum residual = 2.7 kbar. TH calibration included 143 clinopyroxenes; maximum residual = 3.4 kbar. Application of the geobarometer to natural igneous clinopyroxenes returns pressures within ~ 2 kbar of independent pressure estimates (Nimis, 1999).

similar range of pressures (~2-5 kbar) but tend to indicate lower average pressures.

Results for the MA calibration are generally ~1-2 kbar greater than those predicted by both the BH and TH calibrations. Preferred calibrations (MA for syeno-xenoliths and TH for gabbro-norites) produce pressures similar to those indicated by the empirical method of Thy and Nekvasil.

CHAPTER 5. DISCUSSION

The following discussion is divided into three separate sections corresponding to the three principle lines of inquiry stated in the introduction. The petrogenesis of the different plutonic lithologies, including their probable parentage, is considered first. This section aims to describe the lithologic groups in the context of Hualālai volcanism and specifically identify those that may have formed during crystal fractionation of magmas parental to the PWW trachyte. Next, bulk compositions of xenoliths and alkalic lavas at Hualālai are used to infer a potential liquid line of descent (LLD) leading to the PWW trachytes. This is compared against MELTS modeled LLDs, experimental LLDs, and other Hawaiian alkalic LLDs in an effort to further constrain estimates of intensive thermodynamic parameters (e.g., T, P, pH₂O). Finally, potential models explaining the compositional gap in erupted lavas at Hualālai are discussed in view of the newly constrained LLD.

Petrogenesis of Plutonic Fragments

The diversity of xenolith lithologies suggests that they may be formed by different processes and from different parent magmas. In order to apply information contained within the xenoliths to a study of the PWW trachytes, the petrogenesis of different lithologic groups must be ascertained. The following section first questions the style of crystallization (i.e., open-system accumulation or closed-system solidification of magma) and then considers potential parent magmas of, and relationships between, each principle lithologic series.

Cumulates vs. Solidified Magmas

Textures of dioritic xenoliths are not those generally associated with cumulates. Dioritic xenoliths (diorites and monzodiorites) share common interpenetrative allotriomorphic textures, dominated by interfingering, consertal feldspar boundaries. They contain neither apparent cumulus phases nor other petrographic evidence that these rocks are cumulates. Whether these rocks represent melts crystallized entirely as closed systems or were affected by late-stage fluid infiltration and metasomatism is difficult to determine petrographically. The relatively fine grain-size of some of the monzodiorites and diorites (HM06, HM19; table 3.1), however, suggests that in these cases solidification occurred relatively rapidly and was not followed by a protracted high-temperature annealing period. Thus, at least the fine-grained xenoliths may represent melt compositions.

The lithologic distinction between monzodiorites and diorites is arbitrary. The decisive qualification of monzodiorites (higher modes of alkali feldspar) is probably an effect of the crystallization of progressively less anorthitic and more ternary feldspar, which later exsolved into greater proportions of alkali feldspar. Thus, diorites and monzodiorites are inferred to be end-members of a single gradational suite, henceforth referred to as the dioritic xenoliths. Mineral compositions (discussed in further detail later) support this interpretation.

Bulk compositions of dioritic xenoliths also represent plausible liquid compositions. Major element concentrations (except phosphorous) fall between post-shield alkalic basalt and trachyte compositions (fig. 4.1, 4.2). Dioritic concentrations of

P₂O₅ exceed both the alkalic basalt and trachyte compositions by a factor of 2-6.

However, this P₂O₅ peak corresponds with elevated phosphorous concentrations observed in other Hawaiian post-shield alkalic magmas at equivalent MgO contents (e.g., Kohala (Spengler & Garcia, 1988), Mauna Kea (Frey *et al.*, 1990)). High phosphorous concentrations in Hualālai magmas may result from phosphorous enrichment prior to phosphate-saturation (in this case, as apatite) and cannot be explained through mixing of trachyte with parental basalt.

Significant compositional variation (~1 wt% K₂O and TiO₂ and up to ~5 wt% SiO₂, FeO* between samples with similar MgO contents; fig. 4.1) define two groups of dioritic xenoliths: (1) Fe-rich diorites, enriched primarily in FeO* and TiO₂ (all contain FeO* >10 wt%), and (2) Si-rich diorites (FeO* <10wt%, MgO 3-4 wt%). Fe-rich dioritic xenoliths have slightly higher modes of Fe-Ti oxides than other xenoliths. Some of this variation may be due to the evolution of these xenoliths from subtly different parent compositions, however it also suggests minor accumulation of Fe-Ti oxides or infiltration of an Fe-rich melt. Such a melt may occur through extreme localized fractionation and magma segregation (Fodor & Vandermeijden, 1988) or through liquid immiscibility (Philpotts, 1982; Longhi, 1990; Hurai *et al.*, 1998). Thus, while dioritic xenoliths may not represent cumulates, they did not necessarily crystallize in strictly closed-system environments and therefore only offer approximations of original melt composition.

Syenogabbros are dominated by large anorthitic plagioclase laths (~70 vol%) forming a loose-packed orthocumulate framework (Wager *et al.*, 1960), around which other mineral phases have crystallized. In ideal cases, the original bulk magmatic

composition of orthocumulates is conserved, although potentially modified by metasomatism (Wager *et al.*, 1960). While this may be the case for syenogabbros, high concentrations of plagioclase laths are also compatible with accumulation of this phase due to buoyancy forces, causing settling or flotation.

Bulk compositions of syenogabbros are broadly similar to the most evolved alkalic basalts (~5 wt% MgO) found on the surface of Hualālai. Syenogabbro xenoliths deviate in two directions from these compositions: (1) One group is enriched in aluminum, and depleted in other elements, most notably FeO*, TiO₂, P₂O₅, and K₂O, as well as the CaO/Al₂O₃ ratio (fig. 4.1), and (2) The second group is relatively enriched in FeO*, TiO₂, and P₂O₅, and depleted in Al₂O₃ and SiO₂. The first of these trends is likely due to accumulation of plagioclase (~Ab₄₀). The second trend could be related to an accumulation of either Fe-Ti oxides and apatite, or a residual liquid with a similarly enriched composition, which later crystallized into these phases. Enrichment of select elements (e.g., FeO*, TiO₂, and P₂O₅) would lead to a depletion of others (e.g., Al₂O₃ and SiO₂) purely because of mass balance considerations. These trends correspond with increased modes of plagioclase and Fe-Ti oxides, respectively, and support the interpretation of syenogabbros as cumulates. Compositional deviations due to accumulation are far more significant in syenogabbros than in dioritic xenoliths.

Gabbronorites and hornblende gabbronorites have similar densely packed crystalline structures typical of cumulates. Cumulus phases consist of clinopyroxene and plagioclase, and share entire grain boundaries (fig. 3.3a, c). Enclosing orthopyroxene and interstitial Fe-Ti oxides and biotite constitute the remainder, growing interstitially

between clinopyroxene and plagioclase cumulate grains. At ~85 vol% cumulus grains, these gabbronorites are defined as mesocumulates (Wager *et al.*, 1960). Traditionally, mesocumulates represent dense crystal mushes from which residual melt has most likely been extracted through compaction or some other process. Olivine gabbronorites are dominated by linear grain boundaries and polygonal textures (fig. 3.3h). Ubiquitous triple junctions meeting at $\sim 120^\circ$ suggest prolonged periods under high-temperature metamorphic conditions, allowing for re-crystallization by grain boundary migration to minimize interfacial free energy. This annealing process obscured the original texture of the olivine gabbronorites, making any further genetic inferences impossible. Similar granoblastic polygonal textures are commonly found in association with large intrusive complexes, driven by prolonged heating (e.g., Bard, 1986).

Gabbronorites have bulk compositions that correspond with neither alkalic nor tholeiitic lavas found on Hualālai. These xenoliths contain less FeO*, TiO₂, P₂O₅, K₂O, and Na₂O, and more CaO and Al₂O₃ than both alkalic and tholeiitic lavas with similar MgO contents (fig. 4.1). SiO₂ concentrations in the xenoliths are intermediate between alkalic and tholeiitic lavas. Gabbronorite compositions are generally similar to binary mixtures of pyroxene and plagioclase, reflecting the high modal concentrations of these minerals. Similarly, the bulk composition of olivine gabbronorites (approximated using mineral modes and compositions) contains very high concentrations of MgO (~16 wt%), and low concentrations of TiO₂ (0.4 wt%), K₂O (0.06 wt%), and Na₂O (1.4 wt%). This composition is consistent with an accumulation of mafic minerals, such as olivine or

pyroxenes. None of the gabbroites have bulk compositions that suggest closed-system crystallization of a magma.

Poikilitic gabbros, the only coincident xenoliths we will discuss here, are also interpreted as cumulates. Primarily, a mode composed entirely of two mineral phases is not indicative of closed-system crystallization of a naturally occurring melt.

Additionally, plagioclase growth must have ceased before the onset of clinopyroxene crystallization, as plagioclase grains are perfectly euhedral and without plagioclase-clinopyroxene interdigitation. This behavior differs from that of a typical basalt, which, after reaching a cotectic composition, crystallizes several phases simultaneously.

Cessation of plagioclase growth could be explained in a natural melt by a sudden increase in pressure or H₂O content of the system, however these are considered unlikely in most basaltic ocean-island systems. We therefore tentatively interpret the poikilitic gabbros to be formed by accumulation of plagioclase grains into a liquid which had a greater normative pyroxene content. The bulk composition of the poikilitic gabbro closely resembles a binary mixture of clinopyroxene and plagioclase and is dissimilar to both tholeiitic and alkalic lava compositions.

Mg and Fe partitioning indicates whether mafic minerals (clinopyroxene, orthopyroxene and olivine) are in equilibrium with whole rock compositions or whether they are cumulus phases (fig. 5.1). Mg numbers of a melt in equilibrium with clinopyroxene, orthopyroxene, and olivine (table 5.1), were determined by using exchange distribution coefficients $K_d = (X_{Mg}/X_{Fe(2+)})^{melt} / (X_{Mg}/X_{Fe(2+)})^{crystal}$. A valence state of $Fe^{2+}/(Fe^{2+} + Fe^{3+}) = 0.90$ is assigned in order to calculate whole rock Mg numbers

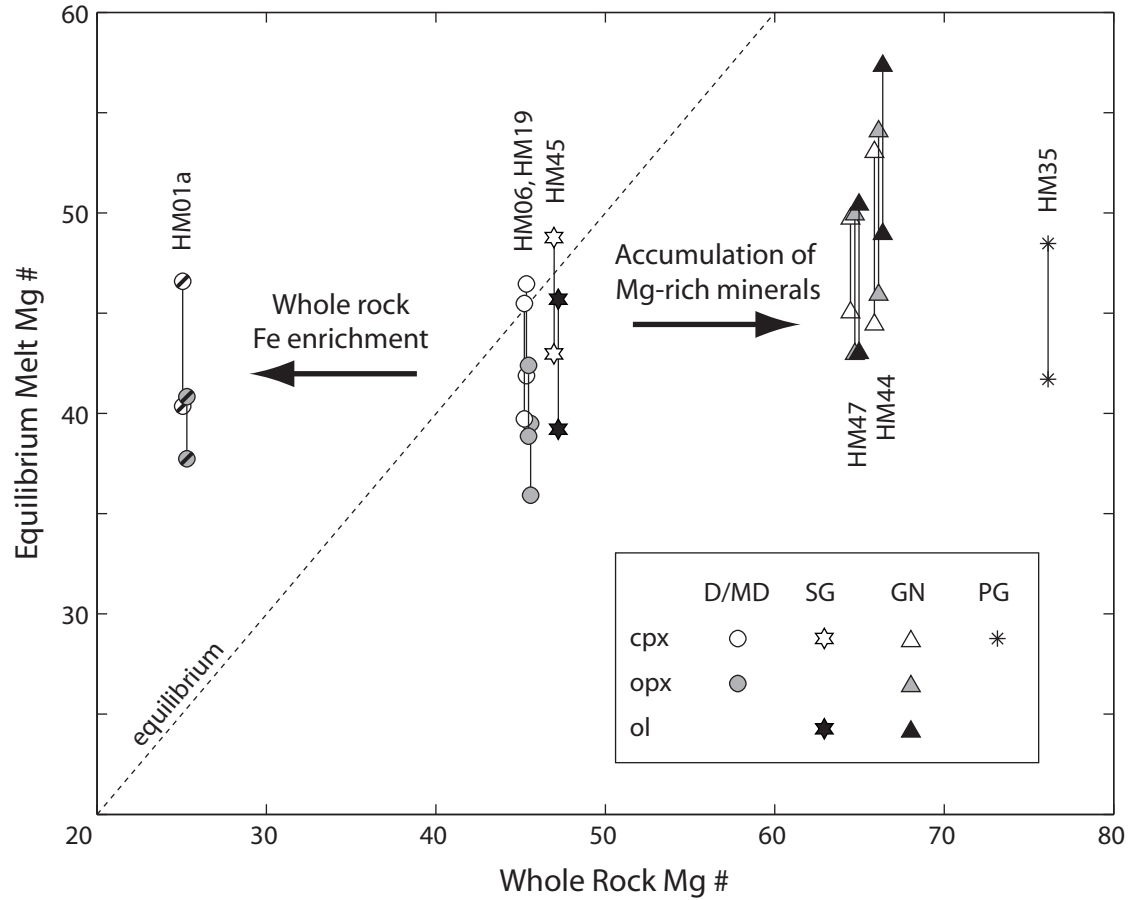


Figure 5.1: Mg numbers of whole rock compositions and melts in equilibrium with mafic minerals. Whole rock Mg numbers ($Mg \# = Mg / (Mg + Fe^{2+})$) are calculated assuming $Fe^{2+} = 90\% Fe^{tot}$ (see table 5.1). Clinopyroxene (cpx), orthopyroxene (opx), and olivine (ol) in dioritic xenoliths (D/MD) and syenogabbros (SG) are in or near equilibrium with whole rock Mg numbers. Fe-rich dioritic xenoliths (symbols with slashes) have lower bulk Mg numbers due to Fe/Ti enrichment and plot above the equilibrium line. Gabbrorite (GN) and poikilitic gabbro (PG) whole rock compositions indicate accumulation of Mg-rich minerals and plot below the equilibrium line.

Table 5.1: Whole-rock, mineral, and equilibrium melt Mg numbers^a.

		Whole Rock ^b	Mineral Compositions ^c			Equilibrium Melt ^d		
			Cpx	Opx	Olivine	Cpx	Opx	Olivine
Trachyte:								
	PWW13		14					
	PA13		17					
Syeno-xenoliths:								
	HM01	D/MD	25	75- 77	69- 70	40- 47	38- 41	
	HM09	D/MD	26					
	AHX01	D/MD	28					
	HM08	D/MD	30					
	AH02a	D/MD	42					
	HM10	D/MD	45					
	HM19	D/MD	45	74- 76	70- 71	40- 45	39- 42	
	HM06	D/MD	46	76- 77	67- 69	42- 46	36- 40	
	HM43	D/MD	-	68- 73		33- 41		
	HM12	D/MD	-	75- 77	67- 67	41- 46		35- 40
	HM02a	D/MD	-	78- 79		45- 50		
	AH04a	SG	38					
	HF01	SG	42					
	AH07	SG	47					
	HM45	SG	47	77- 79	71- 72	43- 49		39- 43
Gabbronorite:								
	HM47	GN	65	78- 79	74- 77	74- 76	45- 50	43- 50
	HM44	GN	66	78- 81	76- 80	78- 80	44- 53	46- 54
	AH10	GN	73					49- 55
	HM50a	HGN	-	78- 81			45- 52	
Poikilitic Gabbro:								
	AHX02	PG	76					
	HM35	PG	-	76- 78			42- 48	

^a $Mg\# = Mg/(Mg+Fe^{2+})$. ^b Whole-rock Mg numbers are calculated assuming $Fe^{2+} = 90\%$ Fe^{total} (Rhodes, 1995). ^c Range of mineral compositions observed in each sample. ^d Mg numbers predicted for equilibrium melts are calculated using the full range of both mineral compositions and partition coefficients. K_d 's of olivine = 0.27-0.33 (Roeder & Emslie, 1970), cpx = 0.23-0.26, opx = 0.27-0.30 (Grove & Donnelly-Nolan, 1986).

(table 5.1), following Rhodes (1995). This ratio (equivalent to $\sim\text{QFM} - 2$ for these samples) is commonly assumed for Hawaiian basalts based on studies of Fe oxidation states (e.g., Ringwood, 1975). Estimates of the iron valence state derived from Fe-Ti oxide thermobarometry are far more oxidized ($\sim\text{QFM} + 2$) and are believed to record late-stage magmatic and sub-solid oxidation, rather than $f\text{O}_2$ in the melt. Only those samples for which both mineral and whole rock data have been collected are included in figure 5.1 (with the exception of the combination of data from two similar poikilitic gabbros).

Mafic minerals in Si-rich dioritic xenoliths (e.g., HM06, HM19) and syenogabbros (e.g., HM45) are in or near equilibrium with whole rock Mg numbers (fig. 5.1). Fe-rich dioritic xenoliths (e.g., HM01, HM09) have lower whole rock Mg numbers (by $\sim 15\text{-}20$) than Si-rich diorites and are not in equilibrium with their mafic minerals. Fe-rich diorites have similar concentrations of the incompatible elements Nb and Zr as other diorites, suggesting that low whole rock Mg numbers are not due solely to increased degree of differentiation. Instead, low whole rock Mg numbers may be caused by Fe enrichment relative to original melt compositions. This is consistent with the hypothesis that Si-rich diorites reflect original melt compositions and that Fe-rich diorites have experienced minor accumulation of Fe-Ti oxides or an Fe-rich melt. Whole rock Mg numbers calculated at $f\text{O}_2 = \text{QFM} + 2$ (suggested by Fe-Ti oxide thermobarometry) are greater than the whole rock Mg numbers shown. Under these oxidized conditions, no minerals are in equilibrium with whole rock compositions.

Mafic minerals in both gabbronorites and the poikilitic gabbro are in equilibrium with a melt with a lesser Mg number than that of the bulk xenoliths (difference in Mg number of ~20-30; fig. 5.1). The disequilibrium state of these xenoliths is independent of how iron is partitioned between $\text{Fe}^{2+}/\text{Fe}^{3+}$ in the bulk sample, as increasing the amount of Fe^{3+} in the whole rock (i.e., assuming $f\text{O}_2 = \text{QFM} + 2$) only increases the whole rock Mg number. These lithologies must represent cumulates, as they are preferentially concentrated in Mg relative to the liquid from which they crystallized.

In summary, textural, bulk compositional, and mineral equilibrium evidence suggests that gabbronorites and poikilitic gabbros are cumulate lithologies. In contrast, Si-rich dioritic xenoliths appear to have crystallized in situ, and may approximate the original liquid composition. Mafic minerals in Fe-rich dioritic xenoliths are not in equilibrium with bulk Mg numbers of these xenoliths. This may be due to a minor amount of Fe-enrichment in these rocks ($< \sim 5$ wt% FeO^*), potentially caused by accumulation of Fe-Ti oxides or late-stage percolation of iron-rich magmatic fluids. Syenogabbros reflect variable accumulation of plagioclase, engulfed in interstitial crystalline products of a residual melt. Some of these rocks experienced similar Fe-enrichment to the dioritic xenoliths, as indicated by bulk composition and modes of Fe-Ti oxides.

Syeno-xenolith Series

Common mineralogy and alkaline affinity suggest that syeno-xenoliths might share a common parent magma. One possibility is that they represent preserved liquids (dioritic xenoliths) and cumulates (syenogabbros) related to the evolution of the PWW

trachyte (Moore *et al.*, 1987; Cousens *et al.*, 2003). Evidence for this scenario would strongly support the proposed formation of the PWW trachyte by fractional crystallization. In this section, the geochemical associations between the syeno-series xenoliths, the trachytes, and alkali basalts erupted from Hualālai are considered in view of trace element concentrations, mineral compositional trends, and states of silica saturation. First, a probable genetic link is established between the syeno-xenolith suite and the PWW trachytes. Second, possible parent magma compositions which generated the combined syeno-xenolith – trachyte suite are considered.

The bulk compositions of dioritic xenoliths lie along an alkalic magmatic trend, intermediate to alkalic basalts and trachyte from Hualālai (fig. 4.2). The lack of significant orthopyroxene or quartz and the presence of an alkali-rich ternary feldspar (which later exsolved into albitic plagioclase and alkali feldspar) also hint at their formation along an alkalic differentiation trend. Additionally, plagioclase compositions in the dioritic xenoliths are similar to those found in evolved alkalic lavas on West Maui and Kohala (An_{15-40}) (Keil *et al.*, 1972; Spengler & Garcia, 1988). Composition of matrix plagioclases (An_{15-37}), clinopyroxenes (Mg # 67-78), and bulk composition (50-56 wt% SiO_2) of dioritic xenoliths all indicate crystallization from a more evolved magma than the subaerial alkalic basalts on Hualālai ($>An_{55}$, $>Mg \# 79$, <49 wt% SiO_2). While no such lavas have erupted from Hualālai, evolved intermediate magmas potentially formed during the differentiation of the PWW trachytes, suggesting a possible relationship between the two suites.

Evidence from trace element concentrations in syeno-xenoliths is not inconsistent with crystallization from a derivative of the PWW trachyte parent magmas. The Zr/Nb ratio is fairly constant (~ 6.75) in the PWW trachytes (fig. 5.2), despite the fractionation of late-stage mineral phases (e.g., apatite, Fe-Ti oxides) which are more accepting of these elements. While there is significant scatter in the syeno-xenolith data, the average Zr/Nb ratio falls near ~ 6.75 (fig. 5.2). A correlation between Zr and Y concentrations suggests that deviations from this ratio in the plutonic rocks may be related to zircon accumulation or depletion. In comparison, tholeiites have an average Zr/Nb of ~ 9.8 ; this ratio is variable, however, as trace element data are very limited (Hammer *et al.*, 2004), and Nb contents are low (< 25 ppm).

Crystal fractionation processes may relate the diorites to the trachytes. Dioritic xenoliths lie along an ever-steepening trend of increasing Nb with decreasing MgO (fig. 5.3). Nb content is higher in alkalic and transitional basalts than in tholeiites at a given wt% MgO, a trend that appears to continue through the dioritic xenoliths, reaching extreme levels of Nb enrichment in the trachytes. Syenogabbros do not lie on this trend, probably because variable accumulation (of plagioclase, clinopyroxene, and Fe-Ti oxides) altered the MgO and Nb contents of these xenoliths. Crystal fractionation can also explain increases in highly incompatible element concentrations (e.g., Nb) in the PWW trachytes accompanied by little variability in highly incompatible element ratios (e.g., Nb/Zr). This is distinguished from compositional variations in tholeiitic and alkalic basalts, which appear to be dominated by partial melting trends (fig. 5.4). Again, there is a large variation in syeno-xenolith Nb/Zr ratios. This may be caused by zircon

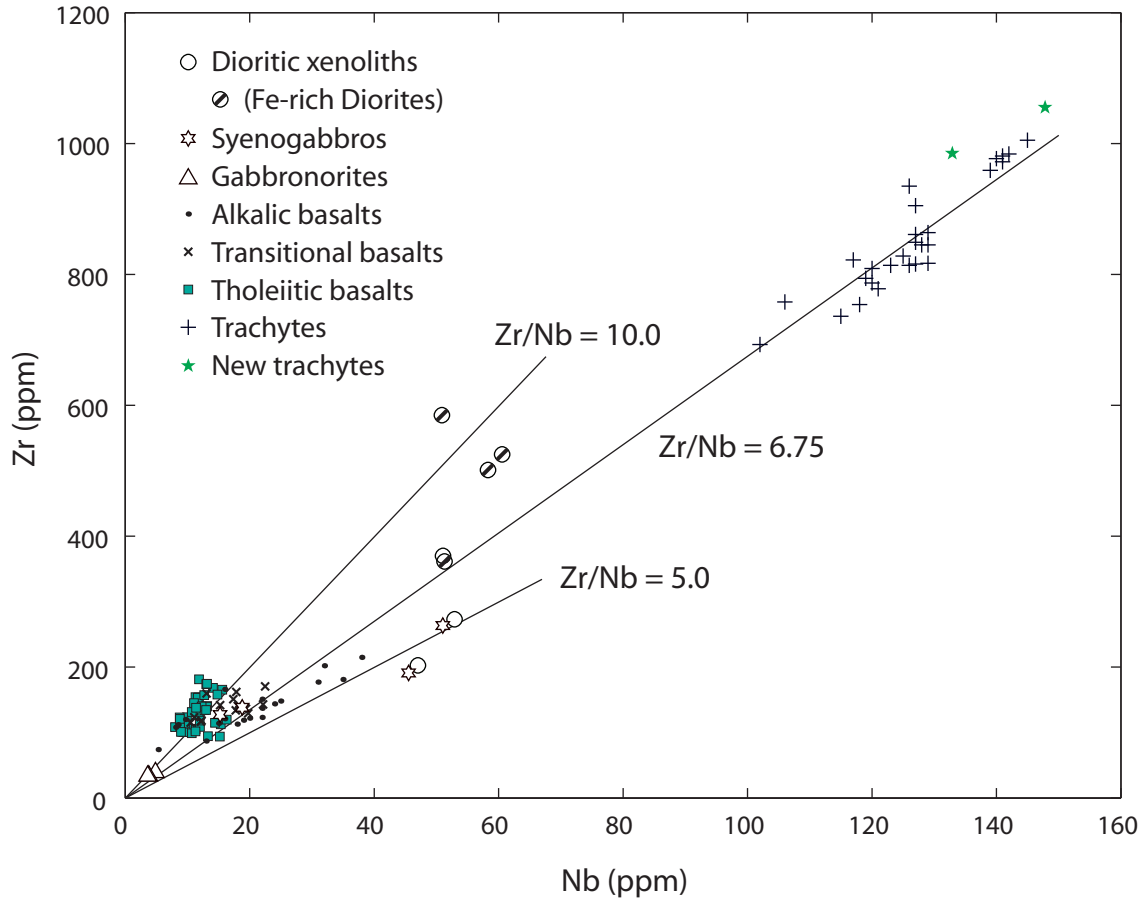


Figure 5.2: Zr and Nb behave highly incompatibly in Hualālai volcanics. All alkalic-series lavas have Zr/Nb ratios of ~6.75. Nearly all tholeiitic lavas have Zr/Nb >6.75, averaging ~9.8. Diorites, monzodiorites, and syenogabbros have intermediate Nb concentrations and cluster around Zr/Nb ~6.75 with significant scatter (Fe-rich diorites are marked with slashes). Transitional data shown are collected from submarine hyaloclastites (Hammer et al., 2004). Error bars smaller than symbol size.

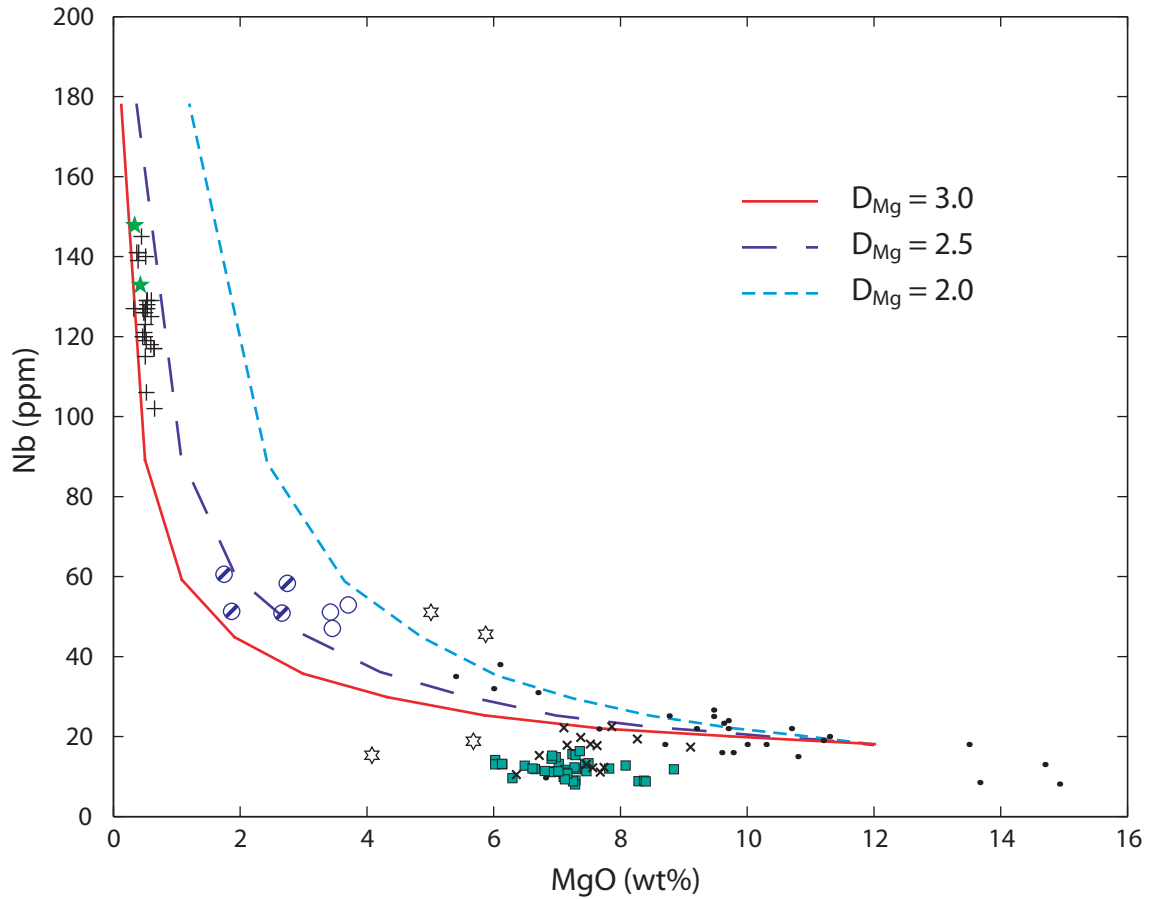


Figure 5.3: Rayleigh fractionation leads to enrichment in highly incompatible elements (e.g., Nb) and simultaneous depletion in compatible elements (e.g., Mg). Fractionation curves are calculated using $D_{\text{Nb}} = 0.006$ (assuming 10% olivine, 80% clinopyroxene, and 10% plagioclase in the fractionating assemblage and using partition coefficients from Rollinson (1993)). D_{Nb} is relatively insensitive to the mode of olivine, clinopyroxene and plagioclase. However, once titanomagnetite joins the fractionating assemblage (at ~ 4 wt% MgO), D_{Nb} increases significantly. D_{Mg} is given for each curve. D_{Nb} and D_{Mg} are functions of the fractionating assemblage and will change along the liquid line of descent. Symbols as given in fig. 5.2. Error bars smaller than symbol size.

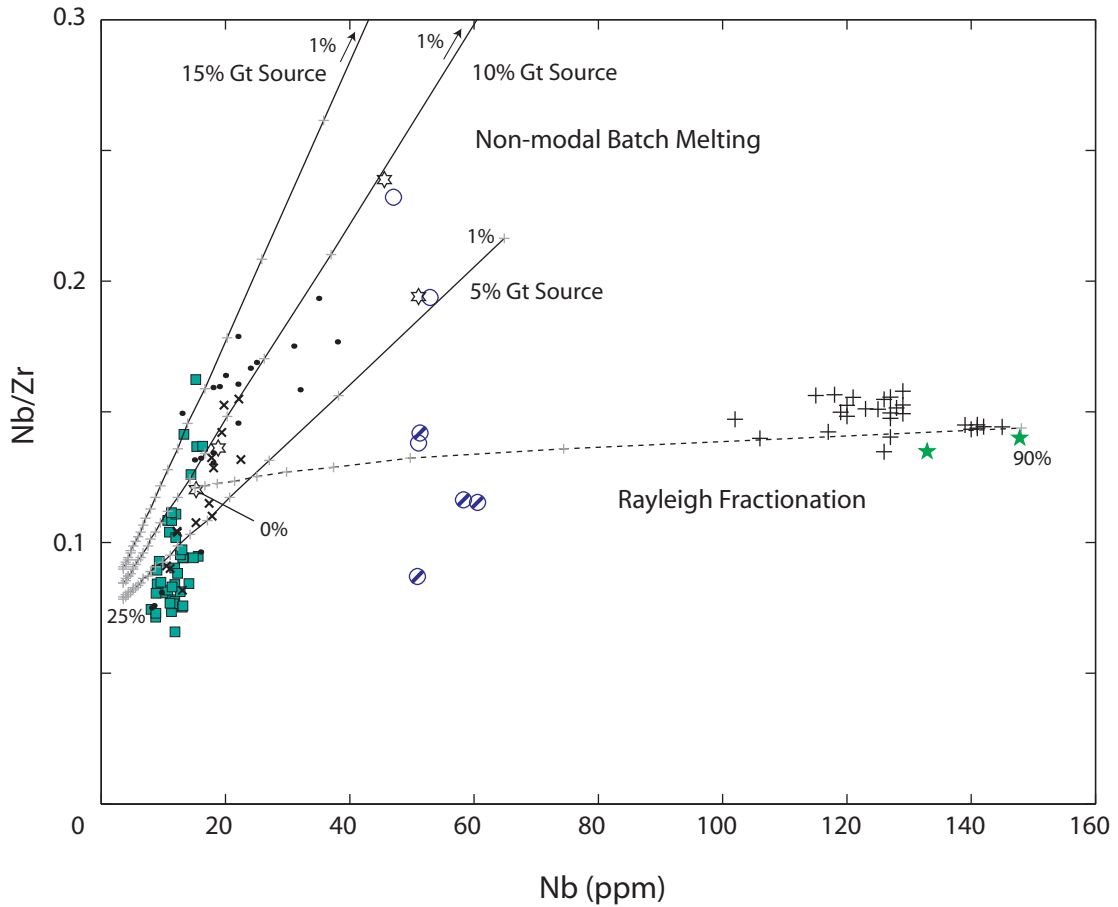


Figure 5.4: Nb/Zr ratios vs. Nb concentrations for Hualalai volcanics and dioritic xenoliths (symbols as in fig. 5.2). The effect of Rayleigh fractionation ($D_{\text{Nb}} = 0.006$, $D_{\text{Zr}} = 0.086$, assuming modes and partition coefficients as in fig. 5.3) and non-modal batch melting (following modes and partition coefficients of Huang & Frey (2003) with garnet mode as indicated) are illustrated. Trachytes are compatible with rayleigh fractionation from a parent melt with Nb/Zr ~0.10-0.15. Spread in Nb/Zr ratio of dioritic xenoliths may suggest either metasomatic enrichment or depletion in either of these elements, or derivation from a range of parent melt compositions.

fractionation/accumulation (as previously mentioned) or by crystal fractionation from a wide range of parent compositions.

Mineral compositions of syeno-series xenoliths also indicate crystallization from similar, but slightly increasingly more evolved melt compositions. In general, syeno-xenoliths span a relatively limited range of plagioclase compositions ($\sim\text{An}_{15-40}$), and tend to have very similar mafic mineral compositions across that range (fig. 5.5). When grouped by lithology, subtle trends emerge. In sequence from syenogabbro, through diorite to monzodiorite, plagioclase becomes less anorthitic (SG: $\text{An}_{32-40}\text{Or}_{3-5}$, D: $\text{An}_{15-37}\text{Or}_{4-13}$, MD: $\text{An}_{17-23}\text{Or}_{5-10}$) and both clinopyroxene (Mg# SG: 75.8-77.6, D: 67.5-78.4, MD: 73.6-76.4) and orthopyroxene (SG: none, D: 69.2-70.0, MD: 66.8-68.7) become progressively less magnesian (table 5.1). Mg numbers of accessory mafic minerals (olivine, biotite, and amphibole) are generally proportional to the Mg number of pyroxene. Combined, these observations suggest that syeno-xenoliths crystallized from an increasingly evolved magma.

On a purely physical and temporal basis, the syeno-xenoliths and trachyte may be derived from a tholeiitic, transitional, or alkalic basaltic parent. Since the PWW trachyte erupted within ~ 20 kyr of the most recent tholeiite lavas, residual tholeiitic magma was potentially present in the magma system of Hualālai. Additionally, some transitional magma may have been generated during the shield to post-shield transition by intermediate degrees of partial melting; such magma might have either never erupted or been covered by later alkalic flows, explaining its absence. If a sub-alkaline parent (i.e., tholeiite or transitional basalt) led to their formation, early extensive crystal fractionation

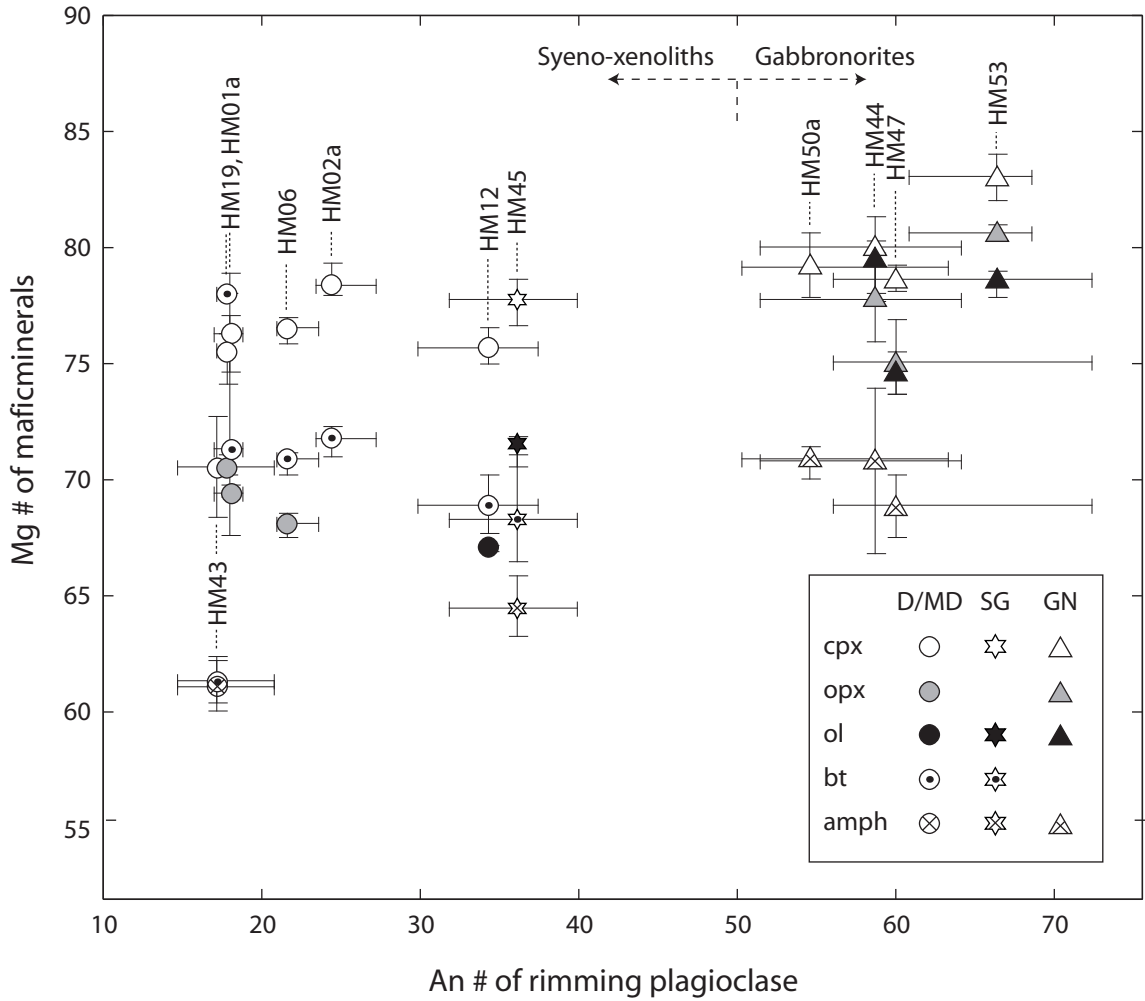


Figure 5.5: Rimming plagioclase and mafic mineral compositions for all syeno-xenoliths and gabbronorites. Compositions shown are averages and ranges for a single xenolith. Cpx = clinopyroxene, opx = orthopyroxene, ol = olivine, bt = biotite, and amph = amphibole.

of alkali-poor phases (e.g., Neumann *et al.*, 1999) would be necessary to concentrate the alkali elements and create the alkalic diorite – trachyte trend (fig. 4.2).

Minor elemental mineral compositions do not indicate the parent magma of the nodules. These compositions can be compared against compositions of minerals in alkalic and tholeiitic lavas to evaluate possible parental magmas (e.g., Fodor & Vandermeijden, 1988; Clague & Bohrson, 1991). While this approach works in principle, the limited data set of mineral compositions in equilibrium with tholeiitic and transitional lavas, sub-solid re-equilibration, and possible metasomatism limit its effectiveness in this specific case. Furthermore, the major element compositions of minerals in lava flows differ from those in syeno-xenoliths, making comparisons difficult.

Melts parental to trachyte must have Nb/Zr values near ~0.1-0.15 (fig. 5.4). Plausible Hualālai magmas that meet this criterion include low Nb/Zr alkalic basalts, high Nb/Zr tholeiite basalts, and transitional basalts recovered from the submarine flanks of Hualālai (Hammer *et al.*, 2004). While these transitional basalts may not have erupted during the shield to post-shield transition, we assume that their composition (i.e., Nb/Zr ratio and degree of silica saturation) is representative of transitional basalts at Hualālai and consider them as potential parental magmas.

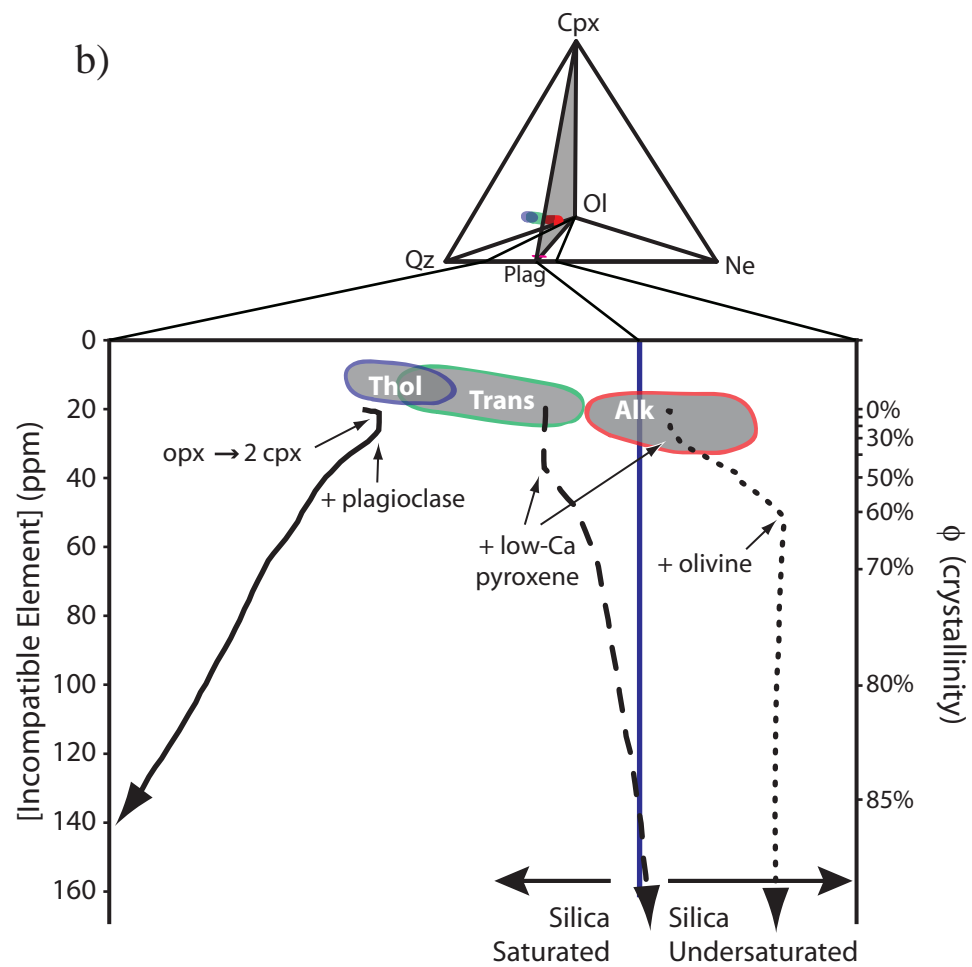
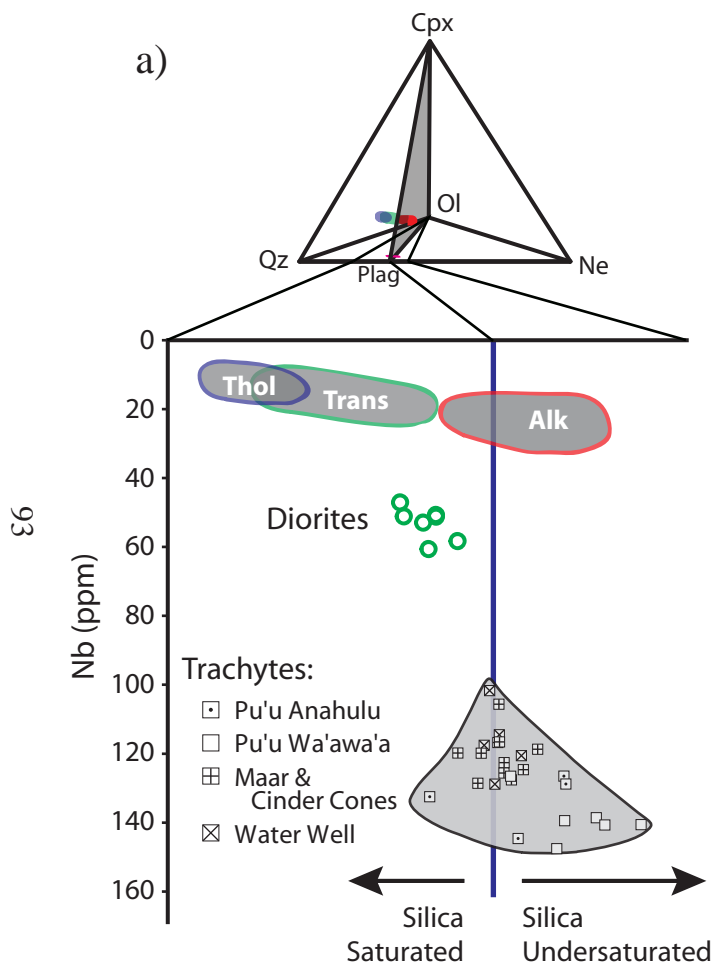
Lead isotopic data of PWW trachytes exhibit substantial overlap with alkalic basalts (Park, 1990; Cousens *et al.*, 2003). $^{206}\text{Pb}/^{204}\text{Pb}$ and $^{208}\text{Pb}/^{204}\text{Pb}$ of tholeiite basalts are generally greater than in alkalic basalts and trachytes, although a single tholeiite sample (out of 14) has Pb isotope ratios comparable to the trachytes (sample KK81-10-10

of Park, 1990). The only analyzed transitional lava also has Pb isotope ratios similar to the trachytes (sample KK81-11-2 of Park, 1990). The Pb data have been interpreted to represent a link between alkalic basalts and the PWW trachyte (Cousens *et al.*, 2003), although the limited transitional data (i.e., the single data point) does not preclude the possibility of transitional affinity. $^{143}\text{Nd}/^{144}\text{Nd}$ and $^{87}\text{Sr}/^{86}\text{Sr}$ ratios are nearly indistinguishable in alkalic and tholeiitic basalts and both overlap with trachyte isotopic compositions.

Normative compositions of diorites suggest that they may have fractionated from a hypersthene normative parent (fig. 5.6a). It is important to distinguish between silica-saturation and alkali content when describing magma compositions. While the two are normally strongly correlated, alkalic basalts, as classified on the basis of a total alkali-silica (TAS) diagram, may plot within the hypersthene-normative volume of the basalt tetrahedron, and sub-alkaline transitional basalts may approach nepheline-normative compositions. Both of these combinations are observed at Hualālai. For this reason, we will use the expressions tholeiitic and alkalic only in reference to classifications based on a TAS diagram (Macdonald & Katsura, 1964; Macdonald, 1968), and use terms explicitly referring to nepheline-, hypersthene-, or quartz-normative composition when degree of silica-saturation is being considered (Yoder & Tilley, 1962).

A critical plane basalt (a basalt composition that falls on or near the critical plane of silica undersaturation) could only be parent to the diorites if it became hypersthene-normative early in its magmatic history (fig. 5.6a). For this to occur, silica-undersaturated phases (those with compositions in the nepheline-normative volume of the

Figure 5.6: a) Silica-saturation of Hualalai volcanics and dioritic xenoliths, including potential alkalic, transitional, and tholeiitic parent basalts. Trachytes are divided geographically into the Pu'u Anahulu and Pu'u Wa'awa'a eruptions north of the summit, maar and cinder cone eruptions east of the summit, and water well trachytes from west of the summit. Dioritic xenoliths are all silica-saturated, unlike alkalic basalts. b) Potential LLDs modeled with MELTS (all equilibrium crystallization runs at 5 kbar total pressure, 0.5 wt% initial water content). The y-axis is plotted in terms of the concentration of an entirely incompatible element, calculated as $[I.E.] = [I.E.]^0 / (1 - \phi)$, where ϕ = crystallinity, a direct MELTS output. ϕ is also indicated on the right axis, for reference. Under these conditions, tholeiitic, transitional, and alkalic basalts behave distinctly. The onset of key mineral phases which affect the LLD with respect to silica-saturation is indicated. Silica-saturation is measured as normative quartz/(quartz + nepheline), where normative components are calculated from relative molar amounts of oxide components using the expressions: nepheline (Ne) = $Al_2O_3 + Fe_2O_3 + Na_2O + K_2O - TiO_2$; quartz (Qz) = $SiO_2 + 3/2 (Al_2O_3 + Fe_2O_3) - 1/2 (FeO + MnO + MgO) - 3/2 CaO - 7/2 (Na_2O + K_2O)$; olivine (Ol) = $1/2 (Al_2O_3 + Fe_2O_3 + FeO + MnO + MgO) - 1/2 (CaO + Na_2O + K_2O)$; clinopyroxene (Cpx) = $TiO_2 + CaO + Na_2O + K_2O - (Al_2O_3 + Fe_2O_3)$. Expressions are derived following Thompson (1982), using SiO_2 , $NaAlSi_3O_8$, Mg_2SiO_4 , and $CaMgSi_2O_6$ additive components and exchange components as in Sack et al. (1987). The critical plane of silica-saturation corresponds with normative plagioclase (plag): $Qz / (Qz + Ne) = 2/3$.



basalt tetrahedron, e.g., nepheline) must be fractionated. Fe-Ti oxides and phlogopite are the only two phases present in the assemblage capable of producing this effect. There is no evidence for substantial fractionation of these phases, however, as neither Fe, Ti, nor Ba (compatible in phlogopite) are significantly depleted relative to alkalic basalts (fig. 4.1). Therefore, it is more likely that dioritic xenoliths evolved from a mildly hypersthene-normative parent, similar to the transitional basalts. This is not the case for other Hawaiian evolved alkalic series (e.g., Laupāhoehoe and Hāwī series) which remain near the critical plane of saturation throughout their evolution (fig. 5.7).

While studies of basalt at low pressures indicate that the critical plane of silica-undersaturation corresponds with a thermal divide (Yoder & Tilley, 1962; Yoder, 1976), there is an increasing appreciation for the role of intermediate to high-pressure clinopyroxene fractionation ($> \sim 5$ kbar) in decreasing silica-saturation of residual liquids and ultimately in crossing this barrier (Fuhrman *et al.*, 1991; Neumann *et al.*, 1999). Crystallization of low-Ca pyroxene is especially effective at decreasing silica-saturation as this phase is more silica-saturated than nearly all basaltic melts. Comparatively, both augite and olivine have compositions near the critical plane and tend not to affect the degree of silica-saturation, while feldspars tend to push melts away from the critical plane. This suggests that the presence of a thermal divide may be a function of the conditions during fractionation, and that, under favorable conditions, hypersthene-normative parents can fractionate towards the critical plane to form nepheline-normative trachytes. To test this mechanism, the change in degree of silica-saturation of MELTS runs was determined during the evolution of a transitional basaltic parent (MELTS runs

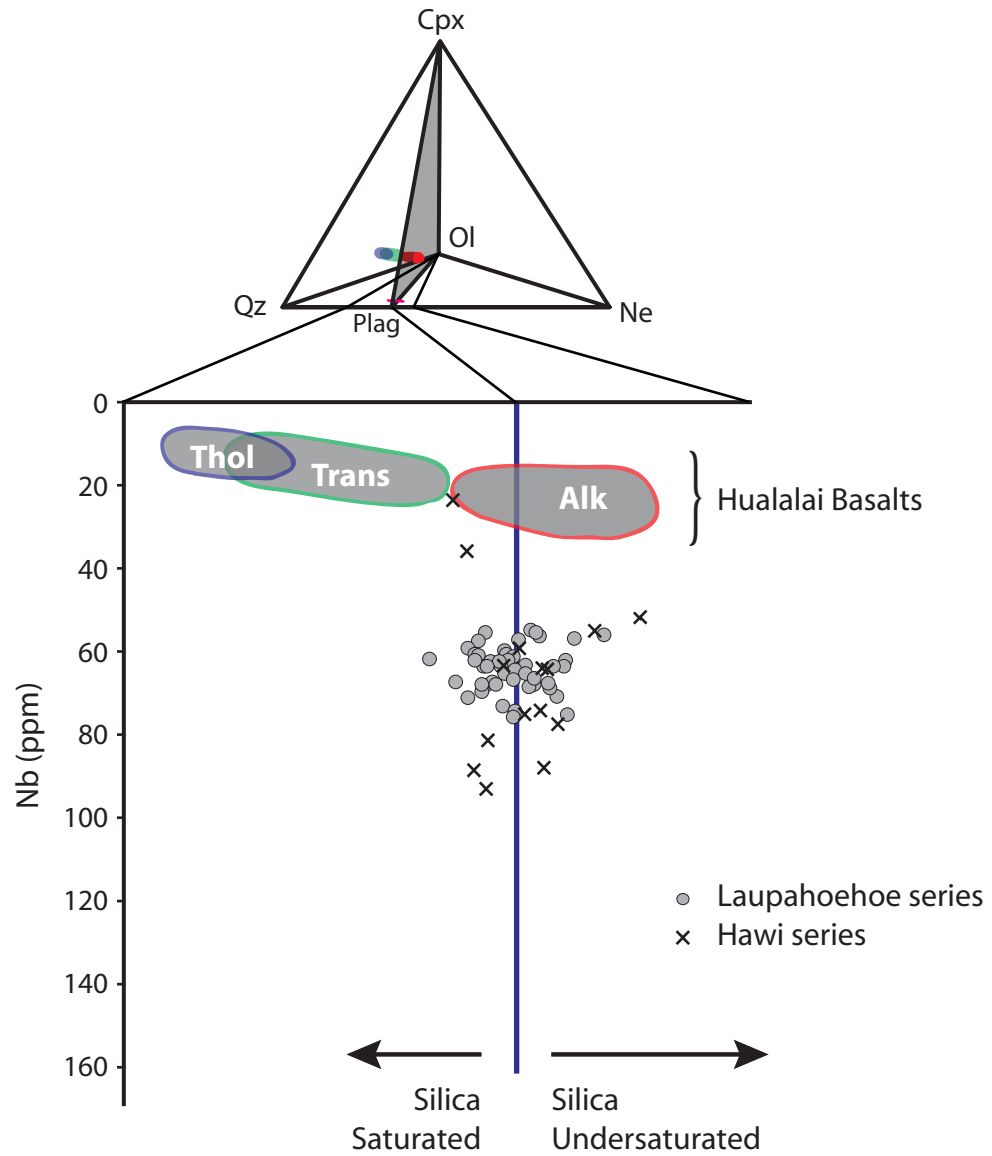


Figure 5.7: Silica-saturation of the Laupāhoehoe series and Hāwī series as described in fig. 5.6. Both of these series straddle the critical plane over all Nb contents. Data sources for Hawaiian alkalic series are listed in appx. C.2.

are discussed in greater detail later). At higher pressures (> 5 kbar), low-Ca pyroxene fractionated and silica saturation decreased (fig. 5.6b). Thus, if the diorites represent intermediate compositions along the PWW trachyte LLD, silica-saturated phases must precipitate in order to drive melt compositions towards the trachytes. This is consistent with moderate pressure phase assemblages, but not with low-pressure (i.e., olivine and plagioclase dominated) assemblages).

One remarkable feature of the PWW trachyte is the correlation between Pb isotopic systematics and degree of silica-saturation/undersaturation. Within the range of $^{206}\text{Pb}/^{204}\text{Pb}$ and $^{208}\text{Pb}/^{204}\text{Pb}$ values spanned by trachytes, Cousens *et al.* (2003) identify distinct geographic clusters of similar radiogenic lead concentrations; trachytes from Pu‘u Anahulu (PA) and Pu‘u Wa‘awa‘a (PWW) have lower $^{206}\text{Pb}/^{204}\text{Pb}$ and $^{208}\text{Pb}/^{204}\text{Pb}$ ratios than trachytes recovered from wells on the western flank and from maars on the southeastern flank. These geographic clusters are also distinguished by degree of silica-saturation; PA and PWW trachytes are nearly all nepheline-normative, while maar and well trachytes are mostly hypersthene-normative. This may indicate limited mixing between an alkalic source (low $^{206}\text{Pb}/^{204}\text{Pb}$ and $^{208}\text{Pb}/^{204}\text{Pb}$, low degree of silica-saturation) and a tholeiitic source (high $^{206}\text{Pb}/^{204}\text{Pb}$ and $^{208}\text{Pb}/^{204}\text{Pb}$, high degree of silica-saturation). If this is the case, the tholeiitic component can account for no more than ~20% of the parent magma (as determined using average tholeiite and alkalic isotopic compositions as endmembers).

Gabbronorite Series

Gabbronorite and diorite contacts (first discussed in the petrography section) suggest an intimate physical relationship between these two lithologies. However, gabbronorite xenoliths have distinctly different mineral assemblages and compositions than syeno-xenoliths, suggesting that they crystallized from separate magmas. Sub-alkaline bulk compositions, the lack of alkali feldspar, and the abundance of orthopyroxene suggest that gabbronorites may represent tholeiitic cumulates. For completeness, possible petrogenetic links between the gabbronorite and syeno-xenolith series are considered. The physical relationship between gabbronorites and diorites is then discussed in order to build a complete model of magmatic processes at Hualālai.

One possible scenario relating gabbronorite and syeno-xenolith series is that the gabbronorites are cumulates formed during fractionation of the same magma that produced the syeno-xenoliths. If so, gabbronorites could only have formed early in the differentiation process, as both high An contents in plagioclase and high Mg numbers in pyroxenes indicate crystallization from a basic magma. Additionally, the cumulus phases in the gabbronorites (clinopyroxene and plagioclase) are not capable of driving residual liquid along the liquid line of descent defined by diorite through trachyte compositions (i.e., at MgO < 4 wt%, fig. 4.1). Specifically, Fe, Ti, and P depletion, and Si enrichment of an alkalic melt require fractionation of additional phases (i.e., apatite, Fe-Ti oxides) which are not present as cumulus phases in gabbronorites.

The presence of orthopyroxene in gabbronorites as an interstitial or enclosing phase (~10 vol%) indicates that residual intercumulus liquids trapped in the xenoliths

were strongly silica-saturated. While dioritic xenoliths have bulk compositions that are hypersthene-normative, they contain only minor orthopyroxene (generally ~0-3 vol%; table 2.1). Orthopyroxene saturation, as well as the precipitation of quartz in one sample (HM06), is almost certainly aided by a late-stage increase in silica activity in the melt due to crystallization of hydrous phases and/or Fe-Ti oxides. Despite this effect, dioritic xenoliths do not contain volume fractions of orthopyroxene comparable to the residual interstitial matrix of the gabbronorites.

Spherical multi-phase inclusions within gabbronorite plagioclase crystals are also orthopyroxene bearing (on average ~ 25 vol%). These inclusions (containing olivine, orthopyroxene, biotite, magnetite, and inferred plagioclase crystallizing along the boundary with the host crystal) are interpreted to represent the crystalline remains of former melt inclusions. The presence of orthopyroxene suggests that, in addition to interstitial melt surrounding the cumulus phases, the former melt surrounding the plagioclase at low crystalline fractions is also strongly silica-saturated. Attempts to reconstruct the original melt composition have failed due to the crystallization of an undeterminable amount of plagioclase along the boundaries with the host plagioclase, and the analytical difficulty of measuring compositions of crystals only a few micrometers wide.

The melt which crystallized to form the gabbronorite cumulates must have been strongly silica-saturated. It seems unlikely that this same melt also formed the mildly silica-saturated syeno-xenoliths. For the same reasons, the gabbronorites could not have crystallized as cumulates from the silica-undersaturated to barely silica-saturated post-

shield alkalic basalts. Instead, the most likely parent of the gabbronorites is a shield-forming tholeiite basalt. Such a parent has previously been inferred for similar lithology xenoliths from Mauna Kea (Fodor & Galar, 1997).

Contacts between gabbronorites and diorites indicate that the two lithologies probably crystallized in similar locations within the volcanic edifice. Smaller average grain-size in diorites proximal to contacts, truncation of large pyroxene and plagioclase grains in the gabbronorites by the contact, and inclusion of small gabbroic clots by the diorite all suggest that gabbronorites predate the dioritic xenoliths (fig. 3.7). While diffusion of volatile species along grain boundaries probably led to reactions with clinopyroxene and the formation of biotite and hornblende (see petrography section and table 3.1), there is no evidence for bulk fluid penetration into the gabbronorites. The coherence of discrete gabbroic clots (HM01b) implies that the gabbronorites solidified prior to the injection of dioritic magma.

Passage of significant time between gabbronorite and diorite emplacement is consistent with the former accumulating from shield-stage tholeiites and the later crystallizing from transitional or alkalic basalts. If the gabbronorites represent shield stage cumulates, they could feasibly predate syeno-xenolith emplacement by up to hundreds of thousands of years (the entire length of the shield stage). Alternatively, if they accumulated during the same magmatic episode in which the syeno-xenoliths formed, presumably during the shield to post-shield transition, then the time between emplacement of the two lithologies may be significantly less than the postulated ~20 kyr evolution of the trachytes (Cousens *et al.*, 2003). Given the constraint that the

gabbronorites must have accumulated and solidified before being invaded by the dioritic magma, it is more likely that they had sufficient time to do so if accumulated during the shield-stage.

Finally, oxide exsolution rods in pyroxenes may be associated with episodes of metamorphic reheating, as suggested by Fleet *et al.* (1980), rather than simple exsolution during magma cooling. This mechanism of formation was proposed after a textural study of naturally occurring oxide exsolution lamellae in clinopyroxenes. Additionally, Fleet *et al.* note that magnetite readily exsolves from pyroxenes upon heating under laboratory conditions. If the Fe-Ti oxide rods formed during prograde metamorphism of the gabbronorites, the emplacement of transitional to alkalic magma nearby could have provided the necessary heat.

Coincident Xenoliths

Glass compositions in poikilitic gabbros indicate that they accumulated from an alkalic magma. Hawaiiite glass inclusions (Mg # 42-44) in plagioclase crystals record the parent melt composition from which plagioclase crystallized (fig. 4.2). Vesicular alkalic basalt glass pockets (Mg # 46-50) correspond with the composition of the host basalt that transported the xenolith to the surface, and may or may not be genetically related to the poikilitic gabbro. Clinopyroxene crystals in the poikilitic gabbro (Mg # 76-78) would be in equilibrium with a melt Mg number of 42-48, overlapping both compositions of the vesicular glass pockets and the more evolved Hawaiiite glass inclusions (appx. A).

Major element equilibrium between clinopyroxene and the host glass, as well as the intimate distribution of vesicular glass pockets and veins throughout the sample

suggest that the clinopyroxene oikocrysts crystallized from the same magma which transported it to the surface. Furthermore, the lack of any subsolidus reactions, which might result from prolonged cooling, and the conchoidal fractures, which are possibly caused by thermal shock, may also indicate that poikilitic gabbros never cooled far below the solidus temperature prior to eruption. This implies that they probably formed during the recent post-shield alkalic period and possibly as cognate cumulates to the ~4.5 ka alkalic eruptions which transported them to the surface. Regardless of which particular batch of magma formed the poikilitic gabbros, we infer that they are related to recent alkalic volcanism (i.e., ~10 ka or younger) and not to the PWW trachyte episode.

Felsic and hornblende-rich veins are both minor lithologies and do not appear to play a significant volumetric role in volcanism on Hualālai. The presence of significant quantities of hydrous minerals, however, does indicate possible concentration of water by extreme differentiation. The presence of Ca-amphibole implies $p_{H_2O} \geq 1.5$ kbar in the hornblende-rich vein (Mertzbacher & Egger, 1984; Rutherford & Hill, 1993; Sisson & Grove, 1993). Cross-cutting relationships indicate that the most recent veins postdate both gabbro-norites and diorites.

Alkalic Liquid Line of Descent

Xenoliths that approximate original melt composition (i.e., dioritic xenoliths) may be used to infer a possible liquid line of descent (LLD) at Hualālai. Crystallization sequence and the dominant fractionating phase at any given point on the LLD are both manifestations of thermodynamic conditions and water content of the magma.

Understanding which phases are actively fractionating leads to insights into those conditions and a better understanding of the compositional evolution of the magma, especially with respect to silica saturation. This section first discusses dominant fractionating assemblages along the LLD, as inferred from major and trace element concentrations. The relative importance of these phases is tested by mass balance modeling. Next, the inferred LLD at Hualālai is compared against experimental and calculated LLDs that result from known thermodynamic conditions. The LLD is also compared against other evolved Hawaiian alkalic series which have been interpreted as crystallizing under moderate pressures. Finally, the effect of pressure on the plagioclase-olivine-clinopyroxene saturated pseudo-cotectic is discussed in the context of the Hualālai LLD.

Liquidus Phases

Four distinct segments are identified along major and trace element trends culminating in the PWW trachytes (fig. 5.8a, b). Segments one and four follow compositional arrays of erupted lavas, while segment two is constrained by diorite compositions. Segment two is poorly constrained because diorites only approximate liquid compositions. Segment one begins with a primitive alkalic basalt (~14 wt% MgO, 10 ppm Nb) and continues through the linear alkalic basalt array. Inclusion of this segment in the LLD, although the alkalic basalts postdate the PWW trachyte eruption and could not have produced the trachytes, implies that these magmas shared a similar parent and crystallized along a similar path. This inference is supported by the continuity between the alkalic basalt and diorite compositions (e.g., Sr vs. Nb, fig. 5.8a; Major

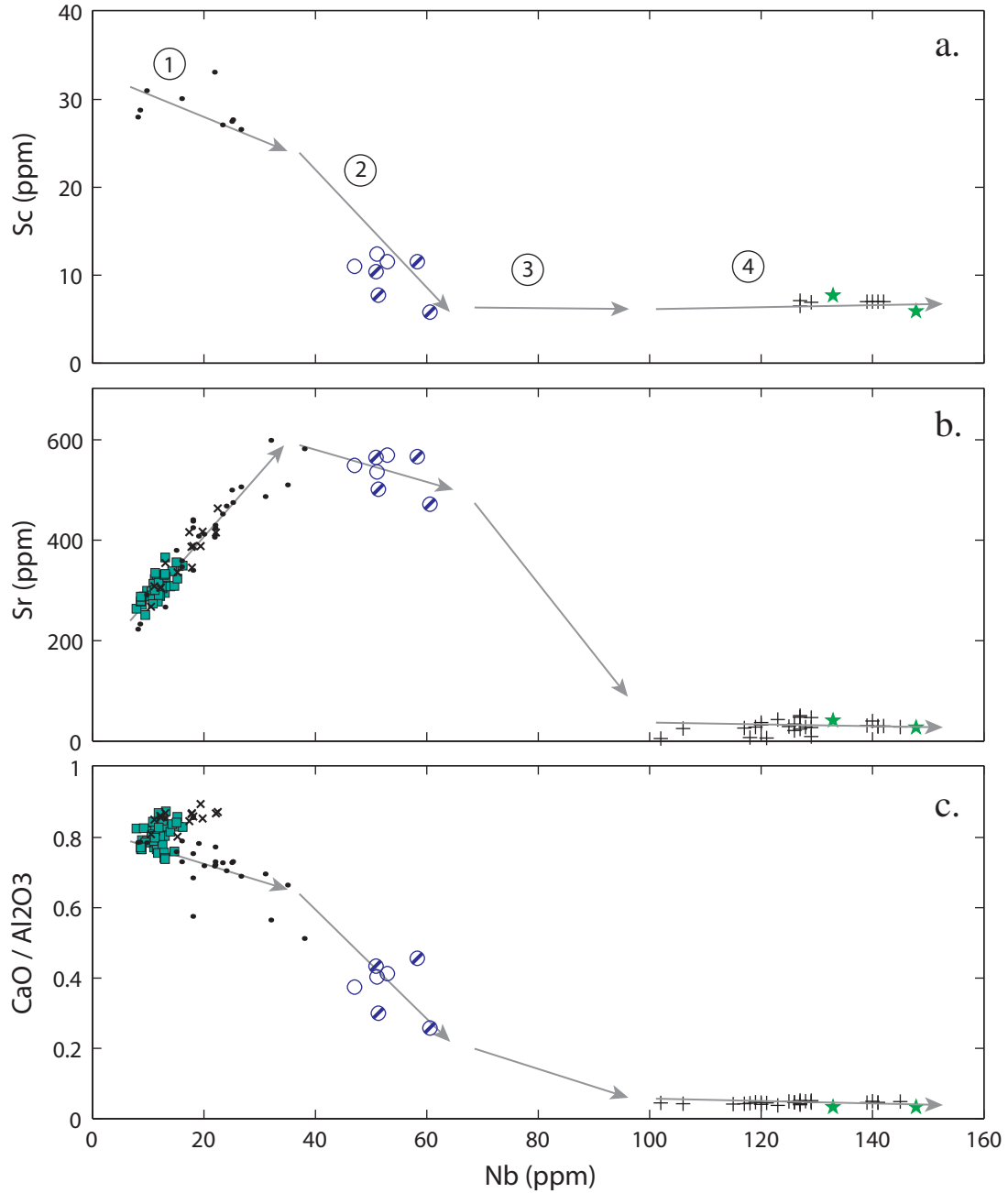


Figure 5.8: Compositional variation of Hualalai volcanics and dioritic xenoliths with Nb (a-c) and Sr (d, e). Inferred liquid lines of descent (LLDs) are indicated and divided into four stages based on fractionating assemblage: (1) Clinopyroxene fractionation, possibly accompanied by olivine, (2) Clinopyroxene-dominated assemblage with minor plagioclase, (3) Plagioclase-dominated assemblage, (4) Ternary feldspar or alkali feldspar present in assemblage. Inferences leading to these divisions are discussed in the text. Reconstructed LLDs assume that recent alkalic basalts (<25 ka), dioritic xenoliths, and the PWW trachyte all fractionated from a similar parent under similar conditions. Symbols as given in fig. 5.2.

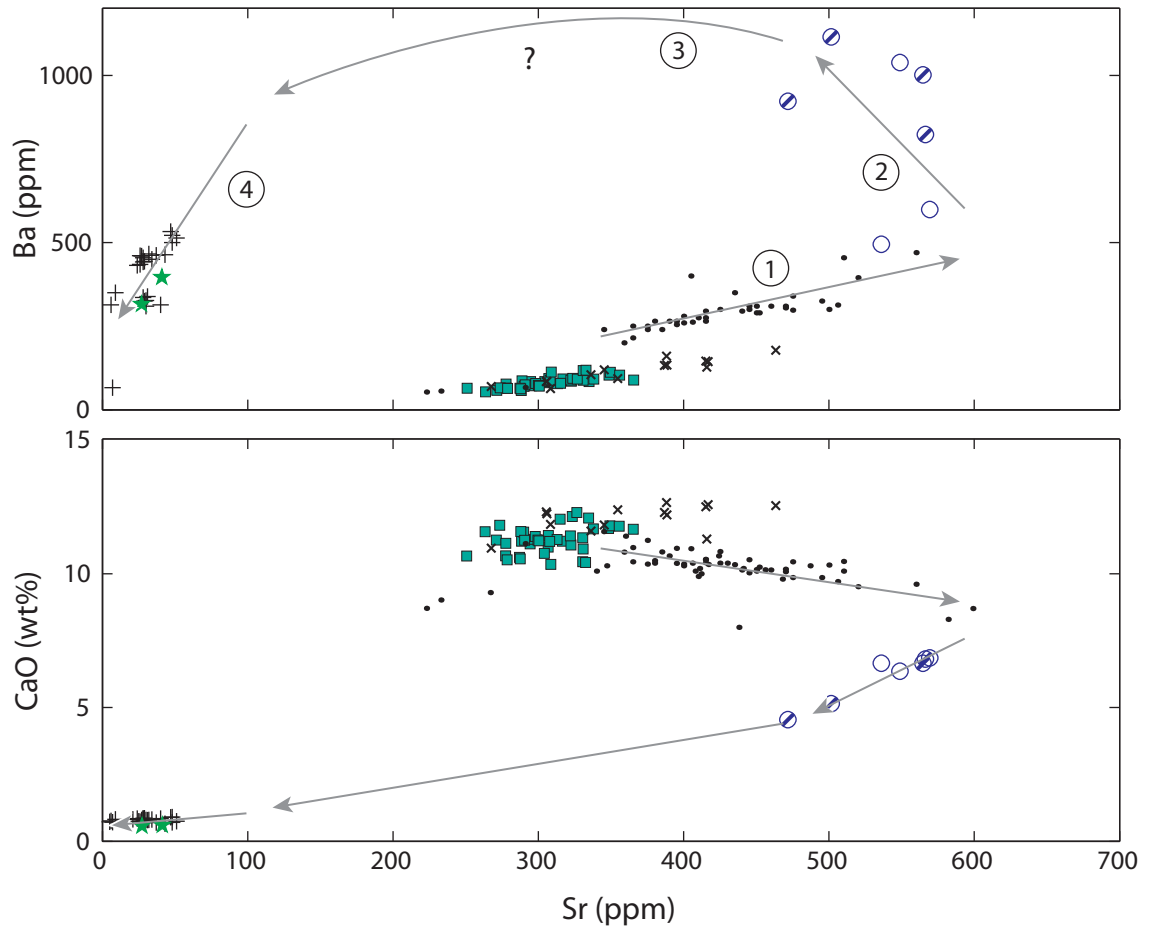


Figure 5.8 (continued): Compositional variation of Hualalai volcanics and dioritic xenoliths with Nb (a-c) and Sr (d, e).

element trends, fig. 4.1). Alternatively, this segment may be unrelated to the evolution of the trachytes. The four segments of the LLD are discussed below.

(1: Nb ~10-40 ppm) Marked by a subtle decrease in both Sc concentrations and CaO/Al₂O₃ ratio, the initial fractionating assemblage includes clinopyroxene and may include olivine. Possible olivine fractionation keeps Sc concentrations from dropping too rapidly and expedites removal of transition-metal elements (Ni, Co). Sr and Ba both behave incompatibly, since no feldspar is fractionating.

(2: Nb ~40-60 ppm) Sr concentrations decrease, indicating onset of plagioclase fractionation. Sc concentrations and CaO/Al₂O₃ ratio decrease more rapidly, however, implying that clinopyroxene is still an important fractionating phase. Ba continues to behave incompatibly. Diorite and monzodiorite nodules solidified during this interval.

(3: Nb ~60-100 ppm) Sc, CaO and CaO/Al₂O₃ ratio decrease less rapidly, while Sr concentrations drop precipitously. These changes suggest an increase in the plagioclase/clinopyroxene ratio of the fractionating assemblage. The behavior of Ba is poorly constrained and is directly correlated with the orthoclase component of the crystallizing feldspar. There are no solidified representatives of this stage. Instead, segment three is inferred to join segments two and four.

(4: Nb >100 ppm) Notable primarily for decreases in Ba concentrations, either fractionating feldspar has become strongly ternary or alkali feldspar has begun to crystallize. Ternary feldspar or alkali feldspar fractionation will both remove K₂O and Ba₂O from the system, causing these oxides to behave compatibly. Potassium contents in

the trachytes are invariant over a large range of Nb and Zr contents, reflecting this fractionation.

The onset of accessory phases can be determined by examining major element data. P_2O_5 and TiO_2 , and to a lesser extent FeO^* (total iron), are all concentrated throughout the entire alkalic basalt series (to ~5 wt% MgO, fig. 4.1). At MgO <4 wt % all of these elements decrease rapidly. Thus, apatite and Fe-Ti oxides join the liquidus between ~4-5 wt% MgO. This timing corresponds with the inferred period of dominant clinopyroxene fractionation (2) noted above. While the impact of Fe-Ti oxide and apatite fractionation significantly affects the concentrations of Fe, Ti, and P, they need not be volumetrically dominant crystallizing phases.

Mass Balance Modeling

Mass balance calculations were performed to test the feasibility of forming diorites and trachytes through crystal fractionation of plausible minerals. Fractionation was modeled between diorite HM10 and three potential parent compositions: a transitional, an alkalic, and a tholeiitic basalt (fig. 5.9). Additionally, fractionation was modeled between a diorite parent (HM10) and a trachyte. Mineral compositions used in mass balance calculations were selected from syenogabbro and diorite mineral analyses (appx. A) with the exception of apatite, which is a published analysis (Cousens *et al.*, 2003). Because mineral compositions vary with melt composition, mineral analyses used in mass balance calculations represent average fractionating compositions. Parent liquids were calculated as the best fitting linear combination of derivative liquids (e.g., diorite, trachyte) and a plausible mineral assemblage (given by the relationship $b = [A]x$, where b

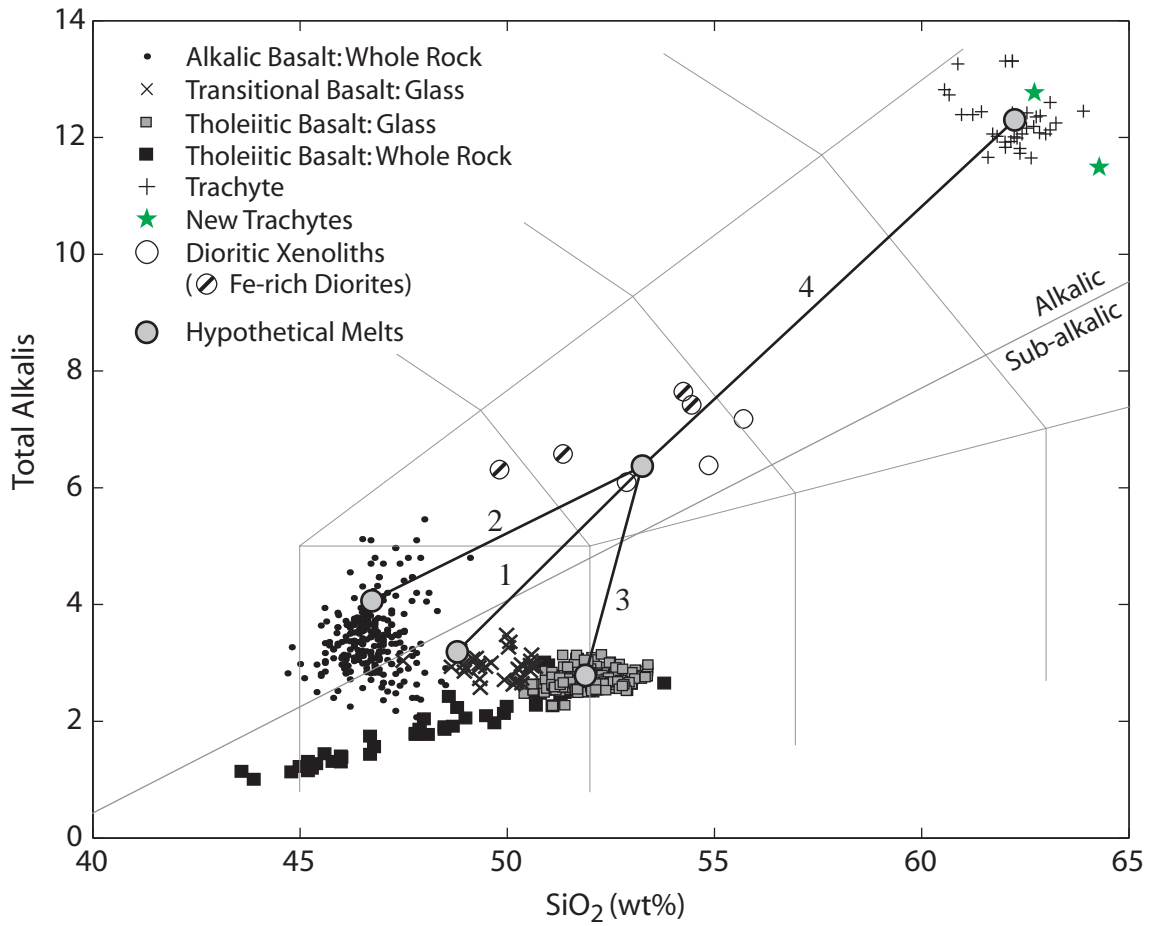


Figure 5.9: TAS diagram illustrating mass balance end-member compositions. Four fractionation paths were tested (1) diorite derivative from a transitional basalt parent, (2) diorite derivative from an alkalic basalt parent composition, (3) diorite derivative from a tholeiitic basalt parent composition, (4) trachyte derivative from a diorite composition. Basaltic parents were chosen to have equivalent MgO contents (~7 wt%).

is a the parent compositional vector, [A] is a matrix composed of mineral and derivative liquid compositions, and x is a vector containing the modes of different phases). Least squares inversion (employing the MATLAB backslash matrix operator “\”) is used to minimize the residual between calculated and observed parent compositions (i.e., solve $x = [A]^{-1}b$). Results are described in appendix B.

Mass balance calculations produced relatively low residuals for diorite derived from alkalic or transitional basaltic parents (appx. B.1,2). Root mean square (rms) errors for these two scenarios are ≤ 0.10 oxide wt% (the rms error is slightly lower for the alkalic parent). The tholeiitic parent produces a worse fit (rms error = 0.41 oxide wt%; appx. B.3) due primarily to its inability to account for the high alkali concentration of the derivative melt. These observations are consistent with the notion that diorites evolved from transitional or hypersthene-normative basaltic parents.

Calculated modes of fractionating phases vary significantly with parent composition. Most importantly, plagioclase dominates the crystalline assemblage of an alkalic parent (~48 wt%) relative to the assemblage of a transitional parent (~26 wt%). Changing the composition of the fractionating plagioclase also alters its mode. Mineral compositions used in the calculations (appx. B) were selected to minimize the residual. In comparison, clinopyroxene modes are relatively insensitive to parent composition (~23 wt% in the alkalic model compared to ~28 wt% in the transitional model). The amount of derivative liquid also varies substantially with bulk composition. The alkalic parent yields diorite only after near-total crystallization (~98% fractionation), while the transitional parent yields diorite after ~65% crystallization.

Although major-element residuals are minimized for an alkalic parent, the calculated modes of mineral and melt phases are not consistent with previously discussed trace element data. Sr concentrations are greater in diorites than in hypothetical alkalic parent basalts (~7 wt% MgO). However, given ~50% crystallization of plagioclase, Sr should instead behave compatibly or nearly compatibly (assuming a partition coefficient between ~1.8-2.8 (Rollinson, 1993)). Additionally, very little residual dioritic melt remains after crystallization of an alkalic basalt (~2 wt%; appx. B.2). Assuming that even further crystallization must take place to produce a trachyte melt, fractionating alkalic basalt to produce trachyte magma requires segregation of liquid from >99% solids. Thus, to produce ~5.5 km³ of trachyte, an alkalic magma parent requires >550 km³ of initial melt. This is considered an inordinately large volume of magma for an ocean island volcano (e.g., Marsh, 2000). The physical consequences of these mass balance calculations suggest that transitional basalt is a more likely parent to the diorite.

Finally, mass balance calculations demonstrate that 17 wt% of trachyte magma can be produced upon fractionation of plagioclase (53 wt%), clinopyroxene (10 wt%), orthopyroxene (9 wt%), ilmenite (4 wt%), magnetite (3 wt%), apatite (2 wt%), and alkali feldspar (1 wt%) from a diorite parent (rms error = 0.16 oxide wt%; appx. B.4). During this fractionation segment, the crystalline assemblage is dominated by albitic plagioclase. Again, exact modes are highly dependent on mineral compositions. Thus, mass balance calculations are consistent with the crystallization of the observed mineral assemblages from a transitional parent. Differentiation of this parent basalt through diorite compositions results in ~6 wt% of residual trachyte magma.

Comparison with MELTS and Experimental Data

The cooling and compositional evolution of a transitional basalt was simulated using the MELTS thermodynamic model (Ghiorso & Sack, 1995) in an effort to recreate the inferred LLD leading from a transitional parent through diorite to trachyte compositions. The MELTS model calculates the evolution path of a magmatic system by iteratively minimizing a specified thermodynamic state function for a given set of intensive conditions (P , f_{O_2} , wt% H_2O). Thus, given a known daughter and a hypothetical parent, crystallization modeling with MELTS may indicate what range of conditions could produce the former from the latter. Both equilibrium and fractional crystallization simulations were run over a variety of intensive conditions. Pressures varied from 0.01-7 kbar, and initial H_2O contents varied from 0.1-1.0 wt%. Oxygen fugacities were also varied, however all runs discussed here were initially set in equilibrium with the QFM buffer, and then were allowed to run unbuffered. The hypothetical parent shown in fig. 5.10 and fig. 5.11 is a transitional basalt (~7.2 wt% MgO).

No fractional crystallization models are able to connect the diorites to trachytes in terms of MgO- Al_2O_3 (fig. 5.10). To produce trachyte compositions (~17-18 wt% Al_2O_3) plagioclase crystallization and fractionation must be delayed until at least ~3 wt% MgO. Plagioclase delay can be achieved through a combination of moderate to high pressures and H_2O contents (e.g., 7 kb, 0.5 wt% H_2O ; 5 kb, 1.0 wt% H_2O (not shown)). However, such a delay leads to higher Al_2O_3 concentrations than those observed in the diorites.

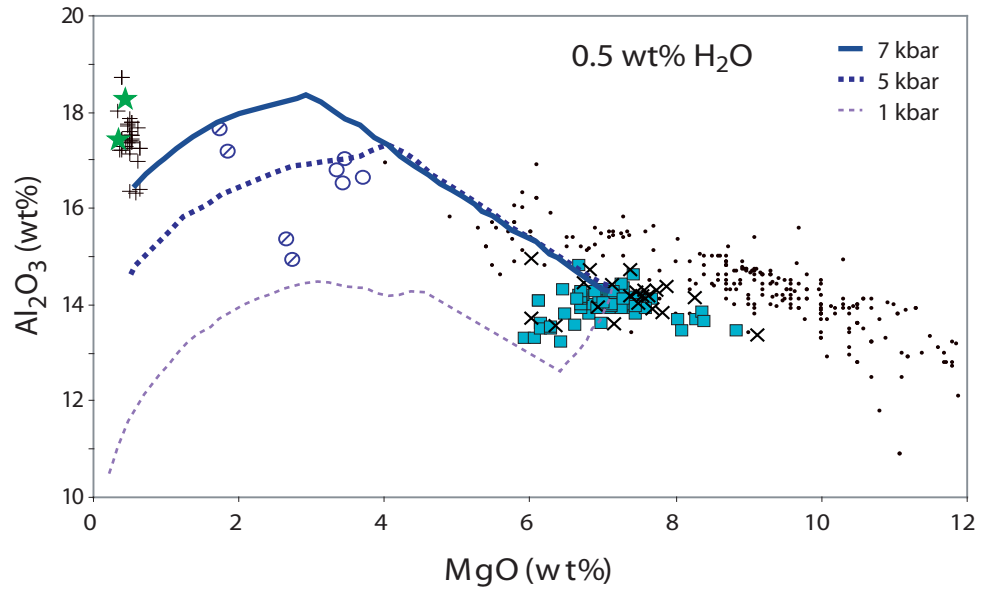


Figure 5.10: Results of fractional crystallization MELTS modeling. Simulations shown initially contain 0.5 wt% H₂O. Pressure varies between 1-7 kbar. No fractional crystallization models produced LLDs passing through both diorite and trachyte compositions. Symbols as in fig. 5.9.

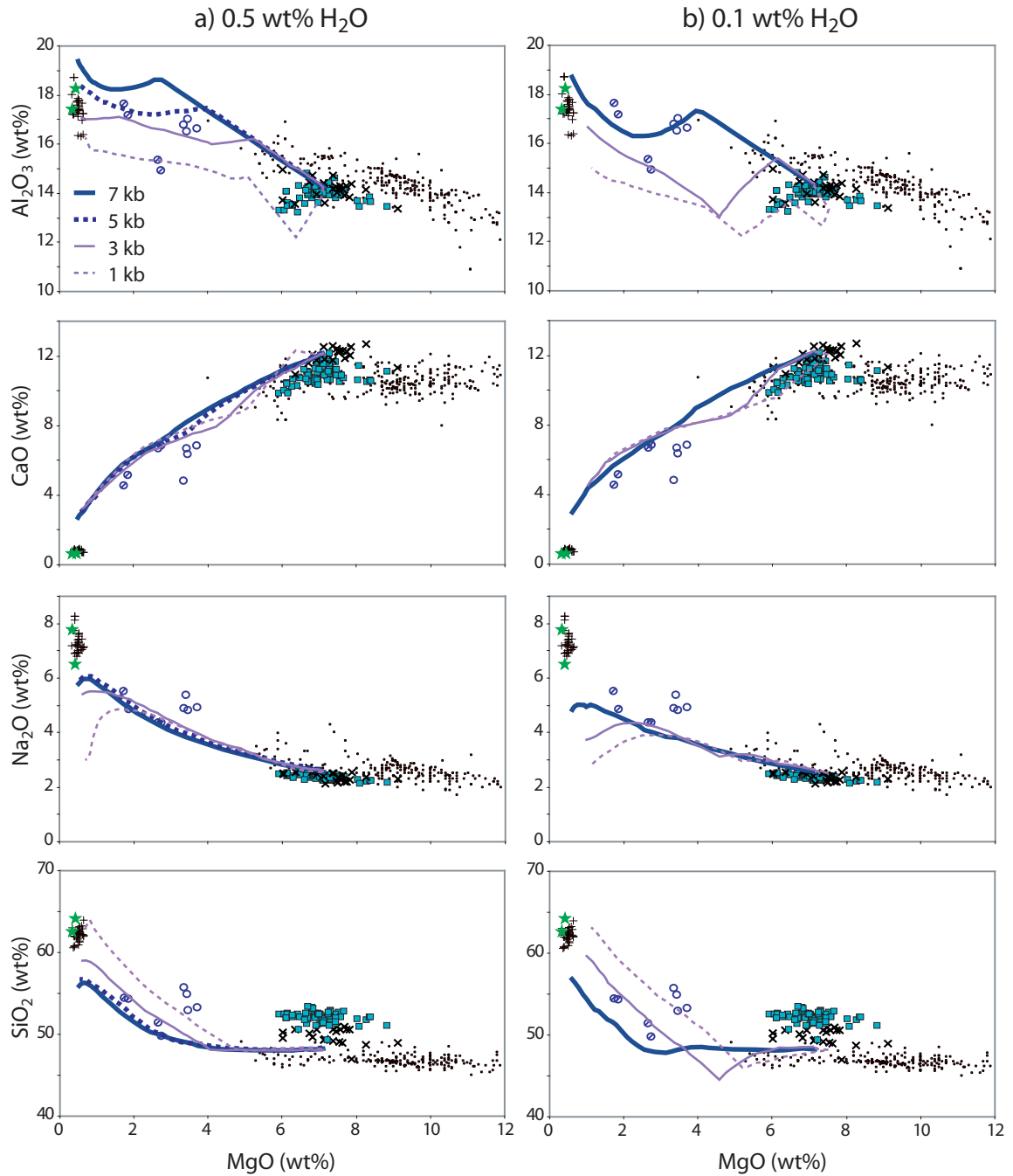


Figure 5.11: Results of equilibrium crystallization MELTS modeling. Simulations shown initially contain a) 0.5 wt% H₂O or b) 0.1 wt% H₂O. Pressure varies between 1-7 kbar by 2 kbar increments. Moderate pressure (3-5 kbar) fractionation trends with initial H₂O concentrations ~ 0.5 wt% best explain diorite and trachyte compositions, although no single simulation explains all of the compositional data. Symbols as in fig. 5.9.

Lower whole-rock Sr concentrations and the presence of rare plagioclase phenocrysts in diorites also indicate that plagioclase has begun to crystallize by ~4 wt% MgO.

Equilibrium crystallization models can produce trends passing through both diorite and trachyte Al_2O_3 concentrations (fig. 5.11). In order to avoid early decreases in Al_2O_3 , plagioclase crystallization must be delayed. Crystallization at moderate pressure and H_2O contents (e.g., 3-5 kbar, 0.5 wt% H_2O ; 5-7 kbar, 0.1 wt% H_2O) leads to moderately delayed plagioclase crystallization (beginning at ~4-5 wt% MgO) and a LLD passing through diorite and trachyte compositions. Of these conditions, the lower pressure estimates (e.g., 3 kbar, 0.5 wt% H_2O) are most compatible with other oxide data. Low pressure (1 kbar) and low H_2O content (0.1-0.5 wt%) typically lead to early dominant plagioclase crystallization. A 1 kbar trend appears unable to produce trachyte compositions even at 1.0 wt% H_2O (not shown).

No combination of intensive conditions can produce dioritic melts with Na_2O concentrations similar to those observed in the diorites (MgO ~3.5 wt%, Na_2O ~ 5 wt%). MELTS runs from high- Na_2O alkalic basalts can produce these compositions; however, these LLDs typically contain greater K_2O concentrations than observed. Alternatively, limited mixing with a trachyte magma may increase alkali concentrations.

No single crystallization simulation fits all of the oxide data. However, all of the phases present in syeno-xenoliths are crystallized in MELTS runs with the exception of kaersutite, a very minor phase that may be stable only at lower temperatures than those explored with MELTS runs. Some of the compositional mismatch may be due to the evolved alkalic nature of the melt being investigated. While the MELTS model has been

calibrated over a wide range of melt compositions, the vast majority of experimental data used to determine solution parameters are anhydrous basaltic melts. The database is particularly sparse for both evolved alkalic melts (trachytes and trachyandesites) and for hydrous alkalic melts (Ghiorso & Sack, 1995).

While MELTS results are not a robust confirmation of specific intensive conditions, they suggest two key observations: (1) Fractionation at < 3kb with low initial H₂O concentrations leads to early plagioclase dominated assemblages and accompanying Al₂O₃ depletion. (2) Fractionation at ≥ 7 kb with ≥ 0.5 wt% initial H₂O content suppresses plagioclase until well after its onset in the natural system as indicated by Sr concentrations. Neither of these trends are consistent with diorite compositions, suggesting instead fractionation along a moderate pressure trend.

Experimental investigations of alkalic LLDs support the qualitative observations drawn from MELTS modeling. The study of Nekvasil *et al.* (2004) of an hypersthene-normative alkalic basalt suite uses a starting composition similar to the alkalic basalts of Hualālai (slightly higher K₂O and lower FeO*, CaO; table 4.2). Mahood & Baker (1986) also experiment on similar initial composition melt (again higher alkali content as well as slightly more TiO₂ and P₂O₅ than Hualālai alkalic basalt; table 4.2). These authors examined the effect of pressure (0-9.3 kbar) and H₂O concentration (<0.04-2 wt% initial H₂O content) on the LLD. The two principal MELTS-derived observations are supported by experimental results:

(1) Low-pressure (1 bar) conditions lead to olivine and plagioclase dominated trends and accompanying Al-depletion. Either greater pressures or higher H₂O contents –

>0.4 wt% H₂O (Nekvasil *et al.*, 2004) – are necessary to suppress this early plagioclase assemblage. Intermediate pressure dry experiments were not run, so the minimum dry pressure needed to achieve suppression in alkalic melts is unknown.

(2) A combination of wet conditions (~2 wt% H₂O) and high pressures (9.3 kbar) suppressed plagioclase in the Nekvasil *et al.* experiments until the bulk composition was <1 wt% MgO. This is incompatible with evidence from syeno-xenoliths. Additionally, kaersutite dominated the crystalline assemblage at MgO <4 wt%. In syeno-xenoliths, kaersutite is only present as reaction blebs within clinopyroxene, not as primary mineral grains. Syeno-xenoliths could not have formed under conditions as hydrous as those explored by Nekvasil.

Comparison with Evolved Post-Shield Hawaiian Alkalic Series

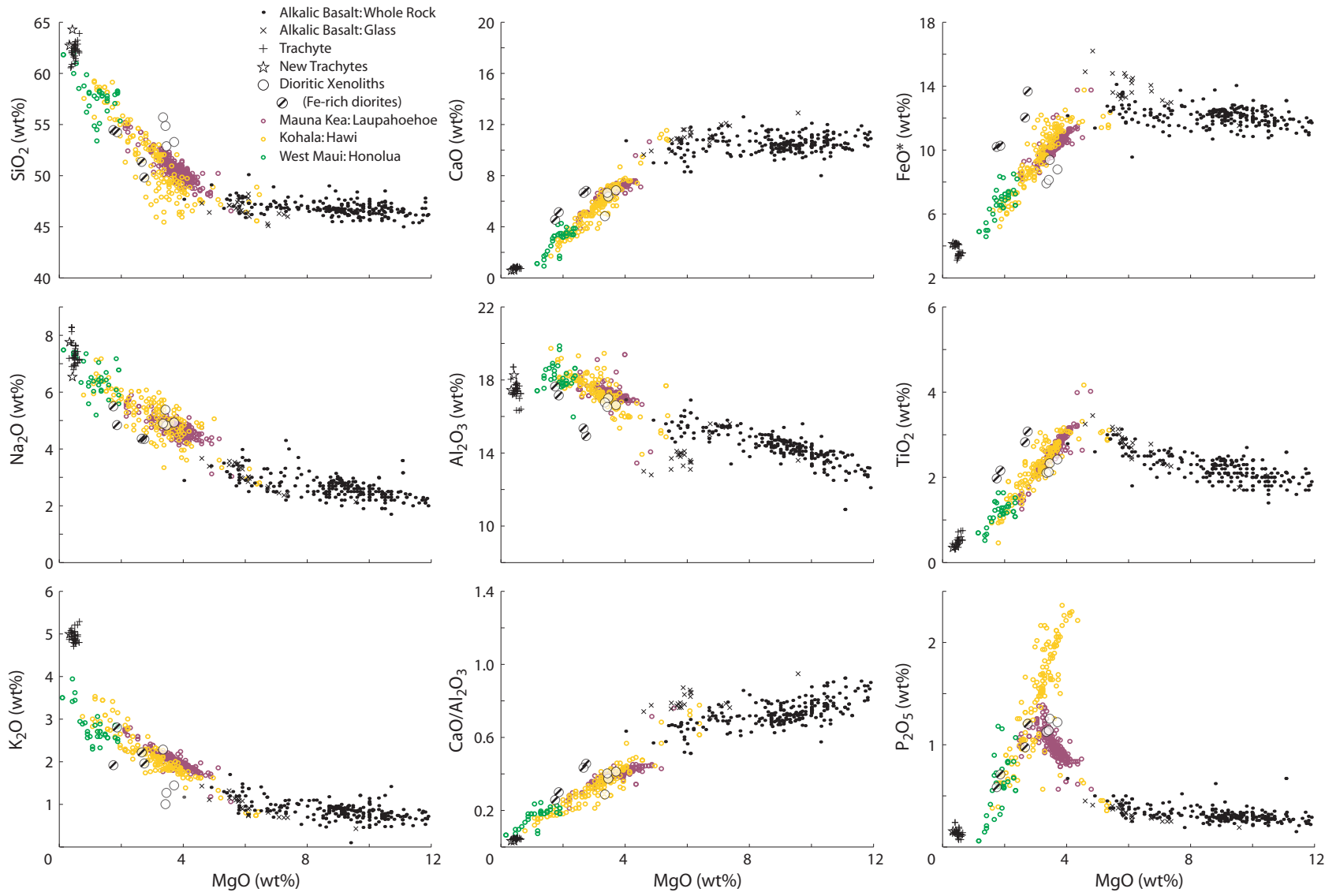
The inferred PWW trachyte LLD is compared against evolved post-shield Hawaiian alkalic series (e.g., Honolua series (West Maui Volcano), Hāwī series (Kohala Volcano), and Laupāhoehoe series (Mauna Kea Volcano)). Common LLDs are interpreted as evidence that these different alkalic series experienced similar thermodynamic conditions during crystal fractionation from parental magmas of similar compositions. Laupāhoehoe volcanics are the least evolved of the series (to ~55 wt% SiO₂), and Honolua volcanics are the most evolved (to ~62 wt% SiO₂). The West Maui volcanics also contain the largest compositional gap among these alkalic trends (~50-53 wt% SiO₂ between the Honolua and Wailuku series), although it is not as extensive as the gap at Hualālai (~49-61 wt% SiO₂).

In general, all of the evolved Hawaiian alkalic suites considered are remarkably similar and distinguished only by subtle differences (fig. 5.12, 5.13; see appendix C.2 for data sources). Average K_2O concentrations are higher in Laupāhoehoe volcanics than in Hāwī volcanics, and higher in Hāwī volcanics than Honolua volcanics. Laupāhoehoe volcanics are also mildly enriched in SiO_2 with respect to Hāwī volcanics. Additionally, concentrations of FeO^* are slightly higher in Hāwī than in Laupāhoehoe volcanics (fig. 5.12). Differences in FeO^* may be related to H_2O content or fO_2 in the melt, either of which will affect the stability of Fe-Ti oxides relative to silicate phases. Variation in FeO^* is insignificant overall, as all three alkalic series follow the classic Fenner trend (fig. 5.14). One notable distinction among these volcanoes is a dramatic spike in the phosphorous content of Hāwī hawaiites, interpreted by Spengler & Garcia (1988) as the signature of a P_2O_5 -enriched source.

Frey *et al.* (1990) propose that the Laupāhoehoe series represents the product of moderate pressure (~8 kb) clinopyroxene-dominated fractionation. Similarities with the Hāwī series led these authors to extend the late-stage moderate pressure fractionation model to include Kohala as well. Specifically, the two series shared (1) their eruption sequence (both were the most recent post-shield eruptions), (2) a compositional gap separating them from previously erupted basalts, and (3) high Al_2O_3/CaO , low Sc, and high Sr (all geochemical indicators of clinopyroxene fractionation in the absence of plagioclase). The Honolua series of West Maui shares a similar major element-defined LLD and comparable Sc and Sr concentrations (Sinton, *unpublished*), suggesting that it too may have fractionated under similar pressure conditions (fig. 5.12).

Figure 5.12: MgO variation diagrams comparing Hualālai volcanics and plutonics against evolved alkalic series from Mauna Kea, Kohala, and West Maui (data sources listed in appx. C.2). See fig. 4.1a, b for a description of Hualālai data.

811



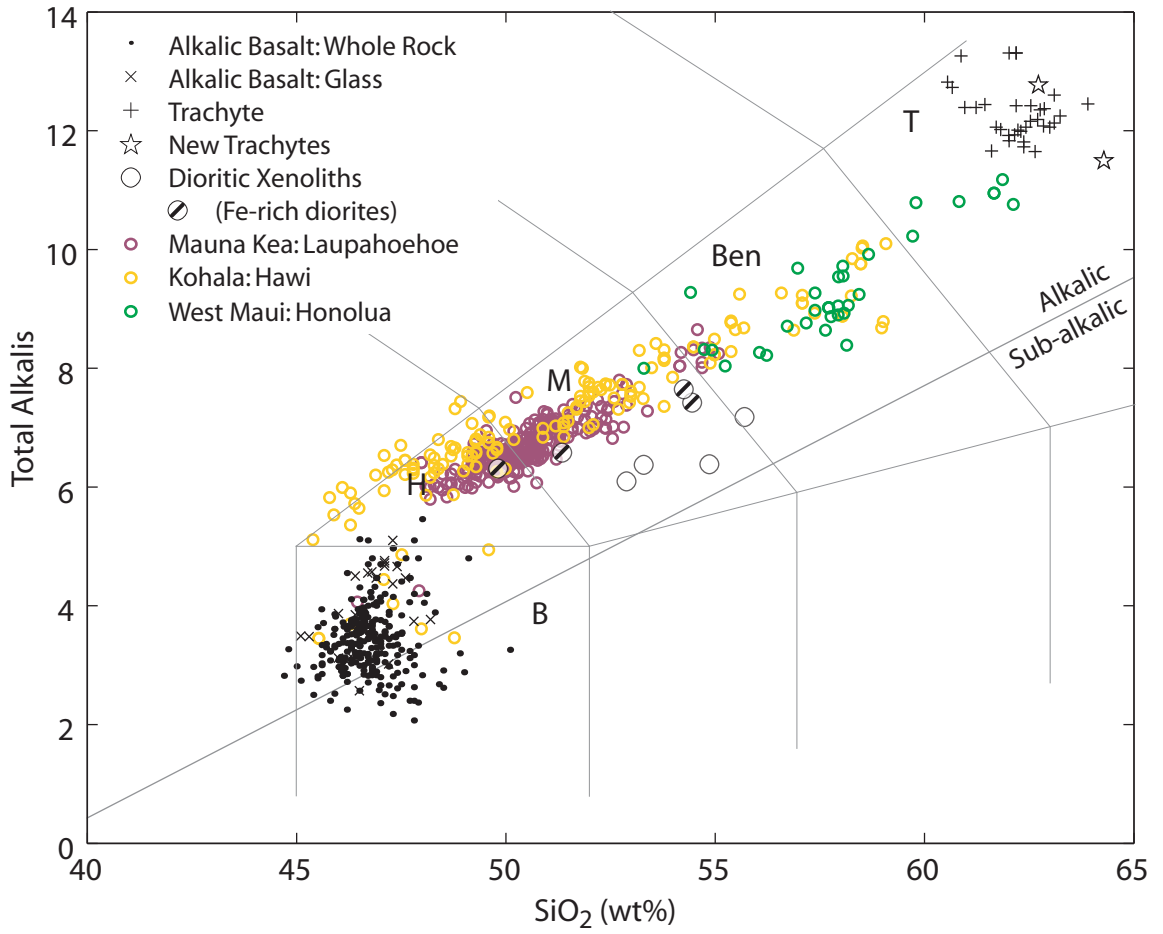


Figure 5.13: TAS diagram comparing Hualalai volcanics and plutonics against evolved alkalic series from Mauna Kea, Kohala, and West Maui, as in figure 5.12.

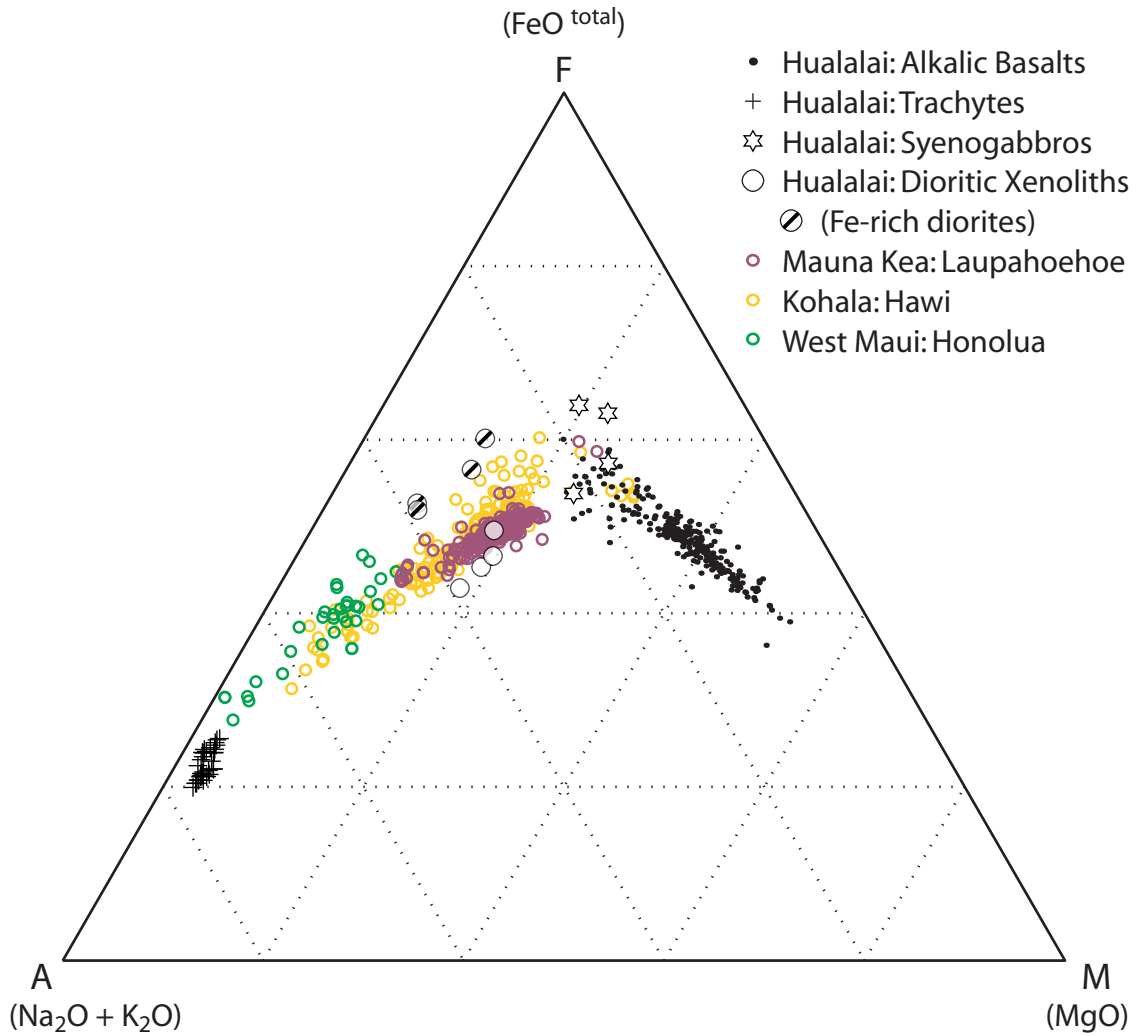


Figure 5.14: Alkalis - FeO^{total} - MgO (AFM) diagram of alkalic series considered in fig. 5.12, 5.13. Hawaiian post-shield alkalic series follow the classic Fenner trend of iron enrichment prior to alkali enrichment. Laupahoehoe series lavas appear less iron-enriched than other Hawaiian alkalic series (e.g., Hawi lavas). Fe-rich dioritic xenoliths (marked by diagonal slashes) are shifted towards the Fe apex.

The inferred LLD of PWW trachytes, as delineated by the dioritic xenoliths, closely resembles those of other Hawaiian alkalic lava suites. Fe-rich dioritic xenoliths have slightly higher FeO* and TiO₂ and lower SiO₂, Al₂O₃, and alkali concentrations, probably due to minor (<5 wt%) Fe-Ti oxide accumulation. Si-rich xenoliths have higher SiO₂ concentration (by ~2-3 wt%) than other alkalic trends, reflecting their mild degree of silica saturation (fig. 5.13). The observation that the hypothetical LLD leading to PWW trachytes resembles moderate-pressure fractionation trends from other Hawaiian alkalic settings is strong evidence that they both evolved by fractionating similar crystal assemblages. This in turn suggests that fractionation at Hualālai also occurred under moderate pressures, as significantly different pressures would lead to different assemblages and mineral compositions.

Three-phase Saturated Pseudo-cotectic

In order to quantitatively estimate pressure of crystallization, normative concentrations of Hualālai alkalic lavas, trachytes and dioritic xenoliths were calculated following Sack *et al.* (1987) (see caption to fig. 5.6). The compositions of melts in equilibrium with plagioclase (Plag), olivine (Ol), clinopyroxene (Cpx), ± nepheline (Ne) at 1 bar forms a plane in the basalt tetrahedron (fig. 5.15), and a linear trend when projected onto a pseudo-ternary diagram (e.g., Ol-Cpx-Ne; fig. 5.16a). As indicated by synthetic simple-system experiments (Presnall *et al.*, 1979) and studies on natural melts (Sack *et al.*, 1987; Frey *et al.*, 1990; Grove *et al.*, 1992), the three-phase (Plag-Ol-Cpx) saturated pseudo-cotectic shifts from Cpx to Ol as pressure increases (fig. 5.16a, 5.17a).

- * Strongly silica-saturated melts:
Andesite, Basaltic Andesite
- Intermediates:
Basalt, Hawaiite, Basaltic Trachy-andesite
- + Silica-undersaturated melts:
Tephrite, Phonotephrite, Tephri-phonolite

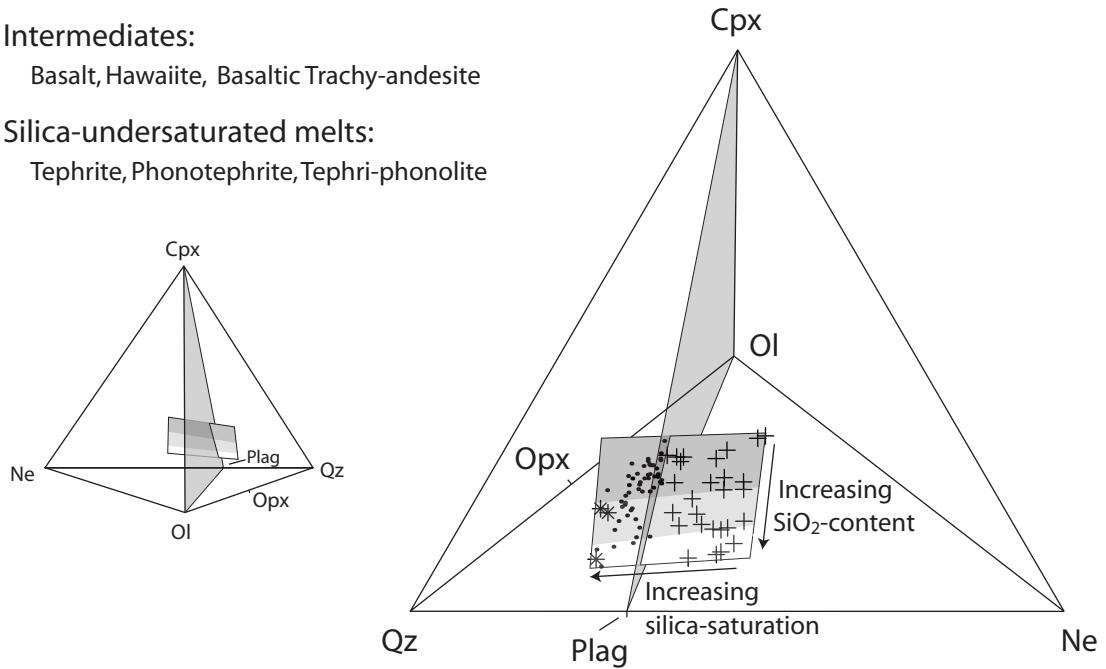


Figure 5.15: The 1 bar Plag-Ol-Cpx saturated pseudo-cotectic defined by experimental melts forms a plane in the basalt tetrahedron; when projected through plagioclase onto the Ol-Cpx-Ne ternary (fig. 5.16), the pseudo-cotectic is curvilinear. Melt compositions are distributed systematically across the pseudo-cotectic. Low-SiO₂ melts (e.g., basalt) are close to the clinopyroxene apex, while high-SiO₂ melts (e.g., trachyandesite) approach the plagioclase join. Likewise, silica-saturated melts (e.g., andesite) fall closer to the quartz apex, while silica-undersaturated melts (e.g., tephrite) fall closer to the nepheline apex. Data sources listed in appx. C.3, normative components calculated as in fig. 5.6. Plag = plagioclase, Ol = olivine, Cpx = clinopyroxene, Ne = nepheline, Qz = quartz.

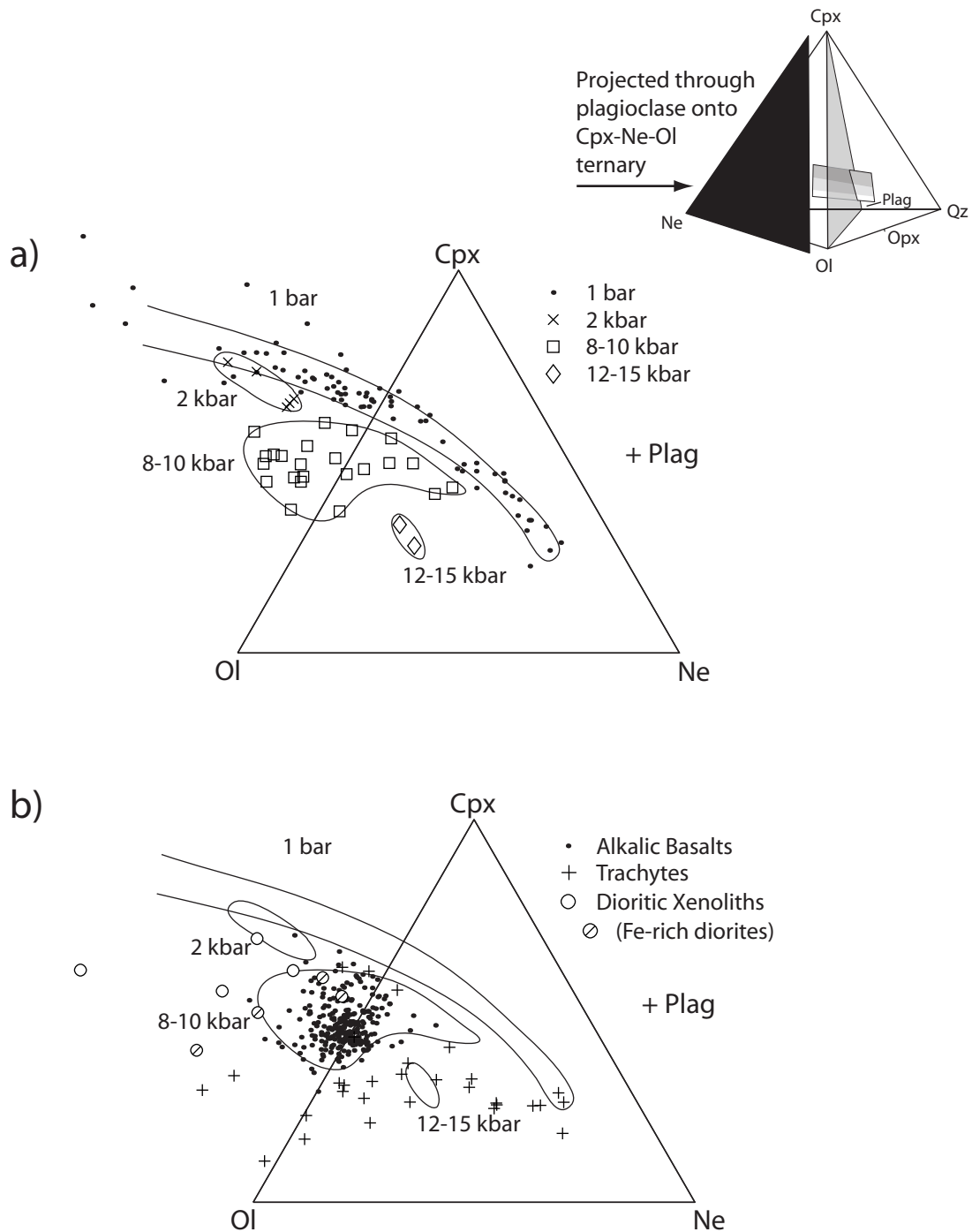


Figure 5.16: Ol-Cpx-Ne pseudo-ternaries. a) Dry experimental melts in equilibrium with Ol, Cpx, and Plag at pressures indicated (data sources listed in appx. B.3). b) Hualalai alkalic volcanics and dioritic xenoliths. Normative components are calculated as in fig. 5 of Sack (1987) and projected through plagioclase.

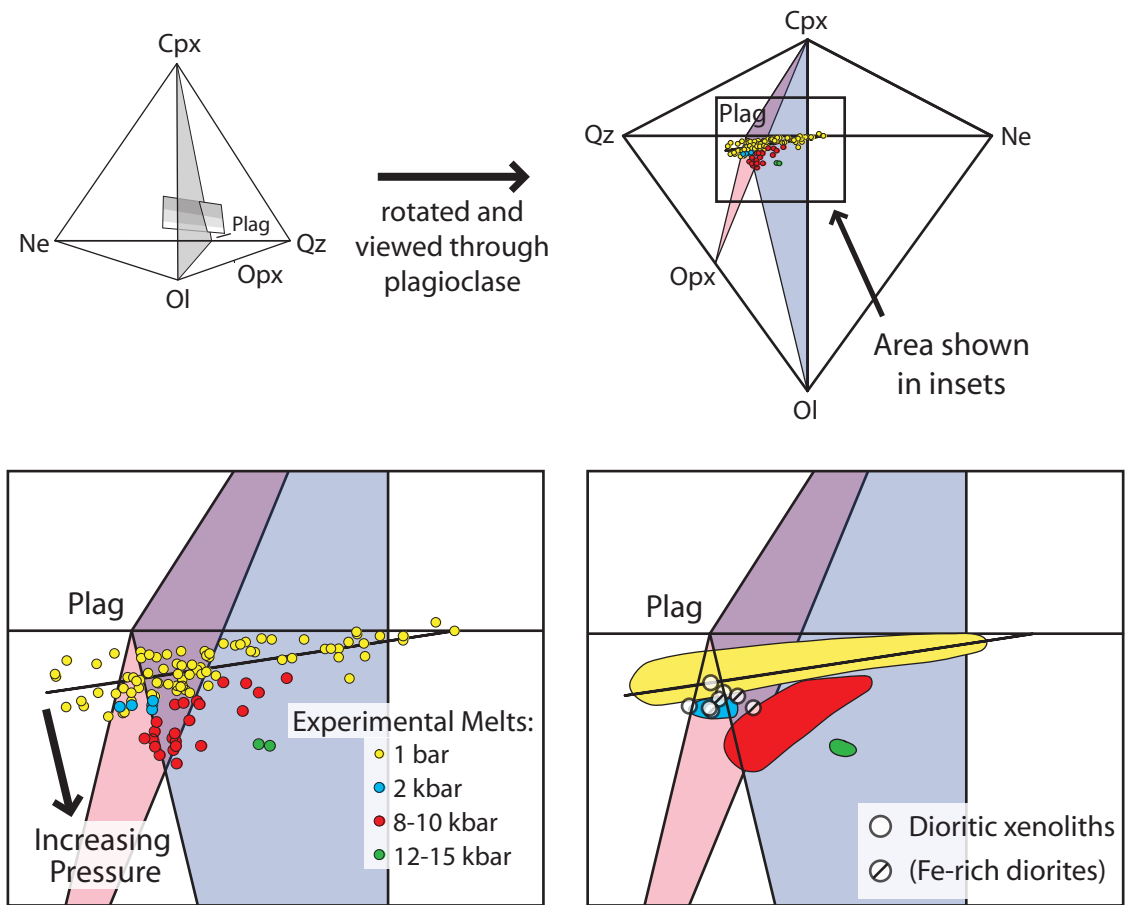


Figure 5.17: Normative compositions of melts projected into the basalt tetrahedron (Ol-Cpx-Ne-Qz) as in fig. 5.15. Insets are not 2-D projections, but rather flattened views of the portion of the basalt tetrahedron outlined by a box above. a) Dry experimental melts, as in fig. 5.16a. b) Hualalai alkalic volcanics and dioritic xenoliths. The 1 bar dry pseudo-cotectic plane (viewed along-plane it appears linear) has been included in each inset for reference. Experimental data confirm a shift of the pseudo-cotectic towards the olivine component as pressure increases. See fig. 5.16 for ternary projections of the same data.

The addition of H₂O also shifts the pseudo-cotectic in the same direction, however, experimental data is insufficient to quantitatively constrain this effect.

Some of the compositional scatter in the pseudo-ternary diagram (especially that apparent in the Hualālai trachytes; fig. 5.16b) is attributable to distortions introduced by projection through plagioclase. As melts evolve, their compositions become enriched in normative plagioclase, and small deviations in other normative components are magnified in the final projection. Thus, while pseudo-ternary projections have the advantage of compressing information into two dimensions for easy viewing, tetrahedral diagrams have the advantage of minimizing projection distortions.

Hualālai dioritic xenoliths are offset from the 1 bar pseudo-cotectic towards olivine, although not as far as the Laupāhoehoe series (Frey *et al.*, 1990). Comparing their compositions with experimental data, dioritic xenoliths are in equilibrium at moderate pressures (they fall between 2 kbar and 8-10 kbar experimental melt compositions). Trachytes also have a greater normative Ol/Cpx ratio, however, none of the pressure-calibrated experimental melts are as evolved as the trachytes, making an accurate comparison difficult. We interpret the normative composition of dioritic xenoliths as further evidence that they fractionated at moderate pressures. If, as we have previously argued, dioritic xenoliths are intermediate liquids along the PWW trachyte LLD, these pressures also indicate the depth of the trachyte reservoir.

Compositional Gap

Hualālai lavas contain a conspicuous compositional gap between alkalic basalts and the PWW trachytes (~49-61 wt% SiO₂). While West Maui volcanics (Honolua and Wailuku series) exhibit a similar, but smaller, gap (50-53 wt% SiO₂), both Mauna Kea (Laupāhoehoe series) and Kohala (Hāwī series) are nearly continuous above ~48 wt% SiO₂. Dioritic plutonics fall within, but do not span, the gap at Hualālai. These newly determined intermediate compositions allow further investigation into the sources of compositional gaps in erupted suites. Specifically, intermediate lavas in the Laupāhoehoe and Hāwī series are compared with their plutonic counterparts from Hualālai, in order to test various petrological and rheological mechanisms for generating a gap. The role of extrinsic factors (e.g., magma supply rate) on generating the compositional gap is considered. Finally, the importance of the trachyte minimum is discussed in the context of the ocean island basalt-trachyte association.

The lack of intermediate lavas on Hualālai is an example of the “Daly Gap,” an observed paucity of intermediate compositions in oceanic alkalic basalt-trachyte suites (Daly, 1925; Chayes, 1963; 1977). Since its origination, the phrase “Daly Gap” has been applied to compositional gaps occurring in silica-saturated ocean island lavas (Geist *et al.*, 1995) and in both island arc and continental volcanic lavas (Lee *et al.*, 1995; Peccerillo *et al.*, 2003). While these gaps are often attributed to crystal fractionation processes, their LLDs are distinct from those of alkalic basalts, and residual magmas are not always trachytic. For these reasons, discussion of the compositional gap at Hualālai may not be generalized to all observed “Daly Gaps”.

Causes for Compositional Gap

Gaps in SiO₂ content between ~50-60 wt% SiO₂ may be explained by unsteady rates of compositional change with crystallization ($d[\text{SiO}_2]/d\phi$, where ϕ is the fraction of solid crystals) (Clague, 1978; Philpotts, 1990; Mushkin *et al.*, 2002). Extensive crystal fractionation of olivine, clinopyroxene, and plagioclase effects little change on melt SiO₂ concentrations (e.g., Boina center, Ethiopia (Barberi *et al.*, 1975)). However, silica and alkali concentrations increase abruptly (by ~10-20 wt% in SiO₂ and ~5-10 wt% Na₂O + K₂O) over a relatively narrow range in crystallinity (~65-80 vol%, dependent on initial composition), due to the onset of titano-magnetite fractionation (Hess, 1989). Assuming constant rates of crystallization, random (i.e., eruptive) sampling of this sequence is unlikely to produce intermediate composition magmas.

The mechanism that created the compositional gap on Hualālai did not operate on either the Hāwī or Laupāhoehoe series (fig. 5.12, 5.13). If unsteady $d[X]/d\phi$ (where X represents the concentration of any given oxide) is solely responsible for the gap, then the Hāwī and Laupāhoehoe series must exhibit a less abrupt enrichment in [X] (i.e., lower overall $d[X]/d\phi$). To test this hypothesis, SiO₂ evolution was plotted against a proxy for crystallinity (fig. 5.18); the horizontal axis in this figure is calculated as $x = ([\text{Nb}] - [\text{Nb}]^0) / [\text{Nb}]$, which is equivalent to ϕ (crystallinity) for a perfectly incompatible element. While Nb is highly incompatible in basaltic melts, it becomes less incompatible once Fe-Ti oxides join the liquidus (magnetite has a mineral/melt partition coefficient of ~0.4-1.0 in basaltic to andesitic melts (Rollinson, 1993)). This causes the ratio $([\text{Nb}] - [\text{Nb}]^0) / [\text{Nb}]$ to under-predict the change in crystallinity at high values of ϕ , effectively

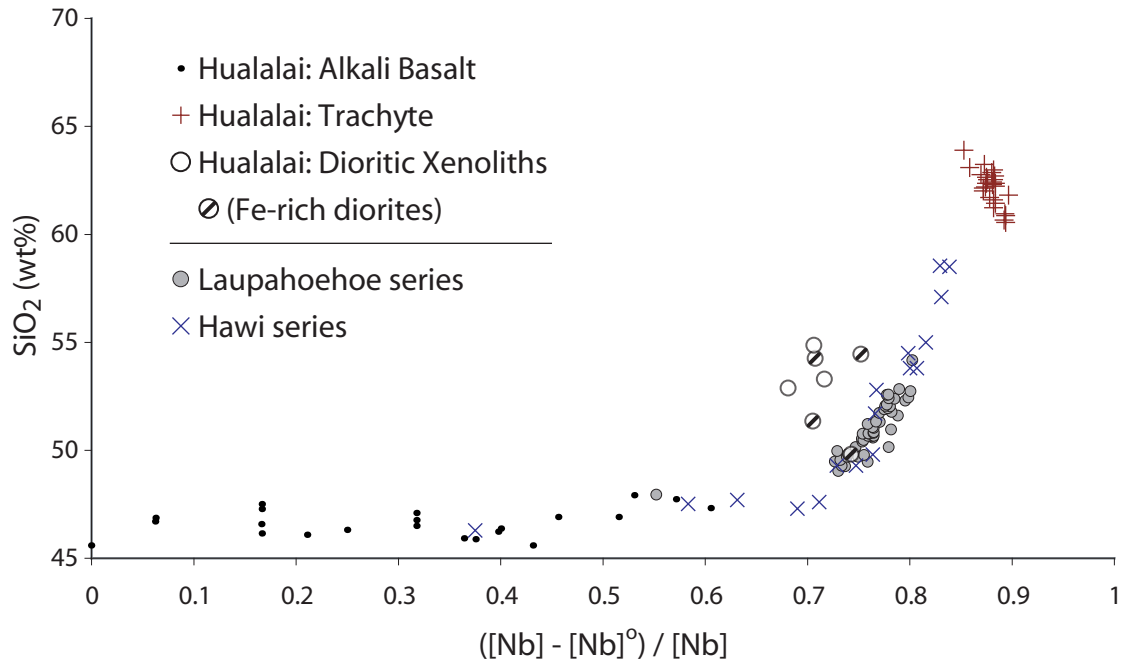


Figure 5.18: SiO₂ concentrations as a function of crystalline fraction ($X = 1 - ([Nb_0]/[Nb])$, as in Clague (1978)). The expression X is a proxy for crystalline fraction, and would be equal to ϕ if Nb were perfectly incompatible along the entire LLD. Increasing compatibility of Nb acts to compress the right-hand side of this figure. Nb₀ = 15 ppm in all cases. Different initial concentrations Nb₀ for Mauna Kea and Kohala may shift the values of X over which silica enrichment takes place (e.g., for Nb₀ = 25 ppm, it occurs between X = 0.60-0.75), but do not affect the rapid silica enrichment. SiO₂ concentrations do not increase in Hawaiian alkalic series until a X ~ 0.65-0.70, after which silica increases rapidly.

compressing the horizontal axis at $x \approx 0.6-1.0$. Despite this distortion, Nb concentrations offer the best estimate of degree of fractionation from a parent magma.

In all three alkalic series, there is an equally dramatic increase in $d[\text{SiO}_2]/d\phi$ around 70-85% crystallinity (fig. 5.18). While the distortion discussed above may accentuate the sudden increase in silica, the important conclusion drawn from this figure is that the PWW trachyte LLD behaves similarly to the Hāwī and Laupāhoehoe series. Similar $d[\text{SiO}_2]/d\phi$ trends in the lava suites, combined with similar LLDs, imply that the presence of a compositional gap on Hualālai and not Mauna Kea or Kohala is not solely attributable to variable $d[X]/d\phi$.

Compositional dependence of viscosity and density also has been invoked to explain the bias in erupted products towards trachytes (Thompson *et al.*, 2001; Peccerillo *et al.*, 2003). These rheological explanations, collectively termed “viscous trapping” models, link a lack of intermediate lavas to high viscosities caused by increasing silica concentrations. Magmas only erupt when either the buoyant force overwhelms the high viscosity (i.e., very low density magmas) or significant volatiles accumulate to again reduce viscosity. These two mechanisms favor bimodal volcanism, filtering out intermediate composition magmas. Both of these models are fundamentally dependent on melt composition. Since LLDs do not vary greatly between the Hualālai, Hāwī, and Laupāhoehoe series, it is unlikely that either of these mechanisms would generate a compositional gap at one volcano and not another. Large differences in volatile contents of primitive melts could affect the efficacy of viscous trapping; however, such variations are not observed in Hawaiian magmas (Davis *et al.*, 2003).

The gap in the Hualālai alkalic series cannot be explained by compositionally dependent mechanisms. Therefore, the lack of intermediate lavas implies either (1) the magma withdrawal rate during differentiation of the PWW trachyte parent was low or inhibited, or (2) crystallization occurred rapidly relative to late post-shield alkalic magmas at Mauna Kea and Kohala, allowing for faster differentiation. Several lines of evidence contradict the latter hypothesis. First, the volume of parent magma involved at Hualālai (~55-100 km³ parent basalt leading to ~5.5 km³ erupted trachyte (Moore *et al.*, 1987; Cousens *et al.*, 2003)) is probably larger than that leading to any single evolved post-shield eruption at Mauna Kea or Kohala. Greater volumes of magma necessitate that more heat be removed from the system, which would lead to slower cooling and crystallization rates. Second, PWW trachyte formation occurred within ~20 kyr of robust shield-stage volcanism, during a thermal regime that is likely hotter than that of late stage post-shield volcanism at Mauna Kea and Kohala. Again, this leads to slower crystallization rates. Finally, the degree of intra-mineral chemical homogeneity in dioritic xenoliths suggests a long period of high temperature re-equilibration, rather than rapid crystallization and sub-solidus cooling. A shallow trachyte reservoir at Hualālai may lead to high heat fluxes and rapid crystallization of a parent magma. However, pressure estimates obtained in this study do not support this possibility.

Role of Extrinsic Factors

Speculatively, several extrinsic factors may have contributed to the apparent protracted repose period during trachyte development and to their ultimate eruption. These include (1) frozen shallow-level conduits impeding ascent, (2) fluctuation in

magma supply, and (3) changes in overall stress regime caused by the North Kona Slump.

Studies at Kilauea and Mauna Loa (e.g., Rowan & Clayton, 1993; Cervelli & Miklius, 2003) suggest that Hawaiian magma pockets feeding tholeiite shield-building eruptions are shallow (~0.5-3.5 km). If the PWW trachyte magma chamber was significantly deeper, as both petrological and mineralogical evidence suggests, then the shield to post-shield transition at Hualālai corresponds with a deepening of the magma system feeding eruptions. The lack of mixed magmas or enclave relationships in tholeiite and alkalic erupted lavas at Hualālai suggests freezing of the shallow shield-stage magma chambers and conduits. This, in turn, might impede magma ascent, as new magma conduits must be formed to transport magma to the surface.

The shield to post-shield transition is commonly linked with a decrease in magma supply rate (e.g., Clague & Dalrymple, 1987; Frey *et al.*, 1990). Abrupt decreases at Kahoolawe, Kauai, and West Molokai led each volcano to erupt only a few alkalic post-shield lava flows, while Lanai and Koolau lack post-shield eruptions (Clague, 1987b; Clague, 1987a). Cousens *et al.* (2003) proposed that a lower magma supply rate at Hualālai volcano during the shield to post-shield transition may have lengthened the repose period, allowing for the formation of the PWW trachytes. However, estimates of magma supply rate during the transition period (0.003-0.005 km³/yr, assuming intrusion of ~55-100 km³ parent basalt over ~20 kyr, as introduced earlier) are similar to eruption rates of alkalic basalt over the past 3,000 years (~0.002 km³/yr) (Moore *et al.*, 1987). Since estimates do not support a lapse in magma supply during the transition, and since

Holocene alkalic basalts erupted regularly (with an average recurrence interval on the order of ~50 yr (Moore *et al.*, 1987)), the prolonged repose interval during trachyte differentiation cannot be clearly related to magma supply rate.

Finally, the North Kona slump, a major mass wasting event on the western flanks of Hualālai and Mauna Loa, may have altered the stress regime throughout the western coast of Hawai‘i, triggering the eruption of the PWW trachytes. This event occurred 100-130 ka (McMurtry *et al.*, 1999), roughly corresponding with the onset of trachyte eruption. Structural evolution of ocean island volcanoes (e.g., faulting, landslides) has commonly been linked with volcanic activity (e.g., Day *et al.*, 1999), although the exact causal relationships are not always clear. By removing large volumes of material, the North Kona slump may have caused a reduction in confining stress, therefore lessening magmatic overpressure and facilitating eruption. Similar catastrophic mass wasting off the western flanks of Oahu is proposed to have provoked eruption of the Kolekole Member of the Waianae Volcanics (Presley *et al.*, 1997), although these lavas are less fractionated than the previous Palehua Member.

Trachyte Minimum

Trachyte is a natural minimum composition; it results from extensive crystal fractionation in a number of alkalic ocean-island suites (e.g., Agua de Pau and Sete Cidades, Azores (Moore, 1990; Renzulli & Santi, 2000), Mauritius (Baxter, 1975)). Analog studies of the simple system quartz-nepheline-kalsilite (petrogeny’s residua system) correlate trachyte compositions with a thermal minimum along the alkali feldspar join (Schairer, 1950). Once the thermal minimum composition is achieved, melt is

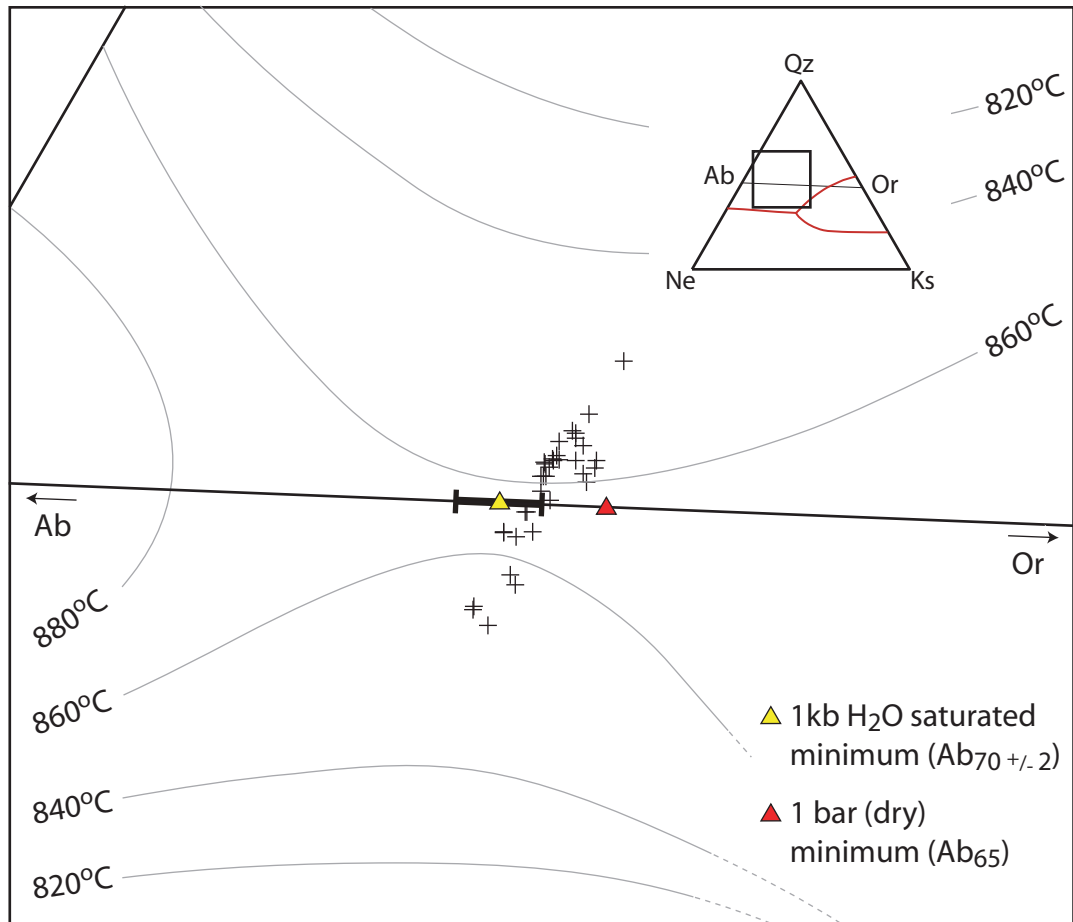


Figure 5.19: Normative trachyte compositions plotted on a weight basis on a quartz (Qz)-nepheline (Ne)-kalsilite (Ks) ternary (petrogeny's residua). Remaining oxide components (e.g., CaO, FeO) account for less than 7 wt% of the trachyte composition. Isotherms and phase boundaries are determined for the simple system Qz-Ne-Ks at $p_{\text{H}_2\text{O}} = 1$ kbar (Tuttle & Bowen, 1958; Hamilton & MacKenzie, 1965). The temperature and composition of the thermal minimum along the albite (Ab)-orthoclase (Or) join varies with $p_{\text{H}_2\text{O}}$. The 2 kbar and 1 kbar H₂O saturated minima correspond to Ab_{70±2} while the 0.5 kbar H₂O saturated and dry minima correspond to ~Ab₆₅ (Schairer, 1950; Tuttle & Bowen, 1958).

compositionally invariant, despite further crystallization (Gittins, 1979). PWW trachyte compositions correspond well with the experimentally determined thermal minimum between 0.5-1 kb p H_2O (fig. 5.19) (Schairer, 1950; Tuttle & Bowen, 1958).

The fractionating assemblage for any given trachyte varies as a function of T, P, p H_2O , and composition. However, recent experiments (Nekvasil *et al.*, 2004) suggest that even under higher H_2O and pressure conditions (~5wt% H_2O , 9.3 kbar total pressure), the equilibrium fractionating assemblage (biotite and ternary feldspar) still leads to a trachyte pseudo-minimum (i.e., 53% crystallization causes virtually no change in SiO_2 , Na_2O , and K_2O contents). We conclude that the occurrence of trachyte on Hualālai, as opposed to the intermediate benmoreites and mugearites found at Mauna Kea and Kohala, is a natural consequence of a longer repose period prior to its eruption. Differences in repose period durations may be caused by one or more extrinsic factors, such as differences in volcanic plumbing (e.g., centralized vs. dispersed conduit system (Cousens *et al.*, 2003)) and regional stress fields (e.g., buttressing neighbors, timing of flank collapse). If trachyte compositions are generally invariant, then steady replenishment, tapping, and fractionation (O'Hara, 1977) of a reservoir after the trachyte minimum has been reached could lead to long-lived trachyte magma chambers such as those observed on Agua de Pao (Widom *et al.*, 1993). Such a scenario may be one possible source for the basalt-trachyte association in ocean island settings.

CHAPTER 6. SHIELD TO POST-SHIELD TRANSITION ON HUALĀLAI VOLCANO

High magma supply and eruption rates during the shield stage (e.g., $\sim 0.05 \text{ km}^3/\text{yr}$ at Mauna Kea (Wolfe *et al.*, 1997), $\sim 0.1\text{-}0.2 \text{ km}^3/\text{yr}$ at Kilauea (Dvorak & Dzurisin, 1993)) are thought to promote the formation of shallow summit magma reservoirs (3-7 km, fig. 6.1a), such as those presently observed at Kilauea and Mauna Loa (Decker *et al.*, 1983; Dzurisin *et al.*, 1984; Cervelli & Miklius, 2003). Ultra-mafic and gabbroic cumulates associated with tholeiite magma (e.g., dunite, wehrlite, gabbro, etc. (Clague, 1987b; Fodor & Galar, 1997)) form along shield stage magma chamber floors and walls. To remain shallow, these magma chambers migrate upwards in the volcanic edifice as the volcano grows, leaving behind a thick sequence of cumulates (Ryan, 1988). Shield stage tholeiites erupted from Hualālai as recently as 133 ka, ~ 20 kyr before the $\sim 5.5 \text{ km}^3$ trachyte eruption of Pu‘u Wa‘awa‘a and Pu‘u Anahulu (Moore *et al.*, 1987).

Over ~ 20 kyr, a minimum of $55\text{-}100 \text{ km}^3$ basaltic magma underwent extensive crystal fractionation (estimated to be $\geq 90\%$ crystallization; fig. 5.4 and (Cousens *et al.*, 2003)) to form trachyte magma. These parent magmas may have been hypersthene-normative transitional or alkalic basalts. Pb isotopes of the trachytes match both post-shield alkalic basalts (Cousens *et al.*, 2003) and transitional tholeiitic basalt from Hualālai (Park, 1990). Additionally, the hypersthene-normative bulk compositions of intermediate liquids (dioritic xenoliths) suggest parental magmas on the silica side of the critical plane (fig. 5.6). Early alkalic or transitional magmas may mix with residual tholeiite magmas

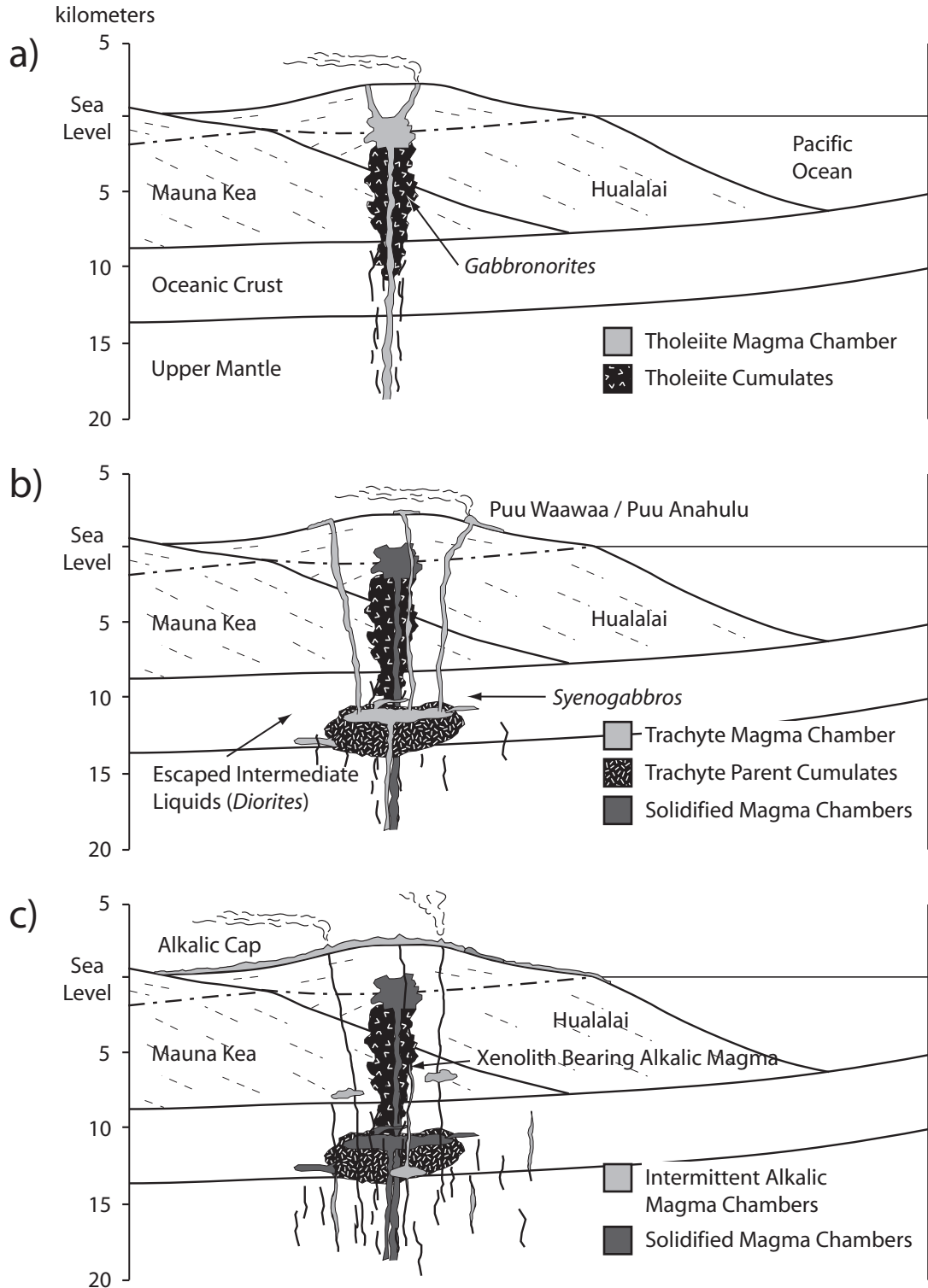


Figure 6.1: The development of the magmatic system at Hualalai Volcano during a) the shield stage (>130 ka), b) the transitional period (~130-90 ka), and c) the post-shield stage (<90 ka). Based on Wolfe et al. (1997), fig. 64.

remaining in the magma system, producing Pb isotope mixing trends. However, assuming residual tholeiite magma has similar Pb isotopic characteristics to those recovered from the submarine flank and analyzed by Park (1990), it could only represent a relatively minor component of a hybrid parent (<20%).

Mineral and bulk compositional indicators suggest that the PWW trachytes formed at ~3-7 kbar (~10-23 km), significantly deeper than shallow shield stage magma storage (fig. 6.1b). This model places the trachyte reservoir in the oceanic crust or upper mantle, rather than within the volcanic edifice as previously suggested (<7 km; Cousens *et al.* (2003)). This new, elevated pressure range for trachyte formation approaches the upper bounds of proposed storage depths of late-stage post-shield alkalic magmas at Mauna Kea (Frey *et al.*, 1990; Wolfe *et al.*, 1997). The oceanic crust and mantle interface is one likely location for magma ponding, due to a plane of weakness generated by differences in elastic properties (Gudmundsson, 1986) and to density differences between the crust and mantle. However, cross-cutting relationships between diorite and gabbronorite xenoliths suggest that the trachyte magma chamber (represented by diorites) resided near a site of former tholeiite fractionation (represented by gabbronorites). From there, intermediate liquids may have escaped from the fractionating magma chamber as dikes and sills, intruding into the gabbronorite cumulate stacks and forming the observed contacts (fig. 6.1b). This constraint suggests that the trachyte magma chamber was situated within a zone previously occupied by tholeiitic magma reservoirs. While the maximum depth of tholeiitic chambers is poorly constrained, it probably lies on the shallower end of the pressure estimates (~4-5 kbar), as higher pressures place the trachyte

chamber within the mantle. Alternatively, if a deep crustal tholeiite magma chamber persists through the shield stage, as proposed by Clague (1987b), the trachyte parent may have occupied and fractionated within this reservoir. The tholeiite cumulates (gabbonorites) co-erupted with the dioritic xenoliths may represent a mushy lining of this chamber, having accumulated from shield stage tholeiites.

Trachyte lavas erupted sporadically from Hualālai for another ~20 kyr after the PWW and PA eruption (Cousens *et al.*, 2003). These lava flows have since been covered by alkalic basalt, making attempts to estimate their volume impossible. Some of the later trachytes are slightly more fractionated than those erupted at PWW, as indicated by REE concentrations, while others (including those recovered at Waha Pele) are compositionally similar (Cousens *et al.*, 2003). The lack of correlation between age of eruption and REE concentration may suggest that as the magma chamber is fractionating and periodically erupting, it is simultaneously being replenished (O'Hara, 1977). This would limit the maximum volume of magma in the system at any given time, while still generating large volumes of cumulates and differentiates. Additionally, continued influx of magma and heat could explain the persistence of a trachyte magma chamber for ~20 kyr. Alternatively, trachyte chemical variations could reflect tapping from different portions of a single zoned reservoir.

Eruption of post-shield alkalic and transitional basalts (as defined by Macdonald & Katsura, 1964) succeed the trachyte eruption, although the oldest exposed basalts are <25 ka (Moore & Clague, 1991). Holocene alkalic basalts are erupted at ~0.002 km³/yr with an average recurrence interval of ~50 yr (Moore *et al.*, 1987). At Mauna Kea, early

post-shield alkalic stage magmas are proposed to fractionate mainly at shallow levels of ~1-2 kbar (Frey *et al.*, 1991; Wolfe *et al.*, 1997). In general, however, the spatial constraints of reservoirs during this time period are poor.

Depth of magma storage during the post-shield stage at Hualālai may be inferred from xenoliths transported in alkalic lavas. If magma chambers serve as “density filters”, sorting xenoliths by density and allowing xenoliths which might have been transported up from greater depths to settle out (Clague, 1987b), the equilibrium depth of xenoliths indicate the minimum depths of magma storage of the host lava. If correct, this notion implies that diorite and syenogabbro xenolith-bearing alkalic magmas did not pond in shallow magma chambers (<3 kbar, the minimum pressure estimate for the trachyte magma chamber). A similar lack of shallow-level storage is also suggested for the 1800-1801 Ka‘ūpūlehu alkalic basalt flow, which transported ultramafic xenoliths last equilibrated at ~4.5-9 kbar (Bohrson & Clague, 1988; Chen-Hong *et al.*, 1992). The majority of prehistoric alkalic lava flows on Hualālai are compositionally similar to these two xenolith-bearing alkali olivine basalts, with only some lavas modified by further shallow crystal fractionation (Clague *et al.*, 1980). This may imply that, after the shield to post-shield transition, magma storage at Hualālai was predominantly limited to deeper reservoirs (> ~3-7 kbar; 6.1c).

CHAPTER 7. CONCLUSIONS

A detailed study of summit xenoliths related to the PWW trachyte episode has helped to shed light on the transition between the shield and post-shield stages at Hualālai. Plutonic nodules considered in this paper fall into three principle categories: syeno-xenoliths, including diorites, monzodiorites, and syenogabbros; gabbronorites, including gabbronorites and olivine gabbronorites; and coincident xenoliths, including anorthosites, hornblende-rich veins, and poikilitic gabbros. Only the syeno-xenoliths are shown to be petrogenetically related to the PWW trachytes. The diorites and monzodiorites may represent frozen intermediate composition liquids, while syenogabbros probably represent cumulates formed during differentiation of the trachyte parent magma. Dioritic xenoliths are the only known intermediates between the trachyte and its basaltic parent.

The most likely parent composition for the diorite – trachyte suite has the following characteristics: (1) Pb isotopic composition similar to alkalic and transitional basalts, (2) Mildly hypersthene-normative composition (fig. 5.6), and (3) Intermediate Nb/Zr ratios, similar to transitional basalts (fig. 5.4). Given these constraints, we conclude the parent magma for this suite to be a transitional or hypersthene-normative alkalic basalt. Early clinopyroxene fractionation evidently led to alkaline oxide enrichment in the parent basalt and evolution along the alkalic trend (fig. 4.2).

Mineral compositions and assemblages from syeno-xenoliths, bulk compositions of both alkalic plutonics and volcanics, and inferred liquid lines of descent of alkalic

magmas at Hualālai quantitatively constrain the depth of formation of the PWW trachytes to ~3-7 kbar. These constraints include:

(1) Clinopyroxene compositions indicate equilibrium pressures of ~3-7 kbar using the geobarometer of Nimis & Ulmer (1998). Ti/Al ratios in clinopyroxenes are in accordance with experimentally determined ratios within this pressure range (Thy & Lofgren, 1992; Nekvasil *et al.*, 2004). An upper pressure bound is provided by feldspar compositions. The observed ternary components in feldspar pairs are not in equilibrium above ~5-10 kbar.

(2) Clinopyroxene (potentially accompanied by lesser olivine) dominates the early fractionation history of the xenoliths, as indicated by decreases in CaO/Al₂O₃ ratio and Sc contents with increasing concentration of highly incompatible elements. Plagioclase crystallization, accompanied by a decrease in Sr contents, does not commence until ~5 wt% MgO. Plagioclase continues to dominate the fractionating assemblage at lower MgO contents. These crystallization sequences resemble moderate pressure sequences determined experimentally in similar bulk compositions (Green & Ringwood, 1967; Mahood & Baker, 1986; Nekvasil *et al.*, 2004) and predicted by MELTS.

(3) The major element LLD at Hualālai is similar to that of the late-stage post-shield alkalic series at Mauna Kea and Kohala. This suggests similarity in intensive parameters during crystal fractionation. Study of the Mauna Kea suite (and by analogy, the Kohala suite as well) points toward fractionation at pressures of ~8 kbar (Frey *et al.*, 1990).

(4) The Ol-Cpx-Plag saturated pseudo-cotectic in Ol-Cpx-Plag-Ne space shifts away from the normative clinopyroxene component towards the olivine component with increasing pressure (Grove *et al.*, 1992). Normative compositions of dioritic xenoliths and lavas from Hualālai plot well off of the experimentally determined 1 bar cotectic. Limited experimental data above 1 bar suggest cotectic crystal fractionation at intermediate pressures (~2-8 kbar).

The unique Pu'u Wa'awa'a trachyte member offers a means of constraining the depth of magma storage during the shield to post-shield transition, an outstanding problem in Hawaiian volcanism. While pressure estimates discussed in this paper do not approach the confidence levels of more refined techniques (e.g., ± 0.5 kbar using the Al-in-hornblende geobarometer (Johnson & Rutherford, 1989a)), they represent the first quantitative estimates derived directly from thermodynamic principles. Recurrence of similar pressure ranges (i.e., ~3-7 kbar) across different techniques strengthens the overall case for a moderate depth trachyte magma chamber. However, applicability of this model to other Hawaiian volcanoes is cautioned, due to the apparently unusual set of circumstances leading to the formation of the PWW trachyte.

APPENDIX A: GEOCHEMICAL DATA

Table A.1: Major element (in oxide wt%) and trace element (in ppm) whole-rock compositions of xenoliths.

Sample ID:	Trachyte:		Dioritic xenoliths:								
	PA13	PWW13	HM06	HM19	HM01	HM09	HM10	AH02a	HM08	AHX01	
notes:	lava	obsidian			Fe-rich	Fe-rich			Fe-rich	Fe-rich	
n:	(2)	(2)	(2)	(2)	(2)	(2)	(2)	(2)	(2)	(2)	
uncertainty ^a											
SiO ₂	(0.25)	64.29	62.72	55.70	54.86	54.45	54.25	53.29	52.88	51.35	49.82
TiO ₂	(0.02)	0.39	0.35	2.11	2.13	1.98	2.16	2.42	2.33	2.83	3.08
Al ₂ O ₃	(0.18)	18.27	17.45	16.77	16.53	17.65	17.16	16.63	17.01	15.35	14.93
Fe ₂ O ₃ ^{tot}	(0.10)	4.52	4.59	8.80	9.04	11.34	11.42	9.77	10.43	13.38	15.20
FeO ^{tot}	(0.09)	4.06	4.13	7.92	8.13	10.20	10.27	8.79	9.38	12.03	13.67
MnO	(0.01)	0.28	0.30	0.09	0.13	0.10	0.15	0.14	0.12	0.19	0.20
MgO	(0.07)	0.43	0.34	3.35	3.43	1.75	1.87	3.71	3.46	2.66	2.75
CaO	(0.12)	0.61	0.58	4.83	6.66	4.55	5.15	6.86	6.36	6.66	6.81
Na ₂ O	(0.16)	6.54	7.77	4.90	5.38	5.50	4.84	4.93	4.83	4.36	4.35
K ₂ O	(0.03)	4.95	5.00	2.29	1.01	1.92	2.81	1.45	1.27	2.22	1.96
P ₂ O ₅	(0.01)	0.16	0.16	1.13	1.14	0.59	0.71	1.22	1.26	0.98	1.21
SUM		100.41	99.25	99.94	100.29	99.80	100.49	100.40	99.93	99.95	100.29
L.O.I.		1.31	0.21	0.11	0.02	-0.004	0.64	0.08	0.06	-0.15	-0.02
Nb	(0.2)	133	148		51	61	51	53	47	51	58
Zr	(1.3)	985	1055		370	525	362	273	203	585	501
Y	(0.6)	53	59		76	62	72	56	56	77	84
Sr	(8.1)	41	27		536	472	502	569	549	565	566
Rb	(1.1)	119	131		4	16	46	15	5	26	19
Th	(0.2)	8.5	8.4		1.6	2.2	4.3	< 1.5	< 1.5	2.8	3.4
Pb	(1.8)	7	7		< 2.0	< 2.1	3	< 2.0	< 2.0	< 2.2	< 2.3
Co	(1.8)	5	15		24	26	28	30	40	45	33
Cr	(9.5)	< 3.0	< 3.0		< 3.1	< 3.0	< 3.1	< 3.2	< 3.1	< 3.2	< 3.2
V	(11)	< 3.4	< 3.4		133	24	27	140	144	40	51
Ba	(9.0)	396	316		495	923	1115	599	1038	1002	823
Sc	(1.2)	8	6		12	6	8	12	11	10	12
Zn	(3.7)	132	195		48	46	52	49	61	92	48
Ni	(5.7)	19	18		20	28	26	25	20	26	25

^a Absolute uncertainty is estimated from the average error between analyzed standards and their published compositions. These reflect uncertainties in the compositions of the standards and errors that can arise in the sample preparation procedure, and are generally higher than analytical precision.

Table A.1 (continued): Major element (in oxide wt%) and trace element (in ppm) whole-rock compositions of xenoliths .

Sample ID:	notes:	Syenogabbros:				Gabbronorites:			Poikilitic Gabbro:
		HM45	AH07	AH04a	HF01	HM44	HM47	AH10	AHX02
n:		(2)	(1)	(2)	(2)	(2)	(1)	(1)	(1)
	uncertainty ^a								
SiO ₂	(0.25)	48.20	45.63	43.82	42.40	49.50	49.37	48.54	49.23
TiO ₂	(0.02)	2.01	2.55	5.11	5.13	0.85	0.84	0.68	0.73
Al ₂ O ₃	(0.18)	19.99	19.59	12.59	12.39	18.85	18.81	20.55	15.95
Fe ₂ O ₃ ^{tot}	(0.10)	10.14	14.02	18.25	18.02	8.53	9.19	6.28	6.51
FeO ^{tot}	(0.09)	9.12	12.62	16.42	16.21	7.68	8.27	5.65	5.86
MnO	(0.01)	0.13	0.16	0.26	0.26	0.12	0.13	0.09	0.10
MgO	(0.07)	4.08	5.68	5.01	5.88	7.57	7.66	7.71	9.43
CaO	(0.12)	11.10	9.01	9.54	10.21	12.50	12.51	15.78	18.64
Na ₂ O	(0.16)	3.02	2.90	3.08	2.87	1.79	1.75	0.81	0.33
K ₂ O	(0.03)	0.73	0.83	1.16	0.76	0.21	0.18	0.22	0.02
P ₂ O ₅	(0.01)	0.18	0.26	1.06	2.37	0.05	0.05	0.04	0.00
SUM		99.56	100.63	99.87	100.26	99.95	100.47	100.72	100.94
L.O.I.		-0.03	-0.18	-0.5	-0.54	0.04	-0.03	0.1	0.17
Nb	(0.2)	15	19	51	46	4	4	5	1
Zr	(1.3)	127	138	263	191	34	34	40	17
Y	(0.6)	20	17	58	92	8	8	8	8
Sr	(8.1)	887	785	576	745	448	453	477	302
Rb	(1.1)	15	22	25	13	4	2	4	1
Th	(0.2)	< 1.5	< 1.6	2.1	< 1.8	< 1.5	< 1.5	< 1.5	< 1.5
Pb	(1.8)	4	< 2.2	< 2.5	< 2.5	< 2.0	< 2.0	< 2.0	< 2.0
Co	(1.8)	33	46	34	41	57	54	45	55
Cr	(9.5)	23	34	25	< 3.5	69	74	719	535
V	(11)	125	281	190	191	160	168	145	203
Ba	(9.0)	307	244	513	492	70	72	104	29
Sc	(1.2)	16	9	22	18	24	21	29	53
Zn	(3.7)	62	86	142	117	63	62	32	22
Ni	(5.7)	32	72	31	22	85	96	147	119

Table A.2: Plagioclase compositions determined by electron microprobe analysis.

	<u>Monzodiorites</u>		<u>Diorites</u>				<u>Syenogabbro</u>		<u>Gabbronorites</u>			<u>Coincident Xenos</u>								
	<u>HM01a</u>	<u>HM06</u>	<u>HM12</u>	<u>HM19</u>	<u>HM43</u>		<u>HM45</u>		<u>HM47</u>	<u>HM53</u>	<u>HM02b</u>	<u>HM23</u>		<u>HM35</u>	<u>HM50b</u>					
	ID:	5-7	1-2	7-8	7-8	1-2	8	Rims	Cores	Rims	Cores	Rims	Cores	Rims	Cores	5-6	5-6	4	2	1
# pts:	(3)	(2)	(2)	(2)	(2)	(1)	(1)	(1)	(1)	(1)	(1)	(1)	(2)	(2)	(1)	(1)	(1)	(1)		
<u>Oxide wt %</u>	<u>accuracy</u> ^a																			
SiO ₂	(0.3)	63.2	63.0	59.5	63.5	63.0	57.7	57.5	52.1	51.9	48.5	50.3	60.2	56.9	53.3	48.0	50.8			
Al ₂ O ₃	(0.3)	22.6	23.0	25.2	22.3	22.6	26.2	26.6	30.0	30.2	32.8	31.5	24.7	27.0	29.4	32.7	31.4			
Fe ₂ O ₃ ^{tot}	(0.02)	0.26	0.34	0.24	0.26	0.22	0.22	0.37	0.37	0.45	0.61	0.34	0.40	0.41	0.38	0.71	0.42			
MgO	(0.01)	0.01	0.00	0.02	0.01	0.01	0.02	0.04	0.03	0.02	0.06	0.02	0.02	0.02	0.02	0.07	0.02			
CaO	(0.15)	3.97	4.38	6.80	3.68	3.71	8.02	8.18	12.22	12.27	15.38	13.65	6.52	8.99	11.89	15.96	13.76			
Na ₂ O	(0.24)	8.52	8.39	7.08	8.52	8.37	6.76	6.58	4.45	4.30	2.56	3.66	7.41	6.06	4.69	2.36	3.65			
K ₂ O	(0.11)	1.43	1.16	1.05	1.59	1.85	0.62	0.54	0.31	0.32	0.12	0.16	0.76	0.70	0.41	0.08	0.12			
Total		100.02	100.31	99.93	99.89	99.80	99.57	99.84	99.53	99.52	99.96	99.64	100.05	100.05	100.16	99.87	100.18			
<u>Cations on basis of 8 Oxygens</u>																				
Si		2.81	2.79	2.66	2.82	2.81	2.60	2.59	2.38	2.37	2.22	2.30	2.69	2.56	2.41	2.21	2.31			
Al		1.18	1.20	1.33	1.17	1.19	1.39	1.41	1.61	1.62	1.77	1.70	1.30	1.43	1.57	1.77	1.68			
Fe ³⁺		0.01	0.01	0.01	0.01	0.01	0.01	0.01	0.01	0.02	0.02	0.01	0.01	0.01	0.01	0.02	0.01			
Mg		0.00	0.00	0.00	0.00	0.00	0.00	0.00	0.00	0.00	0.00	0.00	0.00	0.00	0.00	0.00	0.00			
Ca		0.19	0.21	0.33	0.18	0.18	0.39	0.39	0.60	0.60	0.75	0.67	0.31	0.43	0.58	0.79	0.67			
Na		0.73	0.72	0.61	0.73	0.72	0.59	0.57	0.39	0.38	0.23	0.32	0.64	0.53	0.41	0.21	0.32			
K		0.08	0.07	0.06	0.09	0.11	0.04	0.03	0.02	0.02	0.01	0.01	0.04	0.04	0.02	0.00	0.01			
Z		4.00	4.00	4.00	4.00	4.00	4.00	4.01	4.00	4.01	4.01	4.01	4.00	4.00	4.00	4.00	4.01			
X		1.00	0.99	1.00	1.00	1.01	1.01	1.00	1.01	1.00	0.99	1.00	1.00	1.00	1.01	1.01	1.00			
<u>Mole %</u>																				
An		18.9	20.9	32.7	17.6	17.6	38.3	39.6	59.3	60.2	76.4	66.8	31.4	43.3	57.1	78.6	67.1			
Ab		73.0	72.5	61.3	73.4	72.0	58.2	57.3	38.9	38.0	22.9	32.3	64.3	52.7	40.6	20.9	32.2			
Or		8.1	6.6	6.0	9.0	10.4	3.5	3.1	1.8	1.8	0.7	0.9	4.4	4.0	2.3	0.5	0.7			

^a Absolute accuracy approximated by comparing repeat analyses of standards to their published values.

Table A.3: Alkali feldspar compositions determined by electron microprobe analysis.

	Monzodiorites				Diorites								Syenogabbro		Coincident Xenos	
	<u>HM01a</u>		<u>HM06</u>		<u>HM02a</u>		<u>HM12</u>		<u>HM19</u>	<u>HM43</u>		<u>HM45</u>		<u>HM02b</u>	<u>HM23</u>	
ID:	1-4	5-7	1-2	5-6	5-6	9-10	3-4	13-14	1-2	1-2	13-14	7	12	3-4	1	
# pts:	(4)	(3)	(2)	(2)	(2)	(2)	(2)	(2)	(2)	(2)	(2)	(1)	(1)	(2)	(1)	
<u>Oxide wt %</u>	<u>accuracy</u> ^a															
SiO ₂	(0.9)	64.7	65.0	65.1	64.8	64.6	64.7	64.1	63.7	65.0	64.5	65.1	64.1	64.5	64.6	64.1
Al ₂ O ₃	(0.3)	19.2	19.3	19.1	19.2	19.1	19.3	19.0	19.3	19.3	19.5	19.2	19.0	19.4	19.1	19.1
Fe ₂ O ₃ ^{tot}	(0.02)	0.20	0.19	0.21	0.21	0.12	0.18	0.08	0.16	0.19	0.13	0.13	0.10	0.13	0.22	0.14
MgO	(0.01)	0.00	0.00	0.00	0.00	0.00	0.01	0.00	0.00	0.00	0.00	0.00	0.01	0.01	0.00	0.00
CaO	(0.07)	0.43	0.45	0.37	0.43	0.52	0.60	0.24	0.53	0.51	0.47	0.42	0.19	0.38	0.56	0.28
Na ₂ O	(0.07)	4.32	4.69	4.03	4.32	3.32	3.74	2.45	2.80	4.02	3.95	4.69	2.43	3.04	3.65	2.03
K ₂ O	(0.1)	10.0	9.5	10.5	10.1	11.6	10.9	12.9	12.2	10.4	10.5	9.6	13.1	12.0	11.0	13.6
Total		98.88	99.16	99.36	99.02	99.27	99.45	98.83	98.79	99.47	99.05	99.20	98.96	99.47	99.20	99.24
<u>Cations on basis of 8 Oxygens</u>																
Si		2.97	2.97	2.97	2.96	2.97	2.96	2.97	2.95	2.96	2.95	2.97	2.97	2.96	2.96	2.96
Al		1.03	1.04	1.03	1.04	1.03	1.04	1.04	1.05	1.04	1.05	1.03	1.04	1.05	1.03	1.04
Fe ³⁺		0.01	0.01	0.01	0.01	0.00	0.01	0.00	0.01	0.01	0.00	0.00	0.00	0.00	0.01	0.00
Mg		0.00	0.00	0.00	0.00	0.00	0.00	0.00	0.00	0.00	0.00	0.00	0.00	0.00	0.00	0.00
Ca		0.02	0.02	0.02	0.02	0.03	0.03	0.01	0.03	0.02	0.02	0.02	0.01	0.02	0.03	0.01
Na		0.38	0.41	0.36	0.38	0.30	0.33	0.22	0.25	0.36	0.35	0.41	0.22	0.27	0.32	0.18
K		0.58	0.55	0.61	0.59	0.68	0.63	0.76	0.72	0.60	0.62	0.56	0.77	0.70	0.64	0.80
Z		4.01	4.01	4.01	4.01	4.00	4.01	4.01	4.01	4.01	4.01	4.01	4.01	4.01	4.00	4.01
X		1.00	1.00	0.99	0.990	1.00	1.00	1.00	1.00	0.99	0.99	1.00	1.00	0.99	1.00	1.00
<u>Mole %</u>																
An		2.2	2.3	1.8	2.1	2.5	3.0	1.2	2.6	2.5	2.3	2.1	1.0	1.9	2.8	1.4
Alb		38.8	41.9	36.1	38.7	29.6	33.3	22.1	25.1	36.1	35.4	41.6	21.8	27.2	32.5	18.2
Orth		59.0	55.8	62.1	59.2	67.9	63.7	76.7	72.3	61.4	62.3	56.3	77.2	70.9	64.7	80.4

^a Absolute accuracy approximated by comparing repeat analyses of standards to their published values.

Table A.4: Clinopyroxene compositions determined by electron microprobe analysis.

	Monzodiorites		Diorites			Syeno- gabbro	Gabbronorites			Coincident Xenos		
	<u>HM01a</u>	<u>HM06</u>	<u>HM02a</u>	<u>HM19</u>	<u>HM43</u>	<u>HM45</u>	<u>HM44</u>	<u>HM47</u>	<u>HM53</u>	<u>HM23</u>	<u>HM35</u>	
	ID:	px2	px9	px2	px1	px1	px2	px5	px4	px1	px4b	px1
# pts:	(3)	(3)	(3)	(3)	(2)	(3)	(3)	(3)	(3)	(3)	(3)	
<u>Oxide wt % accuracy^a</u>												
SiO ₂	(0.3)	51.5	52.1	52.1	52.0	51.6	51.1	51.9	51.3	51.3	51.1	49.0
TiO ₂	(0.01)	0.53	0.38	0.43	0.29	0.59	0.78	0.50	0.73	0.84	0.69	1.35
Al ₂ O ₃	(0.12)	1.41	1.16	1.28	0.91	1.32	2.15	1.94	2.32	2.58	1.95	4.41
FeO ^{tot}	(0.05)	8.88	8.43	7.58	9.18	9.96	7.45	6.49	7.79	5.47	7.29	8.34
MnO	(0.01)	0.47	0.31	0.35	0.45	0.41	0.39	0.24	0.22	0.14	0.23	0.18
MgO	(0.1)	14.7	15.2	15.3	14.8	13.6	14.7	15.8	15.6	16.1	14.9	14.5
CaO	(0.1)	21.1	20.9	21.6	20.6	21.0	21.8	21.7	20.9	22.0	22.2	20.7
Na ₂ O	(0.07)	0.58	0.55	0.53	0.61	0.55	0.56	0.43	0.41	0.46	0.48	0.45
K ₂ O	(0.01)	0.04	0.00	0.00	0.00	0.00	0.00	0.00	0.00	0.00	0.00	0.00
Cr ₂ O ₃	(0.03)	0.01	0.01	0.00	0.00	0.04	0.00	0.01	0.01	0.40	0.00	0.05
Total		99.55	99.38	99.52	99.08	99.26	99.17	99.35	99.47	99.66	99.16	99.35
<u>Cations on basis of 6 Oxygens</u>												
Si		1.94	1.96	1.95	1.97	1.95	1.92	1.94	1.92	1.90	1.92	1.85
Ti		0.02	0.01	0.01	0.01	0.02	0.02	0.01	0.02	0.02	0.02	0.04
Al		0.06	0.05	0.06	0.04	0.06	0.10	0.09	0.10	0.11	0.09	0.20
Fe ^{tot}		0.28	0.26	0.24	0.29	0.32	0.23	0.20	0.24	0.17	0.23	0.26
Mn		0.02	0.01	0.01	0.01	0.01	0.01	0.01	0.01	0.00	0.01	0.01
Mg		0.82	0.85	0.86	0.83	0.77	0.82	0.88	0.87	0.89	0.84	0.82
Ca		0.85	0.84	0.87	0.83	0.85	0.88	0.87	0.84	0.88	0.89	0.83
Na		0.04	0.04	0.04	0.04	0.04	0.04	0.03	0.03	0.03	0.03	0.03
K		0.00	0.00	0.00	0.00	0.00	0.00	0.00	0.00	0.00	0.00	0.00
Cr		0.00	0.00	0.00	0.00	0.00	0.00	0.00	0.00	0.01	0.00	0.00
Total		4.03	4.03	4.03	4.03	4.02	4.03	4.02	4.03	4.03	4.03	4.03
<u>Mole % (determined using the QUIIF projection)</u>												
En		48.0	47.9	49.0	46.9	42.4	48.1	50.1	50.2	52.7	48.8	51.5
Wo		41.5	41.7	42.5	41.6	43.3	43.3	42.3	40.3	42.0	43.2	38.3
Fs		10.5	10.4	8.5	11.5	14.3	8.6	7.6	9.5	5.3	8.0	10.2
<u>Atomic Mg #</u>												
100*Mg/ (Mg+Mn+Fe ^{tot})		73.6	75.6	77.5	73.2	70.0	76.9	80.7	77.6	83.7	77.9	75.3

^a Absolute accuracy approximated by comparing repeat analyses of standards to their published values.

Table A.5: Orthopyroxene compositions determined by electron microprobe analysis.

	<u>Monzodiorites</u>			<u>Diorites</u>		<u>Gabbronorites</u>				
	<u>HM01a</u>	<u>HM06</u>		<u>HM19</u>		<u>HM44</u>	<u>HM47</u>	<u>HM53</u>		
ID:	px6	px9	px4	px8	px10	opx1	opx4	opx4	opx1	
# pts:	(3)	(3)	(3)	(3)	(2)	(3)	(3)	(3)	(3)	
<u>Oxide wt %</u>	<u>accuracy</u> ^a									
SiO ₂	(0.3)	53.1	53.0	52.9	53.2	53.2	54.5	53.7	53.6	54.0
TiO ₂	(0.01)	0.18	0.17	0.21	0.18	0.21	0.19	0.32	0.33	0.55
Al ₂ O ₃	(0.12)	0.39	0.43	0.40	0.37	0.38	1.11	1.10	1.35	1.49
FeO ^{tot}	(0.1)	19.1	19.3	19.9	18.4	18.7	13.2	15.2	16.3	12.4
MnO	(0.01)	0.90	0.91	0.64	0.90	0.87	0.43	0.43	0.44	0.28
MgO	(0.1)	24.7	24.2	24.1	24.9	24.7	29.1	27.3	26.6	29.2
CaO	(0.08)	0.94	1.13	0.89	1.02	1.07	0.77	1.15	1.04	1.39
Na ₂ O	(0.07)	0.01	0.03	0.02	0.01	0.01	0.02	0.02	0.02	0.05
K ₂ O	(0.01)	0.00	0.00	0.00	0.01	0.00	0.00	0.00	0.01	0.00
Cr ₂ O ₃	(0.03)	0.00	0.00	0.01	0.01	0.01	0.01	0.00	0.01	0.20
Total		99.47	99.34	99.17	99.11	99.24	99.41	99.40	99.78	99.65
<u>Cations on basis of 6 Oxygens</u>										
Si		1.97	1.97	1.97	1.97	1.97	1.96	1.96	1.95	1.94
Ti		0.00	0.00	0.01	0.01	0.01	0.01	0.01	0.01	0.01
Al		0.02	0.02	0.02	0.02	0.02	0.05	0.05	0.06	0.06
Fe ^{tot}		0.59	0.60	0.62	0.57	0.58	0.40	0.46	0.50	0.37
Mn		0.03	0.03	0.02	0.03	0.03	0.01	0.01	0.01	0.01
Mg		1.37	1.34	1.34	1.38	1.36	1.56	1.48	1.44	1.56
Ca		0.04	0.05	0.04	0.04	0.04	0.03	0.04	0.04	0.05
Na		0.00	0.00	0.00	0.00	0.00	0.00	0.00	0.00	0.00
K		0.00	0.00	0.00	0.00	0.00	0.00	0.00	0.00	0.00
Cr		0.00	0.00	0.00	0.00	0.00	0.00	0.00	0.00	0.01
Total		4.02	4.02	4.01	4.01	4.01	4.01	4.01	4.01	4.02
<u>Mole % (determined using the QUIIF projection)</u>										
En		70.2	69.1	68.4	70.6	69.9	80.0	76.0	74.2	80.5
Wo		1.9	2.3	1.8	2.1	2.2	1.6	2.4	2.1	2.8
Fs		27.9	28.6	29.8	27.3	27.9	18.4	21.6	23.7	16.7
<u>Atomic Mg #</u>										
100*Mg/ (Mg+Mn+Fe ^{tot})		68.7	68.2	67.6	69.7	69.2	79.2	75.7	73.9	80.4

^a Absolute accuracy approximated by comparing repeat analyses of standards to their published values.

Table A.6: Olivine compositions determined by electron microprobe analysis.

	<u>Diorites</u>		<u>Syenogabbro</u>		<u>Gabbronorites</u>						
	HM12		HM45		HM44		HM47		HM53		
ID:	ol2	ol3	ol1	ol5	ol1	ol5	ol1	ol3	ol1	ol10	
# pts:	(2)	(3)	(3)	(3)	(3)	(3)	(3)	(3)	(3)	(3)	
<u>Oxide wt %</u>	<u>accuracy^a</u>										
SiO ₂	(0.3)	36.6	36.6	37.3	37.6	38.7	38.9	38.0	38.4	38.8	38.6
FeO ^{tot}	(0.1)	28.8	28.9	26.2	25.3	20.3	18.7	23.8	22.4	19.5	20.5
MnO	(0.01)	0.70	0.70	0.94	0.80	0.43	0.41	0.46	0.45	0.29	0.28
MgO	(0.2)	33.0	33.0	35.2	36.0	40.5	41.9	37.4	38.8	40.9	40.5
CaO	(0.01)	0.08	0.05	0.06	0.04	0.03	0.02	0.03	0.04	0.03	0.04
NiO	(0.02)	0.04	0.06	0.01	0.01	0.06	0.04	0.05	0.05	0.21	0.23
Total		99.22	99.36	99.77	99.88	99.92	99.94	99.83	100.19	99.81	100.13
<u>Cations on basis of 4 Oxygens</u>											
Si		0.99	0.99	1.00	1.00	1.00	1.00	1.00	1.00	1.00	1.00
Fe ^{tot}		0.66	0.66	0.59	0.56	0.44	0.40	0.52	0.49	0.42	0.44
Mn		0.02	0.02	0.02	0.02	0.01	0.01	0.01	0.01	0.01	0.01
Mg		1.34	1.34	1.40	1.42	1.56	1.60	1.47	1.50	1.57	1.55
Ca		0.00	0.00	0.00	0.00	0.00	0.00	0.00	0.00	0.00	0.00
Ni		0.00	0.00	0.00	0.00	0.00	0.00	0.00	0.00	0.00	0.00
M1+M2		2.01	2.01	2.01	2.01	2.01	2.01	2.00	2.01	2.00	2.01
Total		3.01	3.01	3.00	3.00	3.00	3.00	3.00	3.00	3.00	3.01
<u>Mole % Fo</u>											
100*Mg/ (Mg+Mn+Fe ^{tot})		66.6	66.5	69.8	71.1	77.7	79.6	73.3	75.1	78.6	77.6

^a Absolute accuracy approximated by comparing repeat analyses of standards to their published values.

Table A.7: Titano-magnetite compositions determined by electron microprobe analysis.

	Monzodiorites		Diorites			Syeno- gabbro	Gabbro- norites		Coincident Xenos		
	HM01a	HM06	HM02a	HM12	HM43	HM45	HM44	HM53	HM23	HM35	
	ID: # pts:	ox1b (2)	ox2b (3)	ox10 (2)	ox2b (2)	ox1b (3)	mag5 (1)	ox3b (2)	c8 (3)	ox1b (3)	ox2 (2)
<u>Oxide wt %</u>	<u>accuracy</u> ^a										
TiO ₂	(0.10)	8.52	4.41	4.18	8.48	9.11	6.95	5.13	6.22	4.11	12.81
Al ₂ O ₃	(0.03)	1.32	1.00	1.09	2.94	1.95	2.91	3.10	7.01	1.61	6.64
Cr ₂ O ₃	(0.04)	0.00	0.05	0.43	0.04	0.03	0.05	0.31	17.6	0.07	0.15
FeO ^{tot}	(0.3)	82.8	87.1	87.2	81.3	82.3	83.7	82.8	60.8	86.0	69.9
MnO	(0.02)	0.48	0.28	0.38	0.44	0.60	0.59	0.34	0.28	0.30	0.32
MgO	(0.03)	1.60	1.06	1.05	1.78	0.97	1.47	2.61	4.36	1.46	6.14
Total		94.75	93.90	94.32	94.94	95.01	95.70	94.34	96.28	93.57	95.95
Recalculated (Carmichael, 1967)											
FeO		36.2	33.4	33.2	36.2	37.7	35.5	32.0	31.2	32.5	34.3
Fe ₂ O ₃		51.8	59.7	60.0	50.0	49.6	53.6	56.5	32.9	59.5	39.5
Total		99.94	99.89	100.33	99.96	99.98	101.08	100.01	99.58	99.54	99.91
<u>Cations on basis of 4 Oxygens</u>											
Ti		0.24	0.13	0.12	0.24	0.26	0.19	0.14	0.17	0.12	0.34
Al VI		0.06	0.04	0.05	0.13	0.09	0.13	0.14	0.29	0.07	0.27
Cr		0.00	0.00	0.01	0.00	0.00	0.00	0.01	0.50	0.00	0.00
Fe ³⁺		1.46	1.70	1.70	1.40	1.40	1.49	1.57	0.88	1.69	1.04
Fe ²⁺		1.14	1.06	1.05	1.12	1.18	1.09	0.99	0.93	1.03	1.01
Mn		0.02	0.01	0.01	0.01	0.02	0.02	0.01	0.01	0.01	0.01
Mg		0.09	0.06	0.06	0.10	0.05	0.08	0.14	0.23	0.08	0.32
Sum Cat#		3.00	3.00	3.00	3.00	3.00	3.00	3.00	3.00	3.00	3.00
<u>Mole %</u>											
XTiO ₂		8.5	4.4	4.1	8.6	9.1	6.9	5.3	8.4	4.1	14.2
XFe ₂ O ₃		51.5	59.0	59.3	50.7	49.3	53.6	58.1	44.6	59.7	43.7
XFeO		40.0	36.6	36.5	40.8	41.7	39.4	36.6	47.0	36.2	42.1
<u>Calculated (Stormer, 1983)</u>											
% Usp		23.9	12.5	11.9	25.2	26.9	20.5	14.6	36.3	11.7	38.2
<u>Atomic Mg #</u>											
100*Mg/ (Mg+Mn+Fe ²⁺)		7.2	5.4	5.2	8.0	4.3	6.8	12.6	19.8	7.4	24.0
<u>Atomic Cr #</u>											
100*Cr/(Cr+Al)		0.0	3.6	21.3	0.8	1.1	0.8	6.3	62.8	2.7	1.4

^a Absolute accuracy approximated by comparing repeat analyses of standards to their published values.

Table A.8: Hemo-ilmenite compositions determined by electron microprobe analysis.

	Monzodiorites		Diorites			Syeno-	Gabbronorites			Coincident	
						gabbro				Xenos	
	<u>HM01a</u>	<u>HM06</u>	<u>HM12</u>	<u>HM19</u>	<u>HM43</u>	<u>HM45</u>	<u>HM44</u>	<u>HM50a</u>	<u>HM53</u>	<u>HM23</u>	
ID:	ox5a	ox2a	ox3a	ox6a	ox2a	ilm1	ox1a	ilm2	ti8	ox2a	
# pts:	(3)	(3)	(2)	(3)	(3)	(3)	(3)	(2)	(3)	(2)	
<u>Oxide wt % accuracy^a</u>											
TiO ₂	(0.3)	42.4	36.8	48.3	35.9	47.6	47.4	44.7	42.5	50.2	43.1
Al ₂ O ₃	(0.05)	0.13	0.13	0.14	0.14	0.11	0.14	0.25	0.20	0.25	0.16
Cr ₂ O ₃	(0.01)	0.00	0.01	0.01	0.01	0.00	0.00	0.05	0.10	0.73	0.05
FeO ^{tot}	(0.5)	51.7	56.8	46.0	58.1	47.5	46.6	47.0	51.2	40.7	49.7
MnO	(0.05)	0.78	0.38	0.82	0.42	1.13	1.23	0.52	0.53	0.41	0.49
MgO	(0.02)	2.65	1.91	3.56	1.80	2.34	3.51	5.23	3.15	6.58	3.74
Total		97.60	95.97	98.87	96.38	98.72	98.82	97.76	97.67	98.88	97.23
<u>Recalculated (Carmichael, 1967)</u>											
FeO		32.6	29.3	36.3	28.6	37.5	35.1	30.3	32.1	33.0	31.6
Fe ₂ O ₃		21.2	30.5	10.8	32.8	11.2	12.7	18.5	21.3	8.6	20.1
Total		99.73	99.03	99.97	99.67	99.84	100.09	99.62	99.80	99.75	99.25
<u>Cations on basis of 3 Oxygens</u>											
Ti		0.80	0.71	0.90	0.68	0.89	0.88	0.83	0.80	0.91	0.81
Al VI		0.00	0.00	0.00	0.00	0.00	0.00	0.01	0.01	0.01	0.01
Cr		0.00	0.00	0.00	0.00	0.00	0.00	0.00	0.00	0.01	0.00
Fe ³⁺		0.40	0.59	0.20	0.63	0.21	0.24	0.34	0.40	0.16	0.38
Fe ²⁺		0.68	0.62	0.75	0.61	0.78	0.73	0.62	0.67	0.67	0.66
Mn		0.02	0.01	0.02	0.01	0.02	0.03	0.01	0.01	0.01	0.01
Mg		0.10	0.07	0.13	0.07	0.09	0.13	0.19	0.12	0.24	0.14
Sum Cat#		2.00	2.00	2.00	2.00	2.00	2.00	2.00	2.00	2.00	2.00
<u>Mole %</u>											
XTiO ₂		42.5	36.8	48.6	35.7	47.4	47.8	46.1	42.7	52.5	43.9
XFe ₂ O ₃		21.2	30.6	10.9	32.6	11.1	12.8	19.1	21.4	9.1	20.4
XFeO		36.3	32.6	40.5	31.7	41.5	39.4	34.8	35.9	38.4	35.7
<u>Calculated (Stormer, 1983)</u>											
% Ilm		78.7	69.4	89.1	67.3	88.9	87.1	80.7	78.6	90.9	79.5
<u>Atomic Mg #</u>											
100*Mg/ (Mg+Mn+Fe ²⁺)		12.4	10.3	14.6	9.9	9.7	14.7	23.2	14.7	26.0	17.2
<u>Atomic Cr #</u>											
100*Cr/(Cr+Al)		0.0	7.7	0.0	0.0	0.0	0.0	12.0	25.0	66.7	16.7

^a Absolute accuracy approximated by comparing repeat analyses of standards to their published values.

Table A.9: Phlogopite compositions determined by electron microprobe analysis.

	<u>Monzodiorites</u>		<u>Diorites</u>				<u>Syenogabbro</u>	
	<u>HM01</u>	<u>HM06</u>	<u>HM02a</u>	<u>HM12</u>	<u>HM19</u>	<u>HM43</u>	<u>HM45</u>	
	ID: Bt1	Bt6	Bt2	Bt1	Bt1	Bt1	Bt3	
# pts:	(3)	(3)	(2)	(3)	(2)	(3)	(2)	
<u>Oxide wt %</u>	<u>accuracy</u>							
SiO ₂	(0.6)	37.8	38.6	38.6	37.0	40.15	37.3	36.7
TiO ₂	(0.04)	6.04	5.02	5.42	8.04	4.27	6.60	7.56
Al ₂ O ₃	(0.2)	13.5	12.8	13.2	14.1	12.27	13.1	14.2
Cr ₂ O ₃	n.d.	0.01	0.01	0.04	0.01	0.01	0.00	0.01
FeO ^{tot}	(0.1)	12.5	12.3	11.6	12.4	9.71	15.1	13.1
MnO	(0.01)	0.09	0.06	0.08	0.08	0.10	0.14	0.12
MgO	(0.1)	15.9	16.8	17.0	14.6	19.31	14.0	14.6
CaO	(0.11)	0.03	0.03	0.01	0.01	0.03	0.00	0.01
Na ₂ O	(0.06)	0.34	0.29	0.26	0.22	0.30	0.36	0.34
K ₂ O	(0.10)	8.95	9.00	9.18	9.26	9.17	9.06	9.28
F	(0.13)	0.89	1.50	1.97	0.85	3.10	1.20	0.76
Cl	n.d.	0.34	0.34	0.28	0.29	0.27	0.25	0.23
H ₂ O (calc.)		3.54	3.26	3.08	3.59	2.60	3.39	3.65
O=F		0.37	0.63	0.83	0.36	1.31	0.51	0.32
O=Cl		0.08	0.07	0.07	0.07	0.06	0.06	0.05
Total		99.45	99.25	99.80	99.97	99.93	100.01	100.24
<u>Cations on basis of 3 Oxygens</u>								
Si		5.58	5.71	5.66	5.45	5.83	5.56	5.42
Ti		0.67	0.56	0.60	0.89	0.47	0.74	0.84
Al (IV)		2.35	2.24	2.29	2.44	2.10	2.31	2.47
Al (VI)		0.00	0.00	0.00	0.00	0.00	0.00	0.00
Cr		0.00	0.00	0.00	0.00	0.00	0.00	0.00
Fe ^{tot}		1.55	1.52	1.43	1.53	1.18	1.88	1.62
Mn		0.01	0.01	0.01	0.01	0.01	0.02	0.02
Mg		3.50	3.69	3.71	3.21	4.18	3.12	3.22
Ca		0.00	0.01	0.00	0.00	0.00	0.00	0.00
Na		0.10	0.08	0.07	0.06	0.08	0.11	0.10
K		1.69	1.70	1.72	1.74	1.70	1.72	1.75
F		0.42	0.70	0.92	0.40	1.42	0.57	0.35
Cl		0.08	0.09	0.07	0.07	0.07	0.06	0.06
OH		3.50	3.21	3.02	3.53	2.51	3.37	3.59
Sum Cat#		19.46	19.51	19.49	19.34	19.55	19.46	19.43
X = Int		1.79	1.79	1.79	1.81	1.79	1.83	1.85
Y = Oct		5.74	5.78	5.75	5.64	5.84	5.76	5.70
Z = Tet		7.94	7.94	7.95	7.89	7.93	7.87	7.89
<u>Atomic Mg #</u>								
Mg/(Mg+Mn+Fe*)		69.1	70.8	72.1	67.5	77.8	62.1	66.3

^a Absolute accuracy approximated by comparing repeat analyses of standards to their published values.

Table A.10: Amphibole compositions determined by electron microprobe analysis.

	Diorites		Syenogabbro	Gabbronorites			Coincident Xenos		
	<u>HM43</u>		<u>HM45</u>	<u>HM44</u>	<u>HM47</u>	<u>HM50a</u>	<u>HM50b</u>		
	Amphibole name ^a :	parg kaer	kaer	parg mghst	parg mghst	parg mghst	mghst mghst	mghst mghst	
ID:	amph1 amph4	amph1	amph4 amphA	amph1	amph2	amph1 amph4	amph1 amph4		
# pts:	(4) (3)	(3)	(3)	(3) (1)	(3)	(3)	(3) (2)		
<u>Oxide wt %</u>	<u>accuracy ^b</u>								
SiO ₂	(0.6)	41.7 41.2	40.3	40.2 41.5	41.1	42.3	42.5 42.2		
TiO ₂	(0.04)	4.37 4.75	5.28	4.31 3.53	4.06	3.60	2.09 2.14		
Al ₂ O ₃	(0.2)	10.5 10.7	12.1	12.2 11.2	11.5	11.0	11.8 11.7		
FeO ^{tot}	(0.1)	14.2 13.8	12.5	12.1 12.3	11.9	11.5	11.1 11.2		
MnO	(0.01)	0.26 0.18	0.18	0.11 0.13	0.12	0.16	0.13 0.13		
MgO	(0.1)	11.7 11.7	12.0	12.6 13.2	13.0	13.9	14.7 14.3		
CaO	(0.1)	11.0 11.2	11.6	11.6 11.6	11.6	11.6	11.6 11.6		
Na ₂ O	(0.06)	2.48 2.57	2.49	2.17 2.39	2.11	2.08	2.06 2.08		
K ₂ O	n.d.	1.17 1.17	1.05	1.40 0.73	1.37	1.07	1.05 1.00		
Cl	n.d.	0.25 0.15	0.25	0.43 0.72	0.51	0.30	0.25 0.25		
Total		97.60 97.53	97.74	97.17 97.29	97.36	97.43	97.28 96.70		
<u>Ideal site assignments for 23 Oxygen basis (Leake et al., 1997)</u>									
<u>Tet = 8.00</u>									
Si		6.25 6.19	6.02	6.03 6.19	6.15	6.25	6.23 6.24		
Al (IV)		1.75 1.81	1.98	1.97 1.81	1.85	1.75	1.77 1.76		
<u>C = 5.00</u>									
Al (VI)		0.11 0.09	0.15	0.19 0.17	0.18	0.16	0.26 0.29		
Fe ³⁺		0.10 0.04	0.01	0.11 0.19	0.10	0.19	0.45 0.39		
Ti		0.49 0.54	0.59	0.49 0.40	0.46	0.40	0.23 0.24		
Mg		2.61 2.63	2.67	2.82 2.93	2.89	3.05	3.21 3.15		
Fe ²⁺		1.68 1.69	1.55	1.39 1.31	1.38	1.19	0.84 0.93		
Mn		0.00 0.01	0.02	0.00 0.00	0.00	0.00	0.00 0.00		
<u>B = 2.00</u>									
Mg		0.00 0.00	0.00	0.00 0.00	0.00	0.00	0.00 0.00		
Fe ²⁺		0.00 0.00	0.00	0.02 0.04	0.01	0.04	0.07 0.06		
Mn		0.03 0.01	0.00	0.01 0.02	0.02	0.02	0.02 0.02		
Ca		1.77 1.80	1.86	1.87 1.86	1.86	1.84	1.82 1.83		
Na		0.20 0.18	0.14	0.10 0.09	0.11	0.10	0.09 0.09		
<u>A < 1.00</u>									
Na		0.52 0.57	0.58	0.53 0.60	0.50	0.50	0.49 0.51		
K		0.22 0.22	0.20	0.27 0.14	0.26	0.20	0.20 0.19		
total		15.75 15.79	15.78	15.79 15.74	15.77	15.70	15.69 15.69		
<u>(OH, F, Cl)</u>									
Cl		0.06 0.04	0.06	0.11 0.18	0.13	0.08	0.06 0.06		
<u>Atomic Mg #</u>									
100*Mg/(Mg+Mn+Fe ²⁺)		60.3 60.4	62.9	66.5 68.3	67.3	71.0	77.6 75.7		

^a kaer = kaersutite; mghst = magnesiohastingsite; parg = pargasite. ^b Absolute accuracy approximated by comparing repeat analyses of standards to their published values.

Table A.11: Glass compositions from xenolith HM35 determined by electron microprobe analysis.

		<u>Vesicular Glass Pockets</u>							<u>Glass Inclusions in Plagioclase</u>					
ID:		gl1	gl3	gl4	gl5	gl6	gl7	Avg	2 σ	gl1	gl2	gl4	Avg	2 σ
# pts:		(3)	(2)	(3)	(3)	(2)	(3)	(n=7)		(2)	(2)	(2)	(n=4)	
<u>Oxide wt %</u>	<u>accuracy</u> ^a													
SiO ₂	(0.3)	48.3	47.3	48.7	49.2	49.0	48.3	48.4	(1.3)	49.2	49.5	49.2	49.3	(0.4)
TiO ₂	(0.15)	2.91	3.12	2.89	2.79	2.91	2.54	2.87	(0.3)	2.22	2.29	2.49	2.32	(0.2)
Al ₂ O ₃	(0.1)	14.3	13.9	14.5	14.6	14.4	15.7	14.5	(1.1)	15.7	15.8	15.7	15.7	(0.2)
FeO ^{tot}	(0.2)	13.1	13.2	12.4	12.0	12.8	12.0	12.7	(1.1)	12.7	13.0	13.2	12.9	(0.4)
MnO	(0.03)	0.20	0.19	0.19	0.21	0.20	0.18	0.19	(0.03)	0.22	0.16	0.25	0.20	(0.1)
MgO	(0.19)	5.67	5.90	5.48	5.49	5.53	6.13	5.71	(0.5)	4.97	5.10	4.89	5.02	(0.2)
CaO	(0.15)	11.0	11.2	11.0	10.7	10.9	11.5	11.1	(0.5)	8.59	8.44	9.36	8.80	(0.8)
Na ₂ O	(0.10)	3.23	3.10	3.37	3.28	3.26	2.85	3.18	(0.3)	3.94	3.48	3.62	3.66	(0.4)
K ₂ O	(0.05)	0.97	0.96	0.98	1.02	0.98	0.88	0.96	(0.1)	1.59	1.59	1.25	1.50	(0.3)
P ₂ O ₅	(0.07)	0.38	0.46	0.35	0.37	0.38	0.27	0.37	(0.1)	0.24	0.22	0.25	0.24	(0.03)
Total		100.07	99.30	99.81	99.82	100.32	100.30	99.98	(0.7)	99.29	99.55	100.16	99.61	(0.8)
Total Alkalis		4.20	4.05	4.35	4.30	4.24	3.73	4.14	(0.4)	5.52	5.07	4.87	5.16	(0.6)
<u>Atomic Mg #</u>														
100*Mg/ (Mg+Mn+Fe ²⁺)		45.7	46.5	46.2	46.9	45.6	49.8	46.8	(3.1)	43.2	43.5	41.8	42.8	(1.8)

^a Absolute accuracy approximated by comparing repeat analyses of standards to their published values.

APPENDIX B: MASS BALANCE CALCULATIONS

Table B.1: Mass balance calculations (diorite derivative from a transitional parent)

	<u>Derivative:</u>	<u>Parent:</u>			<u>Modes:</u>	
	Diorite	Transitional Basalt			Phase	wt %
		<u>observed</u>	<u>calculated</u>	<u>difference</u>		
SiO ₂	53.59	48.48	48.34	-0.14	Cpx	28.0
TiO ₂	2.43	2.65	2.56	-0.09	Plag	25.5
Al ₂ O ₃	16.72	14.36	14.29	-0.06	Mag	4.4
FeO ^{tot}	8.84	11.49	11.40	-0.09	Oliv	3.9
MnO	0.14	0.25	0.26	0.01	Ilm	2.8
MgO	3.73	7.13	7.10	-0.03	Alk-Fs	0.9
CaO	6.90	12.20	12.20	0.00		
Na ₂ O	4.96	2.59	2.76	0.17	Diorite Liquid	34.5
K ₂ O	1.46	0.58	0.69	0.11		
P ₂ O ₅	1.23	0.28	0.42	0.15		

r.m.s. error = 0.10

Phases:

	<u>Cpx</u>	<u>Plag</u>	<u>Mag</u>	<u>Oliv</u>	<u>Ilm</u>	<u>Alk-Fs</u>
SiO ₂	53.09	50.80	0.00	37.61	0.00	64.71
TiO ₂	0.15	0.00	7.28	0.00	47.77	0.00
Al ₂ O ₃	0.71	31.46	2.89	0.00	0.15	19.55
FeO ^{tot}	7.36	0.29	87.57	25.56	47.50	0.15
MnO	0.41	0.00	0.69	0.84	1.20	0.01
MgO	15.15	0.01	1.58	35.94	3.38	0.00
CaO	22.73	13.61	0.00	0.05	0.00	0.43
Na ₂ O	0.39	3.57	0.00	0.00	0.00	3.07
K ₂ O	0.01	0.26	0.00	0.00	0.00	12.07
P ₂ O ₅	0.00	0.00	0.00	0.00	0.00	0.00

Table B.2: Mass balance calculations (diorite derivative from an alkalic parent)

	<u>Derivative:</u>	<u>Parent:</u>			<u>Modes:</u>	
	Diorite		Alkalic Basalt		Phase	wt %
		<u>observed</u>	<u>calculated</u>	<u>difference</u>		
SiO ₂	53.59	47.17	47.18	0.00	Plag	47.9
TiO ₂	2.43	2.59	2.58	-0.01	Cpx	22.9
Al ₂ O ₃	16.72	15.57	15.57	0.00	Oliv	9.7
FeO ^{tot}	8.84	12.11	12.10	0.00	Mag	6.3
MnO	0.14	0.17	0.28	0.11	Alk-Fs	6.0
MgO	3.73	7.30	7.29	-0.01	Ilm	4.3
CaO	6.90	10.74	10.73	-0.01	Ap	0.6
Na ₂ O	4.96	3.07	3.02	-0.05		
K ₂ O	1.46	0.98	0.95	-0.03	Diorite Liquid	2.2
P ₂ O ₅	1.23	0.29	0.30	0.01		

r.m.s. error = 0.04

Phases:

	<u>Plag</u>	<u>Cpx</u>	<u>Oliv</u>	<u>Mag</u>	<u>Alk-Fs</u>	<u>Ilm</u>	<u>Ap</u>
SiO ₂	54.84	53.09	37.61	0.00	64.71	0.00	0.24
TiO ₂	0.00	0.15	0.00	7.28	0.00	47.77	0.00
Al ₂ O ₃	28.54	0.71	0.00	2.89	19.55	0.15	0.00
FeO ^{tot}	0.33	7.36	25.56	87.57	0.15	47.50	0.27
MnO	0.00	0.41	0.84	0.69	0.01	1.20	0.16
MgO	0.00	15.15	35.94	1.58	0.00	3.38	0.00
CaO	10.39	22.73	0.05	0.00	0.43	0.00	55.83
Na ₂ O	5.50	0.39	0.00	0.00	3.07	0.00	0.13
K ₂ O	0.40	0.01	0.00	0.00	12.07	0.00	0.00
P ₂ O ₅	0.00	0.00	0.00	0.00	0.00	0.00	43.38

Table B.3: Mass balance calculations (diorite derivative from a tholeiitic parent)

	<u>Derivative:</u>	<u>Parent:</u>			<u>Modes:</u>	
	Diorite	Tholeiitic Basalt			Phase	wt %
		<u>observed</u>	<u>calculated</u>	<u>difference</u>		
SiO ₂	53.59	52.00	51.35	-0.65	Cpx	21.7
TiO ₂	2.43	2.37	1.96	-0.41	Plag	18.7
Al ₂ O ₃	16.72	14.23	14.07	-0.16	Opx	9.1
FeO ^{tot}	8.84	10.24	9.85	-0.39	Mag	2.0
MnO	0.14	0.19	0.27	0.08	Ilm	1.4
MgO	3.73	7.13	7.34	0.21	Alk-Fs	1.2
CaO	6.90	10.90	10.75	-0.15		
Na ₂ O	4.96	2.33	3.07	0.74	Diorite Liquid	46.0
K ₂ O	1.46	0.40	0.87	0.47		
P ₂ O ₅	1.23	0.22	0.56	0.34		

r.m.s. error = 0.41

Phases:

	<u>Cpx</u>	<u>Plag</u>	<u>Opx</u>	<u>Mag</u>	<u>Ilm</u>	<u>Alk-Fs</u>
SiO ₂	53.09	50.80	53.52	0.00	0.00	64.71
TiO ₂	0.15	0.00	0.18	7.28	47.77	0.00
Al ₂ O ₃	0.71	31.46	0.40	2.89	0.15	19.55
FeO ^{tot}	7.36	0.29	19.36	87.57	47.50	0.15
MnO	0.41	0.00	0.90	0.69	1.20	0.01
MgO	15.15	0.01	24.67	1.58	3.38	0.00
CaO	22.73	13.61	0.96	0.00	0.00	0.43
Na ₂ O	0.39	3.57	0.01	0.00	0.00	3.07
K ₂ O	0.01	0.26	0.00	0.00	0.00	12.07
P ₂ O ₅	0.00	0.00	0.00	0.00	0.00	0.00

Table B.4: Mass balance calculations (trachyte derivative from a diorite parent)

	<u>Derivative:</u>	<u>Parent:</u>			<u>Modes:</u>	
	Trachyte	<u>observed</u>	<u>Diorite</u> <u>calculated</u>	<u>difference</u>	Phase	wt %
SiO ₂	63.80	53.59	53.41	-0.18	Plag	52.9
TiO ₂	0.55	2.43	2.33	-0.10	Cpx	9.5
Al ₂ O ₃	17.87	16.72	16.69	-0.04	Opx	9.5
FeO ^{tot}	3.55	8.84	8.74	-0.10	Ilm	4.4
MnO	0.31	0.14	0.21	0.07	Mag	3.1
MgO	0.52	3.73	3.83	0.10	Ap	2.3
CaO	0.87	6.90	6.88	-0.02	Alk-Fs	1.1
Na ₂ O	7.44	4.96	5.28	0.32		
K ₂ O	4.97	1.46	1.64	0.18	Trachyte	
P ₂ O ₅	0.13	1.23	1.03	-0.20	Liquid	17.2

r.m.s. error = 0.16

Phases:

	<u>Plag</u>	<u>Cpx</u>	<u>Opx</u>	<u>Ilm</u>	<u>Mag</u>	<u>Ap</u>	<u>Alk-Fs</u>
SiO ₂	59.99	51.98	52.98	0.00	0.00	0.24	64.52
TiO ₂	0.00	0.63	0.25	43.28	8.05	0.00	0.00
Al ₂ O ₃	24.88	1.37	0.48	0.15	1.39	0.00	19.59
FeO ^{tot}	0.25	10.15	20.57	53.07	88.56	0.27	0.16
MnO	0.00	0.43	0.66	0.74	0.50	0.16	0.00
MgO	0.01	13.64	23.95	2.77	1.49	0.00	0.00
CaO	6.28	21.21	1.07	0.00	0.00	55.83	0.54
Na ₂ O	7.38	0.59	0.03	0.00	0.00	0.13	2.83
K ₂ O	1.21	0.00	0.00	0.00	0.00	0.00	12.36
P ₂ O ₅	0.00	0.00	0.00	0.00	0.00	43.38	0.00

APPENDIX C. GEOCHEMICAL DATA SOURCES

Appendix C.1: References including geochemical data on lavas from Hualālai Volcano.

Symbols indicate the following: † papers including data on Puu Waawaa trachyte member, * papers including whole rock major element data.

- Allegre, C. J., Staudacher, T., Sarda, P. & Kurz, M. D. (1983). Constraints on evolution of Earth's mantle from rare gas systematics. *Nature* **303** (5920), 762-766.
- * † Basaltic Volcanism Study Project (1981). *Basaltic volcanism on the terrestrial planets*. Pergamon Press: New York.
- Bennett, V. C., Esat, T. M. & Norman, M. D. (1996). Two mantle-plume components in Hawaiian picrites inferred from correlated Os-Pb isotopes. *Nature* **381** (6579), 221-224.
- Bennett, V. C., Norman, M. D. & Garcia, M. O. (2000). Rhenium and platinum group element abundances correlated with mantle source components in Hawaiian picrites: Sulphides in the plume. *Earth and Planetary Science Letters* **183** (3-4), 513-526.
- * Bohrsen, W. A. & Clague, D. A. (1988). Origin of ultramafic xenoliths containing exsolved pyroxenes from Hualalai Volcano, Hawaii. *Contributions to Mineralogy and Petrology* **100** (2), 139-155.
- Brandon, A. D., Norman, M. D., Walker, R. J. & Morgan, J. W. (1999). 186Os-187Os systematics of Hawaiian picrites. *Earth and Planetary Science Letters* **174** (1-2), 25-42.
- † Brooks, C. K. (1970). The concentrations of zirconium and hafnium in some igneous and metamorphic rocks and minerals. *Geochimica et Cosmochimica Acta* **34** (3), 411-416.
- † Clague, D. A. (1987). Hawaiian xenolith populations, magma supply rates and development of magma chambers. *Bulletin of Volcanology* **49** (4), 577-587.
- * † Clague, D. A. & Bohrsen, W. A. (1991). Origin of xenoliths in the trachyte at Puu Waawaa, Hualalai Volcano, Hawaii. *Contributions to Mineralogy and Petrology* **108**, 439-452.

- * Clague, D. A., Jackson, E. D. & Wright, T. L. (1980). Petrology of Hualalai Volcano, Hawaii: Implication for Mantle Composition. *Bulletin Volcanologique* **43** (4), 641-656.

- Clague, D. A. & Moore, J. G. (1991). Geology and petrology of Mahukona volcano, Hawaii. *Bulletin of Volcanology* **53** (3), 159-172.

- * † Cousens, B. L., Clague, D. A. & Sharp, W. D. (2003). Chronology, chemistry, and origin of trachytes from Hualalai Volcano, Hawaii. *Geochemistry Geophysics Geosystems* **4** (9), DOI:10.1029/2003GC000560.

- * † Cross, W. (1915). Lavas of Hawaii and their relations. *U.S. Geological Survey Professional Paper* **88**, pp. 1-97.

- † Funkhouser, J. G., Barnes, I. L. & Naughton, J. J. (1968). The determination of a series of ages of Hawaiian volcanoes by the potassium-argon method. *Pacific Science* **22**, 369-372.

- * Garcia, M. O., Muenow, D. W. & Aggrey, K. E. (1989). Major element, volatile, and stable isotope geochemistry of Hawaiian submarine tholeiitic glasses. *Journal of Geophysical Research* **94** (B8), 10,525-10,538.

- † Hamilton, E. I. (1965). Distribution of some trace elements and the isotopic composition of strontium in Hawaiian lavas. *Nature* **206**, 251-253.

- * Hammer, J. E., Coombs, M., Shamberger, P. J. & Kimura, J.-I. (2004). Submarine sliver in North Kona: A window into the early magmatic and growth history of Hualalai Volcano, Hawaii. *Journal of Volcanology and Geothermal Research* **in press**.

- * Helz, R. T. (1976). Phase relations of basalts in their melting ranges at PH₂O=5kb, pt. II. Melt compositions. *Journal of Petrology* **17** (2), 139-193.

- Iwasaki, B. & Katsura, T. (1964). The chlorine content of Hawaiian lavas. *Bulletin of the Chemical Society of Japan* **37**, 1827-1833.

- Jochum, K. P. & Hofmann, A. W. (1997). Constraints on Earth evolution from antimony in mantle-derived rocks. *Chemical Geology* **139** (1-4), 39-49.

- Jochum, K. P., Hofmann, A. W. & Seufert, H. M. (1993). Tin in mantle-derived rocks: constraints on Earth evolution. *Geochimica et Cosmochimica Acta* **57** (15), 3585-3595.

- Jochum, K. P., Stoll, B., Pfänder, J., Flanz, M., Maissenbacher, P., Hofmann, M. & Hofmann, A. W. (2001). Progress in multi-ion counting spark-source mass spectrometry (MIC-SSMS) for the analysis of geological samples. *Fresenius' Journal of Analytical Chemistry* **370** (5), 647-665.
- * Kauahikaua, J., Cashman, K. V., Clague, D. A., Champion, D. & Hagstrum, J. T. (2002). Emplacement of the most recent lava flows on Hualalai Volcano, Hawai'i. *Bulletin of Volcanology* **64** (3-4), 229-253.
- Kurz, M. D., Colodner, D., Trull, T. W., Moore, R. B. & O'Brien, K. (1990). Cosmic ray exposure dating with in situ produced cosmogenic ^3He : results from young Hawaiian lava flows. *Earth and Planetary Science Letters* **97** (1-2), 177-189.
- Kurz, M. D., Jenkins, W. J., Hart, S. R. & Clague, D. (1983). Helium isotopic variations in volcanic rocks from Loihi Seamount and the island of Hawaii. *Earth and Planetary Science Letters* **66**, 388-406.
- † Lessing, P. & Catanzaro, E. J. (1964). $\text{Sr}^{87}/\text{Sr}^{86}$ ratios in Hawaiian lavas. *Journal of Geophysical Research* **69** (8), 1599-1601.
- † Lessing, P., Decker, R. W. & Reynolds, R. C., Jr. (1963). Potassium and rubidium distribution in Hawaiian lavas. *Journal of Geophysical Research* **68** (20), 5851-5855.
- * Macdonald, G. A. (1968). Composition and origin of Hawaiian lavas. In: Hay, R. L. & Anderson, C. A. (eds.) *Studies in volcanology: a memoir in honour of Howel Williams*. *Geological Society of America Memoir* **116**, pp. 477-522.
- Masuda, Y., Yagi, S. & Asayama, T. (1974). Instrumental neutron activation analysis of 13 trace elements in volcanic rocks. *Bulletin of Osaka Prefecture University* **23**, 203-213.
- * Moore, J. G. & Clague, D. A. (1987). Coastal lava flows from Mauna Loa and Hualalai Volcanoes, Kona, Hawaii. *Bulletin of Volcanology* **49**, 752-764.
- * Moore, J. G. & Clague, D. A. (1992). Volcano growth and evolution of the island of Hawaii. *Geological Society of America Bulletin* **104** (11), 1471-1484.
- Moore, J. G. & Fabbi, B. P. (1971). An estimate of the juvenile sulfur content of basalt. *Contributions to Mineralogy and Petrology* **33**, 118-127.
- * † Moore, R. B., Clague, D. A., Rubin, M. & Bohron, W. A. (1987). Hualalai Volcano: A preliminary summary of geologic, petrologic, and geophysical data. In: Decker,

R. W., Wright, T. L. & Stauffer, P. H. (eds.) *Volcanism in Hawaii. U.S. Geological Survey Professional Paper* **1350**, pp. 571-585.

- Newman, S., Finkel, R. C. & Macdougall, J. D. (1984). Comparison of Th²³⁰-U²³⁸ disequilibrium systematics in lavas from three hot spot regions: Hawaii, Prince Edward and Samoa. *Geochimica et Cosmochimica Acta* **48** (2), 315-324.
- * Norman, M. D. & Garcia, M. O. (1999). Primitive magmas and source characteristics of the Hawaiian plume: Petrology and geochemistry of shield picrites. *Earth and Planetary Science Letters* **168** (1-2), 27-44.
- Norman, M. D., Garcia, M. O., Kamenetsky, V. S. & Nielsen, R. L. (2002). Olivine-hosted melt inclusions in Hawaiian picrites: Equilibration, melting, and plume source characteristics. *Chemical Geology* **183** (1-4), 143-168.
- † O'Nions, R. K., Hamilton, P. J. & Evensen, N. M. (1977). Variations in ¹⁴³Nd/¹⁴⁴Nd and ⁸⁷Sr/⁸⁶Sr ratios in oceanic basalts. *Earth and Planetary Science Letters* **34** (1), 13-22.
- † Park, K.-H. (1990). Sr, Nd and Pb isotope studies of ocean island basalts : constraints on their origin and evolution. Columbia University.
- Pickett, D. A. & Murrell, M. T. (1997). Observations of ²³¹Pa/²³⁵U disequilibrium in volcanic rocks. *Earth and Planetary Science Letters* **148** (1-2), 259-271.
- † Piggot, C. S. (1931). Radium in rocks: III. The radium content of Hawaiian lavas. *American Journal of Science* **22**, 1-8.
- Pineau, F. & Mathez, E. A. (1990). Carbon isotopes in xenoliths from the Hualalai Volcano, Hawaii, and the generation of isotopic variability. *Geochimica et Cosmochimica Acta* **54** (1), 217-227.
- † Powell, J. L., Faure, G. & Hurley, P. M. (1965). Strontium⁸⁷ abundance in a suite of Hawaiian volcanic rocks of varying silica content. *Journal of Geophysical Research* **70**, 1509-1513.
- Rison, W. & Craig, H. (1983). Helium isotopes and mantle volatiles in Loihi Seamount and Hawaiian Island basalts and xenoliths. *Earth and Planetary Science Letters* **66**, 407-426.
- * Roeder, P. L. & Emslie, R. F. (1970). Olivine-liquid equilibrium. *Contributions to Mineralogy and Petrology* **29**, 275-289.

- * Ross, C. S., Foster, M. & Myers, A. T. (1954). Origin of dunites and of olivine-rich inclusions in basaltic rocks. *American Mineralogist* **39** (9-10), 693-737.
- * Schilling, J.-G. & Winchester, J. W. (1969). Rare earth contribution to the origin of Hawaiian lavas. *Contributions to Mineralogy and Petrology* **23**, 27-37.
- Sims, K. W. W. & DePaolo, D. J. (1997). Inferences about mantle magma sources from incompatible element concentration ratios in oceanic basalts. *Geochimica et Cosmochimica Acta* **61** (4), 765-784.
- Sims, K. W. W., Depaolo, D. J., Murrell, M. T., Baldrige, W. S., Goldstein, S. J. & Clague, D. A. (1995). Mechanisms of magma generation beneath Hawaii and mid-ocean ridges: uranium/thorium and samarium/neodymium isotopic evidence. *Science* **267** (5197), 508-512.
- * Sims, K. W. W., DePaolo, D. J., Murrell, M. T., Baldrige, W. S., Goldstein, S., Clague, D. & Jull, M. (1999). Porosity of the melting zone and variations in the solid mantle upwelling rate beneath Hawaii: Inferences from ²³⁸U-²³⁰Th-²²⁶Ra and ²³⁵U-²³¹Pa disequilibria. *Geochimica et Cosmochimica Acta* **63** (23-24), 4119-4138.
- * Sobolev, A. V. & Nikogosian, I. K. (1994). Petrology of long-lived mantle plume magmatism: Hawaii, Pacific, and Reunion Island, Indian Ocean. *Petrology* **2** (2), 111-144.
- Staudacher, T., Kurz, M. D. & Allegre, C. J. (1986). New noble-gas data on glass samples from Loihi Seamount and Hualalai and on dunite samples from Loihi and Reunion Island. *Chemical Geology* **56** (3-4), 193-205.
- Stille, P., Unruh, D. M. & Tatsumoto, M. (1986). Pb, Sr, Nd and Hf isotopic constraints on the origin of Hawaiian basalts and evidence for a unique mantle source. *Geochimica et Cosmochimica Acta* **50** (10), 2303-2319.
- Stracke, A., Salters, V. J. M. & Sims, K. W. W. (1999). Assessing the presence of garnet-pyroxenite in the mantle sources of basalts through combined farnium-neodymium-thorium isotope systematics. *Geochemistry Geophysics Geosystems* **1**, (1999GC000013).
- † Tatsumoto, M. (1966). Isotopic composition of lead in volcanic rocks from Hawaii, Iwo Jima, and Japan. *Journal of Geophysical Research* **71** (6), 1721-1733.
- Tatsumoto, M. (1978). Isotopic composition of lead in oceanic basalt and its implication to mantle evolution. *Earth and Planetary Science Letters* **38** (1), 63-87.

- Valbracht, P. J., Staudigel, H., Honda, M., McDougall, I. & Davies, G. R. (1996). Isotopic tracing of volcanic source regions from Hawaii: decoupling of gaseous from lithophile magma components. *Earth and Planetary Science Letters* **144** (1-2), 185-198.
- * † Washington, H. S. (1923). Petrology of the Hawaiian Islands: II. Hualalai and Mauna Loa. *American Journal of Science* **6**, 100-126.
- * Wolfe, E. W. & Morris, J. (1996). *Sample data for the geologic map, island of Hawaii*. U.S. Geological Survey.
- * Yoder, H. S. & Tilley, C. E. (1962). Origin of basalt magmas: an experimental study of natural and synthetic rock systems. *Journal of Petrology* **3** (3), 342-532.

Appendix C.2: References including geochemical data on lavas of the * Hāwī series (Kohala Volcano), † Laupāhoehoe series (Mauna Kea Volcano), and § Honolua series (West Maui Volcano).

- * Basaltic Volcanism Study Project (1981). *Basaltic volcanism on the terrestrial planets*. Pergamon Press: New York.
- § Crocket, J. H. (2002). Platinum-group elements in basalts from Maui, Hawaii: Low abundances in alkali basalt. *Canadian Mineralogist* **40**, 595-609.
- * § Cross, W. (1915). Lavas of Hawaii and their relations. *U.S. Geological Survey Professional Paper* **88**, pp. 1-97.
- * Feigenson, M. D. & Spera, F. J. (1983). Case studies on the origin of basalt II. The transition from tholeiitic to alkalic volcanism on Kohala volcano, Hawaii. *Contributions to Mineralogy and Petrology* **84**, 390-405.
- † Frey, F. A., Wise, W. S., Garcia, M. O., West, H., Kwon, S. T. & Kennedy, A. (1990). Evolution and Mauna Kea Volcano, Hawaii: petrologic and geochemical constraints on postshield volcanism. *Journal of Geophysical Research* **95** (B2), 1271-1300.
- † Kennedy, A. K., Kwon, S. T., Frey, F. A. & West, H. B. (1991). The isotopic composition of postshield lavas from Mauna Kea Volcano, Hawaii. *Earth and Planetary Science Letters* **103**, 339-353.
- * Lanphere, M. A. & Frey, F. A. (1987). Geochemical evolution of Kohala volcano, Hawaii. *Contributions to Mineralogy and Petrology* **95**, 100-113.
- * † § Macdonald, G. A. (1968). Composition and origin of Hawaiian lavas. In: Hay, R. L. & Anderson, C. A. (eds.) *Studies in volcanology: a memoir in honour of Howel Williams*. *Geological Society of America Memoir* **116**, pp. 477-522.
- * Macdonald, G. A. & Katsura, T. (1962). Relationship of petrographic suites in Hawaii. In: Macdonald, G. A. & Kuno, H. (eds.) *Crust of the Pacific basin*. Washington, DC: American Geophysical Union, pp. 187-195.
- * † § Macdonald, G. A. & Katsura, T. (1964). Chemical Composition of Hawaiian Lavas. *Journal of Petrology* **5**, 82-133.
- * Muir, I. D. & Tilley, C. E. (1961). Mugearites and their place in alkali igneous rock series. *Journal of Geology* **69**, 186-203.

- § Sinton, J. M. Unpublished Data.
- * Spengler, S. R. & Garcia, M. O. (1988). Geochemistry of the Hawi lavas, Kohala volcano, Hawaii. *Contributions to Mineralogy and Petrology* **99** (1), 90-104.
- § Tagami, T., Nishimitsu, Y. & Sherrod, D. R. (2003). Rejuvenated-stage volcanism after 0.6-M.Y. quiescence at West Maui Volcano, Hawaii: New evidence from K-Ar ages and chemistry of Lahaina Volcanics. *Journal of Volcanology and Geothermal Research* **120**, 207-214.
- † Tatsumoto, M. (1966). Isotopic composition of lead in volcanic rocks from Hawaii, Iwo Jima, and Japan. *Journal of Geophysical Research* **71** (6), 1721-1733.
- § Velde, D. (1978). An aenigmatite-richterite-olivine trachyte from Puu Koaie, West Maui, Hawaii. *American Mineralogist* **63** (1978), 771-778.
- * § Washington, H. S. & Keyes, M. G. (1928). Petrology of the Hawaiian Islands: IV. Maui. *American Journal of Science* **15**, 199-220.
- † West, H. B., Garcia, M. O., Frey, F. A. & Kennedy, A. (1988). Nature and cause of compositional variation among the alkalic cap lavas of Mauna Kea Volcano, Hawaii. *Contributions to Mineralogy and Petrology* **100**, 383-397.
- * † Wolfe, E. W. & Morris, J. (1996). *Sample data for the geologic map, island of Hawaii*. U.S. Geological Survey.

Appendix C.3: References including experimental three-phase (olivine-clinopyroxene-plagioclase) saturated pseudo-cotectic glass data.

- Grove, T. L., Kinzler, R. J. & Bryan, W. B. (1992). Fractionation of Mid-Ocean Ridge Basalt (MORB). In: Morgan, J. P., Blackman, D. K. & Sinton, J. M. (eds.) *Mantle Flow and Melt Generation at Mid-Ocean Ridges*. Washington, DC: American Geophysical Union, pp. 281-310.
- Mahood, G. A. & Baker, D. R. (1986). Experimental constraints on depths of fractionation of mildly alkalic basalts and associated felsic rocks: Pantelleria, Strait of Sicily. *Contributions to Mineralogy and Petrology* **93** (2), 251-264.
- Nekvasil, H., Dondolini, A., Horn, J., Filiberto, J., Long, H. & Lindsley, D. H. (2004). The Origin and Evolution of Silica-saturated Alkalic Suites: an Experimental Study. *Journal of Petrology* **45** (4), 693-721.
- Sack, R. O., Walker, D. & Carmichael, I. S. E. (1987). Experimental petrology of alkalic lavas: constraints on cotectics of multiple saturation in natural basic liquids. *Contributions to Mineralogy and Petrology* **96** (1), 1-23.
- Thy, P. (1991). High and low pressure phase equilibria of a mildly alkalic lava from the 1965 Surtsey eruption: experimental results. *Lithos* **26** (3-4), 223-243.
- Thy, P. & Lofgren, G. E. (1992). Experimental constraints on the low-pressure evolution of transitional and mildly alkalic basalts: multisaturated liquids and coexisting augites. *Contributions to Mineralogy and Petrology* **112** (2-3), 196-202.
- Thy, P. & Lofgren, G. E. (1994). Experimental constraints on the low-pressure evolution of transitional and mildly alkalic basalts: the effect of Fe-Ti oxide minerals and the origin of basaltic andesites. *Contributions to Mineralogy and Petrology* **116** (3), 340-351.

REFERENCES

- Andersen, D. J. & Lindsley, D. H. (1985). New (and final!) models for the Ti-magnetite/ilmenite geothermometer and oxygen barometer (abstract). *EOS Transactions, American Geophysical Union* **66** (18), 416.
- Andersen, D. J., Lindsley, D. H. & Davidson, P. M. (1993). QUILF: a Pascal program to assess equilibria among Fe-Mg-Mn-Ti oxides, pyroxenes, olivine, and quartz. *Computers and Geosciences* **19** (9), 1333-1350.
- Bacon, C. R. & Hirschmann, M. M. (1988). Mg/Mn partitioning as a test for equilibrium between coexisting Fe-Ti oxides. *American Mineralogist* **73** (1-2), 57-61.
- Baloga, S., Spudis, P. D. & Guest, J. E. (1995). The dynamics of rapidly emplaced terrestrial lava flows and implications for planetary volcanism. *Journal of Geophysical Research* **100** (B12), 24,509-24,519.
- Barberi, F., Ferrara, G., Santacroce, R., Treuil, M. & Varet, J. (1975). A transitional basalt-pantellerite sequence of fractional crystallization, the Boina Centre (Afar Rift, Ethiopia). *Journal of Petrology* **16**, 22-56.
- Bard, J. P. (1986). *Microtextures of Igneous and Metamorphic Rocks*. D. Reidel Publishing Company: Dordrecht.
- Baxter, A. N. (1975). Petrology of the Older Series lavas from Mauritius, Indian Ocean. *Geological Society of America Bulletin* **86**, 1449-1458.
- Bedard, J. H., Francis, D. M., Hynes, A. J. & Madeau, S. (1984). Fractionation in the feeder system at a Proterozoic rifted margin. *Canadian Journal of Earth Sciences* **21** (4), 489-499.

- Bohrson, W. A. & Clague, D. A. (1988). Origin of ultramafic xenoliths containing exsolved pyroxenes from Hualalai Volcano, Hawaii. *Contributions to Mineralogy and Petrology* **100** (2), 139-155.
- Bonnefoi, C. C., Provost, A. & Albarède, F. (1995). The 'Daly gap' as a magmatic catastrophe. *Nature* **378** (6554), 270-272.
- Carmichael, I. S. E. (1967). The iron-titanium oxides of salic volcanic rocks and their associated ferromagnesian silicates. *Contributions to Mineralogy and Petrology* **14** (1), 36-64.
- Cervelli, P. F. & Miklius, A. (2003). The Shallow Magmatic System of Kilauea Volcano. In: Heliker, C. C., Swanson, D. A. & Takahashi, T. J. (eds.) *The Pu'u 'O'o-Kupainaha Eruption of Kilauea Volcano, Hawai'i: The First 20 Years*. U.S. Geological Survey Professional Paper **1676**, pp. 149-163.
- Chappell, B. W. (1991). Trace element analysis of rocks by X-ray spectrometry. *Advances in X-ray Analysis* **34**, 263-276.
- Chayes, F. (1963). Relative Abundance of Intermediate Members of the Oceanic Basalt-Trachyte Association. *Journal of Geophysical Research* **68** (5), 1519-1534.
- Chayes, F. (1977). The oceanic basalt-trachyte relation in general and in the Canary Islands. *American Mineralogist* **62**, 666-671.
- Chen-Hong, C., Presnall, D. C. & Stern, R. J. (1992). Petrogenesis of ultramafic xenoliths from the 1800 Kaupulehu flow, Hualalai volcano, Hawaii. *Journal of Petrology* **33** (1), 163-202.

- Clague, D. A. (1978). The oceanic basalt-trachyte association: an explanation of the daly gap. *Journal of Geology* **86**, 739-743.
- Clague, D. A. (1982). Petrology of tholeiitic basalt dredged from Hualalai Volcano, Hawaii. *EOS Transactions, American Geophysical Union* **63**, 1138.
- Clague, D. A. (1987a). Hawaiian alkaline volcanism. In: Fitton, J. G. & Upton, B. G. J. (eds.) *Alkaline Igneous Rocks*. Oxford: Blackwell, pp. 227-252.
- Clague, D. A. (1987b). Hawaiian xenolith populations, magma supply rates and development of magma chambers. *Bulletin of Volcanology* **49** (4), 577-587.
- Clague, D. A. & Bohrsen, W. A. (1991). Origin of xenoliths in the trachyte at Puu Waawaa, Hualalai Volcano, Hawaii. *Contributions to Mineralogy and Petrology* **108**, 439-452.
- Clague, D. A. & Dalrymple, G. B. (1987). The Hawaiian-Emperor volcanic chain. Part 1: Geologic evolution. In: Decker, R. W., Wright, T. L. & Stauffer, P. H. (eds.) *Volcanism in Hawaii. U.S. Geological Survey Professional Paper* **1350**, pp. 5-54.
- Clague, D. A., Jackson, E. D. & Wright, T. L. (1980). Petrology of Hualalai Volcano, Hawaii: Implication for Mantle Composition. *Bulletin Volcanologique* **43** (4), 641-656.
- Cousens, B. L., Clague, D. A. & Sharp, W. D. (2003). Chronology, chemistry, and origin of trachytes from Hualalai Volcano, Hawaii. *Geochemistry Geophysics Geosystems* **4** (9), DOI:10.1029/2003GC000560.
- Daly, R. A. (1925). The geology of Ascension Island. *Proceedings of the American Academy of Arts and Sciences* **60**, 1-180.

- Davis, M. G., Garcia, M. O. & Wallace, P. (2003). Volatiles in glasses from Mauna Loa Volcano, Hawai'i: Implications for magma degassing and contamination, and growth of Hawaiian volcanoes. *Contributions to Mineralogy and Petrology* **144** (5), 570-591.
- Day, S. J., Carracedo, J. C., Guillou, H. & Gravestock, P. (1999). Recent structural evolution of the Cumbre Vieja volcano, La Palma, Canary Islands: Volcanic rift zone reconfiguration as a precursor to volcano flank instability? *Journal of Volcanology and Geothermal Research* **94** (1-4), 135-167.
- Decker, R. W., Koyanagi, R. Y., Dvorak, J. J., Lockwood, J. P., Okamura, A. T., Yamashita, K. M. & Tanigawa, W. R. (1983). Seismicity and surface deformation of Mauna Loa volcano, Hawaii. *EOS Transactions, American Geophysical Union* **64**, 545-547.
- Dvorak, J. J. & Dzurisin, D. (1993). Variations in magma supply rate at Kilauea volcano, Hawaii. *Journal of Geophysical Research* **98** (B12), 22,255-22,268.
- Dzurisin, D., Koyanagi, R. Y. & English, T. T. (1984). Magma supply and storage at Kilauea volcano. *Journal of Volcanology and Geothermal Research* **21**, 177-206.
- Elkins, L. T. & Grove, T. L. (1990). Ternary feldspar experiments and thermodynamic models. *American Mineralogist* **75** (5-6), 544-559.
- Fleet, M. E., Bilcox, G. A. & Barnett, R. L. (1980). Oriented magnetite inclusions in pyroxenes from the grenville province. *Canadian Mineralogist* **18**, 89-99.

- Fodor, R. V. (2001). The role of tonalite and diorite in Mauna Kea volcano, Hawaii, magmatism: Petrology of summit-region leucocratic xenoliths. *Journal of Petrology* **42** (9), 1685-1704.
- Fodor, R. V. & Galar, P. (1997). A view into the subsurface of Mauna Kea volcano, Hawaii: crystallization processes interpreted through the petrology and petrography of gabbroic and ultramafic xenoliths. *Journal of Petrology* **38** (5), 581-624.
- Fodor, R. V. & Vandermeijden, H. J. (1988). Petrology of gabbroic xenoliths from Mauna Kea volcano, Hawaii. *Journal of Geophysical Research* **93** (B5), 4435-4452.
- Freundt, A. & Schmincke, H. U. (1995). Petrogenesis of rhyolite-trachyte-basalt composite ignimbrite P1, Gran Canaria, Canary Islands. *Journal of Geophysical Research* **100** (B1), 455-474.
- Freundt-Malecha, B., Schmincke, H.-U. & Freundt, A. (2001). Plutonic rocks of intermediate composition on Gran Canaria: the missing link of the bimodal volcanic rock suite. *Contributions to Mineralogy and Petrology* **141** (4), 430-445.
- Frey, F. A., Garcia, M. O., Wise, W. S., Kennedy, A., Gurriet, P. & Albarede, F. (1991). The evolution of Mauna Kea volcano, Hawaii: Petrogenesis of tholeiitic and alkalic basalts. *Journal of Geophysical Research* **96** (B9), 14,347-14,375.
- Frey, F. A., Wise, W. S., Garcia, M. O., West, H., Kwon, S. T. & Kennedy, A. (1990). Evolution and Mauna Kea Volcano, Hawaii: petrologic and geochemical

- constraints on postshield volcanism. *Journal of Geophysical Research* **95** (B2), 1271-1300.
- Frost, B. R. & Lindsley, D. H. (1992). Equilibria among Fe-Ti oxides, pyroxenes, olivine, and quartz: part II. Application. *American Mineralogist* **77** (9-10), 1004-1020.
- Fuhrman, M. L. & Lindsley, D. H. (1988). Ternary-feldspar modeling and thermometry. *American Mineralogist* **73** (3-4), 201-215.
- Fuhrman, T., Frey, F. A. & Park, K.-H. (1991). Chemical constraints on the petrogenesis of mildly alkalic lavas from Vestmannaeyjar, Iceland: The Eldfell (1973) and Surtsey (1963-1967) eruptions. *Contributions to Mineralogy and Petrology* **109**, 19-37.
- Garcia, M. O., Muenow, D. W. & Aggrey, K. E. (1989). Major element, volatile, and stable isotope geochemistry of Hawaiian submarine tholeiitic glasses. *Journal of Geophysical Research* **94** (B8), 10,525-10,538.
- Geist, D. J., Howard, K. A. & Larson, P. (1995). The generation of oceanic rhyolites by crystal fractionation - the basalt-rhyolite association at Volcan Alcedo, Galapagos Archipelago. *Journal of Petrology* **36** (4), 965-982.
- Ghiorso, M. S. & Sack, R. O. (1995). Chemical mass transfer in magmatic processes IV: A revised and internally consistent thermodynamic model for the interpolation and extrapolation of liquid-solid equilibria in magmatic systems at elevated temperatures and pressures. *Contributions to Mineralogy and Petrology* **119**, 197-212.

- Gittins, J. (1979). The Feldspathoidal Alkaline Rocks. In: Yoder, H. S. (ed.) *The Evolution of the Igneous Rocks: Fiftieth anniversary perspectives*. Princeton, NJ: Princeton University Press, pp. 351-390.
- Green, D. H. & Ringwood, A. E. (1967). The genesis of basaltic magmas. *Contributions to Mineralogy and Petrology* **15**, 103-190.
- Green, N. L. & Usdansky, S. I. (1986). Ternary-feldspar mixing relations and thermobarometry. *American Mineralogist* **71** (9-10), 1100-1108.
- Grove, T. L. & Donnelly-Nolan, J. M. (1986). The evolution of young silicic lavas at Medicine Lake Volcano, California: implications for the origin of compositional gaps in calc-alkaline series lavas. *Contributions to Mineralogy and Petrology* **92** (3), 281-302.
- Grove, T. L., Kinzler, R. J. & Bartels, K. S. (1989). Effects of pressure on alumina substitution in igneous augite: an empirical barometer. *EOS Transactions, American Geophysical Union* **70** (15), 1401-1402.
- Grove, T. L., Kinzler, R. J. & Bryan, W. B. (1992). Fractionation of Mid-Ocean Ridge Basalt (MORB). In: Morgan, J. P., Blackman, D. K. & Sinton, J. M. (eds.) *Mantle Flow and Melt Generation at Mid-Ocean Ridges*. Washington, DC: American Geophysical Union, pp. 281-310.
- Gudmundsson, A. (1986). Formation of crustal magma chambers in Iceland. *Geology* **14**, 164-166.

- Guest, J. E., Spudis, P. D., Greeley, R., Taylor, G. J. & Baloga, S. M. (1995). Emplacement of xenolith nodules in the Kaupulehu lava flow, Hualalai volcano, Hawaii. *Bulletin of Volcanology* **57** (3), 179-184.
- Hamilton, E. I. (1965). Distribution of some trace elements and the isotopic composition of strontium in Hawaiian lavas. *Nature* **206**, 251-253.
- Hammarstrom, J. M. & Zen, E.-a. (1986). Aluminum in hornblende: an empirical igneous geobarometer. *American Mineralogist* **71** (11-12), 1297-1313.
- Hammer, J. E., Coombs, M., Shamberger, P. J. & Kimura, J.-I. (2004). Submarine sliver in North Kona: A window into the early magmatic and growth history of Hualalai Volcano, Hawaii. *Journal of Volcanology and Geothermal Research* **in press**.
- Hammer, J. E. & Shamberger, P. J. (2003). Dynamic Sumarine Flanks of Hualalai Volcano, Hawaii. *EOS Transactions, American Geophysical Union* **84** (46), F1529.
- Hess, P. C. (1989). *Origins of Igneous Rocks*. Harvard University Press: Cambridge, MA.
- Huang, S. & Frey, F. A. (2003). Trace element abundances of Mauna Kea basalt from phase 2 of the Hawaii Scientific Drilling Project: Petrogenetic implications of correlations with major element content and isotopic ratios. *Geochemistry Geophysics Geosystems* **4** (6), DOI:10.1029/2002GC00322.
- Hurai, V., Simon, K., Wiechert, U., Hoefs, J., Konecny, P., Huraiova, M., Pironon, J. & Lipka, J. (1998). Immiscible separation of metalliferous Fe/Ti-oxide melts from fractionating alkali basalt: P-T-fO₂ conditions and two-liquid elemental partitioning. *Contributions to Mineralogy and Petrology* **133** (1-2), 12-29.

- Johnson, M. C. & Rutherford, M. J. (1989a). Experimental calibration of the aluminum-in-hornblende geobarometer with application to Long Valley caldera (California) volcanic rocks. *Geology* **17**, 837-841.
- Johnson, M. C. & Rutherford, M. J. (1989b). Experimentally determined conditions in the Fish Canyon Tuff, Colorado, magma chamber. *Journal of Petrology* **30** (3), 711-737.
- Kar, A., Weaver, B., Davidson, J. & Colucci, M. (1998). Origin of Differentiated Volcanic and Plutonic Rocks from ascension Island, South Atlantic Ocean. *Journal of Petrology* **39** (5), 1009-1024.
- Kauahikaua, J., Cashman, K. V., Clague, D. A., Champion, D. & Hagstrum, J. T. (2002). Emplacement of the most recent lava flows on Hualalai Volcano, Hawai'i. *Bulletin of Volcanology* **64** (3-4), 229-253.
- Kauahikaua, J., Hildenbrand, T. & Webring, M. (2000). Deep magmatic structures of Hawaiian volcanoes, imaged by three-dimensional gravity models. *Geology* **28** (10), 883-886.
- Keil, K., Fodor, R. V. & Bunch, T. E. (1972). Contributions to the mineral chemistry of Hawaiian rocks II. Feldspars and interstitial material in rocks from Haleakala and West Maui volcanoes, Maui, Hawaii. *Contributions to Mineralogy and Petrology* **37**, 237-276.
- Le Maitre, R. W., Streckeisen, A., *et al.* (2002). *Igneous Rocks: A Classification and Glossary of Terms*. Cambridge University Press: Cambridge.

- Leake, B. E., Woolley, A. R., *et al.* (1997). Nomenclature of amphiboles: Report of the subcommittee on amphiboles of the International Mineralogical Association, commission on new minerals and mineral names. *American Mineralogist* **82** (9-10), 1019-1037.
- Lee, J. M., Stern, R. J. & Bloomer, S. H. (1995). 40-Million years of magmatic evolution in the Mariana Arc - The tephra glass record. *Journal of Geophysical Research* **100** (B9), 17671-17687.
- Lindsley, D. H. (1983). Pyroxene thermometry. *American Mineralogist* **68** (5-6), 477-493.
- Lindsley, D. H. (1991). Experimental Studies of Oxide Minerals. In: Lindsley, D. H. (ed.) *Oxide Minerals: Petrologic and magnetic significance*: Mineralogical Society of America, pp. 69-106.
- Lindsley, D. H. & Frost, B. R. (1992). Equilibria among Fe-Ti oxides, pyroxenes, olivine, and quartz: part I. Theory. *American Mineralogist* **77** (9-10), 987-1003.
- Lindsley, D. H. & Nekvasil, H. (1989). A Ternary Feldspar Model for all Reasons. *EOS Transactions, American Geophysical Union* **70** (15), 506.
- Longhi, J. (1990). Silicate Liquid Immiscibility in Isothermal Crystallization Experiments. *Proceedings of the Lunar and Planetary Science Conference* **20**, 13-24.
- Macdonald, G. A. (1963). Relative Abundance of Intermediate Members of the Oceanic Basalt-Trachyte Association - A Discussion. *Journal of Geophysical Research* **68** (17), 5100-5102.

- Macdonald, G. A. (1968). Composition and origin of Hawaiian lavas. In: Hay, R. L. & Anderson, C. A. (eds.) *Studies in volcanology: a memoir in honour of Howel Williams. Geological Society of America Memoir* **116**, pp. 477-522.
- Macdonald, G. A., Abbott, A. T. & Peterson, F. L. (1983). *Volcanoes in the Sea*. University of Hawaii Press: Honolulu.
- Macdonald, G. A. & Katsura, T. (1962). Relationship of petrographic suites in Hawaii. In: Macdonald, G. A. & Kuno, H. (eds.) *Crust of the Pacific basin*. Washington, DC: American Geophysical Union, pp. 187-195.
- Macdonald, G. A. & Katsura, T. (1964). Chemical Composition of Hawaiian Lavas. *Journal of Petrology* **5**, 82-133.
- Mahood, G. A. & Baker, D. R. (1986). Experimental constraints on depths of fractionation of mildly alkalic basalts and associated felsic rocks: Pantelleria, Strait of Sicily. *Contributions to Mineralogy and Petrology* **93** (2), 251-264.
- Marsh, B. D. (1981). On the crystallinity, probability of occurrence, and rheology of lava and magma. *Contributions to Mineralogy & Petrology* **78** (1), 85-98.
- Marsh, B. D. (2000). Magma Chambers. In: Sigurdsson, H., Houghton, B., McNutt, S. R., Rymer, H. & Stix, J. (eds.) *Encyclopedia of Volcanoes*. San Diego: Academic Press, pp. 191-206.
- McBirney, A. R., Baker, B. H. & Nilson, R. H. (1985). Liquid fractionation. Part I: basic principles and experimental simulations. *Journal of Volcanology & Geothermal Research* **24** (1-2), 1-24.

- McMurtry, G. M., Smith, J. R., Resig, J., Sherman, C., Torresan, M. E., Herrero-Bervera, E. & Cremer, M. D. (1999). Stratigraphic constraints on the timing and emplacement of the Alika 2 giant Hawaiian submarine landslide. *Journal of Volcanology and Geothermal Research* **94** (1-4), 35-58.
- Mertzbacher, C. & Eggler, D. H. (1984). A magmatic geohygrometer: Application to Mount St. Helens and other dacitic magmas. *Geology* **12**, 587-590.
- Moore, J. G. & Clague, D. A. (1992). Volcano growth and evolution of the island of Hawaii. *Geological Society of America Bulletin* **104** (11), 1471-1484.
- Moore, R. B. (1990). Volcanic geology and eruption frequency, Sao Miguel, Azores. *Bulletin of Volcanology* **52**, 602-614.
- Moore, R. B. & Clague, D. (1991). Geologic Map of Hualalai Volcano, Hawaii. *U.S. Geological Survey Miscellaneous Investigations Series. Map I-2213*.
- Moore, R. B., Clague, D. A., Rubin, M. & Bohrsen, W. A. (1987). Hualalai Volcano: A preliminary summary of geologic, petrologic, and geophysical data. In: Decker, R. W., Wright, T. L. & Stauffer, P. H. (eds.) *Volcanism in Hawaii. U.S. Geological Survey Professional Paper* **1350**, pp. 571-585.
- Mushkin, A., Stein, M., Halicz, L. & Navon, O. (2002). The Daly gap: Low-pressure fractionation and heat-loss from a cooling magma chamber. *Goldschmidt conference Symposium S16*, A539.
- Nekvasil, H., Dondolini, A., Horn, J., Filiberto, J., Long, H. & Lindsley, D. H. (2004). The Origin and Evolution of Silica-saturated Alkalic Suites: an Experimental Study. *Journal of Petrology* **45** (4), 693-721.

- Neumann, E. R., Marti, J., Mitjavila, J., Wulff-Pedersen, E., Simonsen, S. L. & Pearson, N. J. (1999). Evidence for fractional crystallization of periodically refilled magma chambers in Tenerife, Canary Islands. *Journal of Petrology* **40** (7), 1089-1123.
- Nimis, P. (1999). Clinopyroxene geobarometry of magmatic rocks, Part 2: Structural geobarometers for basic to acid, tholeiitic and mildly alkaline magmatic systems. *Contributions to Mineralogy and Petrology* **135** (1), 62-74.
- Nimis, P. & Ulmer, P. (1998). Clinopyroxene geobarometry of magmatic rocks, Part 1: An expanded structural geobarometer for anhydrous and hydrous, basic and ultrabasic systems. *Contributions to Mineralogy and Petrology* **133** (1-2), 122-135.
- Noorish, K. & Hutton, J. T. (1969). An accurate X-ray spectrographic method for the analysis of a wide range of geological samples. *Geochimica et Cosmochimica Acta* **33**, 431-441.
- O'Hara, M. J. (1977). Geochemical evolution during fractional crystallization of a periodically refilled magma chamber. *Nature* **266**, 503-507.
- Park, K.-H. (1990). Sr, Nd and Pb isotope studies of ocean island basalts : constraints on their origin and evolution. Columbia University.
- Peccerillo, A., Barberio, M. R., Yirgu, G., Ayalew, D., Barbieri, M. & Wu, T. W. (2003). Relationships between mafic and peralkaline silicic magmatism in continental rift settings: A petrological, geochemical and isotopic study of the Gedemsa volcano, central Ethiopian rift. *Journal of Petrology* **44** (11), 2003-2032.

- Philpotts, A. R. (1982). Compositions of Immiscible Liquids in Volcanic Rocks. *Contributions to Mineralogy and Petrology* **80**, 201-218.
- Philpotts, A. R. (1990). *Principles of Igneous and Metamorphic Petrology*. Prentice Hall: Englewood Cliffs, NJ.
- Pouchou, J. L. & Pichoir, F. (1988). A simplified Version of the PAP Model for Matrix Corrections in EPMA. In: Newbury, D. E. (ed.) *Microbeam Analysis-1988*. San Francisco: San Francisco Press, pp. 315-318.
- Presley, T. K., Sinton, J. M. & Pringle, M. (1997). Postshield volcanism and catastrophic mass wasting of the Waianae Volcano, Oahu, Hawaii. *Bulletin of Volcanology* **58** (8), 597-616.
- Presnall, D. C., Dixon, J. R., O'Donnell, T. H. & Dixon, S. A. (1979). Generation of Mid-ocean Ridge Tholeiites. *Journal of Petrology* **20** (1), 3-35.
- Renzulli, A. & Santi, P. (2000). Two-stage fractionation history of the alkali basalt-trachyte series of Sete Cidades volcano (Sao Miguel Island, Azores). *European Journal of Mineralogy* **12**, 469-494.
- Rhodes, J. M. (1995). The 1852 and 1868 Mauna Loa Picrite Eruptions: Clues to Parental Magma Compositions and the Magmatic Plumbing System. In: Rhodes, J. M. & Lockwood, J. P. (eds.) *Mauna Loa Revealed: Structure, Composition, History, and Hazards*. Washington, DC: American Geophysical Union, pp. 241-262.
- Ringwood, A. E. (1975). *Composition and Petrology of the Earth's Mantle*. McGraw Hill: New York.

- Roeder, P. L. & Emslie, R. F. (1970). Olivine-liquid equilibrium. *Contributions to Mineralogy and Petrology* **29**, 275-289.
- Rollinson, H. (1993). *Using geochemical data: evaluation, presentation, interpretation*. Prentice Hall: Harlow, England.
- Rowan, L. R. & Clayton, R. W. (1993). The Three-Dimensional Structure of Kilauea Volcano, Hawaii, From Travel Time Tomography. *Journal of Geophysical Research* **98** (B3), 4355-4375.
- Russ, J. C. (1986). *Practical Stereology*. Plenum Press: New York.
- Rutherford, M. J. & Hill, P. M. (1993). Magma Ascent Rates From Amphibole Breakdown - an Experimental Study Applied to the 1980-1986 Mount St-Helens Eruptions. *Journal of Geophysical Research* **98** (B11), 19667-19685.
- Ryan, M. P. (1988). The mechanics and three-dimensional internal structure of active magmatic systems: Kilauea volcano, Hawaii. *Journal of Geophysical Research* **93** (B5), 4213-4248.
- Sack, R. O., Walker, D. & Carmichael, I. S. E. (1987). Experimental petrology of alkalic lavas: constraints on cotectics of multiple saturation in natural basic liquids. *Contributions to Mineralogy and Petrology* **96** (1), 1-23.
- Schairer, J. F. (1950). The alkali feldspar join in the system NaAlSiO₄-KAlSiO₄-SiO₂. *Journal of Geology* **58**, 512-517.
- Scott, W. E., Hoblitt, R. P., Torres, R. C., Self, S., Martinez, M. M. L. & Nillos, J., Timoteo (1996). Pyroclastic Flows of the June 15, 1991, Climactic Eruption of Mount Pinatubo. In: Newhall, C. G. & Punongbayan, R. S. (eds.) *Fire and Mud:*

- Eruptions and Lahars of Mount Pinatubo, Philippines*. Seattle: University of Washington Press, pp. 545-570.
- Shaoxiong, W. & Nekvasil, H. (1994). SOLVCALC: an interactive graphics program package for calculating the ternary feldspar solvus and for two-feldspar geothermometry. *Computers and Geosciences* **20** (6), 1025-1040.
- Sisson, T. W. & Grove, T. L. (1993). Experimental Investigations of the Role of H₂O in Calc-Alkaline Differentiation and Subduction Zone Magmatism. *Contributions to Mineralogy and Petrology* **113** (2), 143-166.
- Spencer, K. J. & Lindsley, D. H. (1981). A solution model for coexisting iron-titanium oxides. *American Mineralogist* **66**, 1189-1201.
- Spengler, S. R. & Garcia, M. O. (1988). Geochemistry of the Hawi lavas, Kohala volcano, Hawaii. *Contributions to Mineralogy and Petrology* **99** (1), 90-104.
- Stormer, J. C. J. (1983). The effects of recalculation on estimates of temperature and oxygen fugacity from analyses of multicomponent iron-titanium oxides. *American Mineralogist* **68** (5-6), 586-594.
- Tait, S. R., Worner, G., Van Den Bogaard, P. & Schmincke, H. U. (1989). Cumulate nodules as evidence for convective fractionation in a phonolite magma chamber. *Journal of Volcanology and Geothermal Research* **37** (1), 21-37.
- Thompson, G. M., Smith, I. E. M. & Malpas, J. G. (2001). Origin of oceanic phonolites by crystal fractionation and the problem of the Daly gap: an example from Rarotonga. *Contributions to Mineralogy and Petrology* **142** (3), 336-346.

- Thompson, J. B., Jr. (1982). Composition space: an algebraic and geometric approach. In: Ferry, J. M. (ed.) *Characterization of Metamorphism through Mineral Equilibria. Mineralogical Society of America, Reviews in Mineralogy* **10**, pp. 1-31.
- Thy, P. (1991). High and low pressure phase equilibria of a mildly alkalic lava from the 1965 Surtsey eruption: experimental results. *Lithos* **26** (3-4), 223-243.
- Thy, P. & Lofgren, G. E. (1992). Experimental constraints on the low-pressure evolution of transitional and mildly alkalic basalts: multisaturated liquids and coexisting augites. *Contributions to Mineralogy and Petrology* **112** (2-3), 196-202.
- Tuttle, O. F. & Bowen, N. L. (1958). Origin of granite in the light of experimental studies in the system NaAlSi₃O₈-KAlSi₃O₈-SiO₂-H₂O. *Geological Society of America Memoir* **74**, pp. 1-153.
- Wager, R., Brown, G. M. & Wadsworth, W. J. (1960). Types of igneous cumulates. *Journal of Petrology* **1**, 73-85.
- Widom, E., Gill, J. B. & Schmincke, H. U. (1993). Syenite nodules as a long-term record of magmatic activity in Agua de Pao Volcano, Sao Miguel, Azores. *Journal of Petrology* **34** (5), 929-953.
- Wolfe, E. W., Wise, W. S. & Dalrymple, G. B. (1997). The Geology and Petrology of Mauna Kea Volcano, Hawaii - A Study of Postshield Volcanism. *U.S. Geological Survey Professional Paper* **1557**, pp. 129.
- Yoder, H. S. (1976). *Generation of basaltic magma*. National Academy of Sciences: Washington, DC.

Yoder, H. S. & Tilley, C. E. (1962). Origin of basalt magmas: an experimental study of natural and synthetic rock systems. *Journal of Petrology* **3** (3), 342-532.